PERFORMANCE ENHANCEMENT OF DISPOSABLE CHAMBER VALVELESS MICROPUMP THROUGH ANNULAR EXCITATION FOR BIOMEDICAL APPLICATIONS

Thesis

Submitted in partial fulfilment of the requirements for the degree of

DOCTOR OF PHILOSOPHY

By

MOHITH S

DEPARTMENT OF MECHANICAL ENGINEERING

NATIONAL INSTITUTE OF TECHNOLOGY KARNATAKA, SURATHKAL, MANGALORE – 575025

September 2021

Dedicated to my parents

DECLARATION

I hereby declare that the Research Thesis titled **"Performance Enhancement of Disposable Chamber Valveless Micropump through Annular Excitation for Biomedical Applications"** which is being submitted to the **National Institute of Technology Karnataka, Surathkal** in partial fulfillment of the requirements for the award of the Degree of **Doctor of Philosophy** in **Mechanical Engineering** is a *bonafide report of the research work carried out by me*. The material contained in this Research Thesis has not been submitted to any other Universities or Institutes for the award of any degree.

Register Number: 165073 ME16F09

Name of the Research Scholar: MOHITH S

Signature of the Research Scholar:

Department of Mechanical Engineering

National Institute of Technology Karnataka, Surathkal

Place: NITK, Surathkal

Date: 24-09-2021

CERTIFICATE

This is to certify that the Research Thesis titled **"Performance Enhancement of Disposable Chamber Valveless Micropump through Annular Excitation for Biomedical Applications"** submitted by **Mr. Mohith S (Register Number: 165073 ME16F09)** as the record of the research work carried out by him, *is accepted as the Research Thesis submission* in partial fulfilment of the requirements for the award of the Degree of **Doctor of Philosophy.**

Dr. Navin Karanth P

(Research Guide)

Date: 27/09/2021

Prof. S M Kulkarni

(Research Guide)

Date: 27/09/2021

Chairman-DRPC

Date: 01/10/2021

DEPARTMENT OF MECHANICAL ENGINEERING
NATIONAL INSTITUTE OF TECHNOLOGY KARNATAKA, SURATHKAL

ACKNOWLEDGEMENT

ABSTRACT

The precise manipulation of fluid with pumping systems has been a technological challenge in microfluidic applications. Micropumps play a significant role in the accurate delivery of fluids in microfluidic systems. Micropumps find extensive applications in different domains such as biomedical, automobile, electronic cooling systems, chemical and biological analysis. Over the past few years, researchers have emphasized different configurations of the micropump with different actuation principles, valves and chamber designs.

Among different configurations of the micropump, piezo actuated mechanical micropumps find extensive application in microfluidic devices for precise delivery of the fluids. The precise and accurate delivery of fluid with piezo actuated micropump enables them to be extensively implemented in biomedical applications. Other advantages of piezo actuated micropump include reliability, miniaturization, the flexibility of integration with subsystems, and quick response. Considering the advantageous feature of the piezo actuated micropump, the present study proposes a novel disposable chamber valveless micropump actuated through an amplified piezoelectric actuator for biomedical applications.

Piezoelectric mechanical micropumps are characterized by the oscillating diaphragm, which deforms under the action of force developed by the piezoelectric actuators inside the pump chamber. The deformation of the diaphragm leads to variation in pressure and volume inside the pump chamber, which in turn pumps the fluid. The performance of the piezo actuated micropump majorly depends on actuator configuration, diaphragm design/actuation principle and valve/chamber design. The proposed micropump is designed with the unique feature of a disposable chamber and employs an amplified piezoelectric actuator as the primary source of actuation. Integrating the disposable chamber as a separate entity with the reusable actuator allows disposal of the chamber after use, thus eliminating the risk of infection or contagion. The retrofit actuator can be reused to accommodate a new chamber for biomedical application.

The micropump is made of polymeric materials like Polymethylmethacrylate (PMMA), Silicone rubber with different parts fabricated through CNC milling, laser cutting, and moulding operation. The micropump chamber, nozzle/diffusers, and the bossed diaphragm constituted the disposable part, and the amplified piezo actuator with structural support formed the reusable part of the micropump. The bossed diaphragm of the pump chamber consists of a central cylindrical protrusion which reduces the formation of wrinkles, allows uniform distribution of stress and transmits force required for micropump actuation. The valveless configuration of the micropump provides the advantage of the static geometric structure free from clogging, blockage, wear and fatigue failure.

Since the deflection of the bossed diaphragm greatly influences the performance of the mechanical micropump, the present work is emphasized on the enhancement of the deflection of the bossed diaphragm, which in turn can enhance the volumetric performance of the micropump. Conventionally the bossed diaphragm is subjected to excitation force on the central bossed region. The application of excitation force on the central bossed region limits the deflection range of the bossed diaphragm. Therefore a novel annular excitation approach is proposed to enhance the deflection range where the diaphragm is subjected to excitation away from the central bossed region.

A detailed study is carried out to compare the deflection behaviour of both central and annular excitation of the bossed diaphragm. The appropriate theoretical background is presented to analyze the amplified piezoelectric actuator, actuation mechanism and the bossed diaphragm. Finite element analysis is carried out to analyze the deflection behaviour of the amplified piezoelectric actuator, actuation mechanism and the bossed diaphragm under central and annular excitation. Experimental characterization is performed to validate the results obtained from finite element analysis of the centrally excited and annularly excited bossed diaphragm.

The experimental characterization is carried out to determine the optimal performance parameters of the micropump with water, fluids mimicking blood plasma,

and whole blood. Initial characterization considered micropump with the centrally excited bossed diaphragm. The effects of factor such as bossed ratio, diaphragm thickness, depth of the micropump chamber, and viscosity of the fluid is considered to optimize the performance of the micropump with central excitation. The second phase of the micropump characterization considered the novel approach of annular excitation of the bossed diaphragm. Characterization of the micropump with central excitation followed a similar approach to that of the micropump with central excitation.

The maximum simulated deflection of the annularly excited bossed diaphragm with the actuation parameters of 150 V, 45.5 Hz is about 1998.4 µm which is far superior to the deflection value 725.91 µm achieved with the centrally excited bossed diaphragm at 150 V, 9.96 Hz. The corresponding maximum deflection measured with the experimental characterization of annularly excited and centrally excited bossed diaphragm is about 1953.4±8.00 µm at 150 V, 43.5 Hz and 717.99±4.00 µm at 150 V, 9.5 Hz. Thus, the annular excitation method for bossed diaphragm delivers a higher deflection range compared with the conventional method of central excitation. The proposed micropump with central excitation delivered the maximum water flow rate of about 7.192±0.147 ml/min and backpressure of 294 Pa at 150 V, 5 Hz. However, the enhancement of the deflection characteristics of the bossed diaphragm under annular excitation leads to performance enhancement of the micropump with the flow rate of 95.10±0.444 ml/min and backpressure of 1472 Pa at 150, 30 Hz.

Keywords: *Valveless Micropump, Bossed Diaphragm, Central Excitation, Annular Excitation, Amplified Piezo Actuator, Blood Mimicking Fluid*

LIST OF CONTNETS

LIST OF FIGURES

LIST OF TABLES

NOMENCLATURE

$K_{piezostack}$	Stiffness of the Piezo Stack
V	Applied Voltage
$(\Delta_{piezostack})_{Free}$	Free Deflection of the Piezo Stack
$(F_{blocked})_{Piezostack}$	Blocked Force of the Piezo Stack
A.F	Amplification Factor
$(\Delta_{piezostack})_{APA}$	Free Deflection of the Amplified Piezo Actuator
$(F_{blocked})_{APA}$	Blocked Force of the Amplified Piezo Actuator
F_{APA}	Force Applied by the Amplified Piezo Actuator
K_{APA}	Stiffness of the Amplified Piezo Actuator
K_{eff}	Effective Stiffness of the Diaphragm
$(K_{eff})_{Central}$	Effective Stiffness of the Centrally Excited Bossed Diaphragm
$(K_{eff})_{Annular}$	Effective Stiffness of the Annularly Excited Bossed Diaphragm
B_r	Bossed Ratio of Diaphragm
y_b	Centre Deflection of the Diaphragm
E	Young's Modulus of the Diaphragm Material
D	Flexural Rigidity of the Diaphragm
γ	Poisson's Ratio of the Diaphragm Material
K_{eff}	Effective Stiffness of the Diaphragm
t	Thickness of the Diaphragm
F_e	Elastic Force of the Diaphragm
F_{ad}	Adhesive Force of the Diaphragm
F_a	Actuation Force
C_{ad}	Adhesive Force Coefficient
r_b	Radius of the Bossed Region
r_c	Radius of the Pump Chamber
r_l	Loading Radius
h_c	Chamber Depth

h_l	Depth of the Residual Liquid
V	Actuation Voltage
f	Frequency of Actuation
Q	Flow Rate of the Micropump
ε	Strain Vector,
D	Electric Displacement
c	Compliance Matrix
d	Piezoelectric Coefficient
e	Dielectric Permittivity
σ	Applied Stress
D	Diameter of the Pump Chamber
d_{ti}	Inner diameter of the Inlet/Outlet Tube
d_{to}	Outer diameter of the Inlet/Outlet Tube
L	Length of the channel of the Nozzle/Diffuser
W_1	Width of the Inlet of the Nozzle/Diffuser
W_2	Width of the Outlet of the Nozzle/Diffuser
θ	Angle of Divergence of the Nozzle/Diffuser
ρ	Density of the Fluid
$\boldsymbol{\eta}$	Dynamic Viscosity of the Fluid

CHAPTER 1

INTRODUCTION

1.1 Miniaturized Fluidic Systems

The rapid growth of sub-millimetre and microscale engineering in recent years has resulted in the development of miniaturized systems and devices. Miniaturization mainly aims at reducing the size of the system with reduced cost and improved performance. A miniaturized device has the advantage of higher speed, lower price, portability, use of disposable materials, lower sample volume, low energy requirements, etc.(Wong and Iwai 2005). The potential advantages of miniaturization have motivated many researchers to develop miniaturized systems which can handle fluids and liquids in the microscale to the nanoscale range. This motivation has led to the development of microfluidics through an integrated approach incorporating micro-scale engineering and fluid mechanics. Microfluidics mainly deals with the manipulation and analysis of the small volume of fluids or liquids. Microfluidic devices are a class of miniaturized pumping systems that can pump, mix, monitor and control the minute volume of the fluids (Sackmann et al. 2014).

Microfluidics proved to be very efficient in chemistry, medicine, biology, molecular analysis, bio-defence, molecular biology, microelectronics, pharmaceuticals, and automobile engineering. Typical applications of microfluidic systems include chemical analysis, biological and chemical sensing, drug delivery, molecular separation, electronic cooling, and environmental monitoring. Precision fluidic control systems for automotive, aerospace and machine tool industries also incorporate the microfluidic systems in their applications (Whitesides 2006; Zhang et al. 2007; Lei 2012). Many researchers have contributed significantly to microfluidics which has led to the development of different microfluidic devices like micropumps, micro-mixers, micro-valves, micro-filters, micro-reactors, and micro-separators for specific applications (Zhang et al. 2007; Lei 2012).

1.2 Miniaturized Pumping Systems

Considering the requirement of microfluidic systems to handle fluid at micro to the nanoscale, researchers and scientists have realized the need for a pumping system that can deliver a minute quantity of fluid at a required pressure sufficient to make the fluid flow through the microfluidic systems. The essential components of a miniaturized pumping system include a miniaturized pump (micropump), reservoir of fluid for pumped and received fluid, flow sensor for flow measurement, signal conditioner unit and a controller for the flow parameters as shown in Figure 1.1.
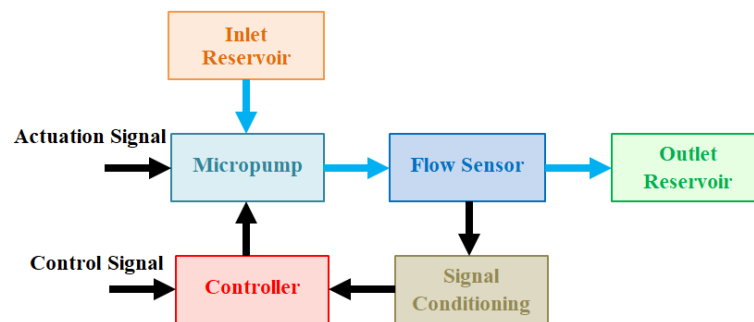
Figure 1.1 Schematic of the miniaturized pumping system

The need for accurate delivery of fluid has resulted in different micropumps with different actuation principles and fabrication technologies. A micropump is a device that can transfer or deliver the working fluid (liquid or gas) at accurate volume from a reservoir to a target. The potential advantages of the micropump include the precise delivery of fluid in microliters to milliliters per second or per minute, the flexibility of integration with different electromechanical systems with effective space reduction (Laser and Santiago 2004; Tsai and Sue 2007; Iverson and Garimella 2008; Wang and Fu 2018). Micropumps incorporated in the microfluidic systems should possess sufficient flow control, a wide range of flow rate, lower power consumption, and high back pressure (Ashraf et al. 2011; Nisar et al. 2008).

1.3 History of the Micropump Development

Different approaches to the development of micropumps are available in literature since their introduction in the late 1970s. Figure 1.2 represents the significant ones carried out between the years 1970 to 1990. The micropump concept

developed by Spencer W J et al. (1978) is the first-ever attempt that incorporated a piezoelectric actuator with active valves to achieve a flow and pressure of 19 µcc/V and 1 mm of Hg/V, respectively. Since this micropump is actuated at a maximum voltage of 100 V, the corresponding pumped volume and pressure are about 1.9µl and 13.33 kPa. The similar concept of micropump is later extended by Van Lintel et al. (1988) with the introduction of passive check valves resulting in an optimal flow of 0.008 ml/min at an input voltage of 100 V at 1 Hz frequency. Stemme and Stemme (1993) presented an improvised concept of micropump with the valveless configuration by using the nozzle/diffuser, which achieved an optimal flow rate of 16 ml/min with a back pressure of 19.6 kPa at 20 V, 100 Hz. The above researchers marked the beginning of micropump development, which built a strong foundation for many researchers to come up with improvised concepts with different geometry, actuation mechanism and fabrication technologies for various applications.
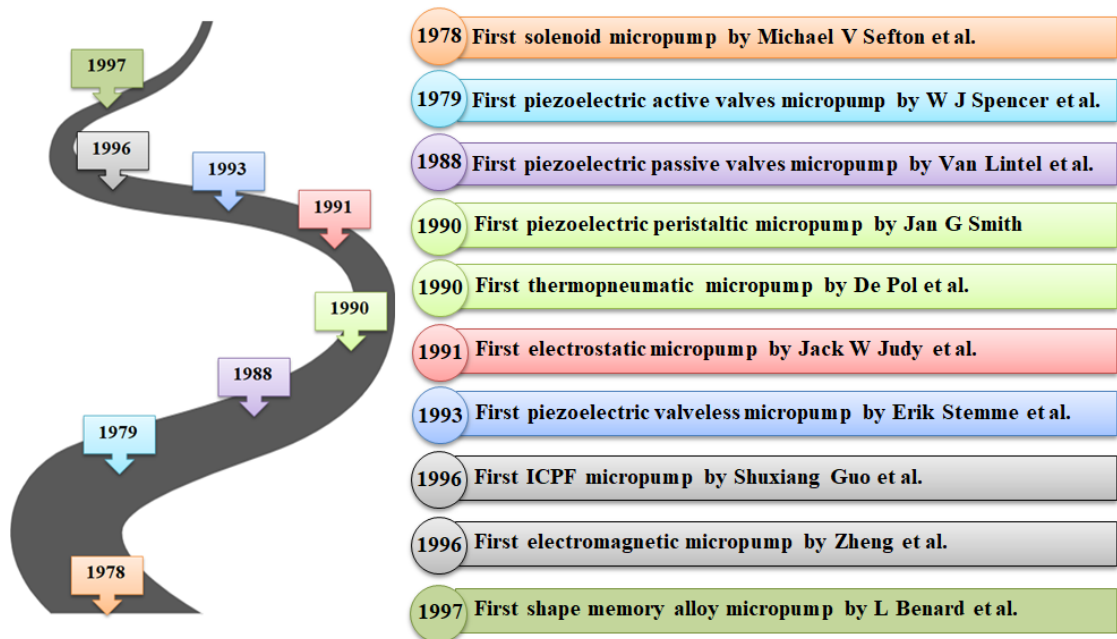
Figure 1.2 History of the micropump development

1.4 Applications of the Micropump

The early stage of micropump development is for delivery/dispensing therapeutic drugs. Micropumps developed between the years 1978 to 1988 are mainly intended to deliver insulin for maintaining the blood sugar level in diabetic patients

(Clemens 1980; Sefton and Burns 1981; Sefton 1982). Further, medical conditions like bone infection, cancer, and tumours have employed micropumps for drug delivery into cancerous cells and bloodstreams (RajSuryanarayanan 1992; Dash and Cudworth 1998). Precise metering and drug distribution at the required rate is an essential aspect of the micropump used for drug delivery/dosing applications (Nisar et al. 2008). Capable of delivering fluid at a micro-nano scale mainly through the microchannels, micropumps have gained considerable significance in chemical/biological analysis systems in the form of µTAS (Micro Total Analysis System). The µTAS with micro pumping systems intends to reduce the quantities of samples and reagents used in the analysis within a limited time and reduced manual intervention. DNA analysis, genomics, proteomics, amplification, sequencing or synthesis of nucleic acids, drug discovery, clinical diagnosis, environmental and food analysis etc. are some of the application areas of µTAS, which incorporates effective pumping mechanisms. Such pumping systems can deliver fluids from pico-litres to micro-litres. Factors like fluid viscosity, pH value, chemical stability, corrosion temperature are considered significant in the design of the micropumps for analysis systems (Tüdos et al. 2001; Reyes et al. 2002; Laser and Santiago 2004; Li 2005). Figure 1.3 highlights the most common applications and timeline of the establishment of micropump in different domain.
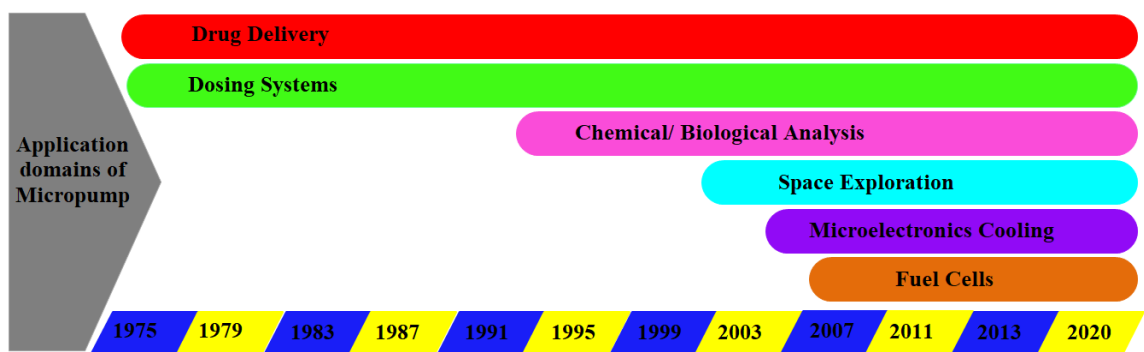
Figure 1.3 Establishment of the micropump applications in different domains

Micropumps find application in space explorations also for assisting the propulsion of mini/microsatellites or space crafts. The reduced size and weight of the micropump technology allow them to integrate with the satellites easily. Since the working medium for propulsion is in gaseous form, larger stroke volumes are required

4

to pump the gases at a pressure sufficient to lift the satellites/spacecraft (Dugue et al. 2001; Xiong et al. 2002; Krpoun and Shea 2009). Micropumps have also served the purpose of continuous heat dissipation in space-constrained electronics through single-phase or two-phase cooling. Capable of delivering liquids or air through the microchannels, the micropumps are effectively used in cooling application resulting in enhanced performance of the electronic devices. Since the flow of fluid associated with the heat sink is through channels, fluid at higher pressures are required, which can reduce the temperature gradient resulting in dissipation of a large amount of heat (Darabi and Ekula 2003; Singhal et al. 2004; Garimella et al. 2006; Sung and Mudawar 2009). Fuel cells that convert chemical energy into electrical energy either in a proton exchange fuel cell (PEMFC) or direct methanol fuel cell (DMFC) employ miniaturized pumps to a greater extent. The application of micropump in the automobile domain mainly focuses on the accurate delivery of liquid fuel (methanol) (Luharuka et al. 2004; Zhang and Wang 2005; Yang et al. 2006).

1.5 Classifications of the Micropump

Micropumps are categorized into two categories, namely mechanical micropumps and non-mechanical micropumps (Laser and Santiago 2004). Mechanical micropumps are characterized by moving mechanical parts like an oscillating diaphragm or a rotor which exerts pressure on the working fluid for pumping. Non-mechanical micropumps convert the non-mechanical energy into kinetic energy, which is utilized to pump the fluid. Figure 1.4 shows the broad classification of the micropumps. Mechanical micropumps, also termed displacement micropumps develop a pulsating flow due to their periodic nature.

Further, displacement pumps fall under reciprocating/oscillating type, incorporating an oscillating diaphragm or reciprocating piston and rotary type with vanes or gears. Most of the micropumps reported are of diaphragm/membrane-type with an actuator causing the oscillations of thin diaphragm/membrane leading to the flow of fluid (Tsai and Sue 2007; Iverson and Garimella 2008; Laser and Santiago 2004; Nisar et al. 2008; Ashraf et al. 2011). A pulsating flow occurs as a result of the oscillating nature of the mechanical micropumps. Centrifugal type micropump is also

a mechanical pump with limited miniaturization due to lower effectiveness at lower Reynolds's number (Laser and Santiago 2004). The diaphragm type micropumps are further categorized based on the type of actuators used for micropump actuation, flow rectification/valve mechanisms and the micropump chamber design.
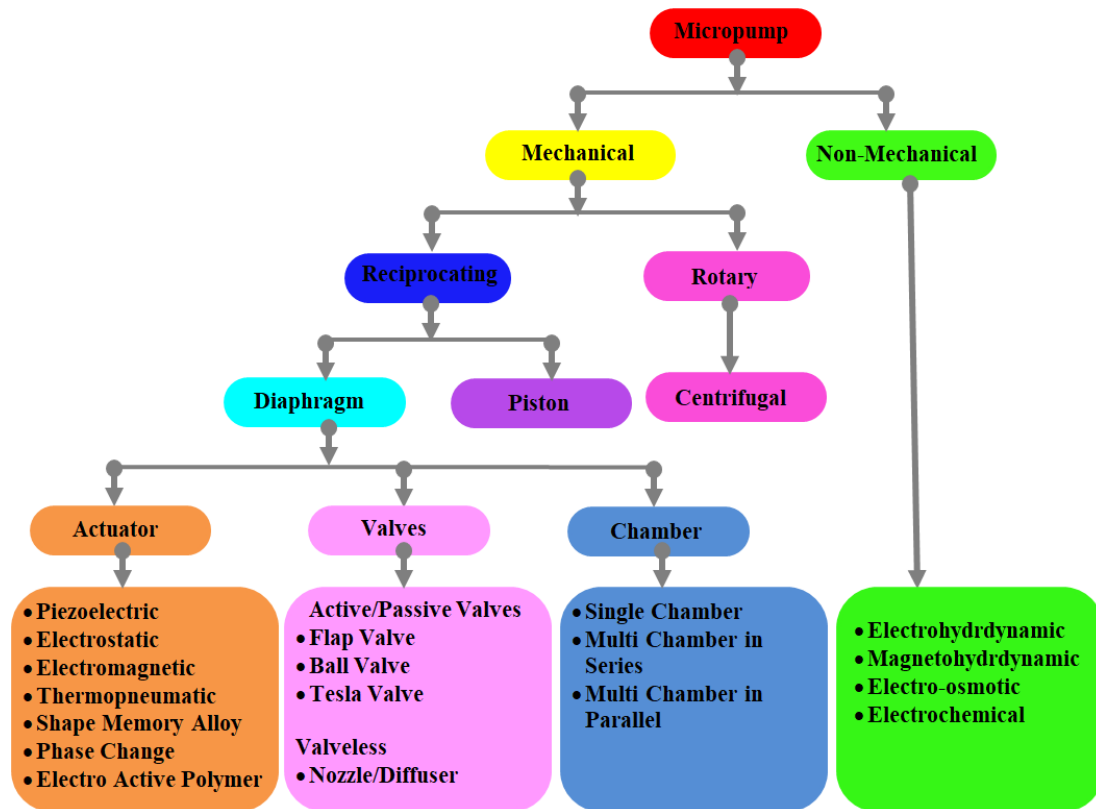
Figure 1.4 Classification of the micropump

The non-mechanical micropumps involve direct interaction with the working fluid through electrical, magnetic or chemical means (Laser and Santiago 2004; Nisar et al. 2008; Zhou et al. 2016). Non-mechanical micropumps deliver a continuous flow of fluids; thus, non-mechanical micropumps are also termed continuous micropumps. The non-mechanical micropumps offer great potential for miniaturization and possess fewer moving parts when compared with mechanical micropumps. However, the phenomenon responsible for pumping fluid in non-mechanical micropumps is practical only on the micro-scale. Since fluid flow occurs due to multi-physics interaction, there is a significant challenge in modelling and quantifying flow characteristics. Besides, some of the dynamic micropumps work with some specific

6

type of fluids. All these limitations of non-mechanical micropump lead to the extensive exploration of mechanical micropumps for different applications.

1.6 Mechanical (Displacement Type) Micropumps

Mechanical micropumps incorporate a reciprocating diaphragm actuated by a physical actuator for pumping the fluid. The general construction of the mechanical/displacement pump consists of a pumping chamber, flexible diaphragm, an actuator, inlet and outlet (Wang and Fu 2018). Oscillations or reciprocation of the membrane/diaphragm in a mechanical micropump occurs through a physical actuator which generates the necessary pressure difference required for pumping the fluid. Figure 1.5 represents the schematic representation of the working principle of the mechanical micropump. The non-directional flow generated by the oscillating diaphragm gets converted to directional flow through the flow rectification mechanism. Typically the mechanical micropumps consider micro-valves such as check valves, ball valves for flow rectification.

The oscillation of the diaphragm causes increased chamber volume, which in turn leads to a decrease in the pressure inside the pumping chamber. This pressure drop causes the fluid to flow from the high-pressure reservoir to the pumping chamber through the inlet while the outlet valve remains closed (Figure 1.5(c)). This phase of the micropump operation corresponds to the supply mode. The flexing of the diaphragm in the opposite direction leads to increased chamber pressure due to decreased chamber volume. This, in turn, leads to the outflow of the fluid from the chamber through the outlet with the inlet valve closed, which corresponds to pumping mode (Figure 1.5(d)). Micropump incorporates two microvalves, namely passive or active valves (Tsai and Sue 2007; Iverson and Garimella 2008; Nisar et al. 2008). Active Valves operates with an actuator that directs the opening and closing of the valve during suction and delivery, whereas passive valves operate by the pressure difference between the inlet and outlet generated due to the oscillation of the diaphragm.
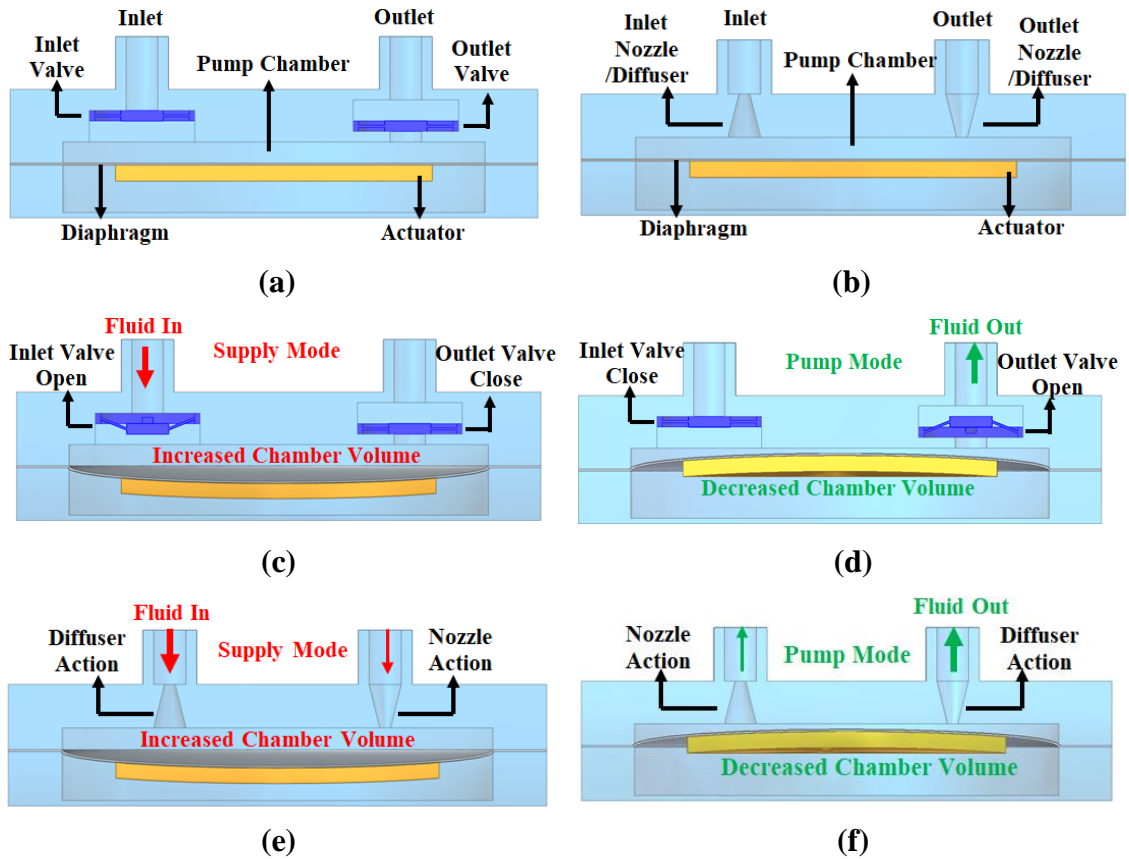
Figure 1.5 (a) Mechanical micropump with valves **(b)** Valveless mechanical micropump **(c)** Supply mode of the micropump with valves **(d)** Pumping mode the micropump with valves **(e)** Supply mode of the valveless micropump **(f)** Pumping mode of the valveless micropump

The flow rectification in mechanical micropumps can also be achieved through the integration of valveless configuration. A valveless micropump does not involve check valves; instead incorporates a static nozzle/diffuser, which performs the functions of valves. During the supply mode, the inlet element acts as a diffuser that offers lower rectification (Figure 1.5 (e)). Thus a significant amount of fluid gets transported through the inlet into the chamber. At the same time, the outlet element acts as a nozzle with higher rectification and minimizes the reverse flow of fluid pumped in the previous cycle. The reverse phenomena occur during the pumping mode, where the outlet acts as a diffuser and inlet as the nozzle (Figure 1.5 (f)). As a result, a larger volume of the fluid flows out of the chamber through the outlet with a

minor portion of the flow through the inlet nozzle (Laser and Santiago 2004; Tsai and Sue 2007; Iverson and Garimella 2008; Nisar et al. 2008; Ashraf et al. 2011).
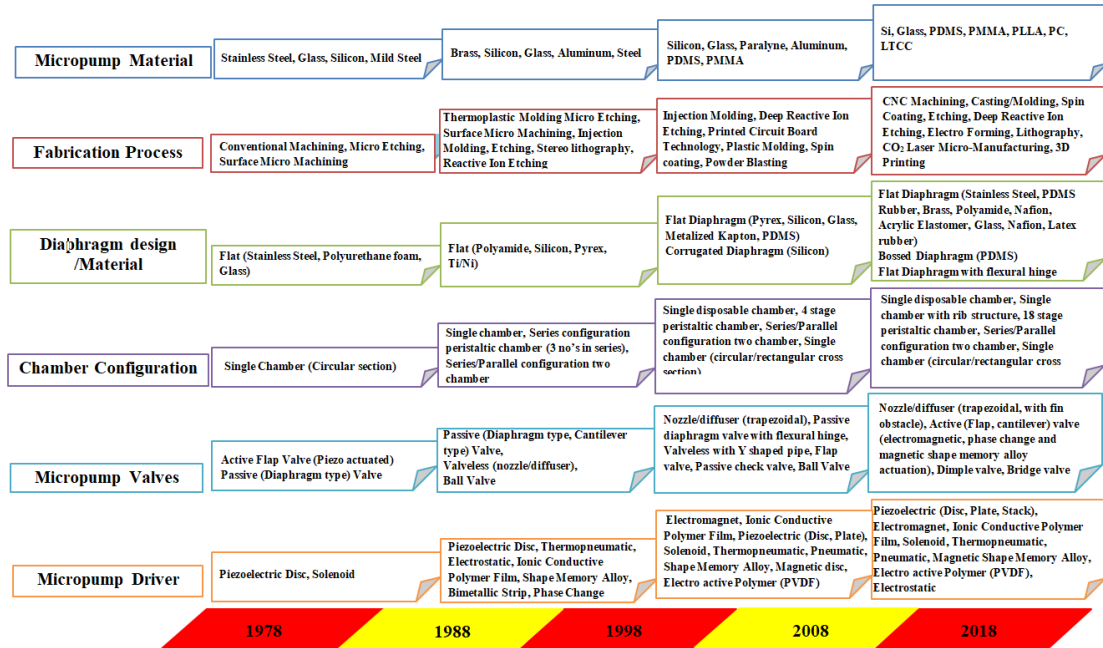
Figure 1.6 Timeline of the mechanical micropump development

The majority of the work carried out in micropump technology is of mechanical/displacement type. Large numbers of researchers have contributed to the development of micropump technology since the introduction of micropump by Spencer et al. (1978). The research work on displacement type micropump always emphasised performance enhancement to have a higher flow rate and higher pressure with accurate flow control. Figure 1.6 represents the timeline of mechanical micropump development from the early 1970s to the present. It is evident from Figure 1.6 that the mechanical micropumps development has travelled a long way in aspects like the actuation principles, flow rectification valves, chamber design, diaphragm design, materials and fabrication process of micropump and micropump materials. A detailed literature review of the mechanical micropump reported over the past few years is presented in chapter 2.

9

1.7 Organization of the Thesis

The present thesis focuses on developing disposable chamber valveless micropump for biomedical applications such as drug delivery, pumping of biological fluids, etc. The thesis consists of 5 charters. The organization of the thesis is as follows.

In **Chapter 2**, a detailed literature review about the mechanical micropump is presented. The literature review focuses on different types of mechanical micropumps, their working principles and performance factors. Further, the literature review also addresses different types of piezoelectric actuators and actuation principles for the micropump. The literature review is concluded with the potential research gap and the objectives of the proposed work.

Chapter 3 discusses the methodology adopted in the development of valveless disposable micropump. In the present work, two configurations of the micropump are proposed. The micropump configuration consisted of bossed diaphragm subjected to central excitation and annular excitation. Detailed theoretical analysis and Finite Element analysis of the diaphragm and actuator configuration is presented. Further, the fabrication and experimental characterization of the proposed micropump is also illustrated.

Chapter 4 aims at presenting the results of the proposed work. The results and discussion mainly focus on the characterization of the actuator, diaphragm and micropump configurations. The comparative study between the Finite Element analysis and experimental characterization of the actuator and the diaphragm is presented. Finally, chapter 4 concludes with the performance assessment of the central and annular configuration of the micropump.

Finally, in **Chapter 5**, the essential findings and conclusions of the present work are summarized and presented.

LITERATURE REVIEW

2.1 Mechanical Micropumps

Due to the constant need for miniaturized systems in microfluidics, many researchers have come up with different types of mechanical micropump for numerous applications. Micropump is a device that helps to pump liquid or gases at the required rate and pressure. Micropump offers the flexibility of integration into different subsystems with the added advantage of accurate and precise flow in micro and millilitres range. The actuation principles implemented for mechanical micropump involve electrical, thermal or magnetic energy. Piezoelectric, electromagnetic, electrostatic, shape memory alloy (SMA), thermo-pneumatic, phase change, ionic conductive polymer film (ICPF), dielectric elastomer film (DEF) are some of the actuators implemented in mechanical micropumps.

The working principle of different types of mechanical micropumps in the valveless configuration is shown in Figure 2.1 to Figure 2.7. The mechanical micropump with valves also follows a similar working principle with the flexible diaphragm integrated with the pump chamber. The difference exists in the principle of flow rectification achieved with valves, as illustrated in Figure 1.5. A detailed summary of the key features of recently reported mechanical micropumps, emphasizing micropump actuators, material/fabrication, flow rectification mechanisms, optimal performance parameters such as flow rate and pressure, and optimal operating parameters geometrical features are presented in Table 2.1 to Table 2.7.

2.1.1 Drivers/ Actuators

Piezoelectric drivers are one of the most common forms of micropump actuation reported by many researchers. Figure 2.1 represents the schematic of the working principle of the piezoelectric actuated micropump. The piezoelectric material is bonded onto a thin, flexible diaphragm which, when subjected to an AC voltage, undergoes bending due to the conversion of electrical energy into mechanical strain

(Polcawich 2009; Aksel and Jones 2010; Minase et al. 2010). The diaphragm deflects due to the mechanical strain developed by the piezo actuator, resulting in pressure variation inside the pump chamber. This pressure variation, in turn, results in the inflow and outflow of the fluid. The performance of piezo-actuated micropump mainly depends on stroke volume governed by the mechanical strain produced.

The polarization limit of the material and the applied voltage determines the mechanical strain, thus controlling the flow rate of the micropump (Laser and Santiago 2004). Most of the Piezo micropumps reported have implemented piezo actuators in the form of a circular disc with the range of diameter (8 mm to 30 mm) and thickness (0.06 mm to 0.215 mm) (Wang et al.2008; Hwang et al. 2008; Dau et al. 2009; Kim et al. 2009; Verma et al. 2009; Wang et al.2010; Luo et al. 2011; Choi et al. 2012; Guan et al. 2012; Guo et al. 2012; Park et al. 2013; Wei et al. 2014; Pečar et al. 2014; Ma et al. 2015; Singh et al. 2015; Cheng et al. 2017). Other forms of the piezo actuator having rectangular cross-section (20 mm × 40 mm) (Singh et al. 2015) and square-shaped (5.5 × 5.5 mm, 4 × 4 mm, 8 × 8 mm) (Aggarwal et al. 2017; Cheng et al. 2017) piezo plate, multi-layered piezo stack actuator (Park et al. 2013) are also reported for micropump actuation. Most of the piezo actuators reported for micropump actuation are readily available in the form of discs or plates (Murata Technologies, Ariose Electronics Taiwan, Sunny Tech Electronics Co. Ltd, APC Int Ltd, USA, etc.), and some of the actuators are made in-house through powder hot pressing (Zhang and Eitel 2013), screen printing (Tseng et al. 2013) and dry powder deposition processes (Cheng et al. 2017).
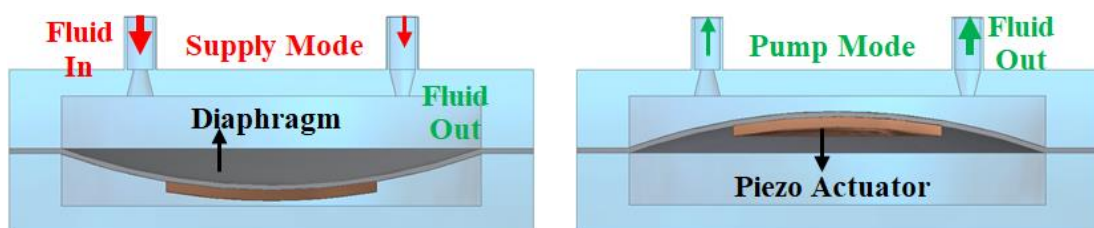
Figure 2.1 Working principle of the mechanical micropump with piezoelectric actuation

Figure 2.2 represents the schematic of the micropump with electromagnetic actuation. Magnetic/electromagnetic micropump works on the principle of generation of repulsive and attractive forces between the permanent magnet and drive coil on the application of electric current, which in turn oscillates the diaphragm or membrane (McDonald et al. 2004; Pan et al. 2005; Chang et al. 2007). The micro-drive coils for electromagnetic actuation are made of materials like Copper and Chromium fabricated through processes such as electron beam evaporation (Lee et al. 2008), electroplating (Ke et al. 2012) PCB based technology (Chang et al. 2013) on a glass substrate. The permanent magnets used are of Neodymium magnet (NdFeB) (Lee et al. 2008; Zhi et al. 2012), which are either attached or embedded into the flexible diaphragm.
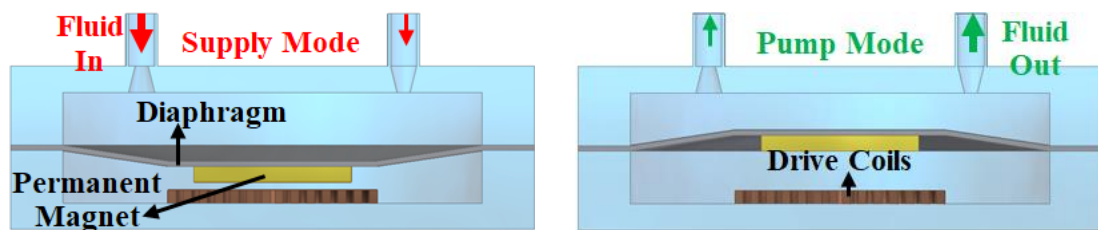
Figure 2.2 Working principle of the mechanical micropump with electromagnetic actuation

Micropump with thermopneumatic and phase change actuation works on the same principle except for the medium used for actuation. Figure 2.3 and Figure 2.4 show the schematic of thermopneumatic and phase change micropump, respectively. Continuous thermal expansion and contraction of air or phase changing material in the secondary chamber exert pressure on the diaphragm surface, causing it to deflect (Nguyen et al. 2002; Kim et al. 2005; Mamanee et al. 2006; Ogden et al. 2014). Phase change actuation employs paraffin, perfluro compounds that undergo a phase transition when subjected to heating cycle (Bodén et al. 2008; Yoo et al. 2008; Svensson et al. 2010; Mousoulis et al. 2011). The source of heat generation is through micro heater made of Chromium/Gold (Cr/Au) (Lin et al. 2008), Platinum/Chromium (Pt/Cr) (Chee et al. 2015) deposited on to glass substrate through Electron Beam Evaporation. Materials like methyl perfluoropropyl ether undergo a phase transition at

the normal skin temperature of the human body. Thus such materials can be utilized as a source of actuation for skin contact actuated micropumps for medical applications (Mousoulis et al. 2011).
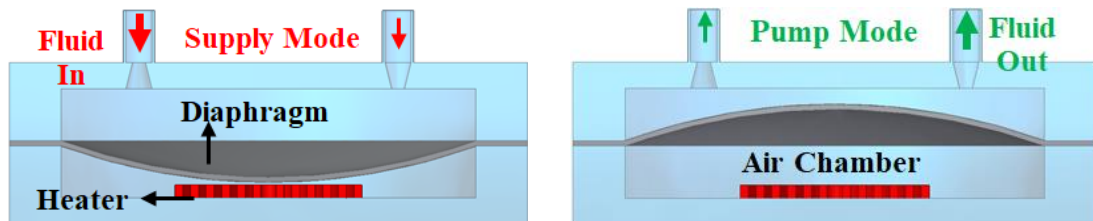
Figure 2.3 Working principle of the mechanical micropump with thermopneumatic actuation
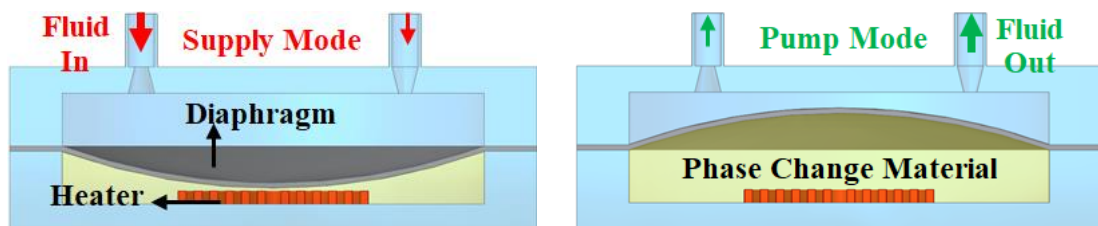
Figure 2.4 Working principle of the mechanical micropump with phase change actuation

The actuation of micropump through the shape memory alloy (SMA) employs either thermal or magnetic source. These materials can undergo a solid phase transition between the austenitic phase at high temperature and the martensitic phase at low temperature. This phase transition phenomenon is reversible, which allows it to remember its original shape and regain it. Mechanical strain developed during the phase transition results in deformation of the micropump membrane (Makino et al. 2001; Fu et al. 2004; Guo et al. 2008; Zainal et al. 2015). Thus, fluid flow occurs due to the change in pump chamber volume, as shown in Figure 2.5. Ni/Ti is the most common form of SMA materials used in micropump actuation, which undergoes the phase transition between 49 °C to 55 °C (Sun et al. 2009). Ni/T Ni–Mn–Ga is another class of magnetic SMA that undergoes deformation in the presence of a magnetic field (Ullakko et al. 2012; Smith et al. 2015).

15
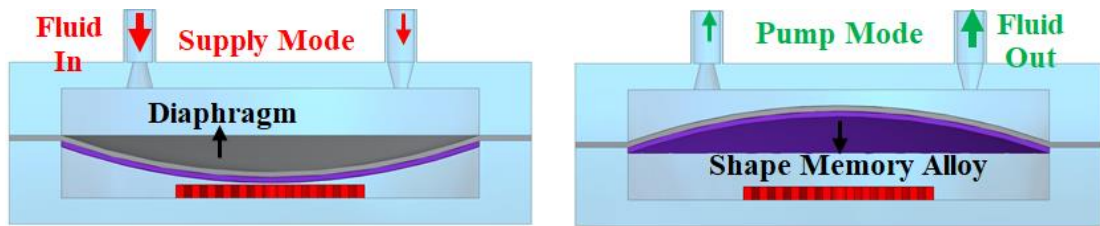
Figure 2.5 Working principle of the mechanical micropump with shape memory alloy actuation

The electrostatic micropump utilizes the force of attraction and repulsion generated between the electrodes, which actuate a flexible diaphragm, as shown in Figure 2.6. Upon application of an electric potential across the electrodes attached to the membrane and pump body, the generated electrostatic force causes the diaphragm to flex, causing a change in chamber volume (increased) and pressure (decreased), resulting in the flow of fluid inside the chamber (MacHauf et al. 2005; E. Paul Braineard and Enoch Amoatey Tetteh 2014; Conrad et al. 2015). Thus pulsating flow is achieved because of continuous change in diaphragm momentum due to the applied voltage. The electrodes usually employ Chromium/Gold Chromium (Cr/Au/Cr), Boron (B) (Kim et al. 2015), and Aluminum (Al) by sputtering, deep reactive ion etching (DRIE). The amount of fluid delivered by electrostatic actuated micropump mainly depends on the diaphragm deflection, which is governed by the electrostatic force generated, which depends on applied electric potential.
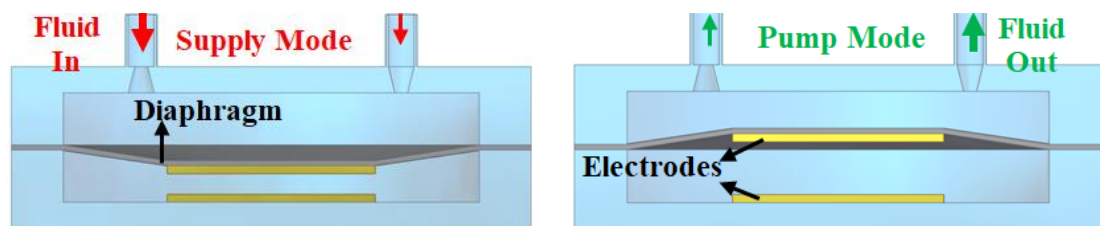
Figure 2.6 Working principle of the mechanical micropump with electro-static actuation

Electro-active polymers (EPA) are another class of material used for micropump actuation, which undergoes deformation in the presence of the electric

16

field. The schematic of the micropump actuation with EPA is as shown in Figure 2.7. EPA actuator consists of a polymer membrane sandwiched between the flexible, compliant electrodes. Application of an external electric field across the electrodes, the polymer films experiences a compressive electrostatic force, leading to horizontal expansion wrapping in the direction of the restricted surface. This, in turn, causes the deformation of the diaphragm bonded onto its surface (Uchida et al. 2002; Guo and Asaka 2003; Pak et al. 2004; Loverich et al. 2006; O'Halloran et al. 2008; Rosset et al. 2009). Deformation of the diaphragm causes variation of pump chamber volume and pressure leading to inflow and outflow of the fluid. Ionic conductive polymer film (ICPF) and dielectric elastomer (DEA) are the two types of EPA reported for micropump actuation. ICPF actuated micropump reported to use Nafion (0.18 mm - 0.6 mm thickness) as an actuator coated with a conductive surface of Gold, Silver or Platinum. The DEA for micropump includes Acrylic elastomers (0.33 mm – 0.5 mm thickness) (VHB 4910 from 3M, USA). The photographs of mechanical micropump with different actuation principles reported by different researchers in recent years are shown in Figure 2.8, Figure 2.9 and Figure 2.10.
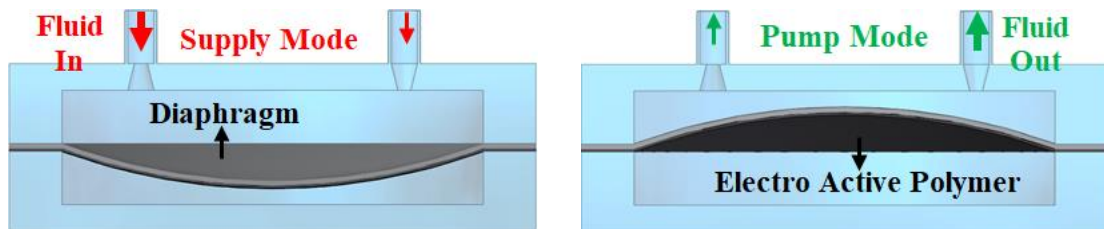
Figure 2.7 Working principle of the mechanical micropump with electro active polymer actuation
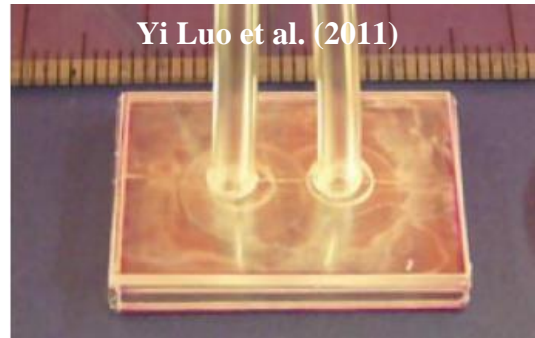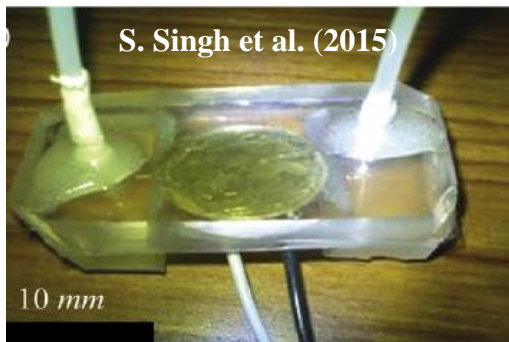
(a) Piezoelectric actuated micropump
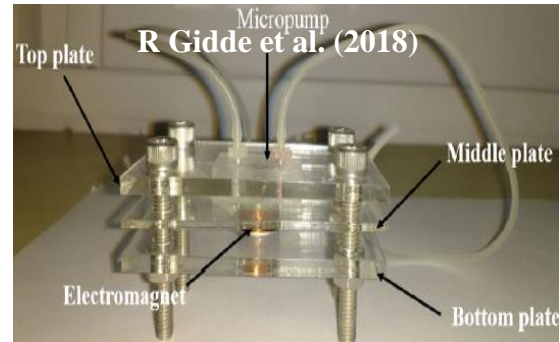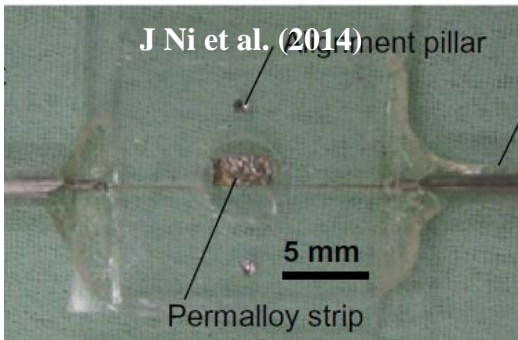
(b) Electromagnetic actuated micropump
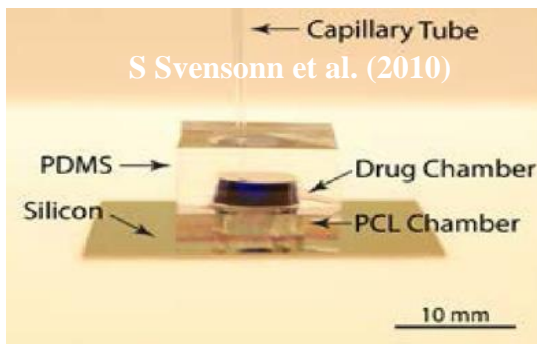
(c) Phase Change actuated micropump

Figure 2.8 (a) Piezoelectric actuated micropump **(b)** Electromagnetic actuated micropump **(c)** Phase Change actuated micropump

Table 2.1 Recently reported mechanical micropump with the piezoelectric actuation

First Author	Structure	Type of Valve	No. of Chambers	Working Fluid	Voltage (V)	Frequency (Hz)	Pressure (kPa)	Flow rate (ml/min)	Size (mm³)
Hwang et al.(2008)	Si-Glass	Valveless	1	Water	150	420	----	0.037	----
Wang et al.(2008)	Si	Valveless	2	Alcohol	120	250	7.7	1.5	----
Kim et al.(2009)	Brass	None	1	----	300	50000	0.940	0.118	----
Dau et al.(2009)	Si	None	1	----	50	7900	0.28	5.2	1×0.01×0.005
Verma et al.(2010)	Si	Valveless	1	Ethanol	6	250	0.743	2.4	30×70
Wang et al.(2010)	PMMA	Valveless	1	DI Water	150	250	1.37	0.6	----
Hwang et al.(2010)	----	None	1	DI Water	25	4	4.8	6.4	----
Luo et al.(2011)	PMMA	Check Valves	1	Water	150	875	14.95	16.4	----
Choi et al.(2011)	PMMA	Valveless	1	Water	320	45	0.912	23	50×50
Guo et al.(2012)	Glass-Si-Cu	Valveless	2	-----	110	2700	----	0.1517	16 ×22×5
Guan et al.(2012)	PDMS	None	1	-----	100	60	0.657	0.345	------
Park et al.(2013)	SS	Check Valves	1	DI water	150	1000	14	3.7	21.75×20×20
Zhang et al.(2013)	LTCC	Valveless	3	Water	100	100	1.55	0.63	15×15×1.2
Tseng et al.(2013)	SS-PMMA	Valveless	1	DI water	160	400	5.3	1.2	------
Wie et al.(2014)	Electropolymer	Valveless	1	DI water	80	3000	10	0.038	---
Pečar et al.(2015)	PDMS-Glass	None	1	DI Water	230	75	36	0.24	---
Singh et al.(2015)	PDMS	Valveless	1	DI water	30	200	0.22	0.02	---
Cheng et al.(2015)	Glass-Ni-SS	None	1	DI water	200	18400	2.35	0.24	16×9×1
Ma et al.(2008)	PMMA	Check Valves	1	Water	80	20	0.2	6.21	---
Ma et al.(2008)	PMMA	Valveless	1	Water	70	70	---	9.1	---
Aggarwal et al.(2008)	Si	Valveless	1	Water	80	1050	3.125	0.35574	10×10
Kant et al.(2008)	PMMA-PDMS	Valveless	1	DI Water	100	128	4.93	0.497	90×75×60
Munas et al.(2008)	PMMA	None	1	Water	20	100	0.245	30.72	100×60×5.5

Table 2.2 Recently reported mechanical micropump with the electromagnetic actuation

First Author	Structure	Type of Valve	No. of Chambers	Working Fluid	Voltage (V)	Frequency (Hz)	Pressure (kPa)	Flow rate (ml/min)	Size (mm³)
Lee et al. (2008)	Glass	None	1	Water	---	720	---	7.2	26×19×4.5
Zhou et al. (2009)	PDMS	Valveless	2	----	---	3	----	0.02773	----
Wang et al. (2010)	Rubber	None	1	Water	---	240	0.57	0.528	26×15×2.5
Zhou et al. (2011)	PDMS	Valveless	1	DI water	---	36.9	0.931	0.3196	20×12×3.5
Shen et al. (2011)	PDMS	Check Valves	3	Water	0.7	12.5	7	2.4	----
Zhi et al. (2012)	TFPM-PDMS	Valveless	1	Ethanol	7.5	15	---	0.130	20×20×6
Ke et al. (2012)	PMMA-PDMS	Ball Valve	1	Water	3	15	0.25	13.2	---
Chang et al. (2013)	PDMS	Valveless	1	DI water	---	5	---	0.47	---
Ni et al. (2014)	PDMS	Check Valves	1	---	---	2	0.55	0.00026	1.5×1.5×0.4
Sima et al. (2015)	PMMA	Ball Valve	1	DI water	----	7.3	1.5	29.4	----
Kawun et al. (2016)	PDMS	Valveless	1	Water	5	12	0.245	0.135	----
Kumar et al. (2016)	PDMS	Valveless	1	DI water	5	20	0.441	0.336	----
Said et al. (2017)	Glass-Si	Valveless	1	---	10	1	---	0.0066	---
Gidde et al. (2018)	PDMS	Valveless	1	DI water	5.3	45	0.35	0.441	----

Table 2.3 Recently reported mechanical micropump with the phase change actuation

Author	Structure	Type of Valves	Chambers	Working Fluid	Voltage (V)	Frequency (Hz)	Pressure (kPa)	Flow rate (ml/min)	Size (mm³)
Boden et al. (2008)	SS-Polyamide	Check Valves	3	Water	1.8	0.21	5000	0.001	---
Yoo et al. (2008)	PDMS	None	2	DI water	----	0.7	----	2.00×10^{-3}	----
Svensson et al. (2010)	SS	Check Valves	3	---	1.5	0.6	9000	0.0063	---
Mousoulis et al. (2011)	PDMS	None	1	DI water	---	---	28.9	0.0288	14×14×8
Boden et al. (2014)	SS-Polyamide	Check Valves	1	Water	7.5	---	2000	0.0012	---
Huang et al. (2014)	Si	None	1	DI water	12.5	60	----	0.270	----

Table 2.4 Recently reported mechanical micropump with the thermopneumatic actuation

Micropump with Thermopneumatic Actuation									
First Author	Structure	Type of Valves	Chambers	Working Fluid	Voltage (V)	Frequency (Hz)	Pressure (kPa)	Flow rate (ml/min)	Size (mm^3)
Lin et al. (2008)	PDMS-Glass	Valveless	1	DI water	4	1	-----	13.23×10^{-6}	----
Liao et al. (2008)	Glass-Si-PDMS	None	3	DI water	5	1.5	0.4	0.002	----
Yang et al. (2009)	PDMS-Glass	None	3	Water	5	1.5	0.397	0.00918	16×18×5.5
Ha et al. (2009)	PDMS-Glass	Check Valves	1	DI water	---	0.3	---	0.08	---
Ha et al. (2011)	PDMS-Glass	None	3	Water	9	1.2	0.49	0.0201	16×18×5
Yang et al. (2011)	PDMS-Glass	Valveless	1	-----	4	1	$1.00\text{x}10^{-5}$	12.3×10^{-6}	---
Ochoa et al. (2012)	PDMS	None	1	Water	----	----	5.86	0.23×10^{-3}	15×15×10
Chee et al. (2015)	PDMS	None	1	Water	---	---	0.4065	0.00286	22×7×4
Chee et al. (2016)	PDMS-Glass	Valveless	1	DI water	----	----	---	0.10205	----
Hamid et al. (2017)	Glass-Si-PDMS	Valveless	1	DI water	12	---	---	1.25×10^{-6}	---
Landari (2017)	PDMS	None	1	Water	11	4	69	0.007	20×20×10

Table 2.5 Recently reported mechanical micropump with the Shape Memory Alloy actuation

Micropump with Shape Memory Alloy Actuation/Magnetic Shape Memory Alloy									
First Author	Structure	Type of Valves	No. of Chambers	Working Fluid	Voltage (V)	Frequency (Hz)	Pressure (kPa)	Flow rate (ml/min)	Size (mm^3)
Guo et al. (2008)	Latex	Check Valve	4	----	9	0.55-0.6	---	3.2	---
Sun et al. (2008)	Latex	None	4	----	2.5	0.1-0.3	---	0.8	80×30×28
Sassa et al. (2012)	PDMS	None	1	----	---	0.15	---	0.06384	25×10×2.5
Ullakkp et al. (2012)	Glass	None	1	DNA	---	---	---	0.252	---
Smith et al. (2015)	Polycarbonate	None	1	Water	---	270	---	1.798	17.5×10×4.7
Saren et al. (2018)	Plastic	None	1	Water	---	320	----	1.6	11×3.1×2.3

Table 2.6 Recently reported mechanical micropump with the electrostatic actuation

Micropump with Electrostatic Actuation									
Author	Structure	Type of Valves	No. of Chambers	Working Fluid	Voltage (V)	Frequency (Hz)	Pressure (kPa)	Flow rate (ml/min)	Size (mm^3)
Lee et al. (2009)	Si	Check Valve	9	Air	100	2800	7.3	0.29	
Lee et al. (2013)	Si	None	1	Air	160	1400	---	0.248	---
Gao et al. (2015)	Si-PDMS	None	1	HT-70	150	1	---	0.06	---
Jeong et al. (2015)	Si-PDMS	None	1	Water	115	2200	---	0.07536	----
Kim et al. (2015)	Si	Check Valve	9	Air	100	17000	12.8	4	25.1×19.1×1
Lee et al. (2016)	Si-Glass	None	1	Water	90	15	---	0.136	---
Uhliget et al. (2018)	Si	Check Valve	1	Isopropanol	100	17000	210	0.001	10×10×0.9

Table 2.7 Recently reported mechanical micropump with the electro active polymer actuation

Micropump with Ionic Conductive Polymer Film (Electro Active Polymer)									
First Author	Structure	Type of Valves	No. of Chambers	Working Fluid	Voltage (V)	Frequency (Hz)	Pressure (kPa)	Flow rate (ml/min)	Size (mm^3)
Nguyun et al. (2008)	PMMA	Check Valve	1	Water	3	3	1.5	0.76	20×20×5
Wie et al. (2010)	PDMS	Check Valve	1	Water	5	2	---	0.202	30×30×27
Santos et al. (2010)	PMMA	Valveless	1	Water	---	0.1	---	0.0082	---
Shoji et al. (2016)	PMMA	Check Valve	1	Water	2	0.5	---	0.3	---
Micropump with Dielectric Elastomer (Electro Active Polymer)									
Pang et al. (2009)	PMMA	Valveless	1	---	4000	0.5	---	0.078	10×16×4.16
Li et al. (2009)	PMMA	Valveless	1	Water	3000	8	---	0.0212	16×10×3
Chee et al. (2016)	PMMA	Valveless	1	Water	4200	3	---	2.52	40×30×7
Ghazali et al. (2017)	PMMA	Valveless	1	Water	4200	3	---	0.042	---
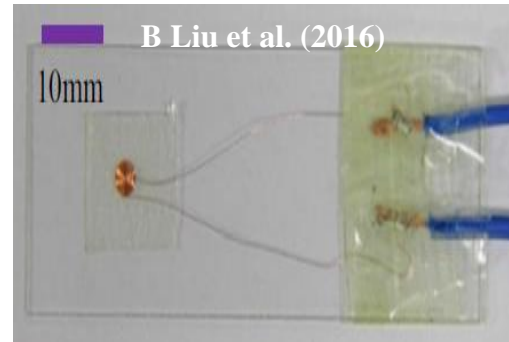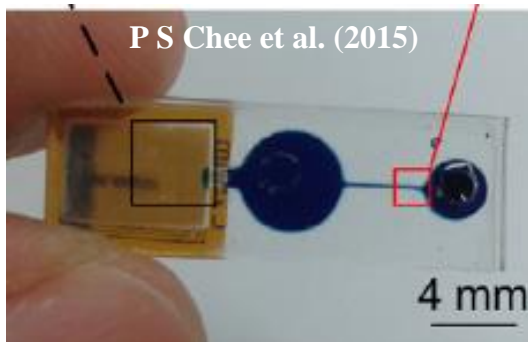
(a) Thermopneumatic actuated micropump
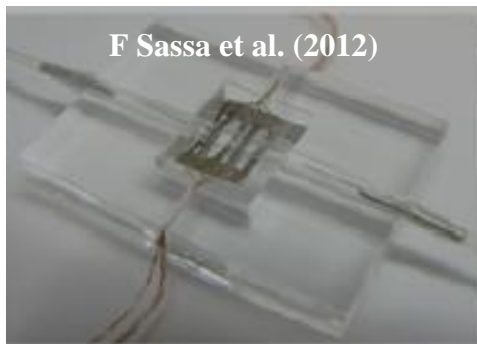
(b) Shape memory alloy actuated micropump
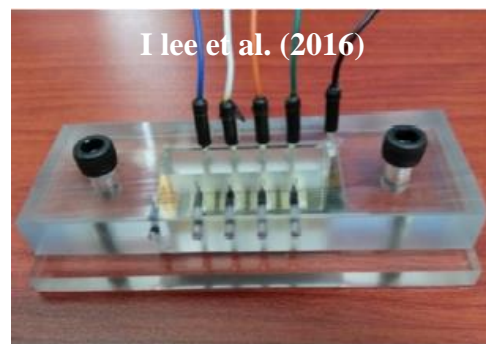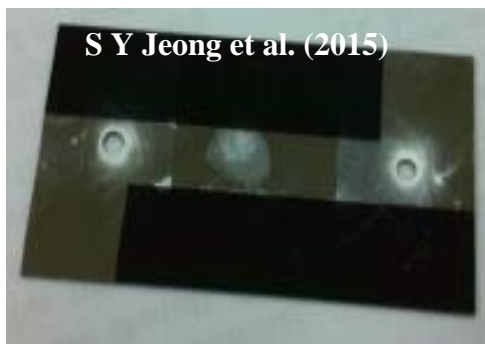
(c) Electrostatic actuated micropump

Figure 2.9 (a) Thermopneumatic actuated micropump **(b)** Shape memory alloy actuated micropump **(c)** Electrostatic actuated micropump
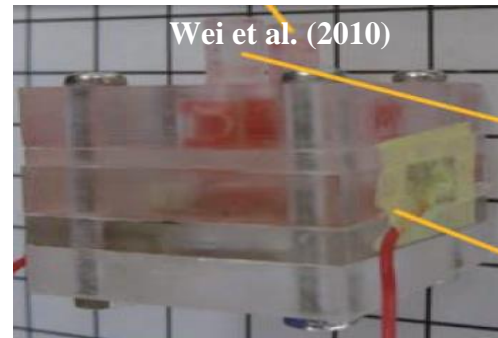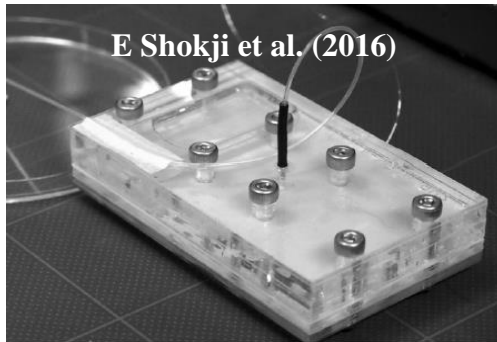
(a) Dielectric Elastomer actuated micropump
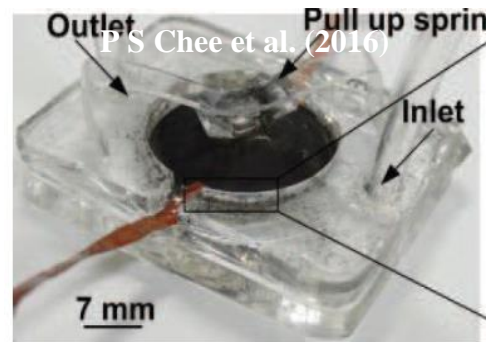
(b) Ionic Conductive Polymer Film actuated micropump

Figure 2.10 (a) Dielectric elastomer actuated micropump **(b)** Ionic Conductive Polymer Film actuated micropump

The performance of mechanical micropump with the emphasis on flow rate and pressure significantly depends on the type of actuator used. Since the mechanical micropumps consist of an oscillating diaphragm, the deflection of the diaphragm determines the swept volume, which in turn depends on the driver configuration. The comparison of performance and operating parameters of recently reported actuation schemes of the mechanical micropump is shown in Figure 2.11 and Figure 2.12. Among all the actuation principles, the flow rate increases with the increase in actuation voltage and frequency. The resonating frequency of the diaphragm determines the optimal flow.
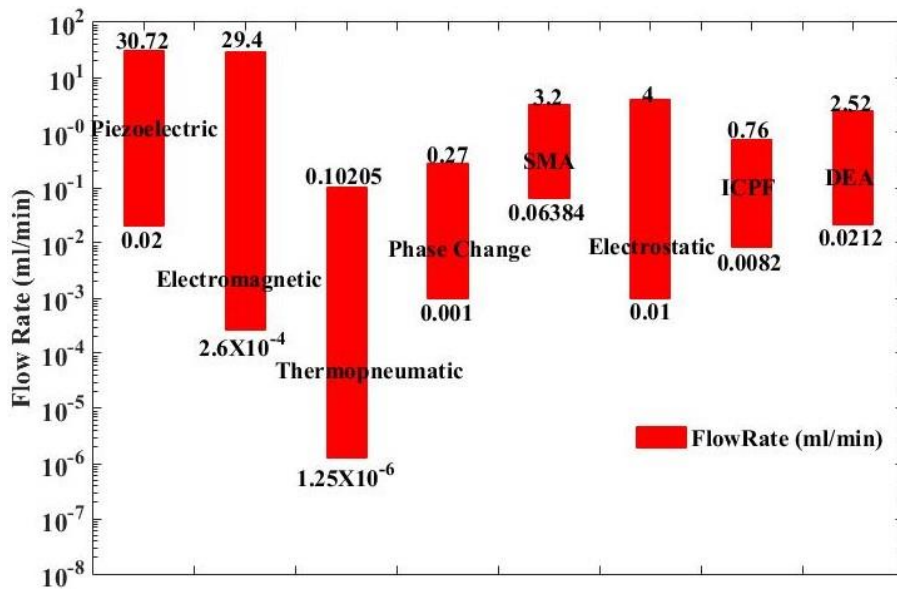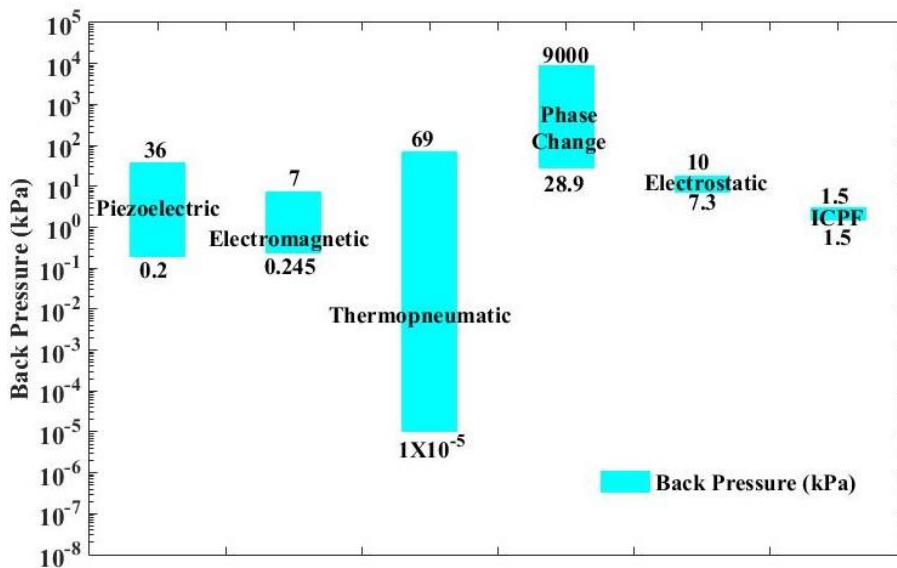
Figure 2.11 Range of **(a)** Flow Rate and **(b)** Back Pressure of the mechanical micropumps with different actuation principles

Piezoelectric actuators are one of the earliest and most commonly used drivers for mechanical micropump. Higher actuation forces coupled with faster response are the key features of the piezoelectric actuators. The typical actuation voltage of the piezo actuator varies between 1 V to 320 V and frequency response of about 50 kHz. The precise control of volume flow from micropump could be achieved with proper control of input voltage to the piezo actuator, which controls the diaphragm deflection.

Circular piezoelectric drivers are found to have a deflection of about 7 μm to 13 μm for a voltage range of 30 V to 200 V (Hwang et al. 2008; Dau et al. 2009; Park et al. 2013; Kant et al. 2017). Materials processing and difficulty in the attachment to the diaphragm are significant disadvantages associated with piezoelectric actuators (Iverson and Garimella 2008; Dong 2012).
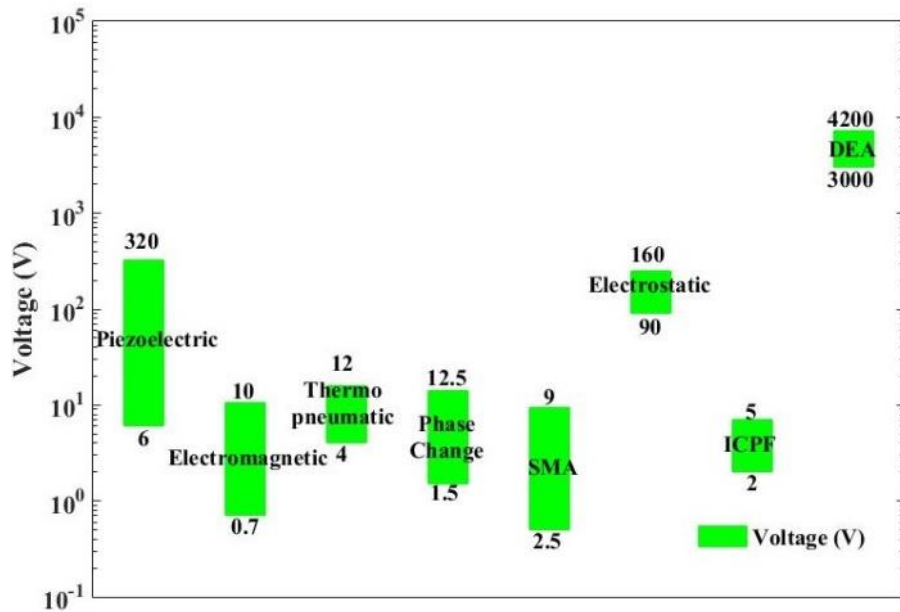
(a)
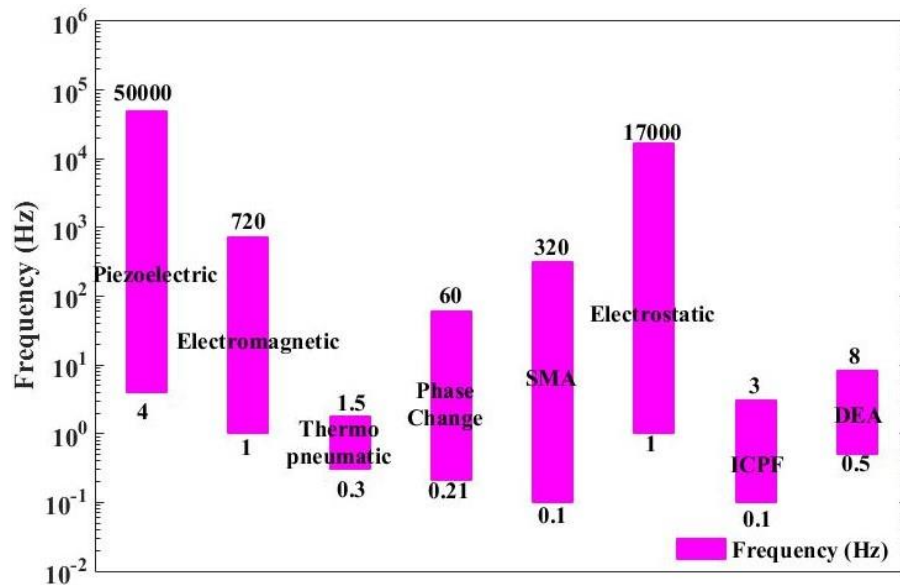
(b)

Figure 2.12 Range of **(a)** Voltage **(b)** Frequency of the mechanical micropumps with different actuation principles

The electromagnetic actuators offer the advantage of higher membrane deflection since they can generate higher force. The other benefits include low voltage actuation, the short response time (Chang et al. 2007; Dong 2012). These actuators have actuation voltage and current ranging between 0.7 V to 10 V and 0.2 A to 7.8 A, with driving frequency ranging between 1 Hz to 720 Hz. PDMS diaphragm with electromagnetic actuation can achieve a deflection range of 1.8 μm to 110 μm when supplied with 0.2 A to 1 A of current (Lee et al. 2008; Wang et al. 2010; Ke et al. 2012; ZHI et al. 2012; Chang et al. 2013; Kumar et al. 2016; Gidde et al. 2019). Electromagnetic actuation offers disadvantages of higher power consumption, heat dissipation and the difficulties associated with integrating magnets and driver coils into the micropump assembly (Dong 2012; Wang et al. 2010b).

With the thermopneumatic/phase change actuation, a higher flow rate could be achieved because of its ability to induce high pressure resulting in higher membrane deflection at lower actuation voltages. Typically thermopneumatic/phase change actuation involves heat as a source of input for pumping the fluid. Most of the thermopneumatic micropump reported in the past consists of electron beam deposited Chromium/Gold (Cr/Au), Titanium/Gold (Ti/Au) or Chromium/Platinum (Cr/Pt) heater element. The literature shows that the air heating and cooling cycle of the thermopneumatic micropump varies from about 20 °C to 63.5 °C. Ha et al. (2009) proposed a Cr/Au heater based thermopneumatic micropump with a heating cycle of 40 °C to 20 °C. The thermopneumatic micropump proposed by Yang et al. (2011) consisted of Cr/Au heater, which achieved a maximum pneumatic chamber temperature of 47 °C, which then cools to room temperature of 25 °C. However, the optimal pumping rate is achieved between the heating and cooling cycle of 40 °C to 25 °C. Similarly, optimal performance is achieved with a thermopneumatic micropump proposed by Hamid et al. (2017) in the temperature range of 33.5°C to 63.5°C with Cr/Pt heater. In terms of voltage and actuation frequency, the operating parameters of the thermopneumatic micropump vary in the range 4 V - 11 V, 1 Hz - 4 Hz.

Boden et al. (2008) proposed the micropump incorporated with paraffin as a phase-changing material with a melting range of 44 °C to 48 °C. The effective pumping of this micropump is observed in the heating cycle between room temperature to 46 °C.

Mousoulis et al. (2011) proposed a micropump with 3M^{TM} Flourinert liquid as a working medium that has a boiling point of 50 °C. However, the operating temperature of this micropump is found to be at 31 °C. The typical voltage and frequency for phase change type micropump range between 1.8 V - 12.5 V, 0.21 Hz - 60 Hz. Diaphragm deflection of about 60 µm to 70 µm is achievable with these actuators at 6 V to 7.5 V. The major drawback which limits the application of thermopneumatic/phase change actuation is that they have reduced response time, especially during the cooling process and low frequency of operation. In addition to this, phase change actuation has a limitation on materials used as a medium for actuation (Nguyen et al. 2002; Ogden et al. 2014).

Shape Memory Alloys as an actuator in micropump has the advantages of high force to volume ratio, high damping capacity, stress and strain recovery upon heating and cooling, chemical resistance, biocompatibility. Unpredictable deformation behaviour due to temperature sensitivity, high power consumption, and a poor cooling rate at high-frequency operations are some of the disadvantages of SMA actuators (Fu et al. 2004; Zainal et al. 2015). Further, small scale integration with high frequency (1 Hz – 17 kHz) operation is easily achievable with Electrostatic actuation. Also, these actuators consume less power, a lower voltage (100 V to 160 V), and a faster response. The lower displacement range limits micropump performance with electrostatic actuation leading to a lower flow rate (Lee et al. 2009; Conrad et al. 2015).

EPA actuators have the advantage of large deformability and faster response but have poor repeatability, affecting micropump performance. ICPF actuation has the lowest actuation voltage range between 2 V - 5 V and a frequency of 0.5 Hz to 3 Hz. Difficulties in the fabrication of ICPF limits its application in micropump actuation (Thanh Tung Nguyenet al. 2008; Santos et al. 2010; Wei and Guo 2010; Shoji 2016). DEA actuators require very high voltage for actuation, which is a significant disadvantage when used as a micropump actuation source. The typical range of DEA actuation voltage is between 3000 V to 4200 V and frequency response is 0.5 Hz to 8 Hz (Pang et al. 2009; Li et al. 2009; Chee et al. 2016; Mohd Ghazali et al. 2017;).

The piezoelectric, electromagnetic and thermopneumatic actuators are reported extensively for micropump actuation, as evident from Table 2.1 to Table 2.7. The phase change type and ICPF actuator are found to have relatively lower actuation voltage when compared with other types of actuation. The piezoelectric actuation resulted in higher flow rate, whereas phase change type actuated micropump could pump the fluid against higher backpressure.

2.1.2 Mechanical Micropump Valves

The flow rectification principle at the inlet and outlet of the pump chamber significantly influence its performance. Usually, the flow rectification of the fluid occurs through microvalves at the inlet and the outlets, which convert the non-directional flow into a directional flow. The selection of flow rectification methods mainly depends on closing pressure, response type, micropump efficiency, material compatibility, etc. (Au et al. 2011; Zhang et al. 2007). Check valves and static geometry valves (nozzle/diffusers) serve to provide directionality to the working fluid.

Most of the literature available on mechanical micropumps has implemented check valves, ball valves that have dynamic characteristics. The check valves or flap valves are usually of rectangular cross-section (cantilever type) or circular cross-section (bridge type) made of materials like silicon (Si), glass or polydimethylsiloxane (PDMS) Ke et al. 2012 ; Ma et al. 2015; Walczak et al. 2017). Figure 2.13 represents the schematic of the microvalves used in mechanical micropumps. The check valves reported for micropumps are either passive type which operates based on the pressure variation inside the chamber (Park et al. 2013)(Ma et al. 2015)(Ni et al. 2014), or active type, which are driven through dedicated actuators. Piezoelectric (Sefton et al. 1979; Zhang et al. 2014; Bonhoeffer et al. 2017), electrostatic (Lee et al. 2009; Yildirim et al. 2012; Kim et al. 2015) , phase change (Bodén et al. 2008; Svensson et al. 2010; Bodén et al. 2014) are of the actuation principles adopted in active valves. Ball valves are also an excellent candidate for flow rectification in the micropump application (Ke et al. 2012; Sima et al. 2015). Table 2.8 and Table 2.9 summarize the different types of microvalves incorporated in the recent micropump.
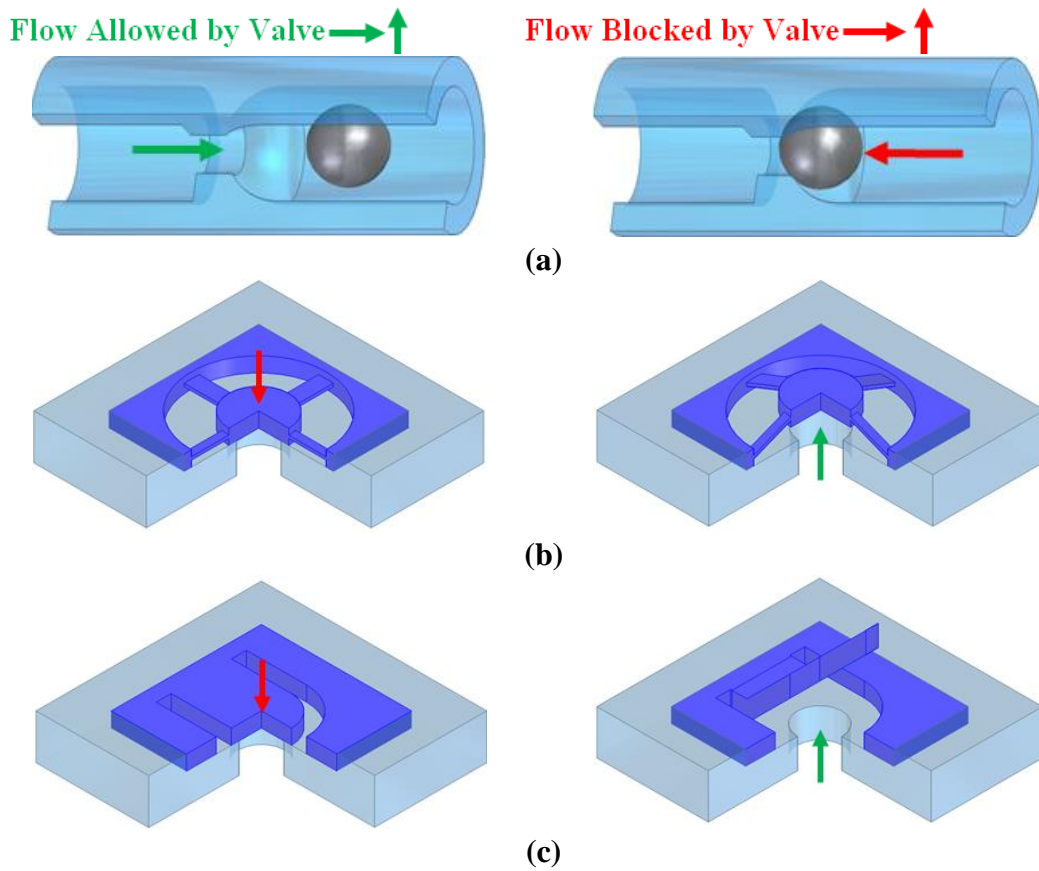
Figure 2.13 (a) Ball valve **(b)** Bridge type check valve **(c)** Cantilever type flap check valve
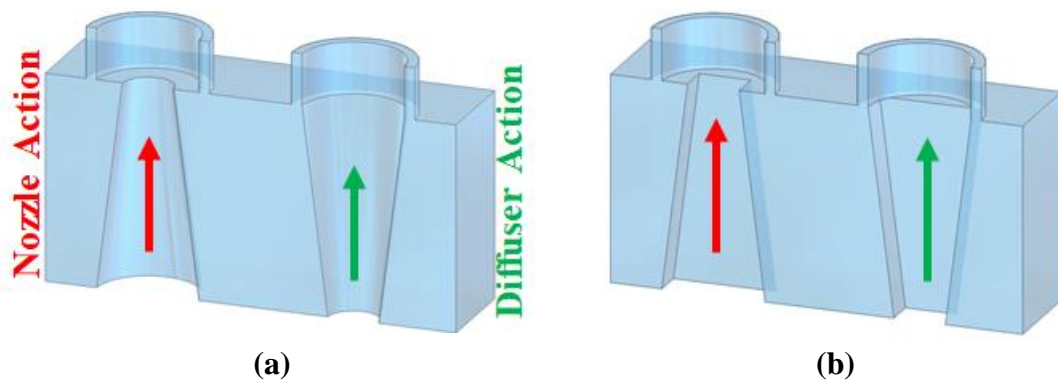
Figure 2.14 (a) Conical Nozzle/Diffuser **(b)** Trapezoidal Nozzle/Diffuser

The second category of flow rectification mechanism employed in mechanical micropumps involves static geometry nozzle/diffusers, which do not include any moving parts. Micropumps with such static geometrical arrangement of the flow

rectification are termed valveless micropumps. The performance of such nozzles/diffusers mainly depends on the inlet/outlet dimensions, channel length and the channel angle (Figure 2.14) (Yuan et al. 2014; Wang et al. 2015). Most of the valveless micropumps have incorporated a flat and conical type of nozzles/diffusers. Table 2.10 represents the complete descriptions of the flat and conical nozzle/diffuser implemented in the recent micropump study. The static behaviour of the nozzle/diffuser is advantageous in overcoming the problems of wear and fatigue failure that exits in check valves.

Table 2.8 Geometrical and performance features of active check valve implemented in mechanical micropump

Active Valves						
First Author	Valve Actuation	Valve Material	Micropump Actuation	Geometry (mm^3)	Flow Rate (ml/min)	Pressure (kPa)
Bode´n et al. (2008)	Phase Change	----	Phase Change	---	0.001	5000
Lee et al. (2009)	Electrostatic	Pyraline	Electrostatic	---	0.29	7.3
Svensson et al. (2010)	Phase Change	SS	Phase Change	---	0.0063	9000
Boden et al. (2014)	Phase Change	Polyamide	Phase Change	---	0.0012	2000
Kim et al. (2015)	Electrostatic	Pyraline	Electrostatic	2×2×0.003	4	12.8

Table 2.9 Geometrical and performance features of passive check valve implemented in mechanical micropump

Passive Valves with Rectangular Cross Section					
Author	Valve Material	Micropump Actuation	Valve Geometry (mm^3)	Flow Rate (ml/min)	Pressure (kPa)
Park et al. (2013)	SS	Piezoelectric	1.24×2.37×0.12	3.7	14
Ni et al. (2014)	PDMS	Electromagnetic	0.35×0.16×0.06	0.00026	0.55
Nguyen et al. (2008)	PDMS	ICPF	3×2×0.5	0.76	1.5
Shoji et al. (2016)	Rubber	ICPF	0.5	0.3	----
Passive Valves with Circular Cross Section					
Author	Valve Material	Micropump Actuation	Valve Diameter(mm)	Valve Thickness (mm)	Flow Rate (ml/min)	Pressure (kPa)
Ma et al. (2015)	PDMS	Piezoelectric	5.8	0.3	6.21	0.2
Ball Type Check Valve					
Author	Valve Material	Micropump Actuation	Ball Diameter (mm)	Flow Rate (ml/min)	Pressure (kPa)
Ke et al. (2012)	Glass-SS	Electromagnetic	2	13.2	0.25
Sima et al. (2015)	Glass-SS	Electromagnetic	2	29.4	1.5

Table 2.10 Geometrical and performance features of nozzle/diffuser (valveless) implemented in mechanical micropump

First Author	Valve Material	Micropump Actuation	Inlet Diameter (mm)	Outlet Diameter (mm)	Channel Length (mm)	Channel Angle	Flow rate (ml/min)	Pressure (kPa)
Conical Nozzle/Diffuser								
Verma et al. (2009)	Si	Piezoelecrtric	0.53	----	5.3	10 °	2.4	0.743
Kang et al. (2016)	PMMA	Piezoelecrtric	0.53	1.18	4.7	10 °	9.1	----

First Author	Valve Material	Micropump Actuation	Inlet Width (mm)	Outlet Width (mm)	Channel Length (mm)	Channel Angle	Flow rate (ml/min)	Pressure (kPa)
Flat Nozzle/Diffuser (Trapezoidal)								
Hwang et al. (2008)	Si	Piezoelectric	0.19	0.35	0.08	6 °	0.037	----
Wang et al. (2008)	Si	Piezoelectric	0.1	0.15	2.5	8 °	1.5	7.7
Zhang et al. (2013)	LTCC	Piezoelectric	0.9	----	5	----	0.63	1.55
Tseng et al. (2013)	Si	Piezoelectric	0.8	----	3.1	10 °	1.2	5.3
Wei et al. (2014)	EP	Piezoelectric	2	----	10	15 °	0.038	10
Singh et al. (2015)	PDMS	Piezoelectric	0.1	----	1.5	10 °	0.02	0.22
Kanth et al. (2011)	PMMA	Piezoelectric	----	----	6	7 °	0.497	4.93
Zhou et al. (2011)	PDMS	Electromagnetic	0.1	0.5	1.6	10 °	0.3196	0.931
Zhi et al. (2012)	PMMA	Electromagnetic	0.1	0.25	2.3	----	0.13	----
Chang et al. (2013)	PDMS	Electromagnetic	0.15	----	1.5	11.3 °	0.47	----
Kawun et al. (2016)	PDMS	Electromagnetic	0.086	0.216	0.949	10 °	0.135	0.245
Kumar et al. (2016)	PDMS	Electromagnetic	0.12	----	1.5	10 °	0.336	0.441
Said et al. (2017)	Si	Electromagnetic	0.05	0.4	1.35	15 °	0.0066	----
Gidde et al. (2018)	PDMS	Electromagnetic	0.1	----	1.1	9 °	0.441	0.35
Yang et al. (2011)	PDMS	Thermopneumatic	0.01	6	----	8 °	1.25×10^{-5}	1×10^{-5}
Ochoa et al. (2012)	Glass	Thermopneumatic	0.2	----	28	12 °	0.10205	5.86
Chee et al. (2016)	PDMS	Thermopneumatic	----	----	10	20 °	1.25×10^{-5}	----
Santos et al. (2010)	PMMA	ICPF	1	2	10	5.72 °	0.0082	----
Ghazali et al. (2017)	PMMA	DEA	0.2	----	1.5	14 °	0.0212	----

The performance of the flow rectification mechanism at the inlet and outlet is critical in the operation of the micropump. The active dynamic geometry microvalves require an additional synchronized actuation scheme according to the oscillation of the pump diaphragm. The application of a separate actuator for valve actuation and additional energy consumption due to this actuator limits the application of active valves. Passive dynamic geometry check valves do not require an additional actuator and can be used effectively for high-frequency operation. The most common form check valves reported are flap-type. The design and material property of such valve play a vital role in the dynamic operation. The check valves are designed to have a natural frequency higher than the pump operating frequency (Park et al. 2013). Fabrication of flap valves incorporates PDMS, Pyriline, and Silicone rubber which offer low stiffness and higher flexibility to valve opening and closing. A rectangular flap valve with a dimension of $3 \times 2 \times 0.5$ mm^3 is found to have a deflection of 0.112 mm at 0.5 kPa pressure (Rosset et al. 2009).

Dynamic geometry valves are capable of withstanding higher back pressure as it offers a barrier to reverse flow. However, the dynamic behaviour of the microvalves leads to wear, fatigue failure in the long run. The stiction of valves onto the valve seat due to the adhesion force can also affect the performance of the microvalve (Iverson and Garimella 2008). A passive PDMS check valve of $0.35 \times 0.16 \times 0.06$ mm^3 is found to have a critical opening pressure of 1 kPa up to which no flow is observed in the forward direction (Ni et al. 2014). Thus the pressure variation must be above the critical opening pressure of the valve to have significant flow through the outlet. Ball valves are equally competitive enough to offer better flow rectification and unidirectional flow, but integrating ball valves into the microfluidic system is a complex process.

Static geometry fluid channels, particularly nozzles/diffusers, are effective in achieving necessary flow rectification in the mechanical micropump. The absence of moving structures is advantageous mainly when the pumping fluid contains particulate matters like cells, drug particles, DNA samples, etc. (Laser and Santiago 2004). The amount of flow rectification of the nozzle/diffusers mainly depends on geometrical features like the inlet/outlet dimensions, divergence angle, and channel

length. S. Singh et al. (2015) and Ranjitsinha R. Gidde et al. (2018) simulated the performance of nozzle/diffuser considering with different geometries of nozzle/diffuser. They concluded that lower divergence angle of nozzle/diffuser resulted in lower rectification efficiency leading to increased flow rate with an increase in divergence angle. A higher value of divergence angle causes flow separation resulting in a reduced flow rate. Observation on channel length revealed that the lower channel length had a lower flow rate due to lesser geometric variation between nozzle/diffuser, whereas the higher value of channel length resulted in increased pressure drop with reduced flow rate. The throat width also had a significant effect on micropump performance. A lower throat width had a lesser flow rate due to the choking effect. The higher value of throat width also results in the drop of flow rate due to lower rectification efficiency.

Nozzle/diffuser with a divergence angle of 10º, a channel length of 1.5 mm and throat size of 0.1 mm is implemented in micropump proposed by S. Singh et al. (2015), which can pump 0.02 ml/min of water with a back pressure of 0.22 kPa. Ranjitsinha R. Gidde et al. (2018) proposed a micropump configuration that delivered an optimal flow rate of 0.441 ml/min and pressure of 0.35 kPa with optimal nozzle/diffuser geometry of 10º divergence angle, a channel length of 1.1 mm and neck width of 0.125 mm.

2.1.3 Chamber Configurations of the Mechanical Micropump

Figure 2.15 schematically represents the different chamber configurations of the mechanical micropump. Most of the mechanical micropumps reported are of single-chamber type. The first mechanical micropump developed by Spencer et al. (1978) incorporated a single chamber configuration. The micropump proposed by Smith et al. (1990) adopted the new concept of the peristaltic chamber with three chambers in a series built on a Si wafer with the piezoelectric actuation. The arrangement of the actuators in the peristaltic micropump is such that the diaphragm flexes in a particular sequence one after the other, leading to the flow of fluid from one chamber to other, as shown in Figure 2.15 (d). Peristaltic micropumps with the piezoelectric drivers (Zhang and Eitel 2013), electromagnetic driver (Shen et al.

2011), thermopneumatic (Liao and Yang 2008; Ha et al. 2009; Yang and Liao 2009), phase change Driver (Bodén et al. 2008; Yoo et al. 2008; Svensson et al. 2010), shape memory alloy (Guo et al. 2008; Sun et al. 2009) and electrostatic (Lee et al. 2009, 20013) are reported. Works of literature on double chamber parallel configuration (Hwang et al. 2008; Le et al. 2009; Guo et al. 2012) of the micropump are also available, which effectively enhances the performance of micropump concerning fluid delivery.

(a) Single Chamber   (b) Double Chamber Series Connection

(c) Double Chamber Parallel Connection

(d) Perilstaltic Chamber
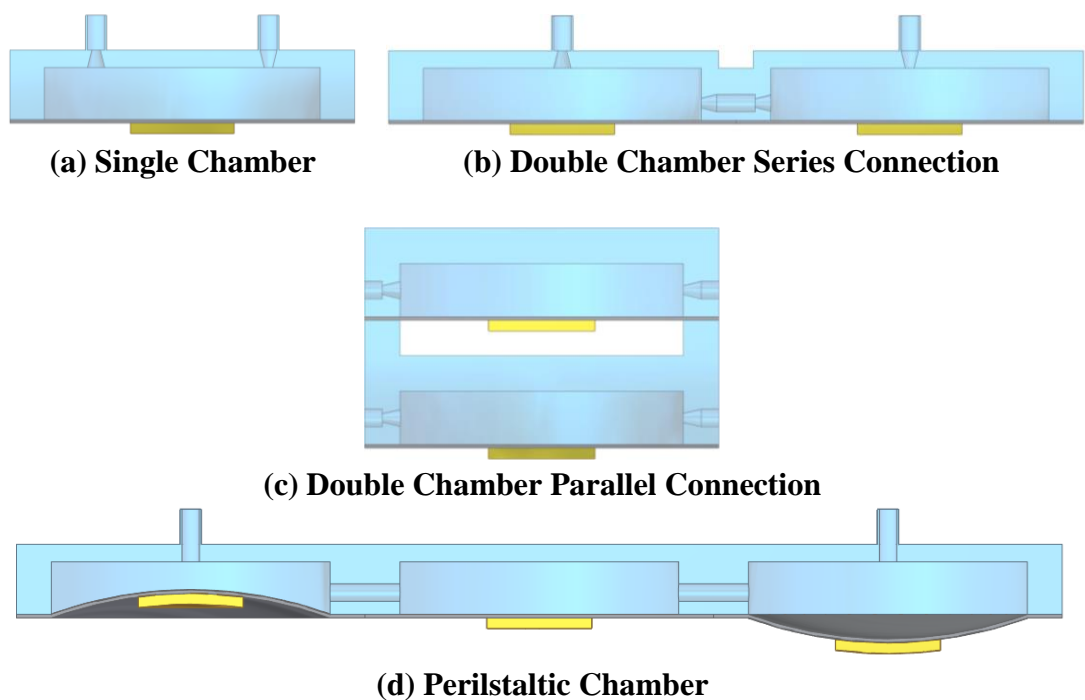
Figure 2.15 Chamber configuration of mechanical micropump

Since the performance of mechanical micropump greatly depends on chamber configuration, well-established chamber design and optimization can lead to performance enhancement of the micropump. Chamber diameter and height are the two critical geometrical factors that affect the performance of mechanical micropump. The flow rate increases with chamber height up to a specific value due to the reduction of the flow losses. Beyond a threshold value, the flow rate decreases with an increase in chamber volume due to higher damping of the fluid accommodated inside the chamber. This prevents the complete transfer of energy from the oscillating diaphragm into the fluid. An increase in the chamber diameter enhances the flow rate due to the increase in the swept volume of the membrane. However, limitations are

36

put on chamber diameter so that micropump can be easily accommodated into microfluidic systems considering their constraints on space and size (Singh et al. 2015; Muzalifah Mohd Saidet al. 2017). Experimental investigation of piezoelectric actuated micropump by H. K Ma et al. (2015) revealed that the micropump could pump 1.35 ml/min and 1.12 ml/min of water with a chamber depth of 1.00 mm and 1.50 mm, respectively, with the same chamber diameter of 10 mm.

Consideration of multiple chamber configurations in the mechanical micropump can also enhance the performance to a greater extent. The electromagnetic micropump proposed by T. Le et al. (2009) with the double-chamber delivered a higher flow rate of 0.02773 ml/min of working fluid which is superior when compared with the flow rate of 0.01961 ml/min from a single chamber micropump when actuated under same actuation current of 0.30 A. Similarly, double-chamber piezo-actuated micropump proposed by Li Guo et al. (2012) outperformed the performance of single-chamber pump by a factor of almost 1.3 with a flow rate of 0.1517 ml/min (double chamber) and 0.115 ml/min (single chamber) when actuated at 110 V.

Multistage peristaltic chamber configuration is also effective in enhancing the flow rate of the micropump. A peristaltic electrostatic micropump developed by Hanseup Kim et al. (2015) with one, two and nine numbers chambers. This particular micropump achieved a flow rate of 2.10 ml/min (at 14 kHz), 3.00 ml/min (at 14 kHz), 4.00 ml/min (at 17 kHz) against the back pressure of 2 kPa, 4.5 kPa and 12.8 kPa respectively corresponding to 1, 2 and 9 chamber configuration when actuated at ±100 V. Though multi-chamber enhances the performance of the micropump, limitations occurs as a result of fabrication complexities, space and size aspects.

2.1.4 Design and Materials of the Diaphragm in Mechanical Micropump

A diaphragm is a force applying surface, which undergoes periodic oscillation due to the excitation from the actuator. Since the pumping volume depends on the deflection of the diaphragm, the design and material selection significantly influence the micropump performance. Most of the micropumps reported have implemented the

flexible flat planar structure of the diaphragms/membranes with different thickness and material properties to have optimum pumping. Table 11 represents the commonly used diaphragm materials, their mechanical properties, and thickness ranges. A lower value of Young's modulus and higher reversible strain of the diaphragm material is a primary requirement that results in higher deflection of the membrane leading to a more significant flow rate (Zhang et al. 2007).

Flat Diaphragm   **Flexural Hinged Diaphragm**

(a) Planar Configuration

Bossed Diaphragm   **Corrugated Diaphragm**

(b) Non Planar Configuration
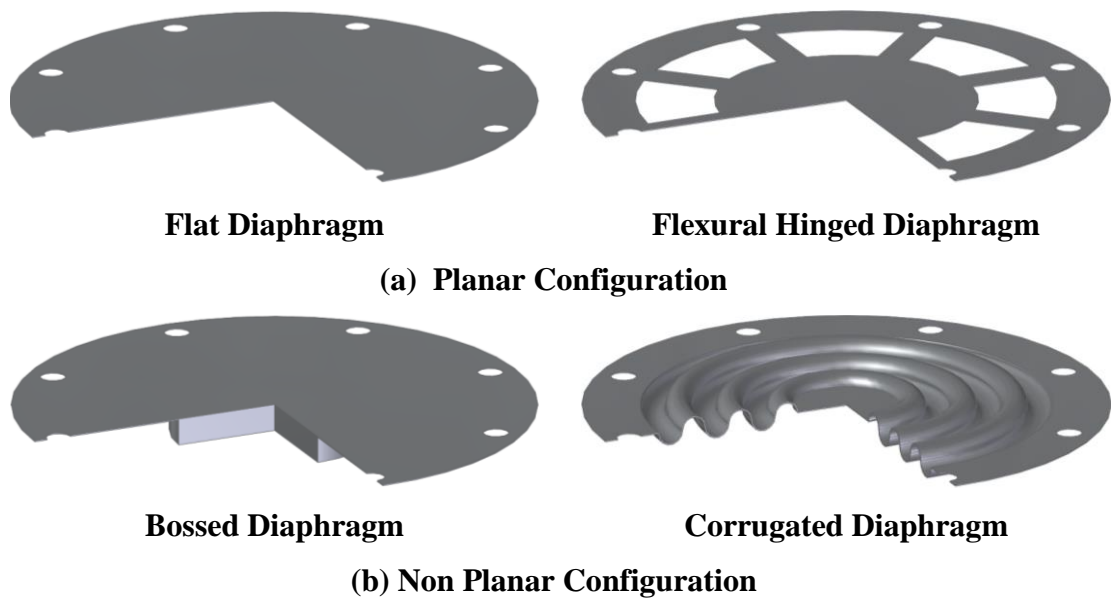
Figure 2.16 Commonly used diaphragm designs in mechanical micropump **(a)** Planar Configuration **(b)** Non planar configuration

Figure 2.16 represents some of the diaphragm designs incorporated in mechanical micropumps. The planar dimensions of the diaphragm decide the overall size of the micropump since it has to accommodate the whole planar surface of the diaphragm. Other planar configuration of the diaphragm with the flexural hinges can effectively enhance diaphragm deflection to increase the swept volume (Ma et al. 2016). Corrugated diaphragms, bossed diaphragms are some of the non-planar configurations implemented in mechanical micropumps to a limited extent. The optimization studies on diaphragms effectively involve finite element analysis, particularly for understanding the frequency response when subjected to different actuation forces. With such approaches, the diaphragm geometry can be optimized to have an efficient micropump operation. Commercial FEM packages like Ansys,

Comsol, etc., are found to be helpful in this regard (Guo et al. 2012; Park et al. 2013; Singh et al. 2015).

Table 2.11 Material properties of different diaphragm materials

Material	Actuation principle	Thickness (mm)	Young's Modulus (GPa)	Poisson's Ratio	Density (Kg/m³)
Glass	Piezoelectric	0.20	62.75	0.2	2540
PDMS	Piezoelectric Electrostatic Electromagnetic Thermopneumatic Phase change	0.011 - 0.40	0.00075 - 0.0015	0.45 - 0.5	965 - 1030
Si	Piezoelectric	0.1	160 - 169	0.27 - 0.3	2300
Electropolymer	Piezoelectric	0.1 - 0.2	0.5	---	---
Stainless steel	Piezoelectric Phase change	0.01 - 0.1	----	0.3	7900
Brass	Piezoelectric	0.15 - 0.25	10.3	0.33	8.4 - 8.73
Polyamide	Electrostatic Thermopneumatic Phase change	0.00015 - 0.003	1130	---	---
Rubber	Piezoelectric Electromagnetic	0.3 - 0.5	---	0.47	1200
Nafion	ICPF	0.18 - 0.6	0.35 - 0.61	---	2500
Acrylic Elastomer	DEA	0.56	---	---	---

The swept volume of the diaphragm is a function of diaphragm deflection, which determines the amount of fluid pumped. Factors like diaphragm designs, materials, geometry, and type of loading play a vital role in assessing the performance of the micropump. Most of the mechanical micropumps reported have implemented a flat planar flexible membrane with a circular or rectangular cross-section. Maximum deflection occurs when the diaphragm is made to oscillate at resonance. The resonance frequency of the diaphragm is determined by the material property and stiffness values which in turn depends on the geometric features like the thickness, cross-sectional area. The deflection of the diaphragm tends to decrease with an increase in the thickness of the membrane due to increased resistance to bending (Singh et al. 2015). However, diaphragm thickness cannot reduce beyond a specific limit due to the problems arising from self-sagging and stiction of the diaphragm surface. A water flow rate of 2.21 ml/min is achieved by HK Ma et al. (2016) with a

polyethene terephthalate diaphragm of 0.10 mm thickness actuated through the piezoelectric disc is superior when compared with a flow rate of 1.15 ml/min achieved with 0.05 mm thickness diaphragm.

The selection of material for mechanical micropump majorly depends on the frequency of vibration, which often depends on the driving mechanism. The application materials PDMS, Parylene, Silicone Rubber, Latex Rubber, etc., are effective in the low-frequency range, which has a lower modulus and tends to offer higher deflection. For drivers associated with higher frequency, higher stiffness diaphragms made of materials like stainless steel, copper, Si, glass, etc., are preferred, offering higher force and faster mechanical response (Iverson and Garimella 2008).

Apart from geometry and material selection, enhancement of diaphragm deflection can be achieved through the implementation of the addition of design features like flexures, corrugations/grooves, slots, bossed structures which reduces the stiffness of the diaphragm to a greater extent (Xu et al. 2016; Zhu et al. 2017; Azizollah Ganji et al. 2018; Roopa et al. 2018a; b). The change in the loading position of the diaphragm also has a significant role in deflection enhancement. Conventionally most micropump diaphragms are loaded centrally, i.e., the actuation force on the diaphragm acts in the central region. Shabanian et al. (2016, 2017) proved a new concept of actuating the membrane circumferentially through the piezo rings, which showed new insight into enhancing diaphragm deflection for micropump application. Shabanian et al. (2016, 2017) proposed the circumferential configuration resulting in deflection of about 0.25 mm with PVC diaphragm (0.1 mm thick and 22 mm diameter), which outperformed the deflection of 0.024 mm of the same diaphragm loaded centrally through the conventional bimorph.

2.1.5 Material and Fabrication Process of the Mechanical Micropump

The early stage of micropump fabrication is purely based on silicon micromachining, as seen in Spencer et al. (1978). As observed from the literature, mechanical micropump technology extensively utilizes Silicon - Glass based micromachining processes for fabrication. Some common microfabrication processes

involve photolithography, anisotropic etching, surface micromachining and bulk micromachining of Si (Kim and Meng 2015). Though microfabrication technology yields superior properties, the high cost of materials and fabrication adds to the disadvantages of this technology. Apart from that, the microfabrication process is highly time-consuming. Improvement in precision fabrication techniques has led to polymer-based materials like PMMA, PDMS, PLLA, PC, etc., in micropump fabrication. Polymeric materials like PDMS can be easily molded by conventional casting technique or spin coating to form the different components such as the chamber body, diaphragm and microfluidic components (Mamanee et al. 2006; Liao and Yang 2008; Yang and Liao 2009; Wang et al. 2010b; Pečar et al. 2014; Ni et al. 2014; Chee et al. 2015; Liu et al. 2016; Norihan Abdul Hamidet al. 2017). Micropumps fabricated with materials like PMMA, PLLA through micro CNC machining (Wang et al. 2008; Thanh Tung Nguyen et al. 2008; Ma et al. 2015; Ma et al. 2016; Chee et al. 2016;), CO_2 based LASER cutting and engraving processes (Shen et al. 2011; Sima et al. 2015 Kant et al. 2017) are also observed in the recent works. Reduced material cost, improved material compatibility, increased strength, and reduction in fabrication cost are some of the advantages features found in the use of polymer-based materials with conventional machining and fabrication processes.

Compatibility of micropump materials with the operating environment is of primary concern, particularly in biological, chemical and electronic applications. The selection of material also influences the type of fabrication process to be adopted in micropump fabrication. Since the operating fluids are continuously in contact with the diaphragm and pump body, chemical stability and biocompatibility of micropump materials are more critical in chemical analysis and biomedical applications. Thermal stability of the micropump material is also an essential factor that has to be taken care of where the micropump materials undergo heating and cooling cycles, particularly with micropumps with thermopneumatic, phase change, SMA actuation inherits an inbuilt heater.

The micro machined Silicon-Glass fabrication process finds extensive application in micropump technology. Silicon-Glass based micromachining is capable

41

of delivering higher geometrical precision, superior fatigue strength and wear properties. Despite such advantageous features, the high cost of manufacture, elaborate manufacturing process, and limited material choice have led to finding alternative materials for micropumps. The recent trend has shown the use of polymer-based materials as an alternative for conventional silicon-based materials due to considerable advancements in the fabrication technology of precision components. Polymer-based materials like PDMS, PMMA, PLLA, etc. have gained significant emphasis on micropump technology due to their superior strength, enhanced structural properties and stability. Additionally, these materials are inexpensive, disposable and are competitive enough to be used in mass production.

2.2 Highlights of the Literature Review on Micropumps

The performance of mechanical micropump with the emphasis on flow rate and pressure development significantly depends on the type of actuator used. Since the mechanical micropumps consist of an oscillating diaphragm, the deflection of the diaphragm determines the swept volume, which in turn depends on the driver configuration. Piezoelectric, electromagnetic and thermopneumatic actuators are reported extensively for micropump actuation. However, the disadvantage of limited frequency response, high power consumption and thermal effects limit applying the electromagnetic and thermopneumatic actuation mechanism in mechanical micropump. Therefore the piezoelectric actuators find extensive application in mechanical micropump, which has the advantage of larger frequency response, lesser power consumption, accurate fluid delivery control, material compatibility and minimum thermal effect. Among the valve configuration employed in mechanical micropumps, the static geometry nozzle/diffuser configuration proved effective over conventional check valves. The ease of fabrication and resistance against fatigue failure led to the widespread application of nozzle/diffuser configuration of the mechanical micropump. However, the nozzle/diffuser configuration develops lower pressure when compared with the check valve configuration. The fabrication complexity involved in the multiple chamber configurations has led to the widespread implementation of single-chamber arrangement in mechanical micropump.

Most of the mechanical micropump proposed in recent years have effectively implemented planar flat diaphragm configuration. Since the diaphragm deflection influences the micropump performance, attempts have been made to implement flexural hinged, corrugated, bossed diaphragm configuration to enhance the flexibility of the diaphragm, thus enhancing the deflection range. Polymer-based materials like PDMS, PMMA, PLLA, etc. have gained considerable significance in the fabrication of micropump due to their enhanced strength, flexibility, ease of availability, disposability and biocompatibility. Besides, the fabrication of micropump through these materials is possible through inexpensive conventional methods such as moulding, spin coating, CNC machining, additive manufacturing. Despite the comparison between different actuation mechanisms of mechanical micropump, obtaining the desired flow and maintaining safety mainly depends on optimizing micropump parameters. Well established numerical modelling, simulations, and experimental approaches would lead to an optimized configuration of micropump, delivering efficient design and performance.

2.3 Mechanical Micropump with Piezoelectric Actuation

Mechanical micropumps with piezoelectric actuators have gained significant consideration in microfluidic applications. The performance of the piezo actuated micropump depends on the type of actuator, operating parameters, diaphragm design and actuation method, valve parameters, chamber design. Figure 2.17 represents the factors affecting the performance of piezo actuated mechanical micropump. The amount of fluid pumped by the piezo actuated micropump is governed by the swept volume by the oscillating diaphragm inside the pump chamber, which depends on the oscillation amplitude of the diaphragm. Factors such as the actuator configuration, material, design and actuation method of the diaphragm predominantly influence the oscillation amplitude of the piezo actuated micropump; thus, the flow rate and the pressure.

Over the years, numbers of mechanical micropump have been reported with different types of the piezoelectric actuator and diaphragm design solely intended to enhance the mechanical micropump performance (Laser and Santiago 2004;

43

Nisar et al. 2008). Most of the micropumps developed till now have effectively implemented piezo actuator in the form of unimorph, bimorph and multi-layer stacks, amplified actuators (Li et al. 2021). The piezoelectric actuators involve the electromechanical interaction of a specific group of materials between the elastic and electrical behaviour. The polarization of the piezoelectric materials at high temperature through the application of a high electric field in a particular direction results in an ordered arrangement of randomly oriented electric diploes. The application of external stimuli in the form of electrical potential across the polarized piezoelectric materials results in the development of mechanical strain, which deforms the micropump diaphragm (Uchino 2008; Wang et al. 2019).
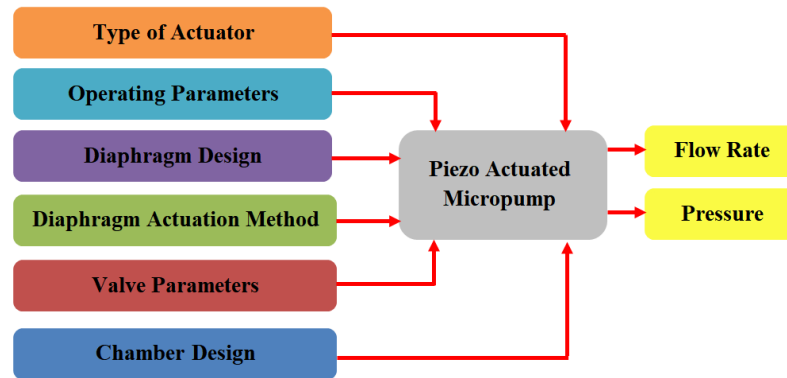
Figure 2.17 Factors affecting the performance of the piezo actuated micropump

Typically the unimorph piezoelectric actuators are characterized by the single layer of piezoelectric materials sandwiched between layers of thin electrically conductive metal electrodes, as represented in Figure 2.18 (a) (Mohith et al 2020). A bimorph piezoelectric actuator also possesses a similar construction feature as that of unimorph, except that it consists of two layers of piezoelectric materials, as shown in Figure 2.18 (b) (Zhu et al. 2011; Kang and Han 2010; Bakhtiari-Shahri and Moeenfard 2019). The unimorph/bimorph piezoelectric actuators are used as a source of actuation in mechanical micropumps in different shapes such as square/rectangular, circular, and ring-shaped or cantilever type. The bending motion generated (Figure 2.18 (c)) by the unimorph/bimorph on the application of the electric potential flexes the diaphragm of the micropump attached to its surface, thus generation necessary oscillation of the diaphragm required for micropump operation (Ma et al. 2016).

Appropriate control of the actuation parameters of the unimorph/bimorph actuator, such as the voltage and frequency, can effectively control diaphragm oscillation, thus precise delivery of fluid to be pumped (Verma et al. 2009; Luo et al. 2011;). Figure 2.19 represents the mechanical micropump reported by researchers with piezo unimorph/bimorph actuators.

(a) Rectangular/ Ring / Cicular/ Cantilever type piezo unimorph actuator

(b) Rectangular/ Ring / Cicular/ Cantilever type piezo bimorph

(c) Deformation patters
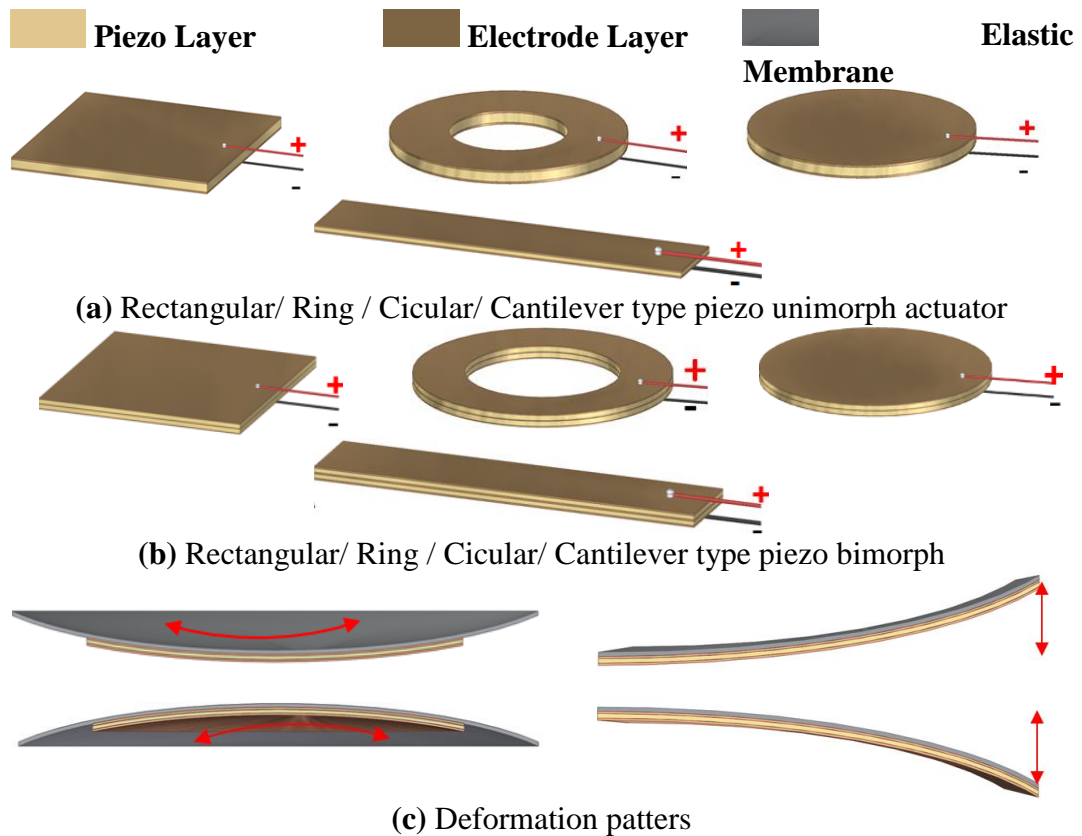
Figure 2.18 Schematic of piezo unimorph/bimorph actuators and deformation patters

(a)   **(b)**   **(c)**
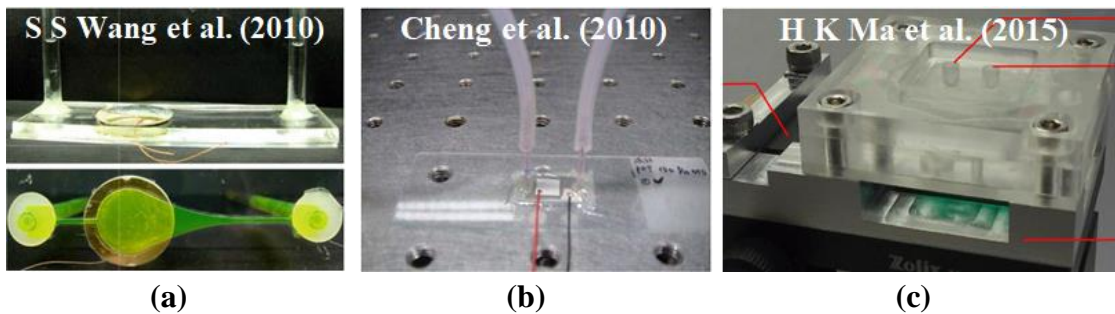
Figure 2.19 Mechanical micropumps with **(a)** Disc type piezo actuator
(b) Rectangular piezo actuator **(c)** Cantilever type piezo actuator

The second category of piezoelectric actuators for micropump actuation consists of multi-layered configuration. Figure 2.20 represents the schematic of the piezo stack actuator. The multilayer piezoelectric actuators also termed piezo stack actuators typically consist of multiple piezoelectric materials stacked one over the other with suitable adhesives (Mohith et al 2020). Each layer of the piezo stack actuator consists of piezoelectric materials with electrodes separated by suitable insulation (Zhang et al. 2017, 2019). The parallel pre-stressed actuators also belong to the group of multi-layered piezo stack actuator, which incorporates pre-stress onto the piezo stack through an elastic mechanism. Such pre-stressed actuators are termed parallel pre-stressed actuators (Heverly et al. 2004; Letty et al. 2005; Jiang and Cheng 2017). Typically such actuator consists of elastic springs integrated parallel to piezo stack actuators, as shown in figure 2.20 (d). The pre-stress springs ensure the stack actuator bears enough tension, thus improving its life and dynamic characteristics (Miku and Technological 2016). Figure 2.21 represents the micropump with a piezo multilayer stack actuator.
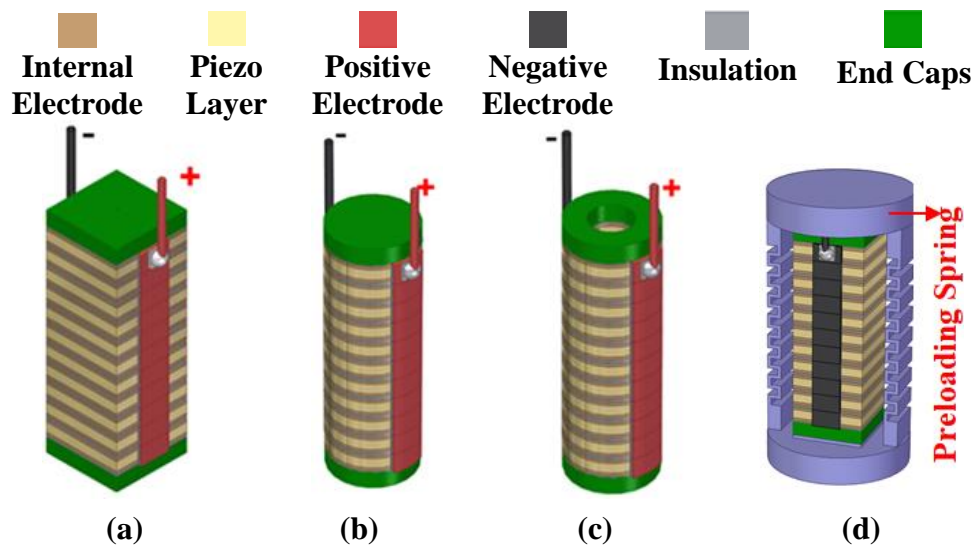
Figure 2.20 Schematic of **(a)** Square section piezo stack actuator **(b)** Circular section piezo stack actuator **(c)** Ring type piezo stack actuator **(f)** Parallel pre-stressed piezo stack actuators actuator (PPA)
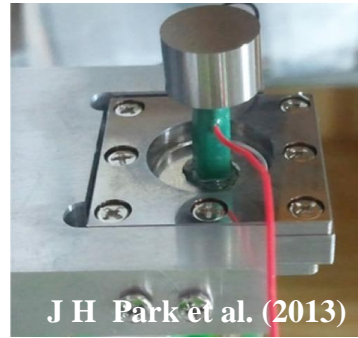
Figure 2.21 Mechanical micropumps with piezo stack actuator

The performance of the piezoelectric actuators specifically for micropump application could be assessed in terms of the range of deflection, blocked force and frequency response of the actuator. Most of the piezo actuators have implemented Lead Zirconate Titanate (PZT), Polyvinylidene fluoride (PVDF) and Zinc Oxide as the active material for micropump actuation. Higher the deflection range and blocked force developed by the actuator, the higher the diaphragm deflection, leading to better performance of the micropump. Table 2.12 and Table 2.13 summarize the different configurations of the piezoelectric actuator, i.e. unimorph; bimorph and multilayer piezo stack actuator reported by different researchers with a range of motion and blocked force achieved.

Apart from piezo unimorph/bimorph and multilayer piezo stack actuators, there is a third category of the piezo actuator that incorporates a flexural-based amplification mechanism with the piezo stack actuator. Such an actuator is termed an amplified piezo actuator (APA) (Mohith et al 2020). Over the past few decades, very few works are reported on the application of APA as a source of actuation for micropump. Typically amplified piezo actuator consists of an external structural amplifier that amplifies the multi-layered piezo actuator (Claeyssen et al. 2007; Wang et al. 2019a). The elastic deformation of the structural mechanisms induced due to the force exerted by the multilayer piezo actuator generates the amplified motion (Wise 1998; Ling et al. 2019).

Table 2.12 Details of the piezoelectric unimorph/bimorph actuators reported in recent years

Author	Type	Actuator Shape/ Material	Dimension (mm)	Actuation Voltage (V)	Deflection Range (μm)	Blocked Force (N)
D O Lee et al. (2011)	Unimorph	Rectangular (PZT)	38.1×12.7×0.254	600	700 to 900	0.2 to 0.4
Asha J et al. (2012)	Bimorph	Cantilever Type (PZT)	36×6.5×0.75	±36	11000	-----
Ashraf et al. (2012)	Unimorph	Disc type (PZT)	⌀=3.00	160	16 to 20	-----
J Ma et al. (2012)	Unimorph	Ring (PZT)	⌀=3.00, t=0.04	100	12.9	-----
El Sayed et al. (2013)	Bimorph	Cantilever Type (PZT)	57.2×31.8×0.38	50	1150	0.1 to 0.15
Y Yuan et al. (2013)	Bimorph	Cantilever Type (ZnO)	1 ×0.5×0.001	10	0.122	-----
W Liu et al. (2013)	Unimorph	Cantilever (PZT)	_ ×_ × 0.28	±5	-15.00 to 18.00	-----
J Choi et al. (2014)	Unimorph	Cantilever (PZT)	_ ×_ × 0.10	140	172.2 to 182	-----
Cheng et al. (2015)	Unimorph	Square (PZT)	5.5×5.5×0.15	200	2.5 to 3.5	-----
H K Ma et al. (2015)	Unimorph	Disc (PZT)	t=0.2	±70	190	-----
R K Jain et al. (2015)	Bimorph	Cantilever Type (PZT)	40×11×0.6	±60	-1500 to 1500	0.230
R K Jain et al. (2015)	Bimorph	Cantilever Type (PZT)	40×11×0.6	±60	-1500 to 1500	0.230
B Ghosh et al. (2017)	Bimorph	Cantilever Type (PZT)	31×9×0.65	±30	-500 to 500	0.104
Y Z Liu et al. (2019)	Bimorph	Cantilever Type (PVDF)	60×20×--	800	10000	-----
A Almeida et al. (2019)	Bimorph	Cantilever Type (PZT)	40×10×0.5	±45	-1000 to 1000	-----
N Chen et al. (2020)	Unimorph	Rectangular(PZT)	11.3×2.5×0.1	±100	-26.7 to +23.1	-----
A Gunda et al. (2020)	Unimorph	Disc (PZT)	⌀=4, t=0.127	±70	7.00 to 8.00	-----
P Shahabi et al. (2020)	Bimorph	Cantilever Type (PZT)	24.53×6.4×0.63	4	60 to 80	-----
A Ali et al. (2020)	Bimorph	Cantilever Type (PZT)	100×30×20	40	3.5	-----

Table 2.13 Details of multi-layer/stacked piezoelectric actuators reported in recent years

Author	Type	Actuator Shape/ Material	Dimension (mm)	Actuation Voltage (V)	Deflection Range (µm)	Blocked Force (N)
D D Jang et al. (2011)	Stack	Ring (PZT)	$\varnothing_O$=35, $\varnothing_I$=14, L=71	150	50	----
D H Wang et al. (2011)	PPA	Square (PZT)	----	200	62.5	----
S B Choi et al. (2012)	Stack	Circular (PZT)	$\varnothing$=13 , L=36	160	3.4	220
B. Sahoo et al. (2012)	PPA	Ring (PZT)	$\varnothing$=8.7, L=36	175	10	1427
M. Meftah et al. (2013)	Stack	Circular (PZT)	5×5×10	150	48.5	950
L Wang et al. (2013)	Stack	Square (PZT)	7×7×32.5	200	45	----
J H Park et al. (2013)	Stack	Square (PZT)	2×3×9	150	13	300
J Jeon et al. (2014)	Stack	Circular (PZT)	$\varnothing$=25 , L=100	150	100	----
Z Xuan et al. (2014)	Stack	Circular (PZT)	$\varnothing$=25 , L=100	1000	80	20000
Y L Yang et al. (2015)	Stack	Square (PZT)	5×5×20	150	20	----
Muralidhara et al. (2015)	Stack	Square (PZT)	10×10×20	150	11.5	----
C Zhou et al. (2016)	Stack	Square (PZT)	7×7×36	120	38	1850
Z Bu et al. (2018)	Stack	Square (PZT)	7×7×32.5	200	45	----
H S Hwang et al. (2019)	Stack	Circular (PZT)	$\varnothing$=25 , L=114	1000	110	----
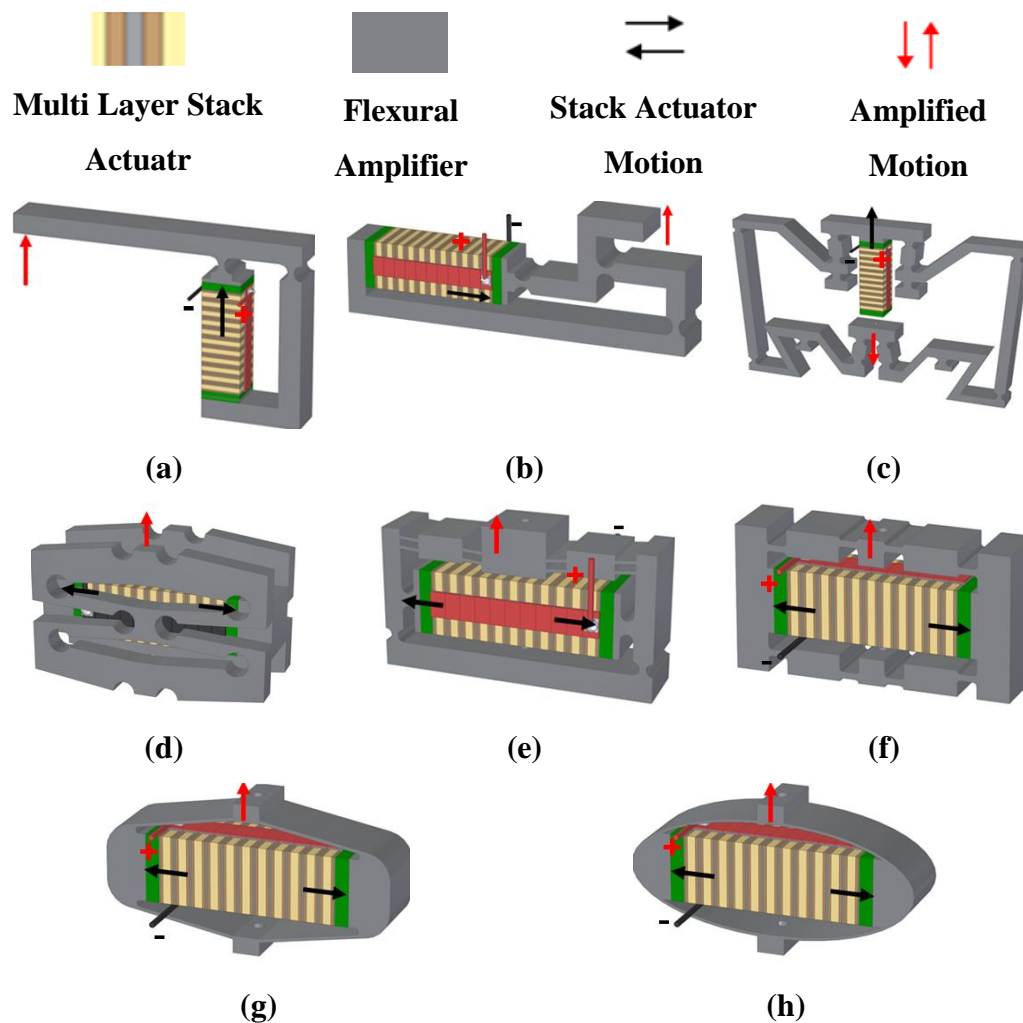
Figure 2.22 (a) Lever type actuator **(b)** Scott-Russell type actuator **(c)** Tensural displacement type actuator (**d**) Honey comb type actuator **(e)** Symmetric five bar type actuator   **(f)** Bridge type actuator **(g)** Rhombus type actuator **(h)** Elleptical type actuator

Figure 2.22 represents the commonly used flexural based amplified piezo actuators in different applications. One of the simplest forms of amplification approach for multi-layered piezo actuators is using the lever principle through flexural hinges, as shown in Figure 2.22 (a). The lever amplified motion achieved through the lever mechanism is parallel to the direction of motion of the piezo stack actuator (Dsouza et al. 2018). Another amplification strategy is the Scott-Russell (S-R) mechanism (Sun et al. 2013; Ai and Xu 2014) (Figure 2.22 (b)), which involves a flexural hinged framework that produces amplified straight-line motion in the right angle direction. The tensural displacement type mechanism (Figure 2.22 (c)) is also known for generating amplified motion through symmetrical compliant mechanism configuration. The

flexural hinges of the tensural amplifier are loaded in tension and bending when the primary multi-layered piezo stack actuator deforms due to applied electric potential (Lai and Zhu 2017).

In addition, honeycomb type (Figure 2.22 (d))(Muraoka and Sanada 2010), symmetric five bar type (Acob et al. 2012) (Figure 2.22 (e)), bridge-type (Figure 2.22 (f)) (Na et al. 2016; Xu 2014) and rhombus/elliptical type (Figure 2.22 (g), Figure 2.22 (h)) flexural amplification mechanisms are also incorporated effectively for enhancing the performance of the piezo actuator (Lu et al. 2014; Pan et al. 2015). All these actuators adopt a similar approach towards amplification. Among the different amplification configurations mentioned above, the lever type and Tensural type produces amplified motion parallel to the direction of motion of the piezo stack actuator. All other types of actuators have their output perpendicular to the direction of motion of the piezo actuator. The rhombus type and elliptical type amplifiers effectively amplify the displacement of the piezo multilayer actuator. Such a configuration of the piezo actuator is free from the risk of fatigue failure due to the absence of flexural hinges. This aspect improves the dynamic performance of the actuator as a whole, thus enhancing the life of the actuator. The summary on the performance of the different amplified piezo actuators reported in recent years is shown in Table 2.14.

Table 2.14 Details of amplified piezoelectric actuators reported in recent years

Author	Type of Mechanism	Piezo/ Mechanism Material	Dimension of Stack (mm)	Actuation Voltage (V)	Range of Stack (μm)	Amplifi- -ation Ratio	Range of APA (μm)	Blocked Force of APA (N)
Y B Ham et al. (2009)	Lever	PZT/SS	2×3×40	100	26	≈26	683	----
Muraoka et al. (2010)	Honey Comb	PZT/Al	5×5×40	150	41	≈10	410	20
X Sun et al. (2013)	S-R	PZT/Al	6.5×6.5×20	100	8.62	≈15.5	134	----
Q Xu et al. (2013)	Bridge	PZT/Al	10×10×18	10	1.45	≈193	280	----
Wenji Ai et al. (2014)	S-R	PZT/Al	∅=12,L=68	100	45	≈22.2	1000	----
S Lu et al. (2014)	Rhombus	PZT/SS	∅=10,L=64	150	60	≈8.33	500	----
Q S Pan et al. (2015)	Rhombus	PZT/SS	18×18×10	1400	34.6	≈4.62	160	----
Y Liu et al. (2016)	S-R	PZT/Al	L=68	100	45	≈16.13	720	----
T W Na et al. (2016)	Bridge	PZT/SS	5×5×18	150	20	≈11	220	----
J W Sohn et al. (2017)	Lever	PZT/SS	5×5×40	150	42	≈9.28	390	----
L J Lai et al. (2017)	Tensural	PZT/Al	----	10	10.48	≈27.5	288.3	----
Dsouza et al. (2018)	Lever	PZT/Al	5x5x20	160	30	≈8.00	240.53	36.8
F Chen et al. (20018)	Bridge	PZT/Al	----	150	122.2	≈38.43	4688	----
W L Zhu et al. (2018)	S-R	PZT/Al	∅=12,L=19	10	5.83	≈5.4	31.4	----
J Liang et al. (2019)	Lever	PZT/Al	∅=12,L=64	100	60	≈2.72	163	----
M Ling et al. (2019)	Rhombus	PZT/Al	10×10×36	120	38	≈31.84	1209.92	----
Y Ding et al. (2019)	S-R, Bridge	PZT/Al	----	120	19.51	≈3.51	68.55	----

The selection of different designs of the piezoelectric actuators is majorly application-specific. The free deflection and the blocked force developed by the piezo actuator can be considered critical features for selecting the piezo actuator for a micropump application. Figure 2.23 compares different piezoelectric actuators based on the free deflection and the blocked force developed. The unimorph/bimorph and cantilever actuators typically offer a higher range of motion but develop a lower range of blocked force (Mohith et al 2020). The stacked piezo actuators offer higher blocked force but lack in terms of free deflection. The actuators in the form of unimorph/bimorph and multi-layer stack actuator need to be bonded onto the diaphragm surface to transmit force or deflection effectively. Such an approach of bonding the actuator leads to a hazardous situation, which results in direct contact of the diaphragm surface, primarily when PZT is employed as an active material that contains lead. Besides, the bonding of actuators results in the loss of expensive actuator in micropump, which requires disposable feature, particularly in biomedical applications. The concept of disposable micropump is of great significance in biomedical application to overcome the problem of contamination. The disposal of micropump in biomedical application with expensive actuator bonded onto diaphragm surface adds to fabrication cost.
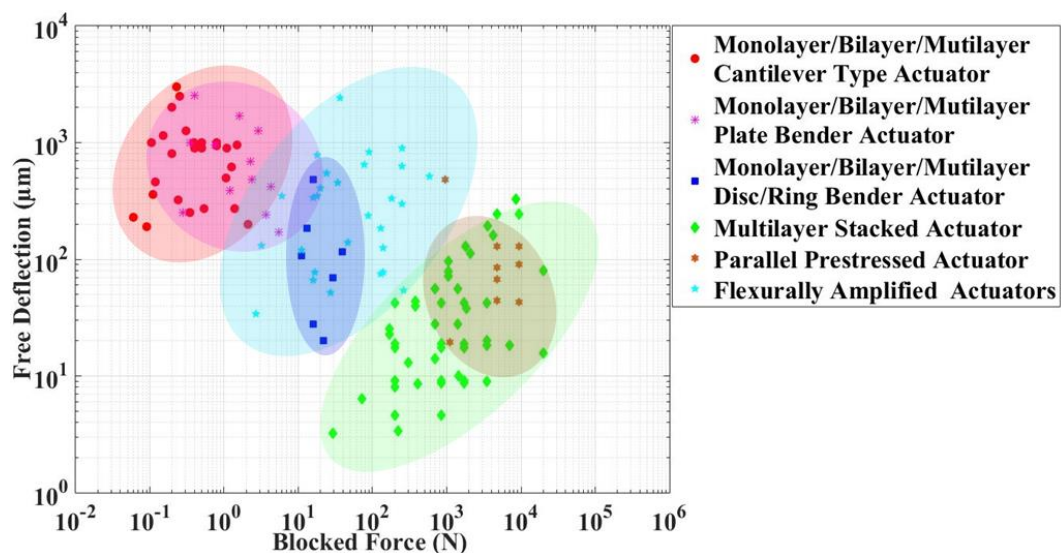
Figure 2.23 Comparison of the performance of unimorph/bimorph, multilayer piezo stack actuator and amplified piezo actuator

53

The integration of the flexural amplifier with the piezo stack actuator can enhance the performance in terms of free deflection but reduces the blocked force (Mohith et al. 2020). However, the range of blocked force developed by the amplified piezo actuators is good enough to operate the mechanical micropump under dynamic conditions. Besides, the amplified piezo actuator offers the advantage of space reduction when compared with multi-layered piezo stack actuators. Further, implementing the amplified piezo actuator with suitable structural arrangements helps to realize the concept of disposable micropump effectively. Thus amplified piezo actuators could be one of the novel approaches of micropump actuation, particularly for biomedical application.

Apart from the actuator configuration, the performance of the piezo actuated micropump could be enhanced by the novel approach of diaphragm design and diaphragm actuation methods which leads to the enhancement of oscillation amplitude. Most of the piezo actuated micropumps reported have effectively implemented flat diaphragm configuration. However, in recent decades, the efforts have been focused on micropump performance enhancement through the unique design of the diaphragm configuration. One such attempt is reported by micropump proposed by Roopa R et al. (2019) Figure (2.24 (a)), which considered a flexural hinge based flat diaphragm for effective reduction of the stiffness leading to enhanced diaphragm deflection. X Y Wang et al. (2016) (Figure 2.24 (b)) proposed a piezo actuated micropump with a non-planar bossed diaphragm configuration which enabled uniform distribution of stress on the diaphragm surface and prevented the formation of wrinkles during the micropump assembly.

The work on micropump reported by A. Shabanian et al. (2016) (Figure 2.24 (c)) proposed a novel approach of the piezo rings for micropump actuation. The application of excitation force away from the central region of the diaphragm resulted in effective enhancement of diaphragm deflection compared with the conventional approach of applying actuation force in the central region. However, above mentioned three configurations have bonded configuration wherein the piezoelectric actuator is integrated with the micropump as a single entity. Such an approach creates a major hurdle for realizing the concept of disposable micropump configuration.

54
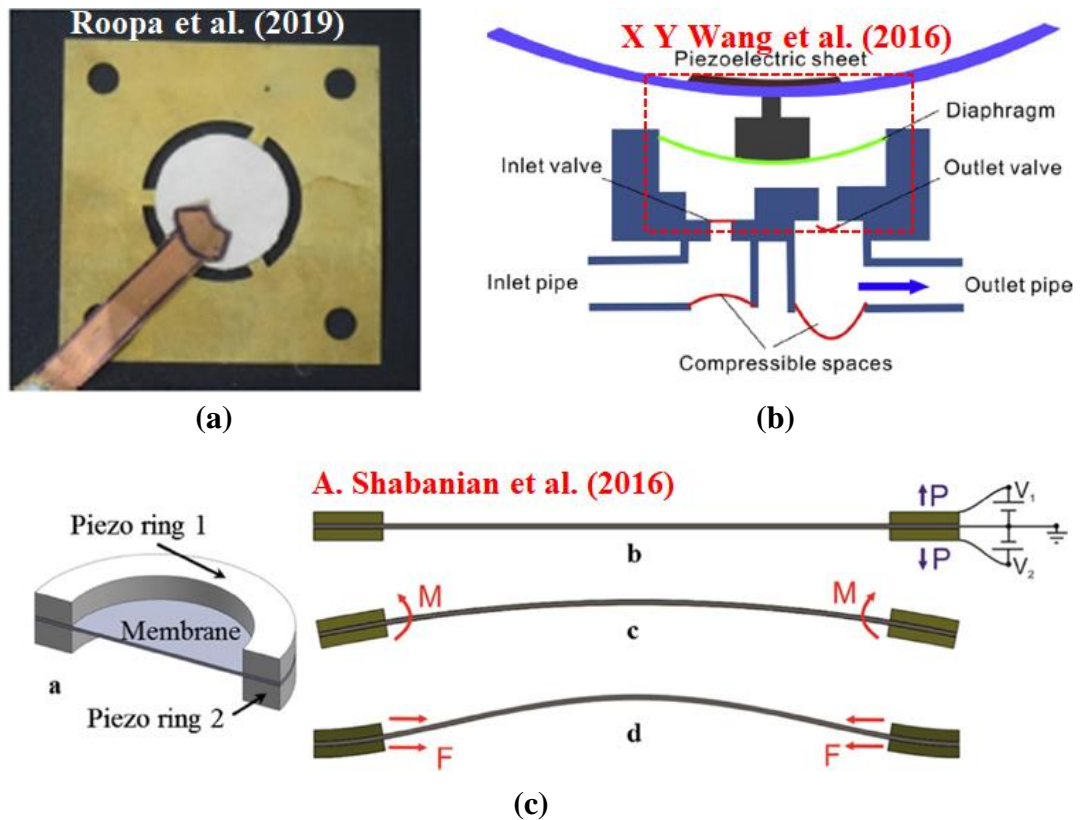
Figure 2.24 Different diaphragm configurations of the piezo actuated mechanical micropump

Thus it is concluded that the performance of the piezo actuated mechanical micropump could be enhanced by implementing actuator configuration, which can generate a large range of motion coupled with reasonable blocked force good enough to cause the oscillation of the diaphragm. Besides, the novel design and actuation approach can also lead to the enhanced performance of the micropump. Therefore, the present study reports a novel disposable chamber micropump concept with an amplified piezoelectric actuator as the primary actuation source. The proposed micropump concept integrates a bossed diaphragm subjected to the novel approach of annular excitation to enhance the volumetric performance.

2.4 Motivation of the Present Work

The general physical, mental health and well-being of people worldwide have been considered to be of most significant importance globally. The research and development in health care mainly focus on improving the medical services to have

better efficiency through the latest technological advancements. Over the past few years, there has been significant research contribution to the health care sector.

The microfluidic pump is gaining considerable significance in the global scenario due to the increased need for micro pumping systems in life science, health care devices, pharmaceuticals, etc. The market for micropump is expanding globally in developed American and European countries and developing countries like China, India. The compound annual growth rate (CAGR) for the micropump market is expected to be around 19.4% from 2017 to 2023. The Americas region captured the most significant market globally for micropump technology and is expected to increase from USD 920.5 million in 2016 to USD 1419.5 million by 2023.

The present work focuses on developing a miniaturized pump for biomedical applications such as drug delivery, pumping and infusion of biological fluids, etc., considering the ever-growing significance and the market for micropump technology. The biomedical application of micropump requires a disposable feature to prevent problems of infection or contamination. Traditionally, the piezoelectric micropump assembly is formed as a single entity with an actuator attached to a diaphragm of the micropump chamber. Considering the risk of contamination, discarding the whole micropump assembly with an expensive actuator adds to the cost. A unique micropump design can address this issue with a separable chamber that can be retrofitted into the actuator.

2.5 Objectives

1. To propose a disposable chamber valveless micropump with the bossed diaphragm, analyze and optimize all the components of this micropump
2. Experimental characterization of the actuator, bossed diaphragm and the micropump chamber
3. Fabrication and experimental testing of the micropump
4. To propose and analyze annular excitation approach for enhancement of the performance of the above micropump

5. Fabrication and testing of the annularly excited micropump to validate the performance enhancement

2.6 Scope of the Present Work

The scope of the present work is focused on the design and optimization of the disposable chamber micropump for biomedical applications. The proposed micropump incorporated a single chamber disposable chamber valveless configuration. The actuation of the proposed micropump is achieved through an amplified piezo actuator (APA) with the bossed diaphragm, which is subjected to central and annular excitation. The Finite Element approach is implemented to investigate the static and dynamic deflection behaviour of the centrally excited bossed diaphragm. Deflection behaviour of the silicone rubber and Polydimethylsiloxane (PDMS) bossed diaphragm having a thickness of 0.2 mm, 0.40 mm, and 0.60 mm and bossed ratio 0.33, 0.50, 0.66 is considered under different actuation voltage and frequency. Optimization of the centrally excited bossed diaphragm is done based on the simulation results. Further, an annular excitation of the bossed diaphragm is proposed to enhance the deflection range with Finite Element Analysis.

Different configurations of the bossed diaphragm are fabricated and experimentally characterized to measure the deflection behaviour under central and annular excitation. The simulation and the experimental results are compared for validation purpose. In addition, a comparative study is carried out to evaluate the enhancement in deflection behaviour of the bossed diaphragm through annular excitation compared to central excitation. Finally, the performance evaluation of the proposed micropump is carried out with a centrally and annularly excited bossed diaphragm. Experimental characterization considered the effect of factors such as the bossed ratio of the diaphragm, diaphragm thickness, micropump chamber depth, fluid density/ viscosity, operating parameters such as voltage and frequency on the performance of the micropump. A comparative study is carried to assess the enhancement in the performance of the micropump with annular excitation over the central excitation.

METHODOLOGY

The biomedical application of micropump requires a disposable feature to prevent problems of infection or contamination. Traditionally, the piezoelectric micropump assembly is formed as a single entity with an actuator attached to a diaphragm of the micropump chamber. Considering the risk of contamination, discarding the whole micropump assembly with an expensive actuator adds to the cost. A unique micropump design can address this issue with a separable chamber that can be retrofitted into the actuator. The following section describes the methodology adopted in the development of disposable chamber micropump for biomedical application.

3.1 Proposed Micropump and analysis of its components

The following section describes the design approach towards the proposed micropump.

3.1.1 Amplified Piezo Electric Actuator (APA) for Micropump Actuation

The proposed micropump is actuated by the flexural amplified piezo actuator (APA-120S) from Cedrat Technologies®. Figure 3.1 represents the photograph of the APA and the actuator mechanism used for micropump actuation. The APA consists of a multi-layered piezo stack (MLA $5 \times 5 \times 20$ mm) embedded inside a flexural amplifier made of spring steel. The flexural amplifier has an overall dimension of $13 \times 28.7 \times 5$ mm. The actuator excitation voltage varies between 10 V to 150 V. Application of electric potential across the multilayer piezo stack actuator generates strain along the x-direction which deforms the flexural amplifier. This, in turn, leads to amplified motion along the z-direction. The motion required for the actuation of the micropump is achieved with the lift rod mechanism integrated with the amplified piezo actuator. The schematic representation of the actuation mechanism before and after actuation is shown in Figure 3.2 (a) and Figure 3.2 (b). The lift road mechanism deforms the diaphragm along the positive z-direction upon applying a voltage across the actuator.
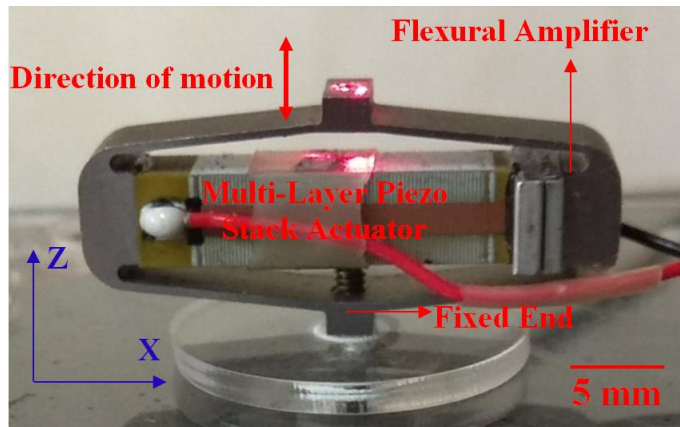
Figure 3.1 APA-120S (Amplified Piezo Actuator) implemented in proposed micropump

(a)   **(b)**
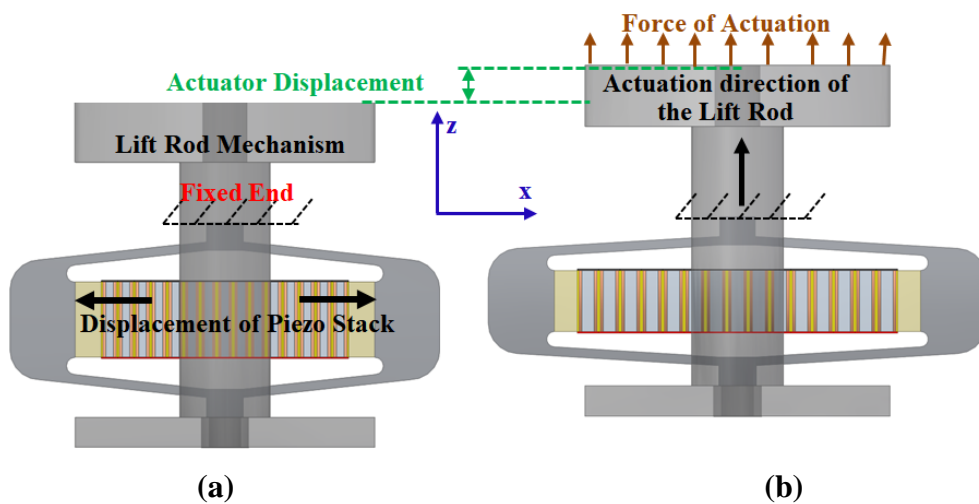
Figure 3.2 Schematic of actuation mechanism **(a)** Before actuation **(b)** After actuation

3.1.2 Valves (Nozzle/Diffuser)

The flow rectification of the fluid in the proposed micropump incorporates the nozzle/diffuser placed at the inlet and outlet of the micropump. During the suction mode, the inlet channel acts like a diffuser allowing maximum fluid to enter the pump chamber, whereas the outlet channel acts like a nozzle resulting in a minimum amount of backflow of the pumped fluid. During the pumping mode, a substantial amount of fluid flows through the diffuser at the outlet during the pumping mode with minimum outflow through the inlet nozzle. Thus there is a net flow of fluid from inlet to outlet in one complete cycle of suction and pumping mode. The performance of

nozzle/diffusers in providing efficient flow rectification significantly depends on its geometrical configuration, particularly the divergent angle, channel length, and inlet/outlet parameters. Figure 3.3 illustrates the schematic of the nozzle/diffuser with the micropump chamber. The micropump proposed by S. Singh et al. (2015), H. K. Ma et al. (2015) and Paul Kawun et al. (2016) have effectively incorporated nozzle/diffuser with a 10º included angle. The proposed micropump design also employs a flat trapezoidal nozzle/diffuser of 10º divergence angle. Considering the fabrication and dimensional constraints, the inlet width, outlet width and channel length of the nozzle/diffuser are fixed at the value of 0.90 mm, 0.50 mm and 2.50 mm, respectively.

(a) Suction Stoke **(b)** Pumping Stroke

(c) Dimensional specification of the nozzle/diffuser
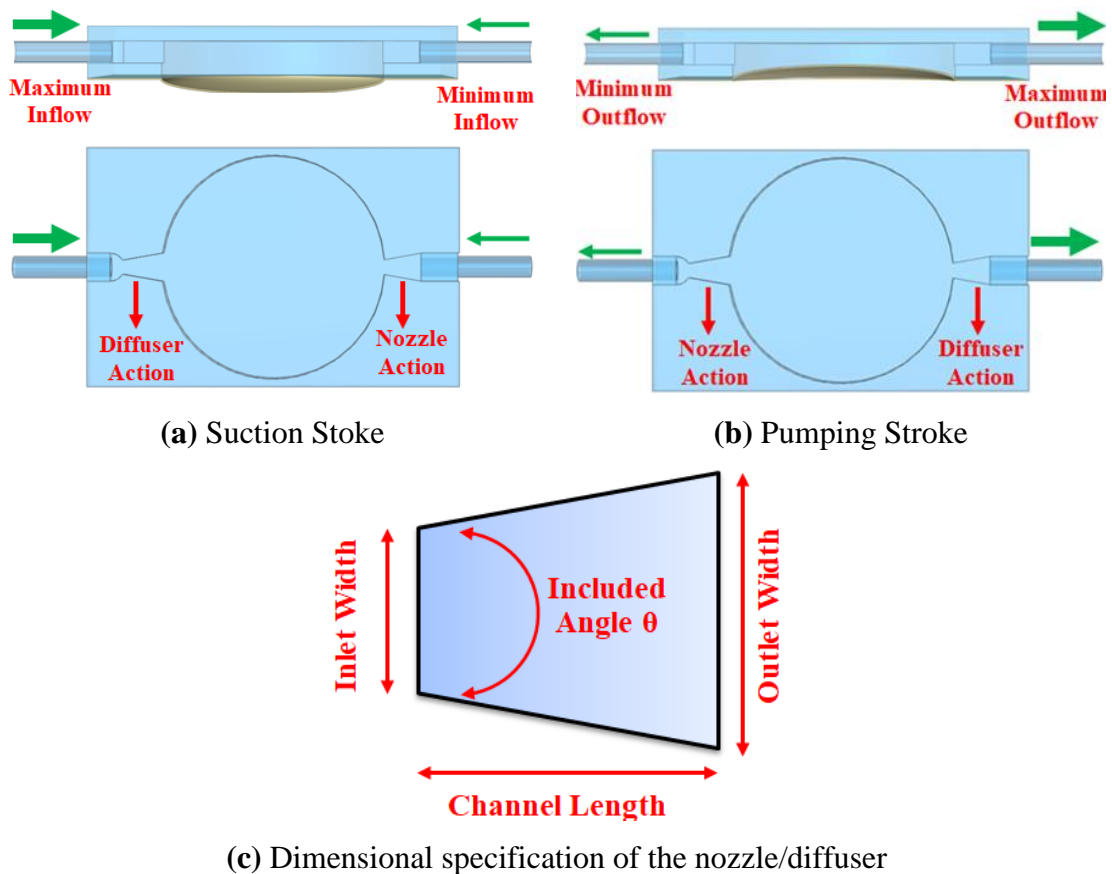
Figure 3.3 Schematic of micropump with nozzle/diffuser **(a)** Suction Stroke **(b)** Pumping Stroke **(c)** Dimensional specification of the nozzle/diffuser

3.1.3 Bossed Diaphragm

In most piezo-actuated micropumps, plain diaphragms are used with the actuator bonded to the diaphragm surface. The presence of bonded actuator along with the diaphragm eliminates the possibility of a disposable chamber. The micropump proposed in the present work incorporates bossed diaphragm to meet disposable chamber requirements. The bossed diaphragm consists of a plain membrane with a central cylindrical protrusion that facilitates contact without bonding between the actuating mechanism and the flexible membrane. The bossed diaphragm also helps to overcome non-uniform stress distribution and wrinkling of the diaphragm during micropump manufacturing (Ma et al. 2015; X Y Wang et al. 2016). The control of deflection of the diaphragm is achievable through proper actuator deflection, which intern depends on potential applied across the actuator. Figure 3.4 (a) and Figure 3.4 (b) represents the schematic of the sectional view and front view of the bossed diaphragm implemented in the proposed micropump.

(a)

(b)
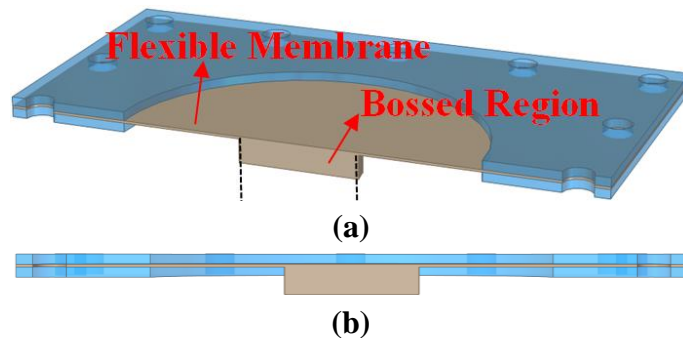
Figure 3.4 (a) Sectional view and **(b)** Front view of the bossed diaphragm

Deflection of the diaphragm is one of the factors which significantly contribute towards the micropump performance. The higher value of diaphragm deflection leads to the increased swept volume inside the pump chamber, which enhances the micropump flow/pressure characteristics. Parameters such as diaphragm material, thickness influences the deflection behaviour of the diaphragm. Materials such as stainless steel, copper, Si, glass, etc., are extensively used in the micropump application. However, these materials possess the higher value of young modulus and modulus of rigidity, thus offering higher deformation resistance leading to lower

deflection. Application of soft polymer materials such as silicone rubber, PDMS, and latex rubber could be alternative diaphragm materials with lower young modulus and rigidity. Such materials tend to offer lower resistance leading to higher deflection (Ma et al. 2015). Thus the proposed concept of micropump employs silicone rubber and PDMS as diaphragm materials. The theoretical and finite element analysis of the bossed diaphragm with silicone rubber and PDMS is carried out in the subsequent chapters considering the effect of parameters such as the material property, thickness and bossed ratio.
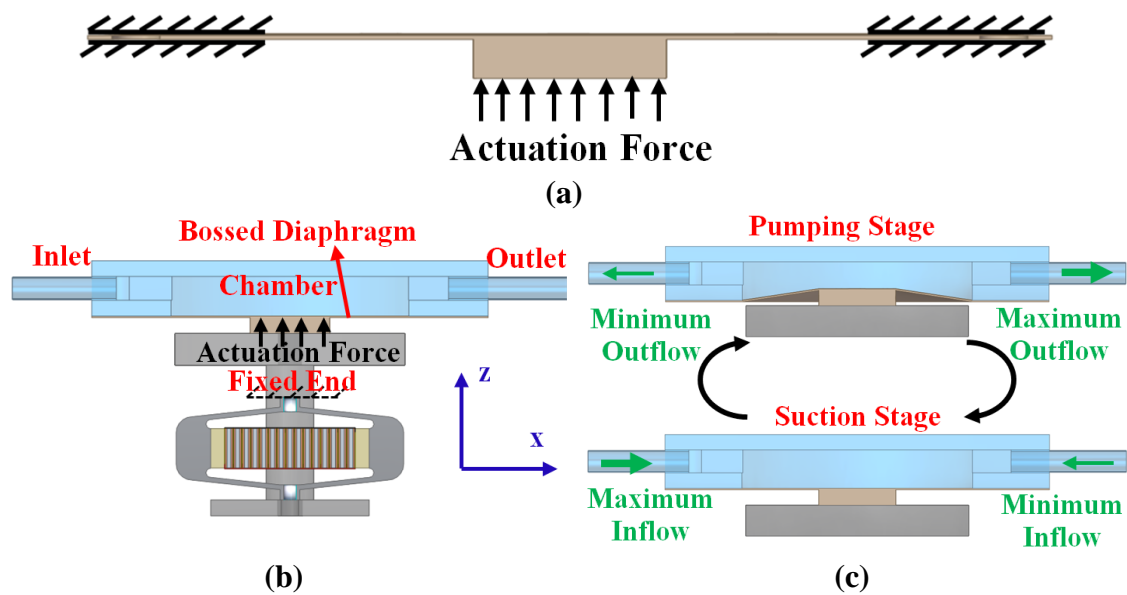
Figure 3.5 (a) Bossed diaphragm subjected to central excitation **(b)** Schematic of the valveless micropump with centrally excited bossed diaphragm **(c)** Pumping Stage/Suction stage

The excitation method of the bossed diaphragm also affects the deflection behaviour under dynamic operation. The central and annular excitation of the bossed diaphragm is considered in the present study. Conventionally the bossed diaphragm is subjected to actuation force on the central cylindrical bossed region. Figure 3.5 (a) and Figure 3.5 (b) represents the schematic of the conventionally adopted central excitation method for mechanical micropump. The force transmitted from the actuator through the lift rod deforms the diaphragm along the positive z-direction. The upward motion of the bossed diaphragm (Figure 3.5 (b)) pumps the fluid out of the chamber

through the outlet. When the diaphragm regains its original position (Figure 3.5 (b)), the pressure inside the chamber drops, leading to fluid inflow into the pump chamber. This cycle of pumping and suction continues resulting in the pulsating flow as long as the actuator is supplied with excitation voltage.

The limitation of the oscillation amplitude of the central excitation of the bossed diaphragm could be overcome with the help of a novel approach of annular excitation. Figure 3.6 (a) and Figure 3.6 (b) represents the schematic of the proposed novel approach of annular excitation of the bossed diaphragm, where the actuation force from the actuator is applied on the diaphragm away from the central region. The proposed novel method of annular excitation is inspired by the works of Shabanian et al. (2016) and Pradeesh et al. (2019). Shabanian et al. (2016) reported a novel method of excitation of the micropump diaphragm through an annular ring-type piezo bimorph actuator which delivered a better deflection range when compared with the conventional approach of central excitation with disc-type piezo bimorph. Pradeesh et al. (2019) reported their work on the optimal position of the proof mass on the cantilever beam with a piezoelectric actuator for energy harvesting. The dynamic excitation of the cantilever beam mounted with the proof mass at its free resulted in enhancement of the oscillation amplitude.

In the annular excitation, the bossed diaphragm is subjected to dynamic loading away from the central bossed region. Under the dynamic actuation conditions, the bossed region acts like a suspended proof mass which undergoes higher amplitude of oscillation due to the elastic property of the thin membrane. Also, the diaphragm under annular excitation can oscillate along the negative z-direction, which increases the effective swept volume of the micropump, thus enhancing the pump performance. Figure 3.6 (c) represents the proposed micropump with the pumping stage and suction stage under annular excitation. The maximum deflection of the diaphragm occurs when it oscillates at the resonance condition when excited harmonically. The performance of annular excitation depends on parameters such as material property, the thickness of the flexible membrane, bossed diameter and proof mass.
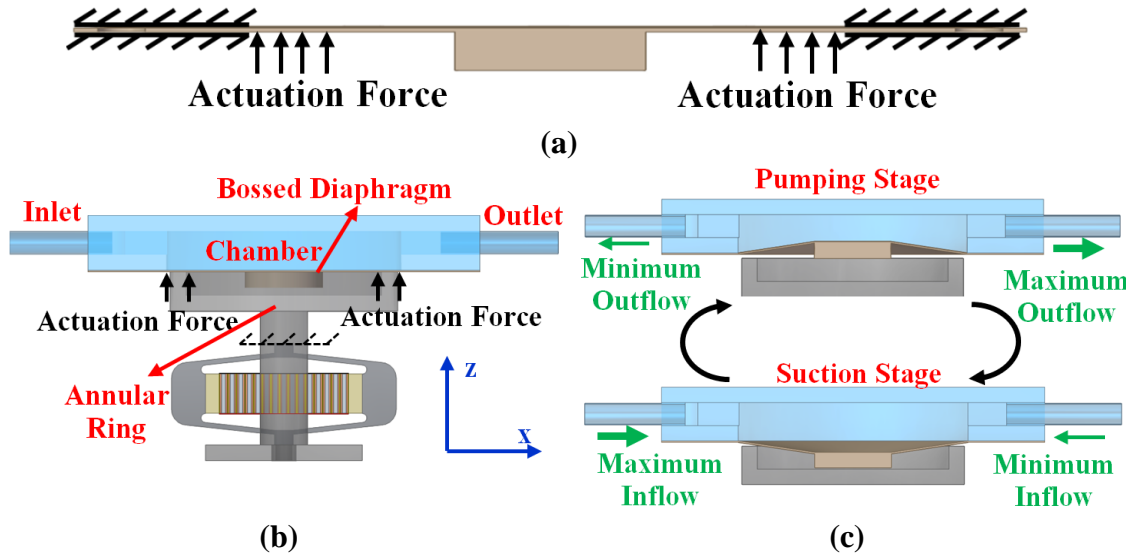
Figure 3.6 (a) Bossed diaphragm subjected to annular excitation **(b)** Schematic of the valveless micropump with annularly excited bossed diaphragm **(c)** Pumping Stage/Suction stage

3.2 Theoretical Analysis

The following section illustrates the theoretical analysis of the amplified piezo actuator, bossed diaphragm and micropump chamber, which play a vital role in determining the performance of the micropump.

3.2.1 Theoretical Analysis of the Amplified Piezo Actuator

The present novel concept of diaphragm actuation employs an amplified piezo actuator as a source which typically consists of multilayer piezo stack actuators as the primary actuator. The mechanical strain developed by the different piezoelectric layers of the multilayer actuator due to the applied electric field gets amplified through the flexural amplifier. Equation 3.1 and equation 3.2 represents the electro-mechanical interaction of the piezoelectric materials (strain-charge form). The consecutive relations are based on the assumption that the total stain developed in the piezoelectric element is the sum of the actuation strain due to the applied voltage and the mechanical strain due to applied stresses (Mohith et al. 2021).

$$\{\boldsymbol{\varepsilon}\} = [\boldsymbol{c}]\{\boldsymbol{\sigma}\} + [\boldsymbol{d}]\{\boldsymbol{E}\} \tag{3.1}$$

$${D} = [d]^t{\sigma} + [e]{E} \tag{3.2}$$

where, ε is the strain vector, D (C/m^2) is electric displacement, c (m^2/N) is the compliance matrix, d (m/V) is piezoelectric coefficient, e (F/m) is dielectric permittivity, σ (N/m^2) is the applied stress, E (V/m) applied electric field. Since the piezoelectric material exists as orthotropic materials, the matrix representation of the constitutive piezoelectric relation in the matrix form is represented in equation 3.3 and equation 3.4.

$$\begin{Bmatrix} \varepsilon_1 \\ \varepsilon_2 \\ \varepsilon_3 \\ \varepsilon_4 \\ \varepsilon_5 \\ \varepsilon_6 \end{Bmatrix} = \begin{bmatrix} c_{11} & c_{12} & c_{13} & 0 & 0 & 0 \\ c_{21} & c_{22} & c_{23} & 0 & 0 & 0 \\ c_{31} & c_{32} & c_{33} & 0 & 0 & 0 \\ 0 & 0 & 0 & c_{44} & 0 & 0 \\ 0 & 0 & 0 & 0 & c_{55} & 0 \\ 0 & 0 & 0 & 0 & 0 & c_{66} \end{bmatrix} \begin{Bmatrix} \sigma_1 \\ \sigma_2 \\ \sigma_3 \\ \sigma_4 \\ \sigma_5 \\ \sigma_6 \end{Bmatrix} + \begin{bmatrix} 0 & 0 & d_{31} \\ 0 & 0 & d_{32} \\ 0 & 0 & d_{33} \\ 0 & d_{24} & 0 \\ d_{15} & 0 & 0 \\ 0 & 0 & 0 \end{bmatrix} \begin{Bmatrix} E_1 \\ E_2 \\ E_3 \end{Bmatrix} \tag{3.3}$$

$$\begin{Bmatrix} D_1 \\ D_2 \\ D_3 \end{Bmatrix} = \begin{bmatrix} 0 & 0 & 0 & 0 & d_{15} & 0 \\ 0 & 0 & 0 & d_{24} & 0 & 0 \\ d_{31} & d_{32} & d_{33} & 0 & 0 & 0 \end{bmatrix} \begin{Bmatrix} \sigma_1 \\ \sigma_2 \\ \sigma_3 \\ \sigma_4 \\ \sigma_5 \\ \sigma_6 \end{Bmatrix} + \begin{bmatrix} e_{11} & 0 & 0 \\ 0 & e_{22} & 0 \\ 0 & 0 & e_{33} \end{bmatrix} \begin{Bmatrix} E_1 \\ E_2 \\ E_3 \end{Bmatrix} \tag{3.4}$$

Typically the multi-layered piezoelectric actuators consist of several piezo monolayers stacked one over the other with suitable electrode and insulation layers. The total displacement achieved with multilayer piezo stack layer equals to the sum of the displacement produced by individual layers. For a multi-layered piezoelectric actuator with 'n' number of piezo layers polarized along d_{33} direction with stiffness $K_{piezostack}$ and applied voltage 'V', the overall free stroke $(\Delta_{piezostack})_{Free}$ and the blocked force $(F_{blocked})_{Piezostack}$ achieved is represented by equation 3.5 and equation 3.6 (Mohith et al. 2021).

$$(\Delta_{\textbf{Piezostack}})_{\textbf{Free}} = \textbf{n}\textbf{d}_{\textbf{33}}\textbf{V} \tag{3.5}$$

$$(\textbf{F}_{\textbf{blocked}})_{\textbf{Piezostack}} = \textbf{K}_{\textbf{Piezostack}}\Delta_{\textbf{Piezostack}} \tag{3.6}$$

Further, integrating a flexural amplifier with the piezo stack actuator enhances the range of motion by an amplification factor A.F (equation 3.7). The blocked force

developed by the amplified piezo actuator depends on the stiffness of the flexural amplifier KAPA represented by equation 3.8. The piezo actuator blocked force and deflection have a complementary relationship with each other. The blocked force is maximum when the motion of the actuator is restricted. The actuator achieves maximum deflection when no external force acts against the direction of stroke.

$$(\Delta_{\textbf{APA}})_{\textbf{Free}} = (\textbf{A}.\textbf{F})\Delta_{\textbf{Piezostack}} \tag{3.7}$$

$$(\textbf{F}_{\textbf{blocked}})_{\textbf{APA}} = \textbf{K}_{\textbf{APA}}(\Delta_{\textbf{APA}})_{\textbf{Free}} \tag{3.8}$$

When attached with the diaphragm, the stiffness of the diaphragm offers resistance to the stroke of the actuator. The range of stroke Δ_{APA} generated by the actuator when integrated with the diaphragm of stiffness K_{eff} is represented in equation 3.9. With the increase in the external resistance, the range of stroke by the actuator decreases. The expression for force developed by the APA when attached to diaphragm is represented in equation 3.10 (Mohith et al. 2021).

$$\Delta_{\textbf{APA}} \approx (\Delta_{\textbf{APA}})_{\textbf{Free}}\frac{\textbf{K}_{\textbf{APA}}}{\textbf{K}_{\textbf{APA}} + \textbf{K}_{\textbf{eff}}} \tag{3.9}$$

$$\textbf{F}_{\textbf{APA}} \approx (\textbf{F}_{\textbf{blocked}})_{\textbf{APA}}\frac{\textbf{K}_{\textbf{eff}}}{\textbf{K}_{\textbf{APA}} + \textbf{K}_{\textbf{eff}}} \tag{3.10}$$

3.2.2 Theoretical Analysis of the Bossed Diaphragm

The following section presents a theoretical analysis to understand the effect of material property, thickness, bossed ratio and loading radius on the stiffness of the bossed diaphragm. Figure 3.7 (a) and Figure 3.7 (b) represents the dimensional parameters of both centrally and annularly excited bossed diaphragm. The expression for the effective stiffness of bossed diaphragm with thickness 't', young's modulus 'E', poisons ratio 'γ' subjected to force 'F' is given by equation 3.11 (Young and Budynas 2002; Ma et al. 2015)
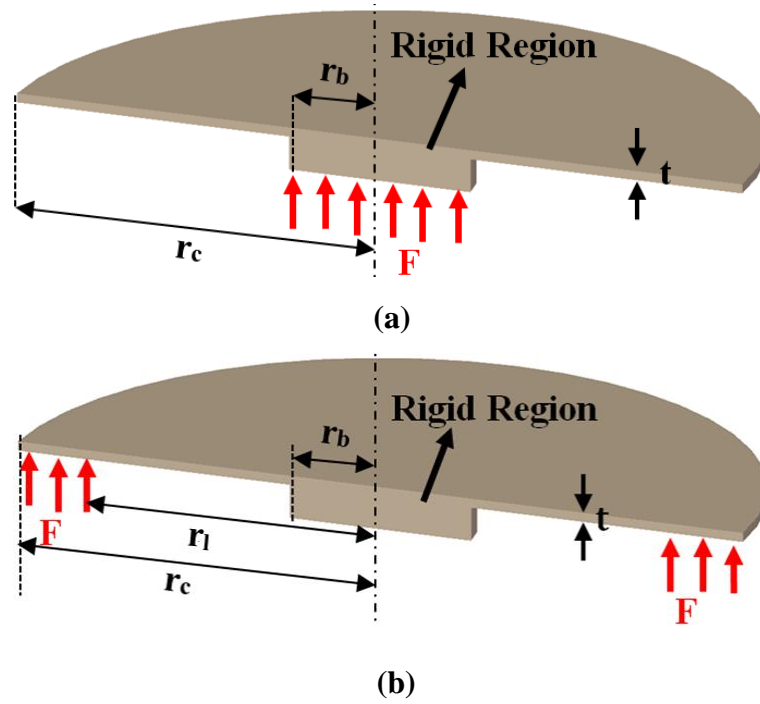
Figure 3.7 Dimensional specification of **(a)** bossed diaphragm with centre excitation **(b)** bossed diaphragm with annular excitation

$$(K_{eff})_{central} = \frac{2\pi B_r D}{r_c^2 \left(\frac{C_2 L_6}{C_5} - L_3\right)} \qquad (K_{eff})_{annular} = \frac{\pi (r_c^2 - r_l^2) D}{r_c^4 \left(\frac{C_2 L_{14}}{C_5} - L_{11}\right)} \qquad (3.11)$$

Where,

r_c is the effective diaphragm radius

r_b radius of the bossed region

r_l radius of annular loading

B_r bossed ratio, $\quad B_r = \frac{r_b}{r_c}$

$$D = \frac{Et^3}{12(1-\gamma^2)}$$

$$C_2 = \frac{1}{4}\left\{1 - B_r^2\left(1 + 2\ln\left(\frac{1}{B_r}\right)\right)\right\}$$

$$C_5 = \frac{1}{2}(1 - B_r^2)$$

$$L_3 = \frac{B_r}{4}\left[(B_r^2 + 1)\ln\left(\frac{1}{B_r}\right) + B_r^2 - 1\right]$$

$$L_6 = \frac{B_r}{4}\left(B_r^2 - 1 + 2\ln\frac{1}{B_r}\right)$$

$$L_{11} = \frac{1}{64}\left(1 + 4\left(\frac{r_L}{r_c}\right)^2 - 5\left(\frac{r_L}{r_c}\right)^4 - 4\left(\frac{r_L}{r_c}\right)^2\left[2 + \left(\frac{r_L}{r_c}\right)^2\right]\ln\frac{r_c}{r_L}\right)$$

$$L_{14} = \frac{1}{16}\left[1 - \left(\frac{r_L}{r_c}\right)^4 - 4\left(\frac{r_L}{r_c}\right)^2\ln\frac{r_c}{r_L}\right]$$
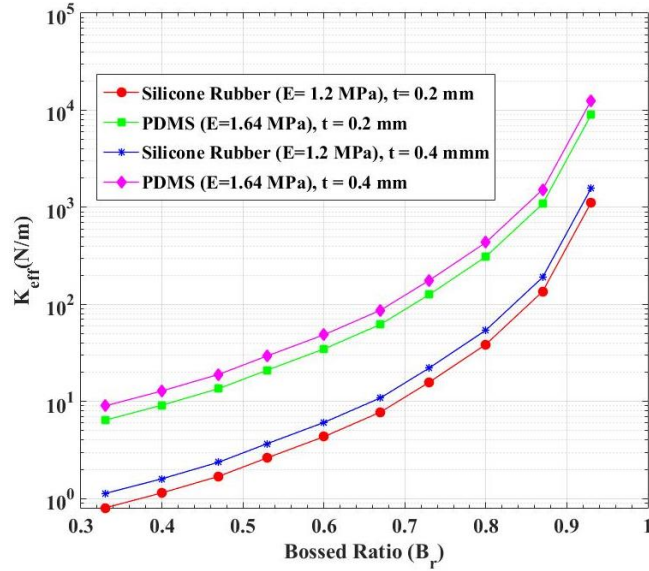
(a)
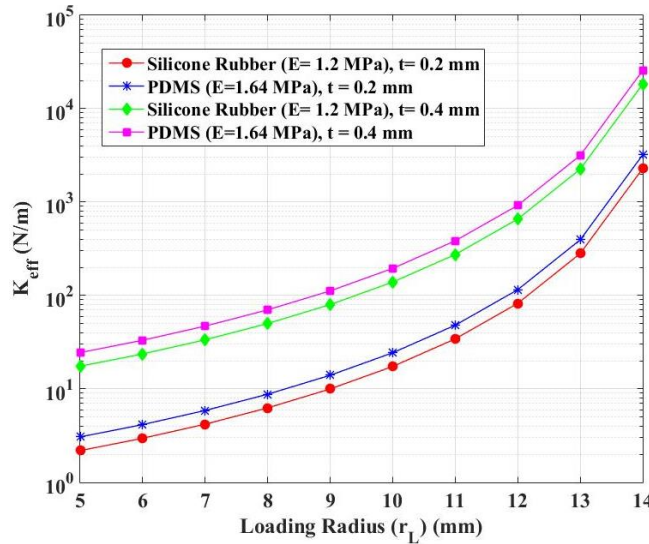
(b)

Figure 3.8 (a) Variation of effective stiffness with bossed ratio for a bossed diaphragm of radius (r_c) 15.00 mm **(b)** Variation of effective stiffness with loading radius for a bossed diaphragm of radius (r_c) 15.0 mm

The materials such as silicone rubber (E = 1.2 MPa) and PDMS (E =1.64 MPa) with the thickness value of 0.20 mm and 0.40 mm are considered for theoretical analysis of the bossed diaphragm. The diameter of the diaphragm is fixed at 30.00 mm. The theoretical analysis considered the effect of variation of the bossed ratio and the loading radius on the effective stiffness of the above mentioned diaphragms. The stiffness of the bossed diaphragm increases exponentially with the increase in the bossed ratio, the diaphragm thickness, young's modulus and the loading radius (Ma et al. 2015), as observed from Figure 3.8 (a) and Figure 3.8 (b).

The resistance for deformation of the diaphragm is minimum when the application of load corresponds to the central cylindrical region. However, with the increase in the bossed region, the effective stiffness increases (Figure 3.8 (a)), leading to increased resistance for deformation. Further, as the point of application load moves away from the central region, the effective stiffness increases (Figure 3.8 (b)). From the above theoretical analysis, it can be concluded that the silicone rubber bossed diaphragm with the bossed ratio of 0.33 and thickness 0.20 mm has a lower value of stiffness which could deliver better deflection performance under central excitation. Under annular excitation, the silicone rubber bossed diaphragm with the bossed ratio of 0.33, thickness 0.20 mm, and loading radius 5.00 mm possess a lower stiffness. Due to the geometrical and fabrication constraints, the loading radius is fixed at a value of 10.00 mm for annular excitation. The subsequent sections of the work consider the effects of diaphragm thickness, material property, bossed ratio and loading radius on the deflection performance through the finite element analysis and experimental study.

3.2.3 Theoretical Analysis of the Micropump Chamber

In the proposed micropump, the disposable chamber is closed on the top, and a bossed diaphragm is attached on the bottom side, as shown in Figure 3.9. At the end of pumping action, the residual liquid is present on the diaphragm surface inside the chamber, forming a thin liquid layer. Due to the thin layer of liquid on the diaphragm, the adhesive force acts on the diaphragm surface. Mathematical formulation and theoretical analysis are carried out to understand the effect of the adhesion force

acting on the surface, which tries to resist the downward motion of the diaphragm. Figure 3.9 also represents the different forces acting on the diaphragm when the diaphragm is about to return to its equilibrium position, i.e., commencing of supply mode.
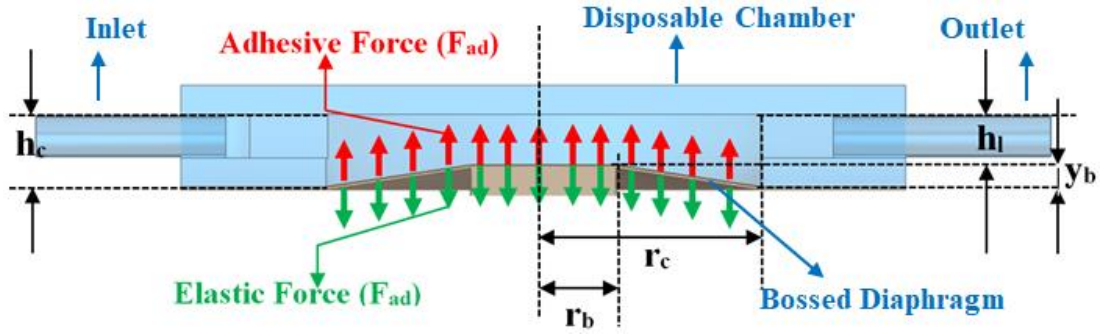
Figure 3.9 Representation of different forces acting the diaphragm during the commencement of supply mode. (F_{ad} is the adhesive force acting on the diaphragm surface due to the residual liquid in the chamber; F_e is the elastic force of the diaphragm; r_b, r_c is the bossed radius and chamber radius respectively; h_c, h_l, y_b are Chamber depth, residual liquid height, diaphragm deflection respectively).

From the assumption of thin film approximation, the pump containing a liquid of viscosity (μ), pressure distribution expression can be represented as (H. K. Ma et al. 2016),

$$\frac{\partial p}{\partial r} = \frac{6\mu r}{h^3}\frac{dh}{dt} + \frac{C(t)}{r} \tag{3.12}$$

From Figure 3.9, the height of the liquid retained on the diaphragm surface varies as a function of the radius of the diaphragm. For $r \leq r_b$, $h = h_l$ i.e. the height of the liquid retained (h_l) in the bossed region of the diaphragm remains constant up to r_b. But beyond r_b, the height of the residual liquid varies with the radius from h_l to h_c.

Therefore, for $r_b \leq r \leq r_c$,

$$h = \left(\frac{r - r_b}{r_c - r_b}\right)(h_c - h_l) + h_l$$

Integration of equation (4) with $p = p_o$ at $r = r_c$ fetches the value of p.

$$p = -3\mu\frac{dh}{dt}\frac{(r_c - r_b)^3}{(h_c - h_l)^2}\frac{[r_c h_l - r_b h_c + 2r(h_c - h_l)]}{[r_c h_l - r_b h_c + r(h_c - h_l)]^2} + C_1 \tag{3.13}$$

For $r_b \leq r \leq r_c$

$$p = 3\mu\frac{dh}{dt}\frac{r^2}{h_l^3} + C_2 \tag{3.14}$$

For $r \leq r_b$

Where,

$$C_1 = p_0 - 3\mu\frac{dh}{dt}\frac{(r_c - r_b)}{h_c^2(h_c - h_l)^2}[r_c h_l - 2r_c h_c + r_b h_c]$$

$$C_2 = p_0 - 3\mu\frac{dh}{dt}\left[\frac{r_b^2}{h_l^3} + \frac{(r_c - r_b)}{(h_c - h_l)^2}\left[\frac{[r_c h_l - 2r_b h_l + r_b h_c]}{h_l^2} + \frac{r_c h_l - 2r_c h_c + r_b h_c}{h_c^2}\right]\right]$$

The adhesive force F_{ad} acting on the diaphragm is expressed as

$$F_{ad} = \int_0^{2\pi}\int_0^{r_c}(p - p_o)\,r\,dr\,d\theta$$

$$= \int_0^{2\pi}\left(\int_0^{r_b}(p - p_o)\,r\,dr + \int_{r_b}^{r_c}(p - p_o)\,r\,dr\right)d\theta \tag{3.15}$$

Thus,

$$F_{ad} = 6\pi\mu\frac{dh}{dt}C_{ad} \tag{3.16}$$

Since $h_l = h_c - y_b$

$$F_{ad} = -6\pi\mu C_{ad}\frac{d(h_c - y_b)}{dt}$$

Therefore the final expression for the adhesive force given by

$$F_{ad} = 6\pi\mu C_{ad}\frac{dy_b}{dt} \tag{3.17}$$

Where,

$$C_{ad} =$$

$$\frac{r^2\alpha}{2}\Big|_0^{r_b} - \frac{r^4}{4h_l^3}\Big|_0^{r_b} + \frac{r^2\beta}{2}\Big|_{r_b}^{r_c} -$$

$$\frac{(r_c-r_b)^3}{(h_c-h_l)^4}\left[\frac{(r_ch_l-r_bh_c)^2}{r(h_c-h_l)+(r_ch_l-r_bh_c)} + 3(r_ch_l - r_bh_c)\ln\big(r(h_c - h_l) + (r_ch_l -\right.$$

$$\left.r_bh_c)\big) - 2\big(r(h_c - h_l) + (r_ch_l - r_bh_c)\big)\right]\Bigg|_{r_b}^{r_c} \tag{3.18}$$

$$\alpha = \frac{r_b^2}{h_l^3} + \frac{(r_c - r_b)}{(h_c - h_l)^2}\left[\frac{[r_ch_l - 2r_bh_l + r_bh_c]}{h_l^2} + \frac{r_ch_l - 2r_ch_c + r_bh_c}{h_c^2}\right] \tag{3.19}$$

$$\beta = \frac{(r_c - r_b)}{h_c^2(h_c - h_l)^2}[r_ch_l - 2r_ch_c + r_bh_c] \tag{3.20}$$

Where C_{ad} corresponds to the adhesive force coefficient acting on the oscillating diaphragm, and its value mainly depends on the chamber diameter, chamber depth, and the residual liquid and bossed ratio of the diaphragm. The optimization of the micropump chamber depth is done based on the mathematical formulations of the adhesive force due to the liquid retained on the diaphragm surface at the end of the pumping stroke. A chamber diameter of 30.00 mm is considered to facilitate the manufacturing and compare the performance of the micropump.

The force of adhesion acting on the diaphragm surface depends on the amount of fluid retained on the diaphragm surface, which depends on the micropump chamber depth. Figure 3.10 represents the variation of the numerically simulated adhesive force coefficient (C_{ad}) (chamber diameter 30 mm) with diaphragm deflection (y_b) for different chamber depth (h_c) and bossed ratio (B_r). The value of C_{ad} increases exponentially with an increase in diaphragm deflection and expands rapidly when the diaphragm deflection approaches the chamber depth (Ma et al. 2015).
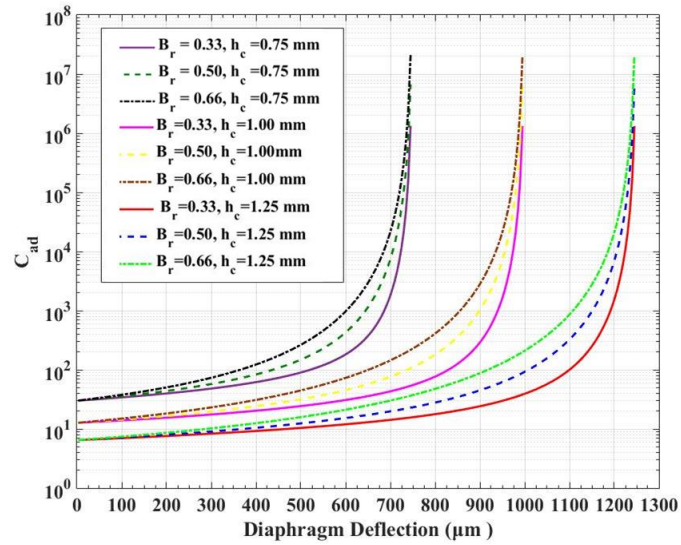
Figure 3.10 Variation of adhesive force coefficient with diaphragm deflection for chamber diameter of 30.00 mm.

Though the higher deflection of the diaphragm leads to a larger swept volume, the influence of adhesive force on the diaphragm increases significantly, resulting in lower performance. However, if the deflection of the diaphragm is much lower than the chamber depth, the influence of the force of adhesion depends largely on the amount of liquid retained on the diaphragm surface, which in turn depends on the depth of the chamber. Also, the increase in the bossed ratio adds to the increased influence of adhesive force on the diaphragm as seen from Figure 3.10. The influence of adhesive force is also found to decrease with increased chamber depth. This effect occurs as a result of the increase in the thickness of the fluid layer on the diaphragm surface after the pumping process. Further, as observed from equation 3.17, the adhesive force is directly proportional to the viscosity of the fluid μ. Thus an increase in the viscosity of the fluid also significantly increases the adhesive force on the surface of the diaphragm. The results of adhesive force analysis are presented in chapter 4, where different chamber depths of the disposable chamber and fluids of different viscosity are considered for experimental evaluation.

3.3 FEA Analysis of the Amplified Piezo Actuator and the Bossed Diaphragm

This section highlights the finite element analysis (FEA) of the multilayer piezo stack actuator, amplified piezoelectric actuator, actuation mechanism and the bossed diaphragm. The FE analysis of multilayer piezo stack actuator, amplified piezoelectric actuator and actuation mechanism is focussed on deflection and blocked force characteristics. Further, the FE analysis of bossed diaphragm emphasized optimization of diaphragm configuration concerning the materials, thickness, bossed ratio and loading method. The FE analysis is performed in COMSOL 5.3 with the piezoelectric device and solid mechanics platform. Figure 3.11 represents the meshed configuration, and boundary condition of the piezo stack actuator amplified piezo actuator and the actuation mechanism. The free tetrahedral meshing element is considered for meshing configuration the actuator configuration.

(a) Multi-Layer Piezo Stack Actuator	(b) Amplified Piezo Actuator

(c) Actuation Mechanism with Lift Rod
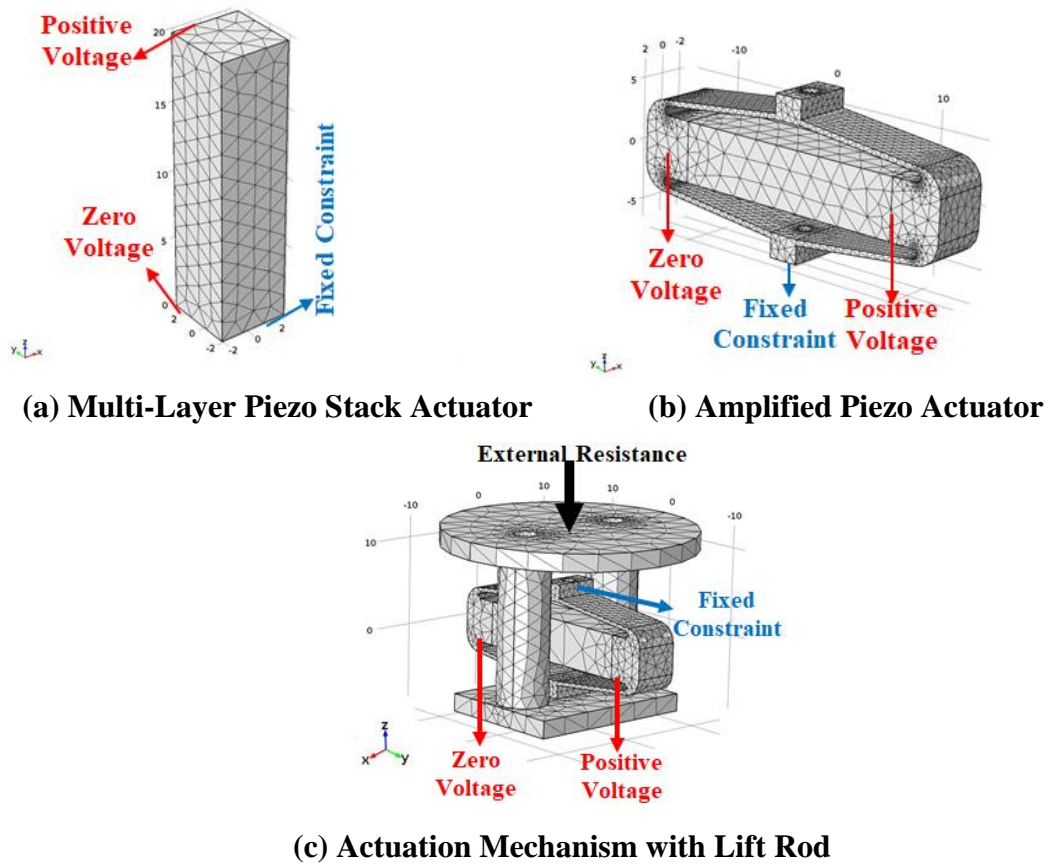
Figure 3.11 Meshed configurations and boundary conditions of **(a)** Multi-layer piezo stack actuator **(b)** Amplified piezo actuator **(c)** Actuation mechanism with lift rod

Table 3.1 Properties of the multi-layer piezo stack actuator, amplified piezo actuator and lift rod mechanism

Property	Value
Piezo Stack Actuator (PZT-5H), (5 × 5 × 20 mm)	
Stiffness Matrix (N/m^2)	$\begin{bmatrix} 12.6 & 7.95 & 8.41 & 0 & 0 & 0 \\ 7.95 & 12.6 & 8.41 & 0 & 0 & 0 \\ 8.41 & 8.41 & 11.7 & 0 & 0 & 0 \\ 0 & 0 & 0 & 2.3 & 0 & 0 \\ 0 & 0 & 0 & 0 & 2.3 & 0 \\ 0 & 0 & 0 & 0 & 0 & 2.325 \end{bmatrix} \times 10^{10}$
Piezoelectricity (C/m^2)	$\begin{bmatrix} 0 & 0 & -6.5 \\ 0 & 0 & -6.5 \\ 0 & 0 & 23.3 \\ 0 & 17 & 0 \\ 17 & 0 & 0 \\ 0 & 0 & 0 \end{bmatrix}$
Permittivity (F/m)	$\begin{bmatrix} 1700 & 0 & 0 \\ 0 & 1700 & 0 \\ 0 & 0 & 1470 \end{bmatrix}$
Density (Kg/m^3)	7500
Flexural Amplifier (Spring Steel) (28.7 × 13 × 5 mm)	
Young's Modulus (N/m^2)	210×10^9
Density (Kg/m^3)	7500
Poisons Ratio	0.3
Lift Rod Mechanism (Aluminium)	
Young's Modulus (N/m^2)	70×10^9
Density (Kg/m^3)	2700
Poisons Ratio	0.33
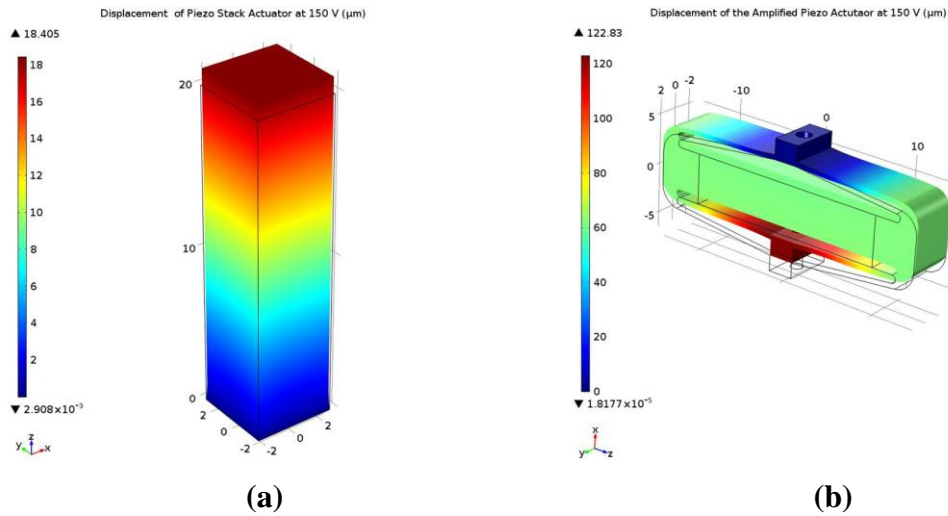
Figure 3.12 Displacement of the **(a)** piezo stack actuator **(b)** amplified piezo actuator at 150 V

The multi-layered piezo stack actuator is modelled as a single rectangular entity having dimensions 5×5×20 mm with physics controlled meshing. The voltage of 150 V/20 mm is applied across the piezo stack actuator. Figure 3.12 (a) represents the simulation results of free deflection of the piezo stack actuator without any external load. The free stroke of the piezo stack actuator is about 18.405 μm for an input voltage of 150 V. The FEM simulation of the amplified piezo actuator consisting of a piezo stack and flexural amplifier followed a similar approach as that of the piezo stack actuator. Figure 3.12 (b) represents the simulated free stroke of the amplified piezo actuator. The maximum deflection of the amplified piezo actuator is about 122.83 μm for an input voltage of 150 V. Thus, the displacement of the multilayer stack actuator gets amplified by a factor of about 6.674.

A lifting rod is integrated with the amplified piezo actuator to transmit the motion from the actuator to the diaphragm. Figure 3.13 (a) represents the simulation results of the amplified piezo actuator with the lift rod mechanism without any external resistance. Considering the geometrical features, the overall weight of the lift rod mechanism is about 6.6 grams. The displacement of the amplified piezo actuator with the lift rod mechanism is about 122.8 μm at an input voltage of 150 V, which matches the range of displacement achieved with the amplified piezo actuator alone.

In spite of the integration of lift rod mechanism, no loss in motion occurs in the overall deflection achieved. However, when subjected to external resistance force, the displacement of the actuator decreases. Figure 3.13 (b) represents the displacement achieved with the actuator when subjected to the external blocking force of 37.5 N and input voltage of 150 V. As observed from figure 3.13 (b), the motion of the actuation mechanism is blocked in the upward direction resulting in almost zero displacement. Therefore the external load of 37.5 N corresponds to the maximum blocked force of the actuator.

(a)   (b)
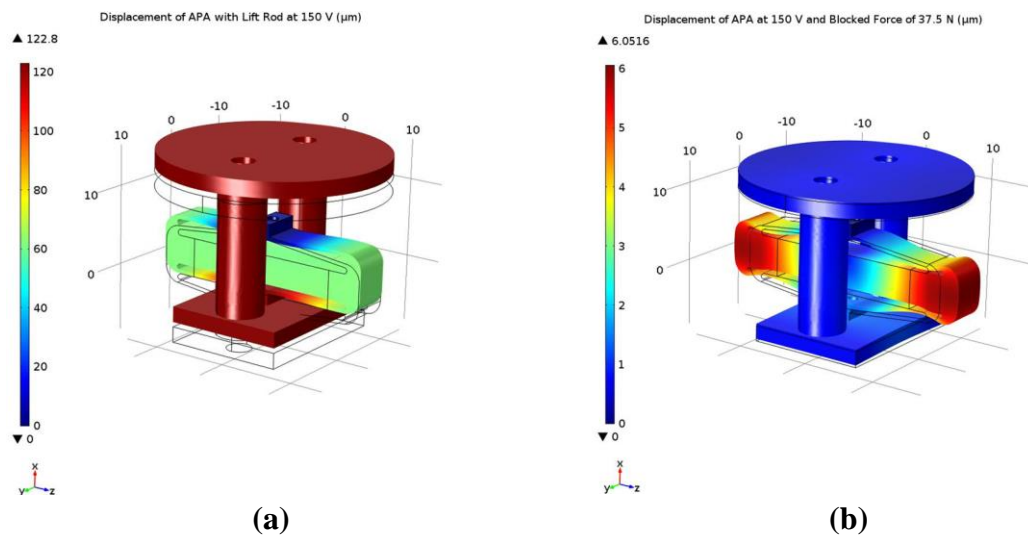
Figure 3.13 Displacement of amplified piezo actuator with the lift rod **(a)** At no load and 150 V input **(b)** At blocked force of 37.5 N and 150 V

Further in this section, the FE analysis of the bossed diaphragm is performed to evaluate the effect of thickens bossed ratio, material property and method of excitation on the diaphragm deflection. The modelling and meshing of the bossed diaphragm followed a similar approach to that of the actuator, which considered the free tetrahedral element. Figure 3.14 represents the meshed configuration and boundary conditions of the bossed diaphragm adopted in FE analysis. The actuation force is calculated based on equation 3.10 corresponding to the voltage range of 0 to 150 V. The bossed diaphragms are subjected to static, modal and harmonic analysis under central and annular excitation to determine the static and dynamic behaviour. Table 3.2 represents the dimensional and material properties of the bossed diaphragm considered for the analysis.

(a) Meshed Bossed Diaphragm   **(c) Annular Excitation**
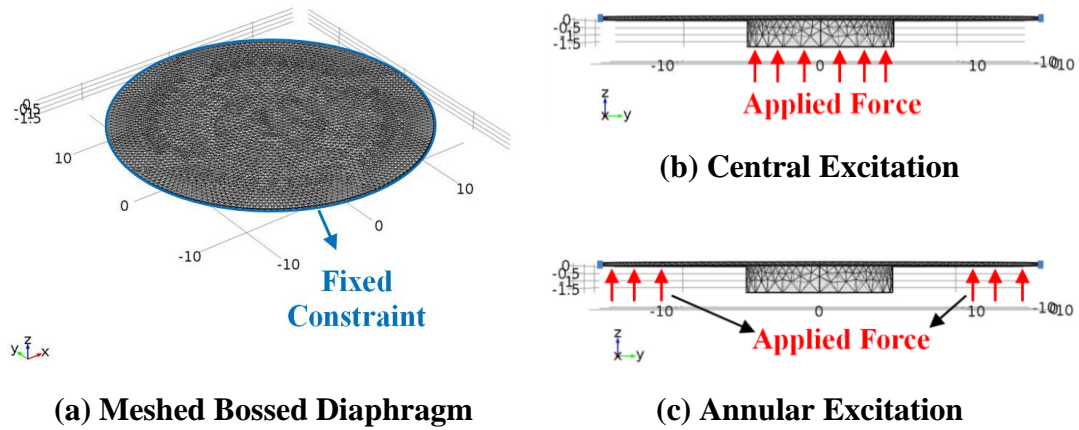
Figure 3.14 (a) Meshed configurations of the bossed diaphragm **(b)** Central excitation **(c)** Annular Excitation

Table 3.2 Dimensions and materials properties of the bossed diaphragm for FE analysis

Properties	Silicone Rubber	Polydimethylsiloxane (PDMS)
Young's Modulus (MPa)	1.20	1.64
Density (kg/m^3)	1070	965
Poisons Ratio	0.47	0.49
Effective radius (r_c) (mm)	15	15
thickness (t) (mm)	0.2,0.4,0.6	0.2
Bossed Ratio (B_r) (mm)	0.33, 0.5, 0.66	0.33
Thickness of the Bossed Region (mm)	2.00	2.00

Figure 3.15 represents the simulation results of deformation of the bossed diaphragm with thickness 0.20 mm and bossed ratio of 0.33, 0.50 and 0.66, respectively, which are subjected to static analysis under actuation force corresponding to actuation voltage of 150 V. The corresponding simulated displacement of silicone diaphragm is found to be 137.59 μm, 120.19 μm and 105.86

79

µm respectively. The increase in the stiffness with the bossed ratio leads to the drop in the deflection of the diaphragm.
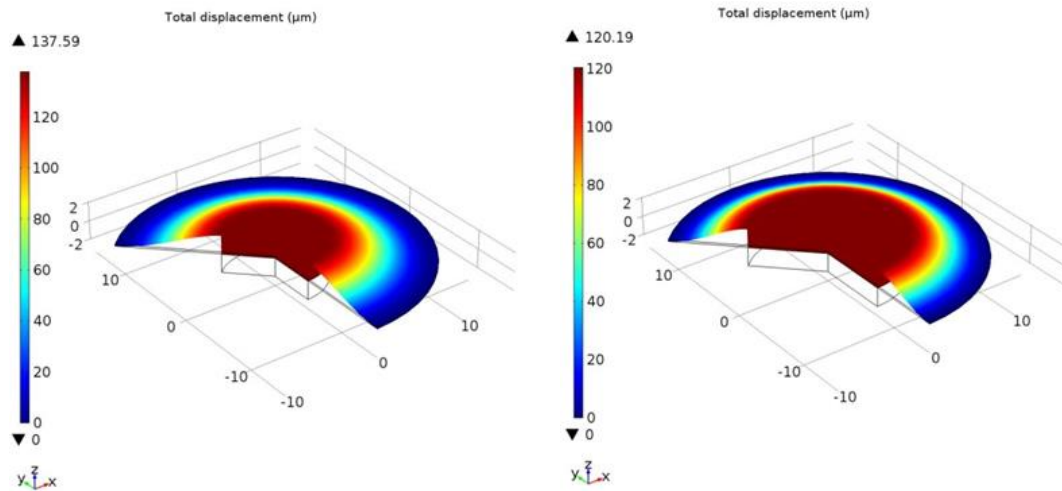
(a) B_r= 0.33, r_c=15.00 mm

(b) B_r= 0.50, r_c=15.00 mm
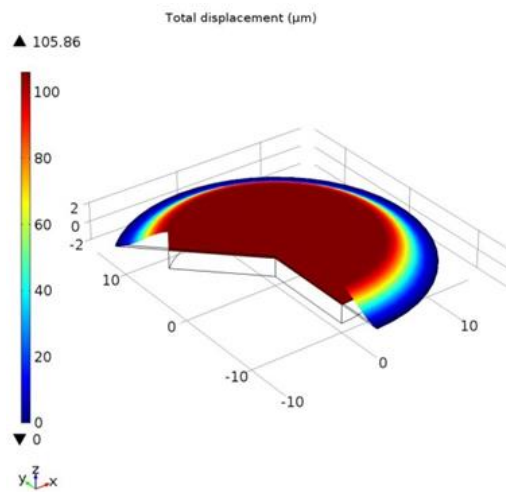
(c) B_r= 0.66, r_c=15.00 mm

Figure 3.15 Comparison of displacement of centrally excited silicone rubber diaphragm of thickness 0.2 mm with bossed ratio of 0.33, 0.50, and 0.66 respectively

Further, the thickness and material property of the diaphragm also affects the diaphragm deflection. Figure 3.16 compares the simulated deflection achieved with the silicone rubber diaphragm of thickness 0.20 mm, 0.40 mm, 0.60 mm and bossed ratio of 0.33. The simulated displacement of silicone rubber diaphragm of 0.40 mm and 0.60 mm thickness with bossed ratio 0.33 is about 112.96 µm and 93.307 µm,

which were far less than the displacement achieved with the 0.20 mm thickness diaphragm, which is about 137.59 μm. This drop in the diaphragm deflection clearly illustrates the effect of increased stiffness with the increased thickness. In addition, the young's modulus of the diaphragm material also affects the performance of the bossed diaphragm, which is evident from the simulated result shown in Figure 3.17, where the displacement of the polydimethylsiloxane (PDMS) diaphragm (E = 1.65 MPa) is about 127.26 μm which is less than the displacement of the silicone rubber diaphragm (E = 1.20 MPa) which is about 137.59 μm.

(a) t = 0.20 mm, B_r= 0.33, r_c=15.00 mm   (b) t = 0.40 mmm, B_r= 0.33 r_c=15.00 mm

(b) t = 0.60 mmm, B_r= 0.33 r_c=15.00 mm
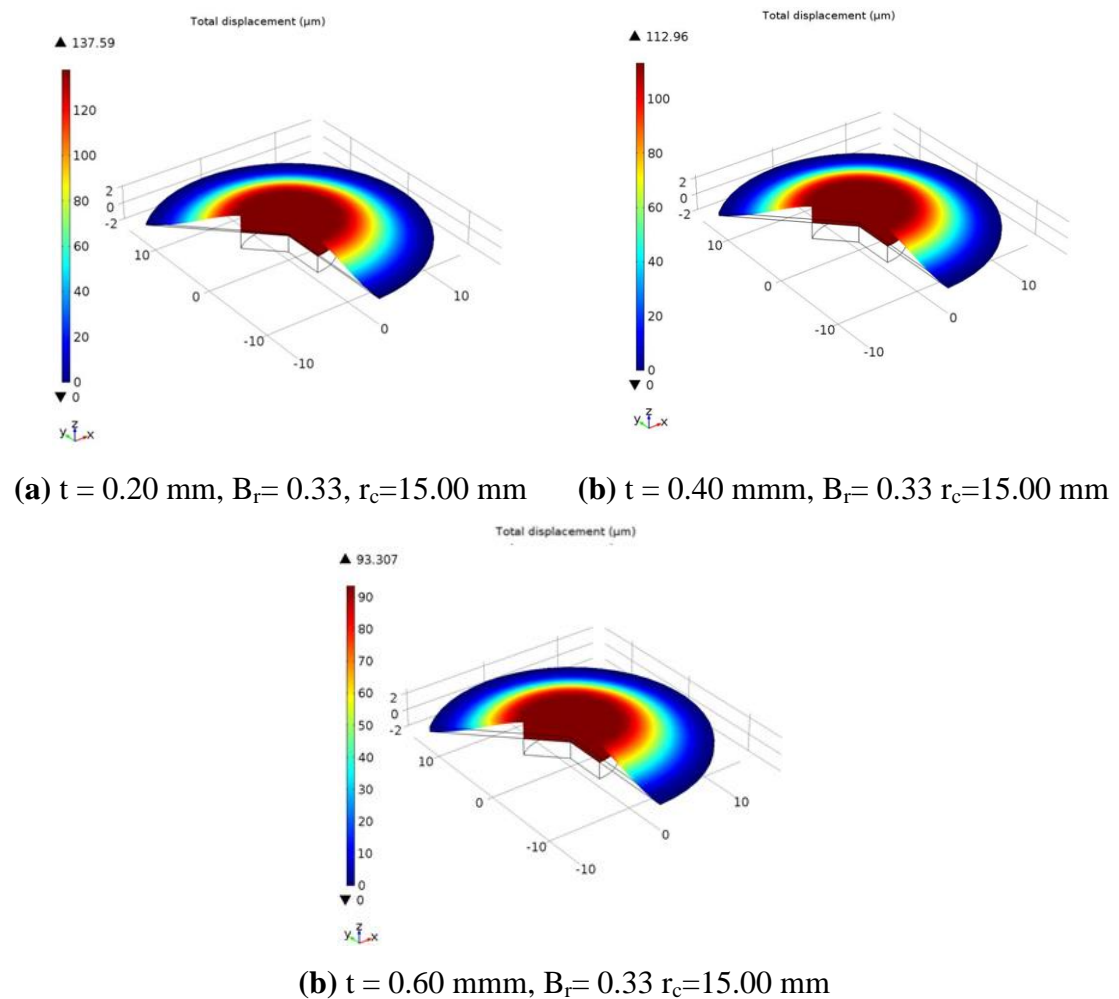
Figure 3.16 Comparison of displacement of centrally excited silicone rubber diaphragm with **(a)** thickness 0.20 mm and bossed ratio 0.33 **(b)** thickness 0.40 mm and bossed ratio 0.33 **(c)** thickness 0.60 mm and bossed ratio 0.33

(a) E = 1.20 MPa, t = 0.20 mm,   **(b)** E = 1.64 MPa, t = 0.20 mm,

B_r= 0.33, r_c=15.00 mm B_r= 0.33, r_c=15.00 mm
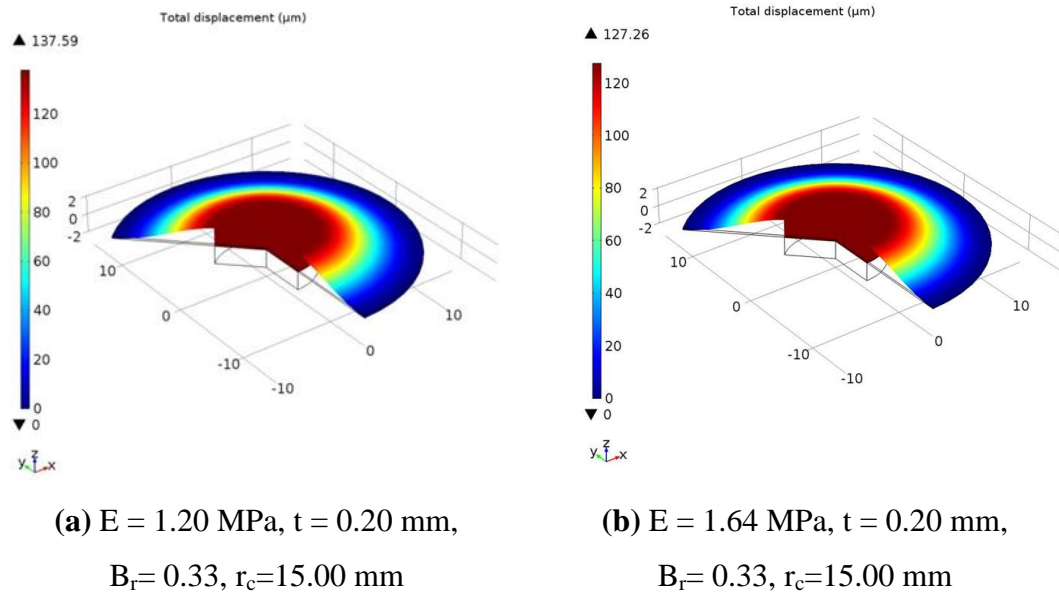
Figure 3.17 Comparison of displacement of centrally excited **(a)** silicone rubber diaphragm (E = 1.20 MPa) thickness 0.20 mm and bossed ratio 0.33 **(b)** Polydimethylsiloxane diaphragm (E = 1.64 MPa) thickness 0.20 mm and bossed ratio 0.33

From the FE static analysis it is evident that the diaphragm with the lower stiffness offer better displacement. Thus the diaphragm made of silicone rubber with bossed ratio 0.33 and the thickness 0.2 mm delivers better displacement behaviour when compared with other configurations. Further enhancement of the diaphragm deflection could be achieved with the application of the excitation force away from the central bossed region with the annularly as represented in figure 3.7 (b). Figure 3.18 (a) and 3.18 (b) represents the simulated displacement of the centrally excited and annularly excited silicone rubber bossed diaphragm with t = 0.20 mm, B_r= 0.33, r_c=15.00 mm, corresponding to force at actuation voltage of 150 V.

(a)

(b)
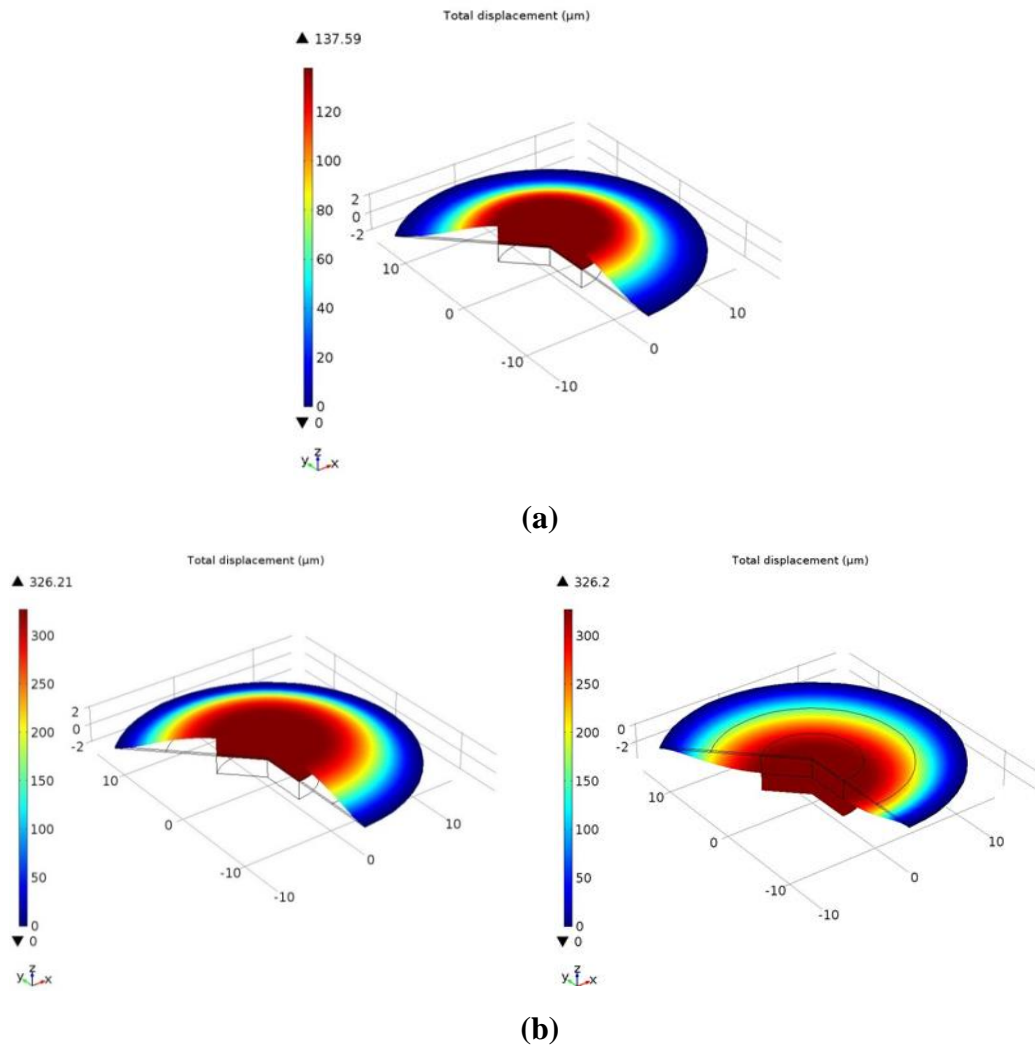
Figure 3.18 Comparison of displacement of bossed diaphragm with **(a)** Central excitation (E = 1.20 MPa, t = 0.20 mm, Br= 0.33, r_c=15.00 mm) **(b)** Annular excitation (E = 1.20 MPa, t = 0.20 mm, Br= 0.33, r_c=15.00 mm, r_l=10.00 mm)

When the bossed diaphragm is subjected to the central loading, the diaphragm has the flexibility to deflect in the upward positive z-direction, as represented in Figure 3.18 (a). When the same configuration of the diaphragm is subjected to the annular excitation, it allows the centrally suspended bossed region to oscillate with the higher amplitude. In addition, the suspended bossed region can move in the negative direction, thus increasing the effective stroke of the diaphragm, which can enhance the micropump performance. As observed from Figure 3.18, the deflection of

the annularly excited diaphragm is about 326.21 μm along positive and negative z directions, which is superior to the centrally excited diaphragm.

(a) Modal Frequency 1= 9.96 Hz

(b) Modal Frequency 2= 23.71 Hz

(c) Modal Frequency 3= 23.74 Hz

(b) Modal Frequency 4= 85.48 Hz

(e) Modal Frequency 5= 90.82 Hz

(d) Modal Frequency 6 = 91.02 Hz
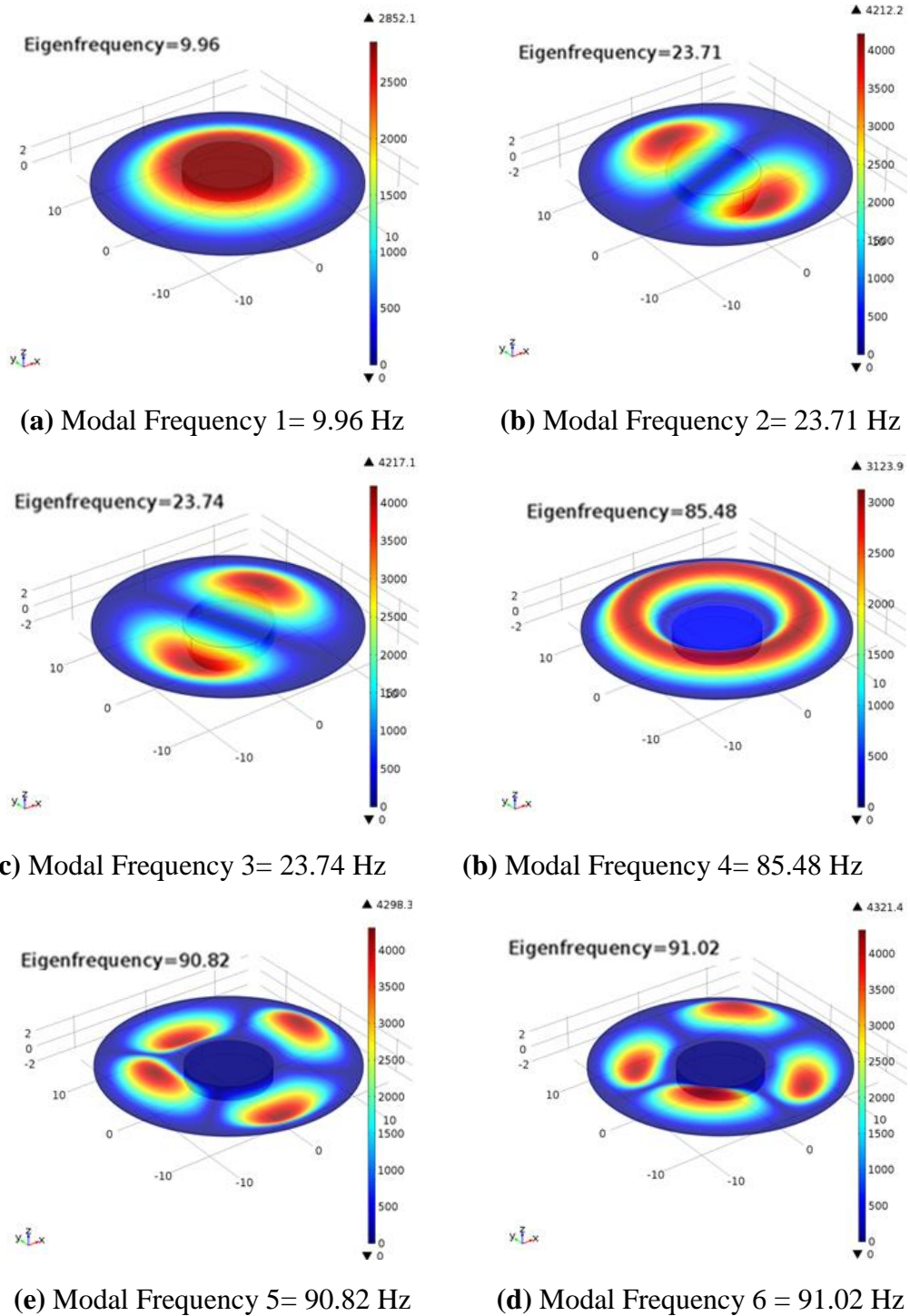
Figure 3.19 Mode shapes of the centrally excited silicone rubber bossed diaphragm t=0.2 mm, B_r= 0.33 and r_c=15.00 mm

(a) Modal Frequency 1= 45.52 Hz   **(b)** Modal Frequency 2= 81.81 Hz

(c) Modal Frequency 3= 81.93 Hz   **(d)** Modal Frequency 4= 269.69 Hz

(e) Modal Frequency 5= 270.13 Hz   **(f)** Modal Frequency 6= 271.17 Hz
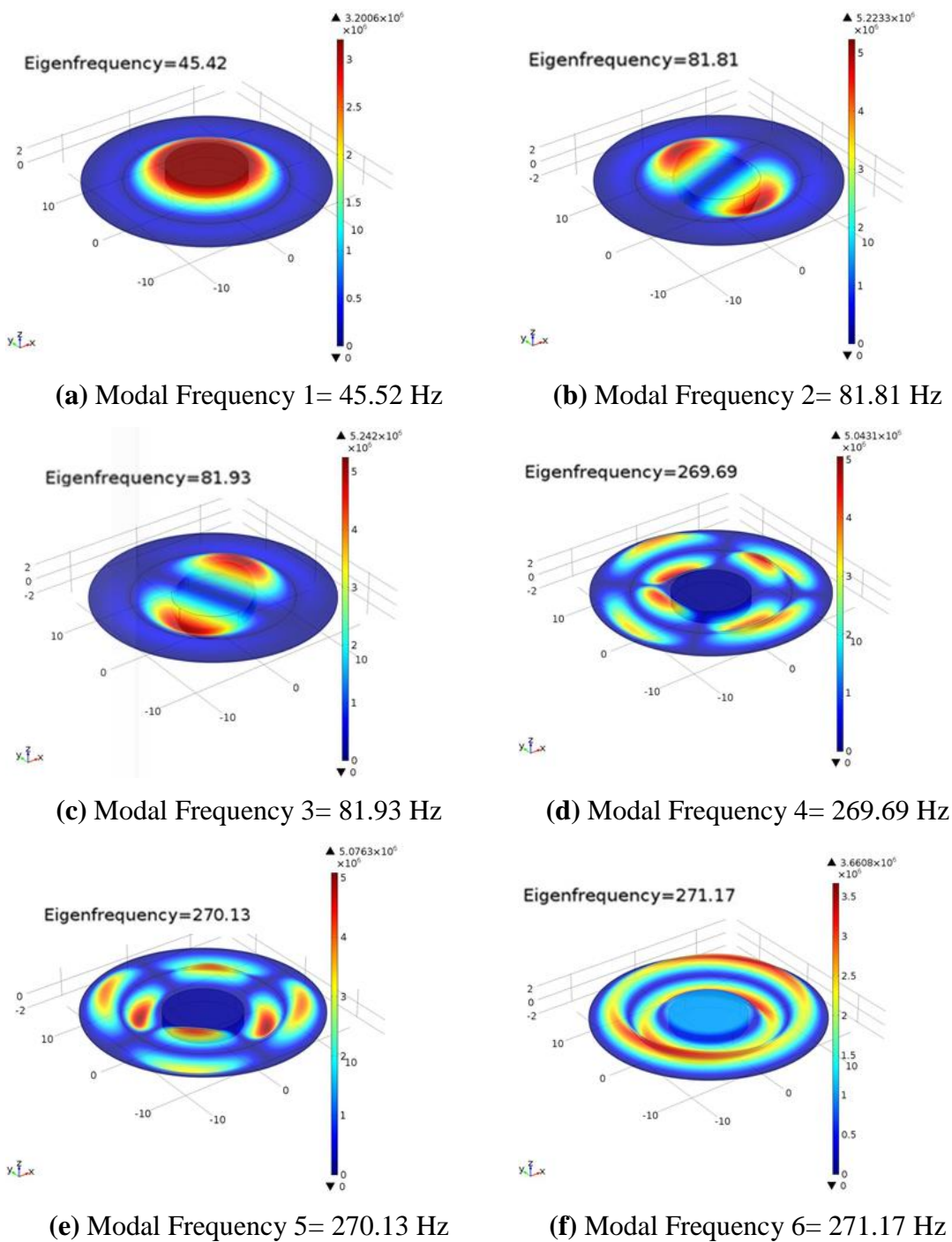
Figure 3.20 Mode shapes of the annularly excited silicone rubber bossed diaphragm t=0.2 mm, B_r= 0.33, r_c=15.00 mm and r_l=10.00 mm

Figure 3.19 and Figure 3.20 represents the different mode shapes of the silicone rubber bossed diaphragm under centrally excited and annularly excited

conditions. As observed in Figure 3.19 and Figure 3.20, the suitable mode of deformation of the diaphragm for the optimal working of micropump occurs with the first mode of oscillation. The deformation of the diaphragm under other modes does not produce a convenient deformation pattern for micropump functioning. Thus, the first mode of oscillation of the bossed diaphragm is preferred for the effective working of the micropump.

During the dynamic operation, the diaphragm attains maximum deflection when the actuation frequency approaches the natural frequency of the diaphragm. Thus the frequency of actuation corresponding to maximum deflection of the diaphragm significantly influences the micropump performance. According to FEA results, the first mode of oscillation of the centrally loaded diaphragm occurs at 9.96 Hz. However, the first modal frequency of the annularly excited configuration corresponds to 45.42 Hz, which is very high when compared with the first modal frequency of the centrally excited bossed diaphragm. The increase in modal frequency is attributed due to the increased stiffness of the annular excitation configuration. Since the maximum deflection of the diaphragm occurs at a frequency corresponding to the first modal frequency, the enhancement of frequency response of the annularly excited bossed diaphragm will effectively enhance the frequency response of the micropump. This, in turn, extends the frequency bandwidth of the micropump leading to enhanced flow rate and pressure.

When integrated with the micropump, the dynamic response of bossed diaphragm majorly contributes towards the performance of the micropump. Figure 3.21 and figure 3.22 represents the different stages of the dynamic response of the bossed diaphragm when excited centrally and annularly corresponding to the first mode of oscillation. Through FEA, the maximum deflection of the centrally excited diaphragm was found to be about 725.91 µm at 9.96 Hz when subjected to force corresponding to excitation voltage of 150 V of the amplified piezoelectric actuator. It is evident from Figure 3.19 that the centrally loaded diaphragm can deform only along the positive direction due to the geometrical constraints associated with the actuation configuration adopted. The dynamic response of the similar configuration of the

bossed diaphragm when excited annularly with a loading radius r_l=10.00 mm is observed to be about 999.20 µm along the positive and negative z-direction at 45.42 Hz. Application of excitation force annularly results in oscillation of the central bossed region along both positive and negative z-direction resulting in an increased swept volume of the diaphragm which in turn enhances the net volume of the fluid displaced, i.e. the flow rate of the micropump. The detailed results of the FE analysis are presented in chapter 4.
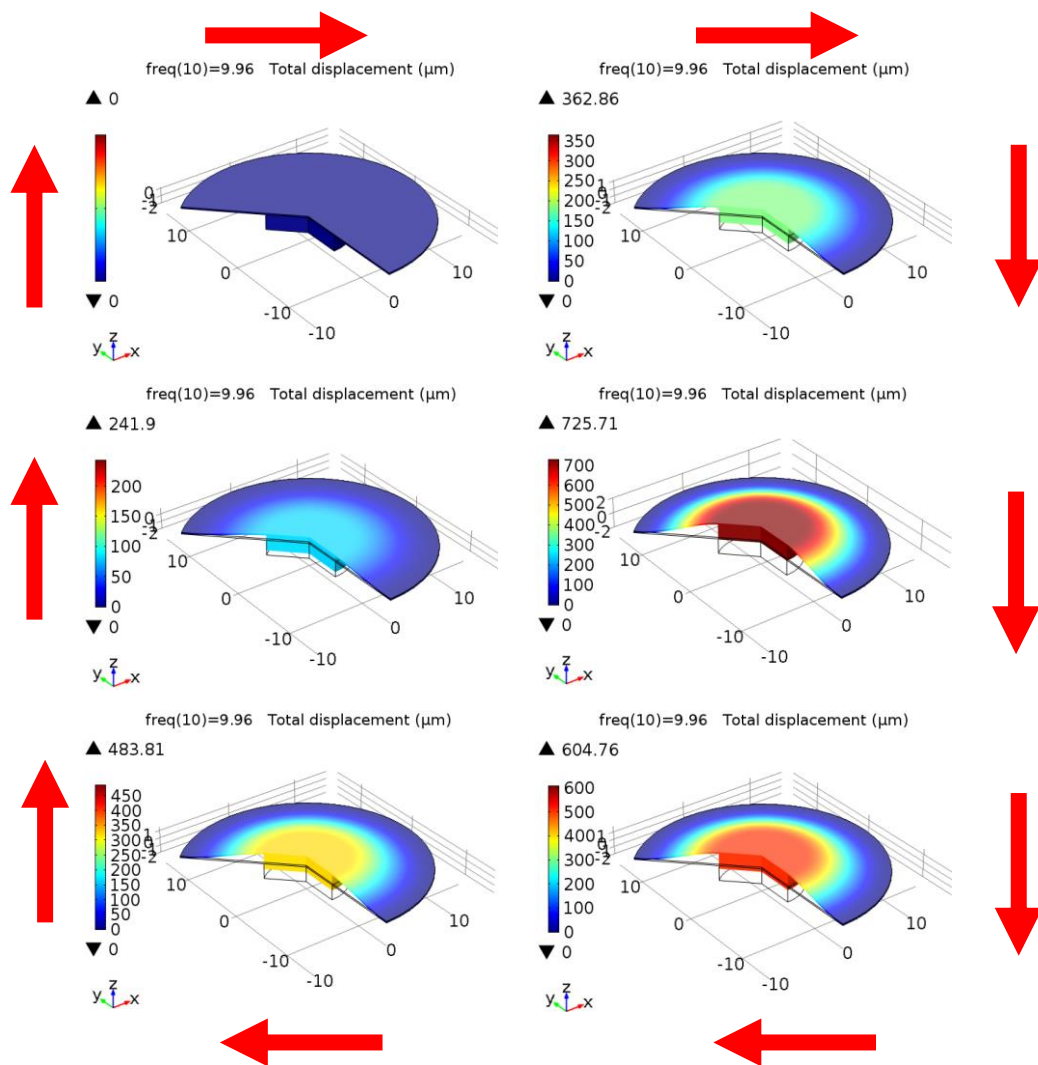
Figure 3.21 Different stages of deformation (simulation cycle time of 10 seconds) of the centrally excited bossed diaphragm with t=0.2 mm, B_r= 0.34 and r_c=15.00 mm at 9.96 Hz for a force corresponding to actuation voltage of 150 V.
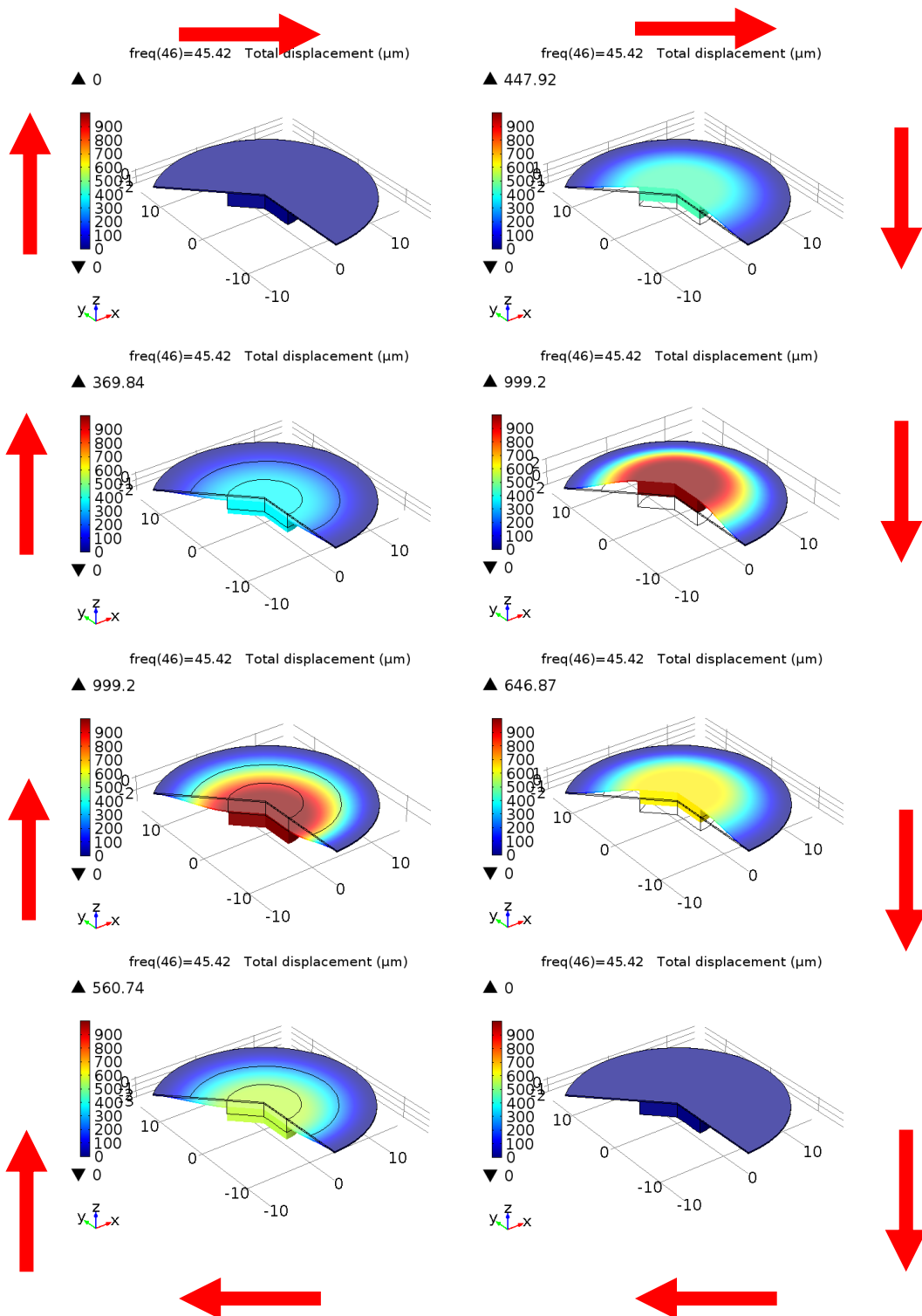
Figure 3.22 Different stages of deformation (simulation cycle time of 10 seconds) of the annularly excited diaphragm with t=0.2 mm, Br= 0.33, r_c=15.00 mm and r_I=10.00 mm at 45.42 Hz for a force corresponding to actuation voltage of 150 V

3.4 Configuration of the Proposed Micropump with Disposable Chamber

Two configurations of the micropump with a disposable chamber are proposed in the present work. The proposed micropump considered with the disposable chamber having bossed diaphragm made of silicone rubber with thickness 0.20 mm and bossed ratio of 0.33, 0.50 and 0.66. The diaphragm is actuated through central excitation and annular excitation. The proposed design of the micropump with the central excited bossed diaphragm and the disposable chamber is shown in Figure 3.23.
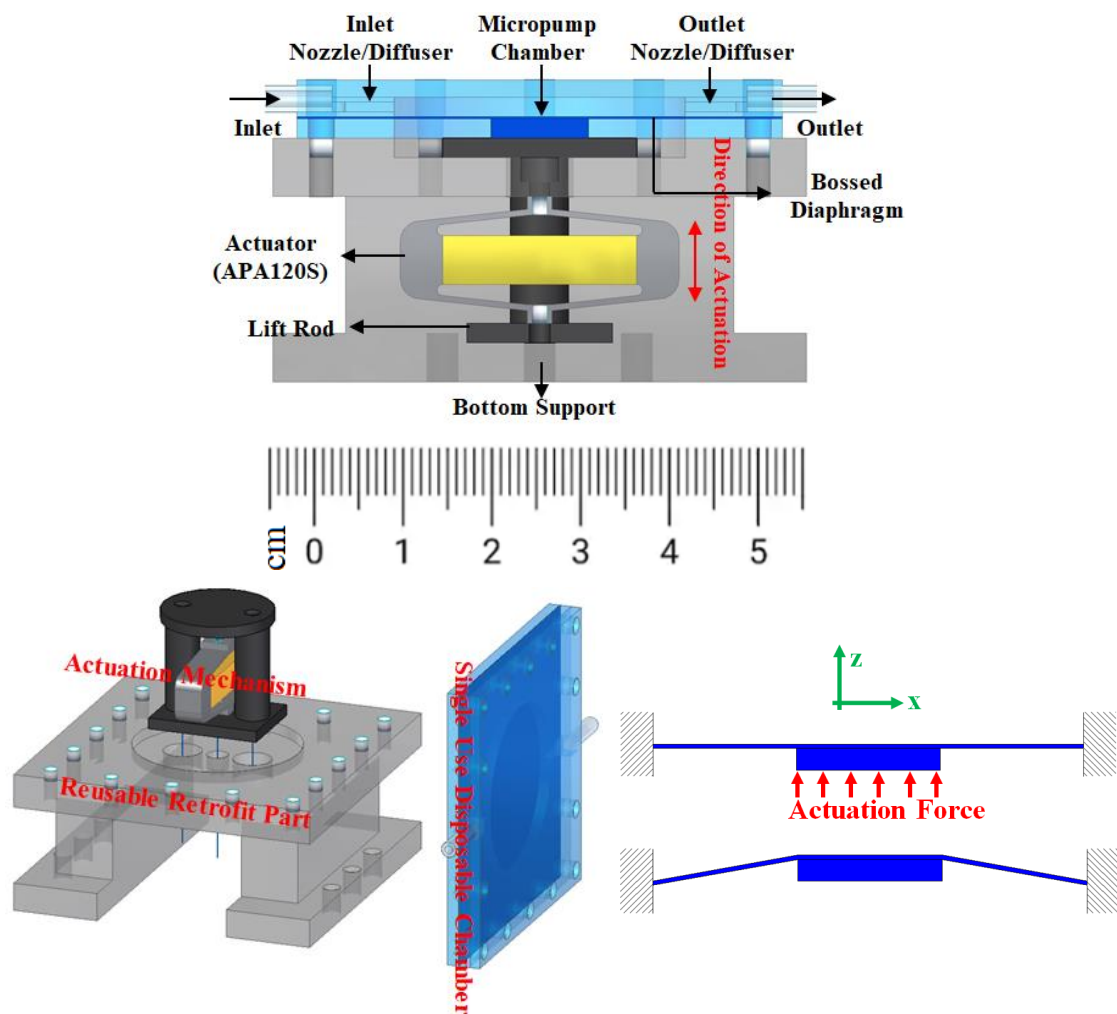
Figure 3.23 Proposed disposable chamber valveless micropump with bossed diaphragm subjected to central excitation

The proposed pump has several structural parts like the bottom support, bossed diaphragm, pump chamber and the inlet/outlet tubes. The individual parts are

systematically assembled on one over the other. The actuation source for the proposed micropump incorporates the amplified piezo actuator (APA-120S) from Cedrat® Technologies. The amplified Piezo Actuator used for the present work includes a piezo multi-layer actuator ($5 \times 5 \times 20$ mm3) made from PZT (Lead Zirconate Titanate) inside a diamond-shaped flexural amplifier. Together with the bottom support, the actuation mechanism is made as the reusable part, whereas the chambers, diaphragm with nozzle/diffuser, are the disposable parts. The disposable parts of the micropump are made of polymer-based materials. In biomedical application, this part of the micropump takes care of the contamination.

On applying the electric potential across the multilayer stack actuator, it undergoes mechanical strain along the x-direction. Further, the flexural amplifier amplifies the strain produced by the stack actuator, thus providing an amplified motion and force along the positive z-direction. The lift rod transfers the force generated by the amplified piezo actuator onto the bossed region of the diaphragm. As a result, the diaphragm deflects in the positive z-direction. This, in turn, results in decreased chamber volume and increased chamber pressure, causing the outflow of the fluid from the pump chamber through the outlet, causing pumping mode. When the voltage across the actuator drops to zero, the diaphragm regains its original position causing an increase in the chamber volume, which allows the fluid to enter into the chamber through the inlet thus causing suction mode.t. The trapezoidal nozzle/diffuser element provides the flow rectification of the liquid during the supply and pumping mode. During the suction, there exists diffuser action at the inlet, allowing more fluid to enter into the chamber when compared to the nozzle action at the outlet with minimum outflow. A more significant proportion of fluid flows out through the outlet during the pumping mode due to the diffuser action. At the same time, a minimal amount fluids flows through the inlet due to nozzle action.

The second configuration of the disposable valveless micropump works similar to the previous configuration except for loading on the diaphragm. Figure 3.24 represents the schematic of the proposed disposable chamber valveless micropump with bossed diaphragm subjected to annular excitation. The micropump sequence under the annular excitation remains the same as that of the centrally excited

diaphragm. However, the annular excited bossed diaphragm can oscillate along both positive and negative z-direction resulting in increased swept volume, thus increasing the flow rate. The fabrication of the proposed micropump with central and annular excitation and respective components are discussed in the next part.
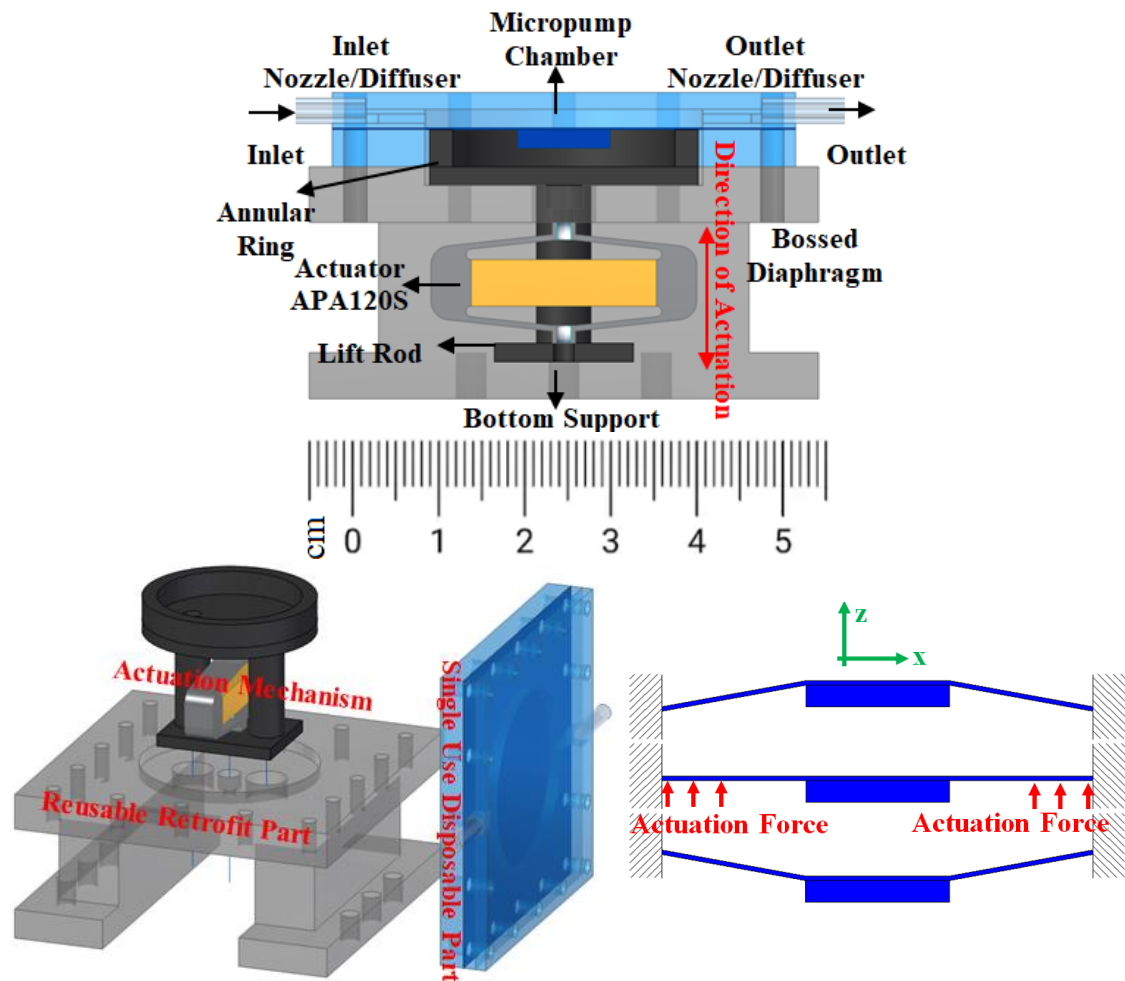
Figure 3.24 Proposed disposable chamber valveless micropump with bossed diaphragm subjected to annular excitation

3.5 Fabrication of the Proposed Micropump

The following section describes the approaches adopted in the fabrication of the disposable valveless micropump.

3.5.1 Disposable part of the Micropump

The disposable part of the proposed micropump consisted of a pump chamber with nozzle/diffuser with inlet/ outlet tubes, a bossed diaphragm, top cover. The bossed diaphragm for the present study is fabricated through the moulding process. A milling operation is carried out to machine the mould cavity of the appropriate dimension on a polymethyl methacrylate (PMMA) plate of 10.00 mm thickness to prepare the moulds for the bossed diaphragm. The bossed diaphragms in the present study are made of silicone rubber and Polydimethylsiloxane (PDMS).

Suitable proportions of the silicone rubber (25:1) and the PDMS (10:1) liquid components are mixed with their corresponding curing agents, stirred well and kept in the vacuum chamber to remove the air bubbles. Typically silicone rubber and PDMS are cured with Benzoyl Peroxide and Ethyl benzene as the curing agent respectively. The prepared sample is then poured into the mould and allowed to undergo room temperature curing for about 48 hours. The prepared membrane of the silicone rubber and PDMS is stretched and fixed onto a laser cut PMMA plate to avoid wrinkles and ensure a uniform surface. Table 3.3 represents the material property and dimensional specification of the fabricated silicone rubber and PDMS diaphragm. Figure 3.25 represents the fabricated bossed diaphragm with silicone rubber.

Table 3.3 Dimensions and material property of the bossed diaphragm for experimental characterization

Properties	Silicone Rubber	Polydimethylsiloxane (PDMS)
Young's Modulus (MPa)	1.20	1.64
Density (kg/m^3)	1070	965
Poisons Ratio	0.47	0.49
Effective radius (r_c) (mm)	15	15
thickness (t) (mm)	0.2	0.2
Bossed Ratio (B_r) (mm)	0.33, 0.5, 0.66	0.33
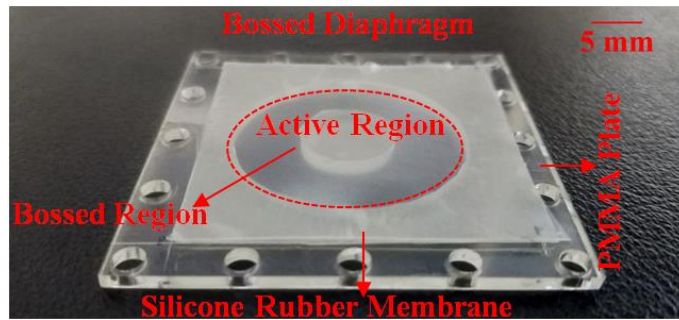
Figure 3.25 Fabricated bossed diaphragm with silicone rubber
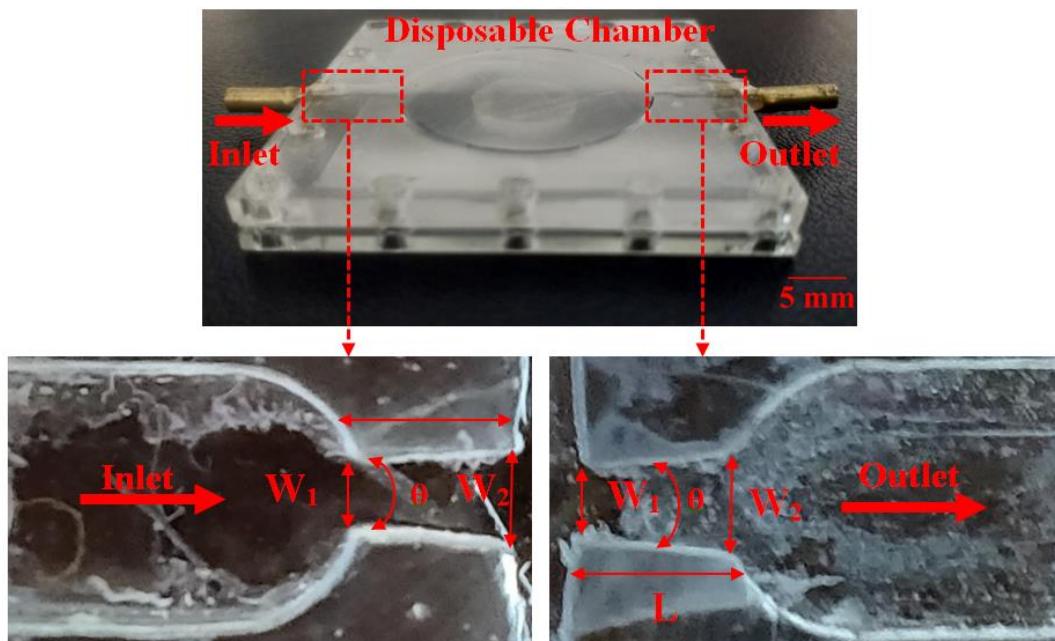
Figure 3.26 Photograph of the pump chamber taken in micro lens camera, having nozzle/diffuser manufactured using laser cutting process

S. Singh et al. (2015), H. K. Ma et al. (2015) and Paul Kawun et al. (2016) have fabricated a valveless micropump with a 10º trapezoidal nozzle/diffuser. In the proposed micropump design similar nozzle/diffuser of 10º angle is used. The pump chamber and the nozzle/diffuser are fabricated from PMMA by low power CO_2 laser cutting process. Figure 3.26 shows the photograph of the pump chamber with nozzle/diffuser taken in the micro-lens camera. Two identical trapezoidal nozzle/diffusers are cut on the same component together with the pump chamber. Different chamber depths ranging from 0.75 to 2.00 mm with an increment of 0.25

mm are considered for experimental evaluation. Table 3.4 represents the dimensional specification of the pump chamber and nozzle/diffuser.

Table 3.4 Specification of the micropump chamber and the nozzle/diffuser implemented in the micropump

Micropump Chamber and Nozzle/Diffuser Parameter	
Diameter of the Pump Chamber D	30.00 mm
Chamber Depth, h_c	0.75 to 2.00 mm, Increment of 0.25 mm
Inner diameter of the Inlet/Outlet, d_{ti}	1.60 mm
Outer diameter of the Inlet/Outlet, d_{to}	3.00 mm
Length of the channel, L	2.50 mm
Width of the Inlet, W_1	0.50 mm
Width of the Outlet, W_2	0.94 mm
Angle of Divergence, θ	10º

3.5.2 Actuation Mechanism of the Micropump

The actuation mechanism of the micropump constituted an amplified piezo actuator (APA-120S) and base which supports the disposable chamber. The amplified piezo actuator consists of a multilayer piezo stack actuator embedded inside a flexural amplifier. The pump base is made of PMMA (polymethyl methacrylate) material machined to the required dimension using conventional CNC milling operation. Figure 3.27 (a), 3.27 (b), and 3.27 (c) represent the reusable part of the actuation mechanism of the proposed micropump. The deflection produced by the APA gets transferred to the diaphragm through the lift rod. Appropriate control of the input voltage to the actuator effectively controls the deflection range of the actuator, which in turn controls diaphragm deflection. The actuation mechanism for central excitation and annular excitation (Figure 3.27 (b) and Figure 3.27 (c)) is similar in construction except for the annular excitation configuration integrates an annular ring for application of actuation force away from the central bossed region of the diaphragm.
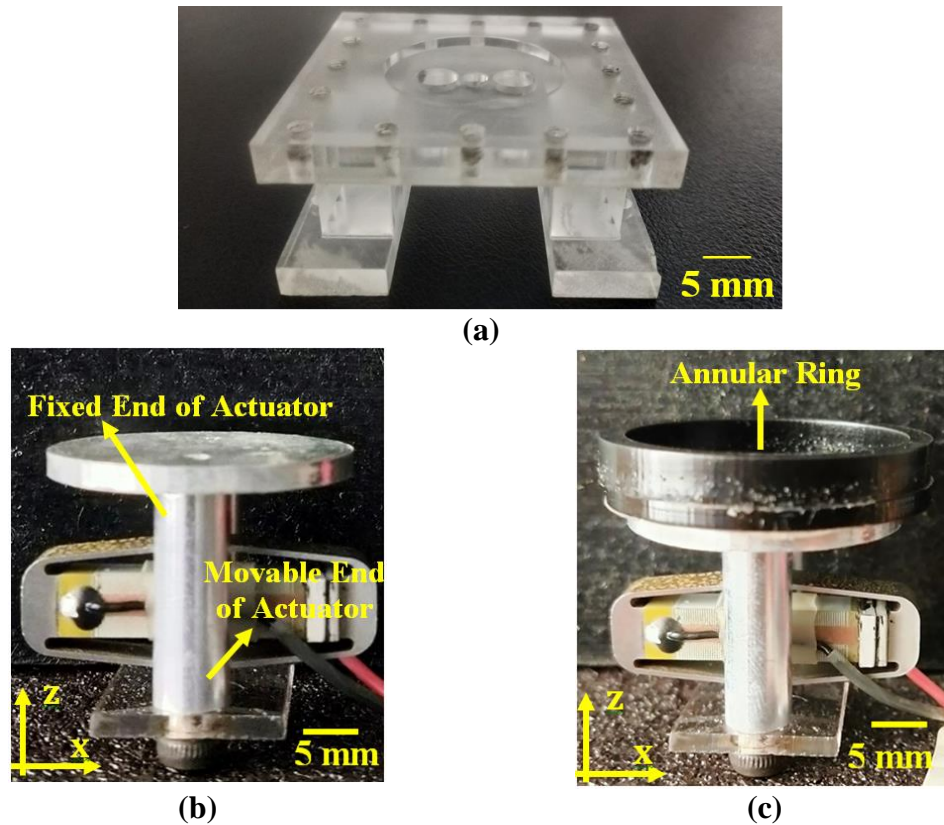
Figure 3.27 (a) Bottom reusable support structure, Actuation mechanism for **(b)** Centrally excited configuration **(c)** Annularly excited configuration

3.5.3 Micropump Assembly

The fabricated diaphragm is stretched over the PMMA plate with the central cylindrical protrusion (bossed region) attached in the centre. The bossed diaphragm intern is attached to the pump chamber using silicon adhesive tape, constituting the disposable chamber. The actuation mechanism and the bottom support structure are integrated to form the reusable part of the micropump. The assembled view of the micropump with central excitation emphasized with different entities is shown in Figure 3.28. The annular excitation configuration also follows a similar approach with the addition of an annular ring with the actuation mechanism. The final assembled micropump has a cross-sectional dimension of 55×55 mm, with the height of the micropump varying between 30.25 mm to 32.25 mm. The experimental procedure of the characterization of the bossed diaphragm and the micropump is covered in the next part.
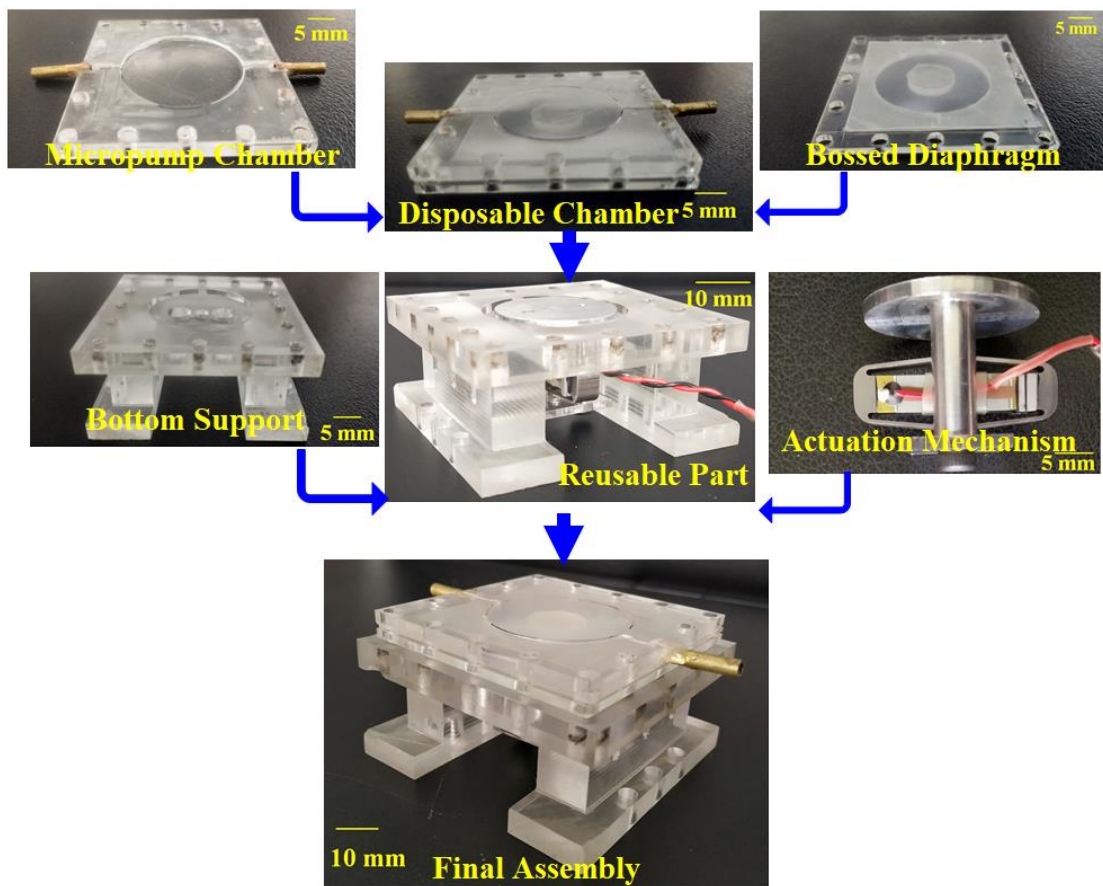
Figure 3.28 Photograph of the assembled micropump

3.6 Experimental Characterization of the Actuator, Bossed Diaphragm and the Micropump

The fabricated bossed diaphragm and micropump are characterized, and the performance evaluation is conducted experimentally. The following section presents the experimental setup for the experimental characterization of the actuator, actuator mechanism, the bossed diaphragm and the proposed disposable chamber valveless micropump.

3.6.1 Characterization of the Actuator and the Actuation Mechanism

The characterization of the actuator involved measurement of the displacement range and blocked force developed when subjected to a static external voltage. The required voltage for driving the actuator is delivered by a function

generator module of the National Engineering Laboratory Virtual Instrumentation Suite (NI-ELVIS). The function generator produces a sinusoidal signal of amplitude ranging between 0.50 V - 7.5 V. This signal further amplified through a linear voltage amplifier (LA-75 from Cedart Technologies®) of gain factor 20 to deliver sufficient voltage required for driving the actuator. Thus the net output of the amplifier varies between 10 V - 150 V. The laser displacement sensor from Microepsilon (Opto-NCDT 1402) is used to measure the deflection produced by the actuator. In order to measure the blocked force, the piezoelectric actuator is subjected to incremental loads until the deflection of the actuator drops to zero. Figure 3.29 (a), 3.29 (b), and 3.29 (c) represent the experimental set used for the characterization of the actuator and actuation mechanism. The results of the experimental characterization of the actuator and actuation mechanism are presented in chapter 4.
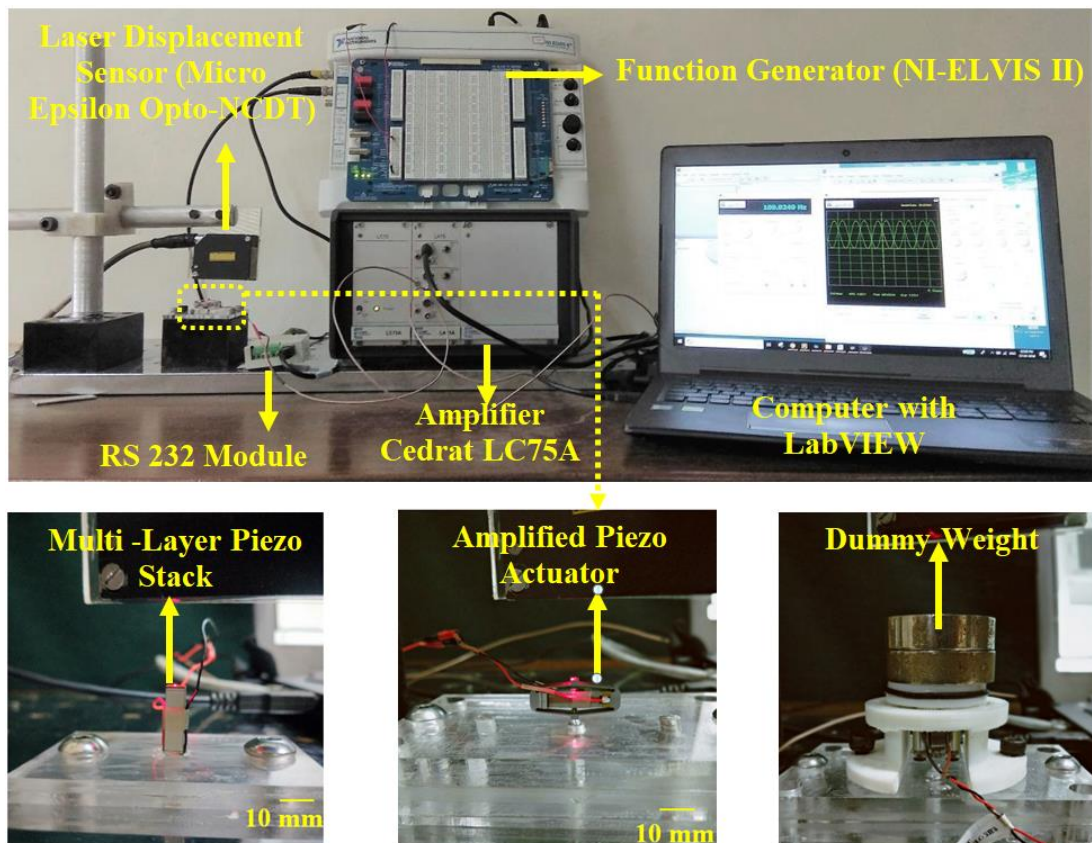
Figure 3.29 (a) Experimental setup for the characterization of the actuator **(b)** Multi-layered piezo stack actuator and Amplified Piezo Actuator (APA-120S) **(c)** Measurement of blocked force of the Amplified Piezo Actuator

3.6.2 Characterization of the Bossed Diaphragm

The fabricated bossed diaphragm is mounted with the bottom support, as shown in Figure 3.30. The deflection of the bossed diaphragm is experimentally measured through a laser displacement sensor with different voltage and frequency of the input sinusoidal signal to APA in the actuation mechanism. The experimental setup of the diaphragm deflection measurement is represented in Figure 3.30. The experimental characterization involves measuring the deflection of the bossed diaphragm for different thickness, material, bossed ratios and loading configurations. The results obtained from the characterization of the bossed diaphragm are presented in chapter 4.
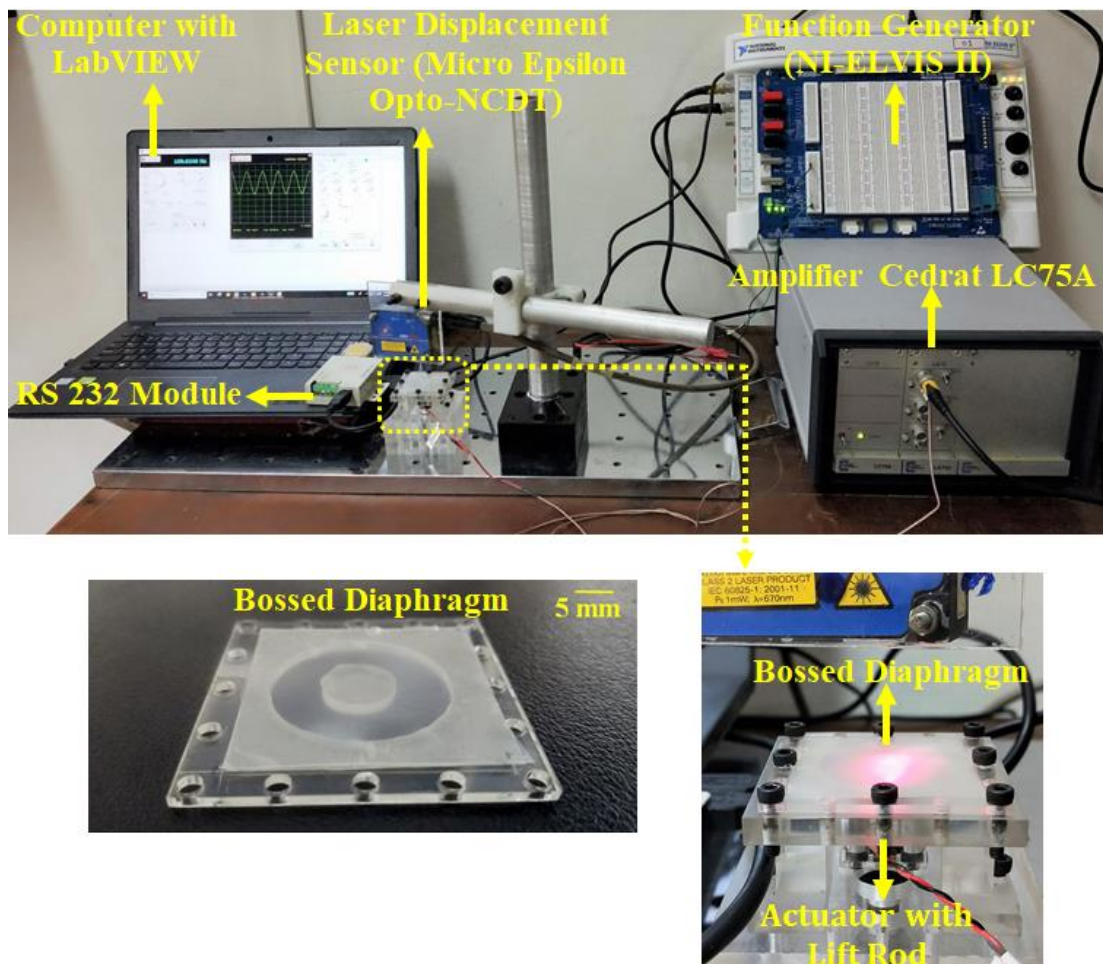
Figure 3.30 Experimental setup for characterization of the bossed diaphragm

3.6.3 Testing of Micropump

The micropump performance assessment involves measuring the mass flow rate of the pumping fluid for a different range of frequencies and voltage values of the actuation signal and converting the mass flow rate into the volume flow rate. A sinusoidal signal generated from a function generator (NI-ELVIS II) is amplified through linear amplifier voltage (LA-75 from Cedart Technologies®, Amplification Factor 20). The amplified sinusoidal signal drives the actuator APA-120S of the actuation mechanism with the amplitude of 10 V to 150 V and frequency less than 70 Hz. The performance of the micropump is tested for different working fluids such as water (100%), blood plasma mimicking (90% Water + 10% Glycerol), and blood mimicking fluid (80% Water + 18% Glycerol+ 2 % Propylene) (Karpienko K et al.2016; Oglat A A et al. 2017) at room temperature.

Figure 3.31 shows the photograph of the experimental setup used in the testing of the micropump. The flow characterization involved collecting pumped fluid in the measuring jar and measuring the mass of fluid accumulated for a pre-set time through a precision weighing scale. The five numbers of trials are performed, and the mean value of the flow rate with corresponding standard deviation is considered for experimental measurements to justify the reliability of the experimental data. The levels of reservoirs were adjusted such that the liquid level in the inlet reservoir matches with outlet reservoir level. This prevents the self-generated flow due to the syphoning effect. Thus the micropump pumps fluid only when actuation signals are applied to the actuator.

The pressure characteristics measurement of the proposed micropump considered the difference in the height between the inlet and outlet reservoir. The height of the outlet reservoir was varied until the flow rate reaches zero, which corresponds to the blocking pressure of the micropump. The measurement of flow and pressure characteristics of the blood plasma and blood mimicking fluid followed the same above approach. Table 3.5 represents the properties of the fluid used in the experiments. The results of the micropump characteristics are tabulated and presented in chapter 4.
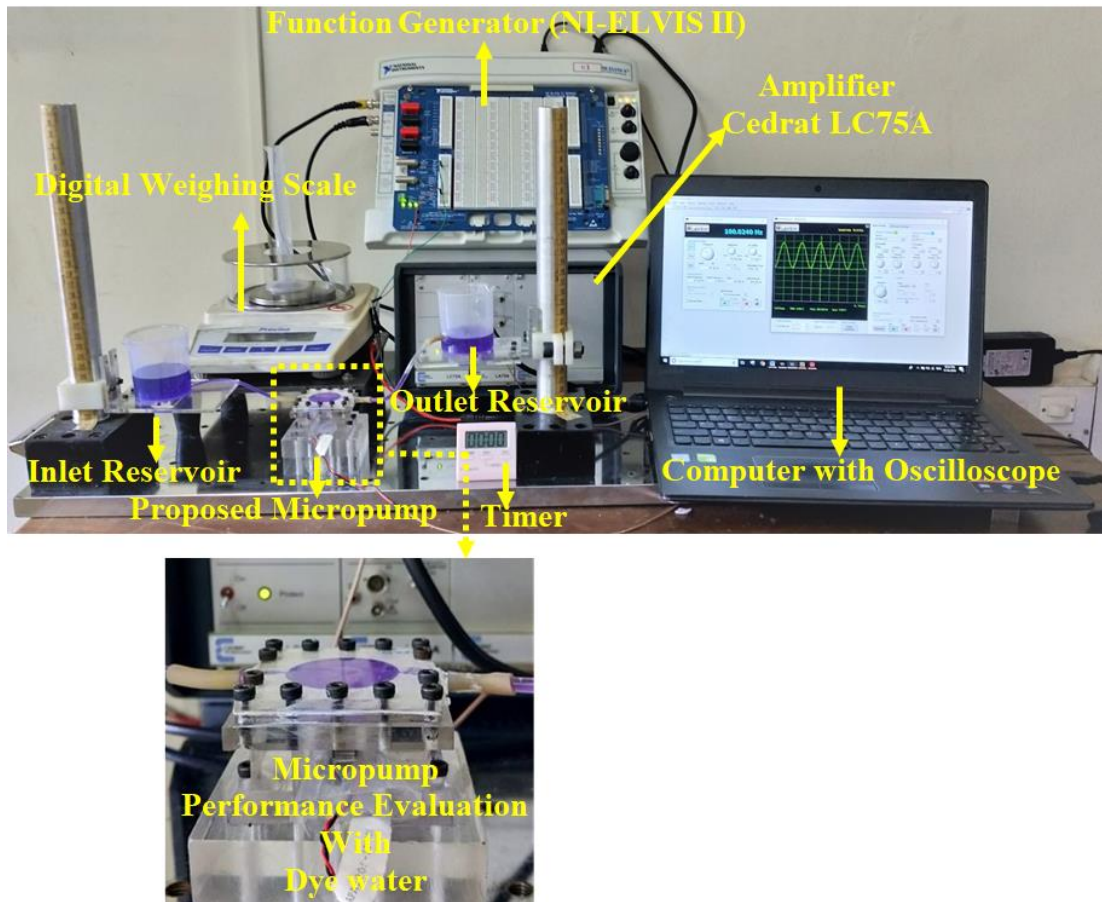
Figure 3.31 Experimental setup for performance evaluation of the proposed micropump

Table 3.5 Properties of fluids used in micropump characterization

Fluid Composition	Density (ρ) (kg/m^3)	Dynamic Viscosity (μ) (mPas)
100 % Water	1000	0.83482
90% Water + 10% Glycerol (Blood Plasma)	1025	1.1345
80% Water + 18% Glycerol+ 2 % Propylene Glycol (Blood Mimicking Fluid)	1040	4.00

RESULTS AND DISCUSSIONS

In this chapter, the results of the finite element analysis and experimental work analysed earlier are presented. Initially, the results of the finite element analysis of the multi-layer piezo stack actuator, amplified piezoelectric actuator and bossed diaphragm are presented. Subsequently, experimental results of the multi-layer piezo stack actuator, amplified piezoelectric actuator, bossed diaphragm and the proposed micropump are presented.

4.1 Finite Element Analysis of the Amplified Piezoelectric Actuator

In this section, the FE analysis of the piezo stack and amplified piezo actuator is presented as explained in section 3.3.
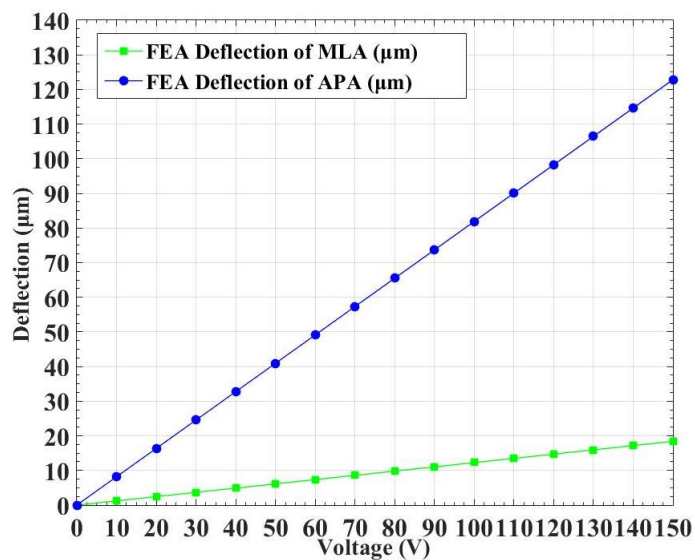
Figure 4.1 Variation of simulated deflection of multilayer piezo stack actuator and amplified piezo actuator with respect actuation voltage

The result obtained from the deflection analysis of the actuator used in micropump actuation is sown in Figure 4.1 and Figure 4.2. The simulated deflection of the multilayer piezo stack actuator and the amplified piezoelectric actuation varies

linearly with respect to the actuation voltage, as represented in Figure 4.1. The maximum deflection of 18.408 µm is achieved with the multilayer piezo stack actuator when the input actuation voltage is set to 150 V. Similarly, the simulated maximum deflection of the amplified piezo actuator obtained through FEA is 122.8 µm. Thus, the flexural amplifier of the amplified piezo actuator is expected to have an amplification factor of 6.67.
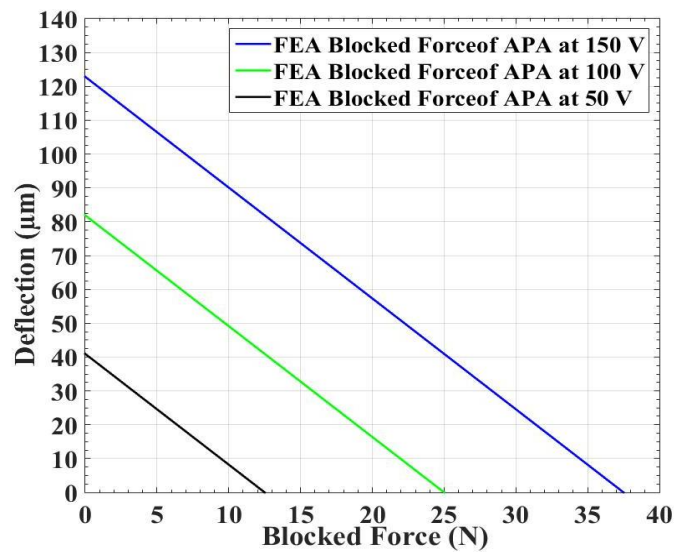
Figure 4.2 Variation of simulated blocked force with respect to deflection of APA at different voltage

The blocked force of the amplified piezo actuator determines the force exerted by the actuator on the diaphragm. Thus blocked force of the APA is an important parameter to be considered. Figure 4.2 represents the variation of the simulated blocked force and deflection of the APA. The APA maximum simulated free deflection is about 122.8 µm 81.88 µm and 40.94 µm at 150 V, 100 V and 50 V input, respectively, when the blocked force is zero. The simulated maximum blocked force achieved is 37.5 N, 25 N and 12.5 N, corresponding to actuation voltage of 150 V, 100 V and 50 V, respectively, where the deflection of the actuator is zero.

4.2 Finite Element Analysis of the Bossed Diaphragm with Central Excitation

The finite element analysis of the bossed diaphragm is performed to evaluate the effect of the diaphragm thickness, material and bossed ratio on the deflection behaviour, as explained in section 3.3. Figure 4.3 represents the variation of simulated deflection with respect to actuation voltage of the actuator for centrally excited silicone rubber bossed diaphragm. The simulated deflection varies linearly with respect to the actuation voltage for all the bossed diaphragm configurations mentioned above. However, the deflection range dropped with the increase in the bossed ratio due to the increased stiffness of the silicone rubber diaphragm with the bossed ratio. The maximum simulated deflection of the bossed diaphragm with bossed ratio 0.33, 0.50 and 0.66 is about 137.59 µm, 120.190 µm and 105.86 µm, respectively at 150 V.
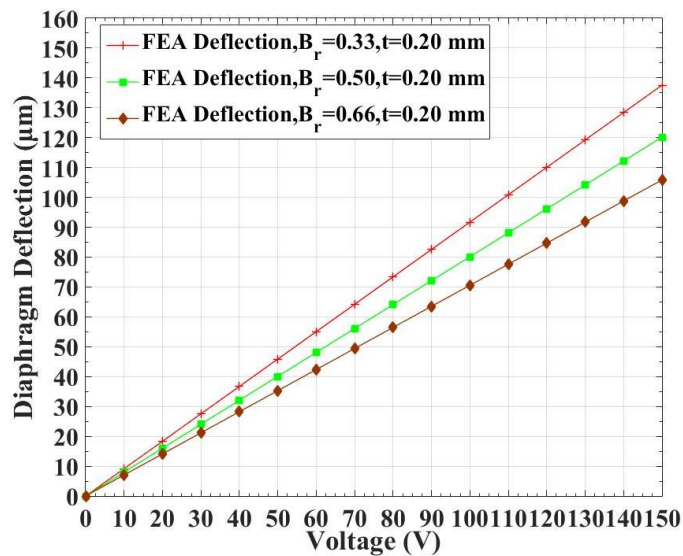
Figure 4.3 Variation of simulated displacement of centrally excited silicone rubber bossed diaphragm (t=0.20 mm) with different bossed ratio values

The thickness of the diaphragm also significantly influences the deflection range of the diaphragm. Figure 4.4 represents the variation of the deflection results obtained from the static analysis of the centrally excited silicone rubber bossed diaphragm with different thickness values. The contribution of increased thickness of the diaphragm towards increased stiffness leads to a drop in the deflection value of the

diaphragm with the increase in thickness value. The simulated deflection of the silicone rubber bossed diaphragm varies linearly with the increase in the actuation voltage. The maximum simulated deflection of the silicone rubber bossed diaphragm of bossed ratio 0.33, and thickness of 0.20 mm, 0.40 mm, and 0.60 mm is about 137.59 μm, 112.96 μm and 93.307 μm respectively for an input voltage of 150 V of the actuator.
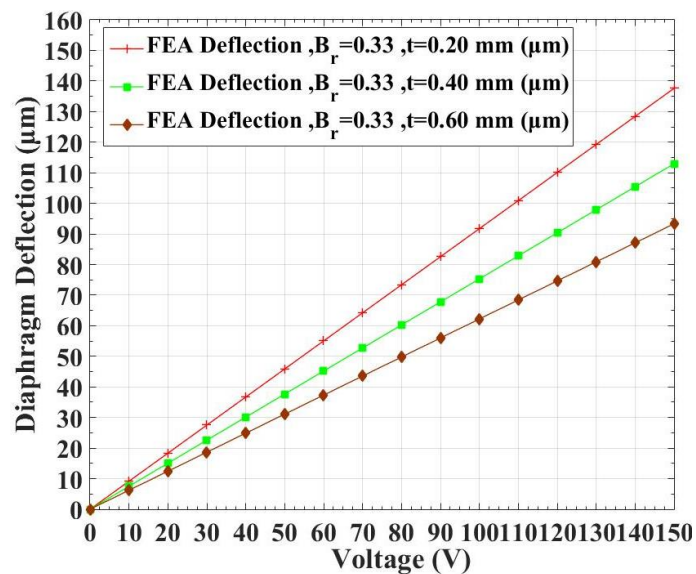
Figure 4.4 Variation of simulated displacement of centrally excited silicone rubber bossed diaphragm (B_r=0.33) with different thickness values

Apart from bossed ratio and thickness, the young's modulus of the diaphragm also significantly influences the deflection behaviour of the bossed diaphragm. The stiffness of the bossed diaphragm effectively increases with the increase in the young's modulus of the material. Figure 4.5 represents the variation of simulated deflection of the centrally excited silicone rubber (E = 1.2 MPa) and Polydimethylsiloxane (PDMS) (E = 1.65 MPa) with respect to actuation voltage having bossed ratio of 0.33 and thickness 0.20 mm. Linear variation in deflection is observed with respect to actuation voltage for both silicone rubber and the PDMS diaphragm. It is evident from Figure 4.5 that the increase in the young's modulus of PDMS membrane resulted in a lower range of deflection when compared with the silicone rubbers, which possess lower young's modulus. The maximum simulated

deflection of 137.59 µm and 127.26 µm is achieved with silicone rubber and PDMS diaphragm with bossed ratio 0.33, the thickness of 0.20 mm depicting the drop in deflection value due to increased young's modulus.
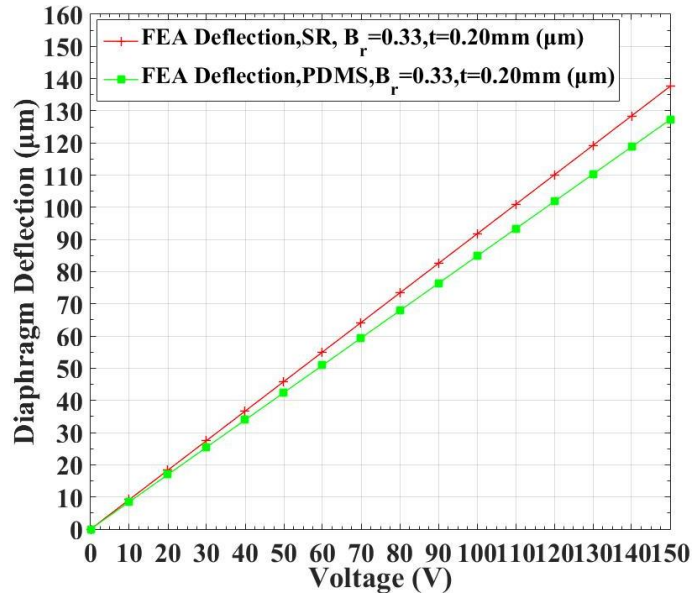
Figure 4.5 Variation of simulated displacement of centrally excited silicone rubber and PDMS bossed diaphragm (B_r=0.33, t=0.20 mm)

Thus it is concluded that the silicone rubber diaphragm with the bossed ratio of 0.33 and thickness of 0.20 mm developed maximum deflection when compared with the FE results of other configurations of centrally excited silicone rubber diaphragm. However, when integrated with the micropump, the bossed diaphragms will be subjected to dynamic loading conditions. Thus, understanding the dynamic behaviour of the diaphragm is one of the crucial aspects. The silicone rubber bossed diaphragm with the bossed ratio of 0.33, and a thickness of 0.20 mm is subjected to harmonic analysis to determine its dynamic performance.
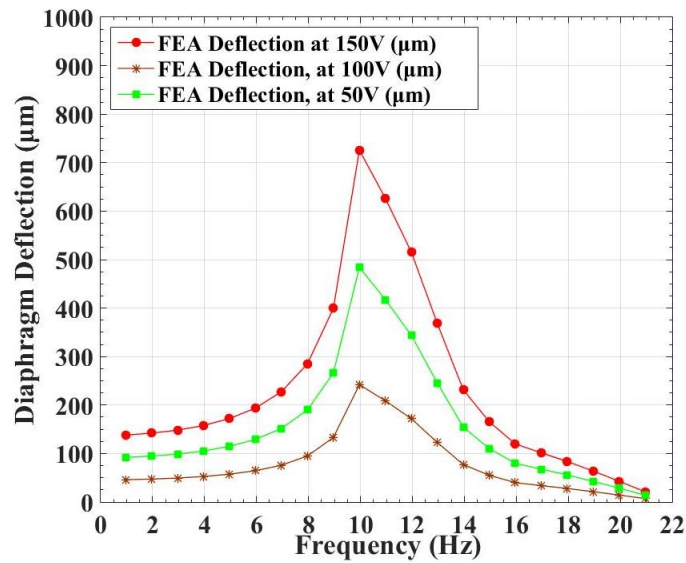
Figure 4.6 Variation of simulated displacement of centrally excited silicone rubber bossed diaphragm (B_r=0.33, t=0.20 mm) with respect to actuation frequency and voltage
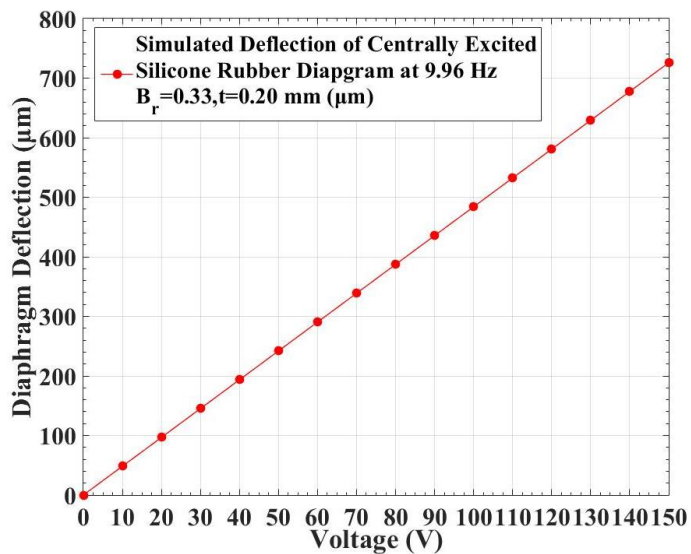
Figure 4.7 Variation of simulated displacement of centrally excited silicone rubber bossed diaphragm (B_r=0.33, t=0.20 mm) with respect to actuation voltage at 9.96 Hz

A frequency sweep analysis is performed to determine the frequency corresponding to the maximum deflection of the diaphragm. Figure 4.6 represents the variation of the simulated deflection of the silicone rubber bossed diaphragm with respect to actuation frequency at 150 V, 100 V and 50 V. The deflection of the bossed

diaphragm increased with increased actuation frequency and attained peak deflection at a frequency corresponding to the first modal frequency of the centrally excited silicone rubber diaphragm. Thus, the maximum deflection of the diaphragm occurs when the diaphragm oscillates under resonance condition where the actuation frequency corresponds to 9.96 Hz, as evident from Figure 4.6. The simulated peak deflection of 725.91 μm, 483.9 μm and 242.01 μm is achieved with the bossed diaphragm at 150 V, 100 V and 50 V, respectively, corresponding to the frequency of 9.96 Hz. Figure 4.7 shows the simulated displacement of the centrally excited silicone rubber bossed diaphragm with respect to actuation voltage at a frequency of 9.96 Hz.

4.3 Experimental Characterization of the Amplified Piezo Actuator

In the present section, the results obtained from the experimental characterization of the actuator are presented in terms of deflection and blocked force characteristics. Figure 4.8 (a) represents the results of the experimental characterization of the multilayer piezo stack actuator and amplified piezo actuator (APA-120S). The deflection of the actuator is measured under the voltage range of 10 V to 150 V with the 10 V increment. The experimental deflection of the multilayer piezo stack actuator and the amplified piezo actuator is found to vary almost linearly with respect to the actuation voltage.

The multi-layered piezo stack actuator delivered a maximum deflection of about 19.92±2.00 μm when actuated at 150 V. Further, the deflection of the multilayer piezo stack actuator is amplified through a flexural amplifier resulting in maximum deflection of 124.51±2.00 for the same input voltage of 150 V. Thus, the deflection of stack actuator gets amplified by a factor of about 6.25. The maximum deflection of the multilayer piezo stack actuator and the amplified piezo actuator obtained through FEA is about 18.408 μm and 122.8 μm, consistent with the experimental results. The comparison of simulated and experimental deflection of APA is presented in Figure 4.8 (a). The simulated and experimental deflections are found to agree with each other.
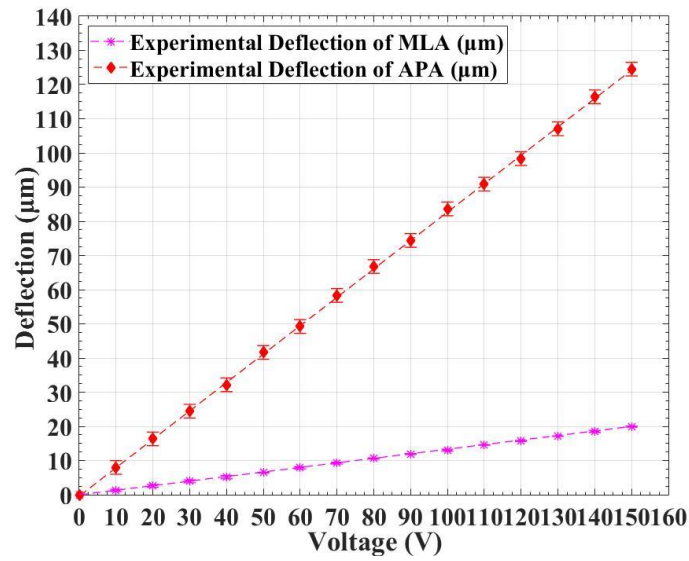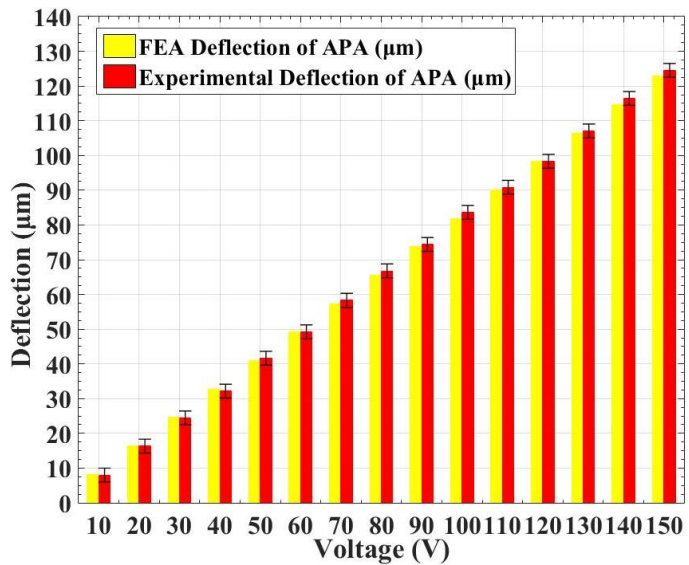
Figure 4.8 (a) Variation of experimental deflection of the APA with respect actuation voltage **(b)** Comparison of simulated and experimental deflection of APA with respect to actuation voltage

Further characterization of the APA focussed on the determination of blocked force characteristics. The actuator is subjected to incremental loads to determine the maximum blocking force where the actuator deflection drops to zero. Figure 4.9 (a) represents the variation of blocked force with the deflection of the APA. With the increase in the external load on the actuator, the deflection of the actuator dropped

continuously and attained zero deflection. The variation in the deflection and blocked force is observed to be linear (D'Souza et al. 2018)
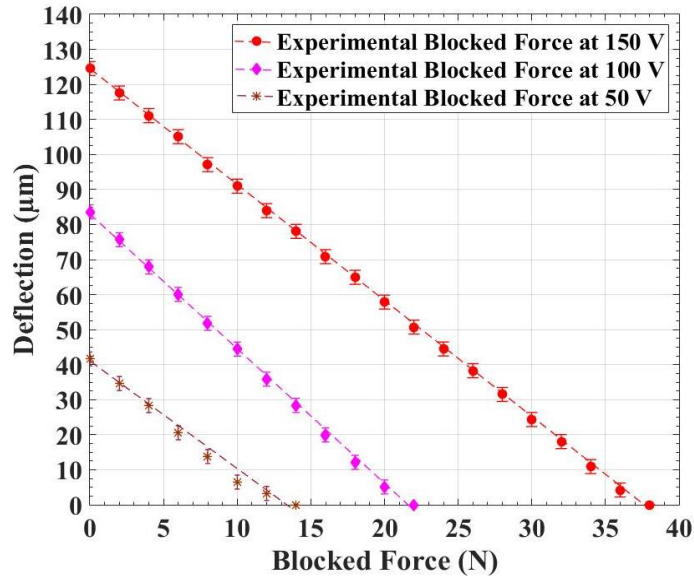
(a)
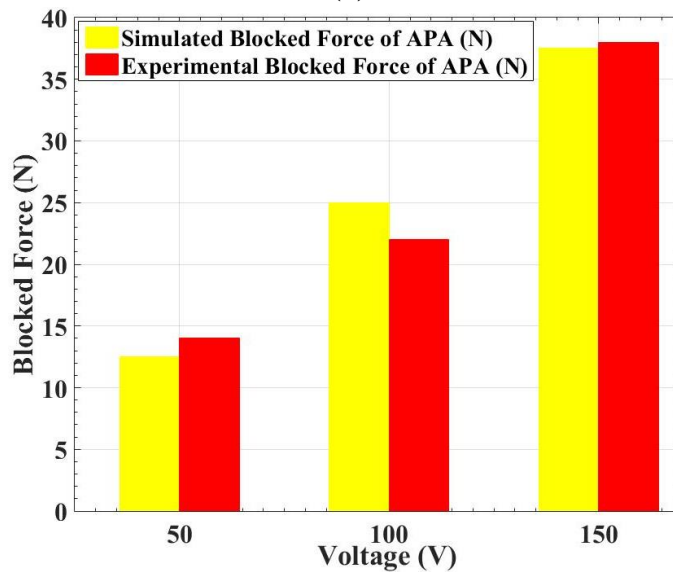
(b)

Figure 4.9 (a) Variation of experimental blocked force with respect to deflection of APA at different voltage **(b)** Comparison of simulated and experimental blocked force with respect to deflection of APA at different voltage

The maximum experimentally measured blocked force of 38 N is achieved with the amplified piezoelectric actuator, which is comparable with the FEA blocked force of 37.5 N when actuated at 150 V. The finite element and experimental blocked

force at 100 V and 50 V are about 25 N, 12.5 N and 22 N, 14 N respectively. Figure 4.9 (b) represents the comparison of the simulated and the experimental blocked force achieved with the amplified piezo actuator (APA-120S).

4.4 Experimental Characterization of the Centrally Excited Bossed Diaphragm

The following section presents the results of experimental characterization of the bossed diaphragm with central excitation.

4.4.1 Effect of Bossed Ratio, Thickness, Material Property on the Deflection of the Centrally Excited Bossed Diaphragm

The performance of the mechanical micropump majorly depends on the deflection of the diaphragm which in turn depends on the thickness, bossed ratio, material property, and excitation method. Figure 4.10 represents the variation of experimental deflection of the centrally excited silicone rubber bossed diaphragm with respect to the actuation voltage. As observed in Figure 4.10, the bossed ratio of the silicone rubber diaphragm significantly affected the deflection of the diaphragm. An increase in the bossed ratio of the diaphragm substantially increases the stiffness of the diaphragm. As a result, resistance to deformation increases leading to a reduction in the deflection of the diaphragm (Ma et al.2015). The maximum deflection of the silicone bossed diaphragm with bossed ratio 0.33, 0.50, 0.66 corresponding to actuation voltage of 150 V is found to be 136.5±0.5 μm, 120±1.00 μm and 105±1.00 μm, respectively. The corresponding deflection obtained from the FE analysis of silicone bossed rubber diaphragm with the bossed ratio of 0.33, 0.50 and 0.66 is about 137.59 μm, 120.190 μm and 105.86 μm when simulated with actuation voltage of 150 V. Figure 4.11 represents the comparison of the simulated and experimental deflection of the centrally excited silicone rubber bossed diaphragm (t=0.20 mm) with different bossed ratio values.
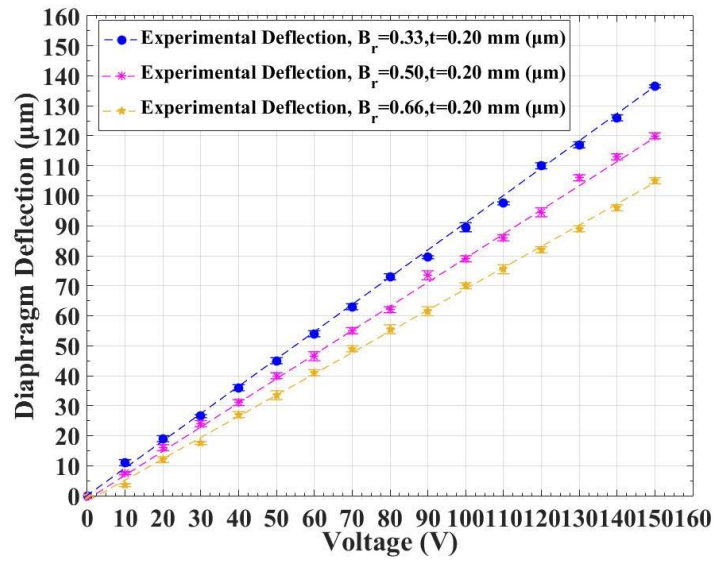
Figure 4.10 Variation of experimental deflection of centrally excited silicone rubber bossed diaphragm (t=0.20 mm) with different bossed ratio values
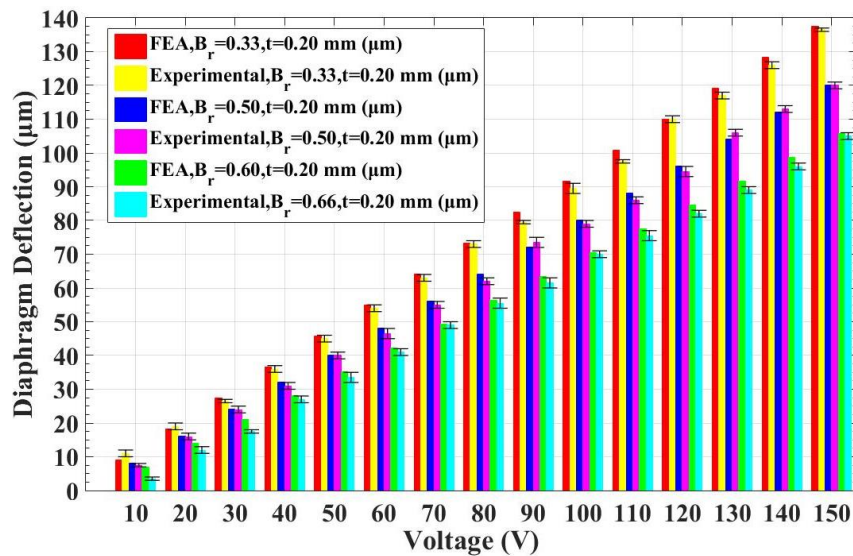
Figure 4.11 Comparison of the simulated and experimental deflection of centrally excited silicone rubber bossed diaphragm (t=0.20 mm) with different bossed ratio values

The increase in the thickness of the diaphragm is another factor that contributes towards increased stiffness of the bossed diaphragm. Figure 4.12 represents the variation of the deflection of the silicone rubber bossed diaphragm with

the bossed ratio of 0.33 and different thickness values. With the increase in the thickness, the deflection of the bossed diaphragm reduced due to increased resistance to deformation. The experimental results of the diaphragm deflection with the bossed ratio of 0.33 and thickness values of 0.20 mm, 0.40 mm and 0.60 mm about 136.5±0.50 µm, 111±1.00 µm and 90.12±1.00 µm when the actuation voltage is set to 150 V.
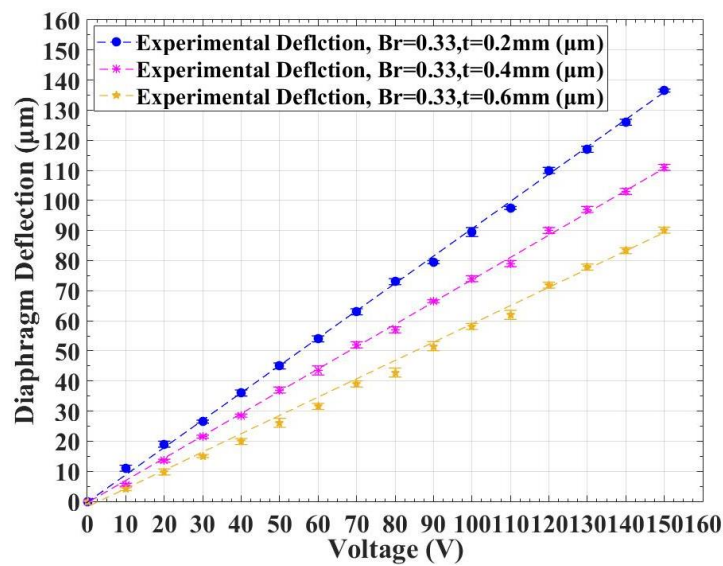
Figure 4.12 Variation of experimental deflection of centrally excited silicone rubber bossed diaphragm (B_r=0.33) with different thickness values

Figure 4.13 represents the comparison of the simulated and experimental deflection of centrally excited silicone rubber bossed diaphragm (B_r=0.33) with different thickness values. The maximum simulated deflection of the silicone rubber diaphragm with a similar configuration is about 137.59 µm, 112.96 µm and 93.307 µm, respectively, for an actuation voltage of 150 V. The simulated and experimental deflection of the diaphragm with different thickness values is found to agree with each with the close agreement.
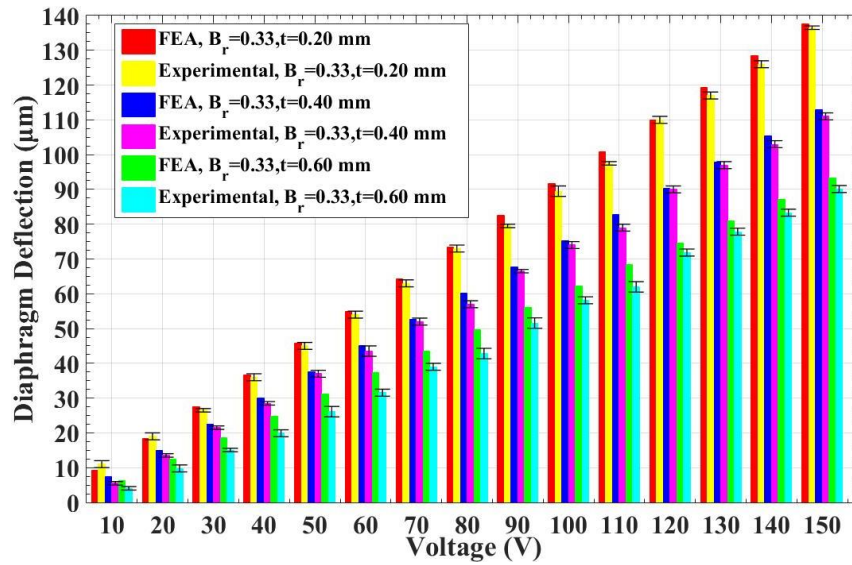
Figure 4.13 Comparison of simulated and experimental deflection of centrally excited silicone rubber bossed diaphragm (B_r=0.33) with different thickness values
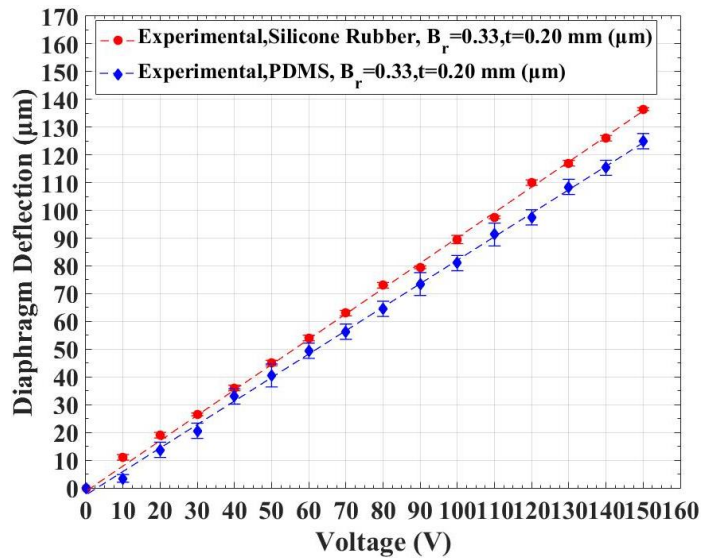
Figure 4.14 Variation of experimental deflection of centrally excited silicone rubber and PDMS bossed diaphragm (B_r=0.33, t=0.20 mm)

A similar trend of decrease in deflection of bossed diaphragm is observed with an increase in the young's modulus when the diaphragm is centrally excited. Figure 4.14 represents the variation of deflection behaviour of the silicone rubber diaphragm (E = 1.20 MPa) and PDMS diaphragm (E = 1.64 MPa) with the bossed

ratio of 0.33 and thickness 0.20 mm. It is evident from figure 4.13 that the increased value of young's modulus value reduces the deflection of the diaphragm due to the increased stiffness. A silicone rubber and PDMS diaphragm with the bossed ratio of 0.33 and thickness of 0.20 mm delivered maximum deflection of 136.5±0.50 µm and 124.9±2.50 µm respectively at 150 V input of the actuator, which indicated the effect of increased young's modulus. Figure 4.15 compares the simulated and experimental deflection of centrally excited silicone rubber, and PDMS bossed diaphragm (Br=0.33, t=0.20 mm). The maximum simulated deflection of the silicone rubber and PDMS diaphragm is about 137.59 µm and 127.260 µm at 150 V, which also agree with the experimental results.
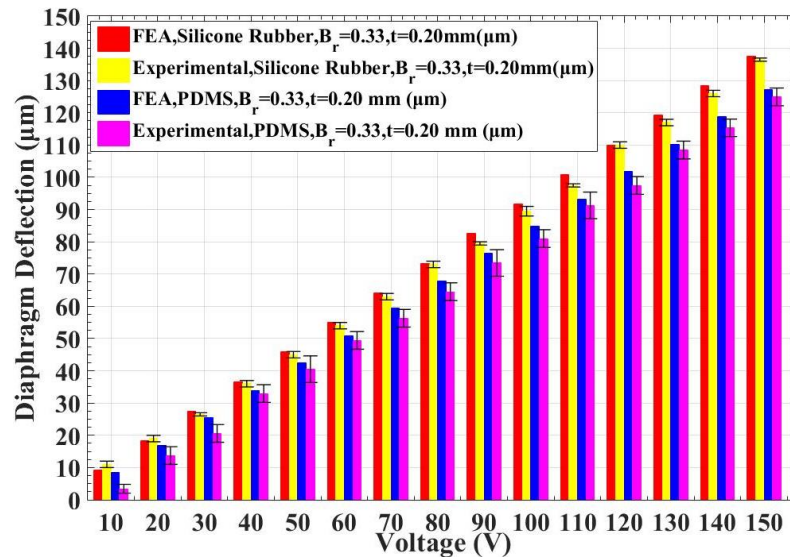
Figure 4.15 Comparison of simulated and experimental deflection of centrally excited silicone rubber and PDMS bossed diaphragm (B_r=0.33, t=0.20 mm)

4.4.2 Dynamic Response of the Centrally Excited Bossed Diaphragm

The micropump operates under dynamic conditions; thus, the excitation frequency of the bossed diaphragm significantly influences its performance. Excitation of the bossed diaphragm at a frequency close to the first modal frequency leads to resonant oscillation of the diaphragm (Ma et al. 2016). This, in turn, leads to the oscillation of the diaphragm with higher amplitude leading to the increased swept volume inside the pump chamber. The bossed diaphragm with the bossed ratio of 0.33

115

and thickness of 0.20 mm is found to deliver maximum deflection through the static analysis. Hence, the dynamic analysis of the diaphragm s performed for the above configuration of the bossed diaphragm. An experimental sweep is performed to estimate the frequency corresponding to the maximum deflection of the bossed diaphragm at actuation voltage of 50 V, 100 V and 150 V.
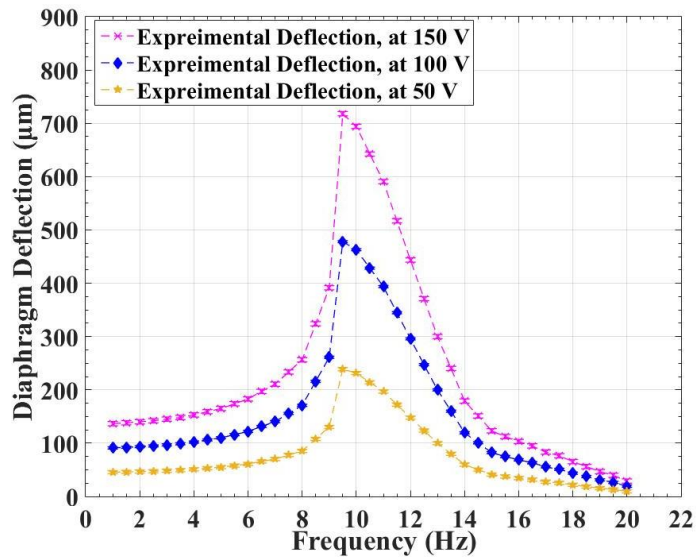
Figure 4.16 Variation of experimental displacement of centrally excited silicone rubber bossed diaphragm (B_r=0.33, t=0.20 mm) with respect to actuation frequency

Figure 4.16 represents the variation of deflection of the centrally excited silicone rubber bossed diaphragm (B_r = 0.33, t = 0.20 mm) with the actuation frequency at 50 V, 100 V, and 150 V. The deflection of the centrally excited bossed diaphragm increases with increase in the actuation frequency. The deflection value reaches a maximum value when the actuation frequency approaches the first modal frequency of the diaphragm. The frequency corresponding to the maximum deflection of the centrally excited bossed diaphragm is about 9.50 Hz, which matches the simulated first modal frequency of value 9.96 Hz.
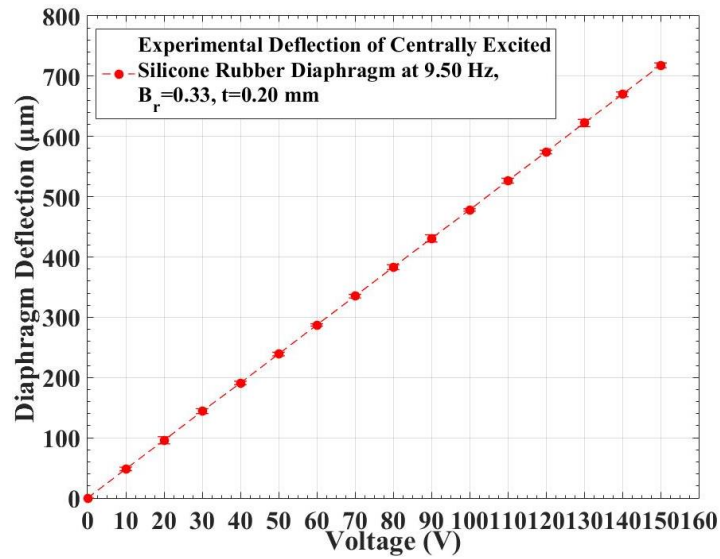
Figure 4.17 Variation of experimental displacement of centrally excited silicone rubber bossed diaphragm (B_r=0.33, t=0.20 mm) with actuation voltage at 9.50 Hz
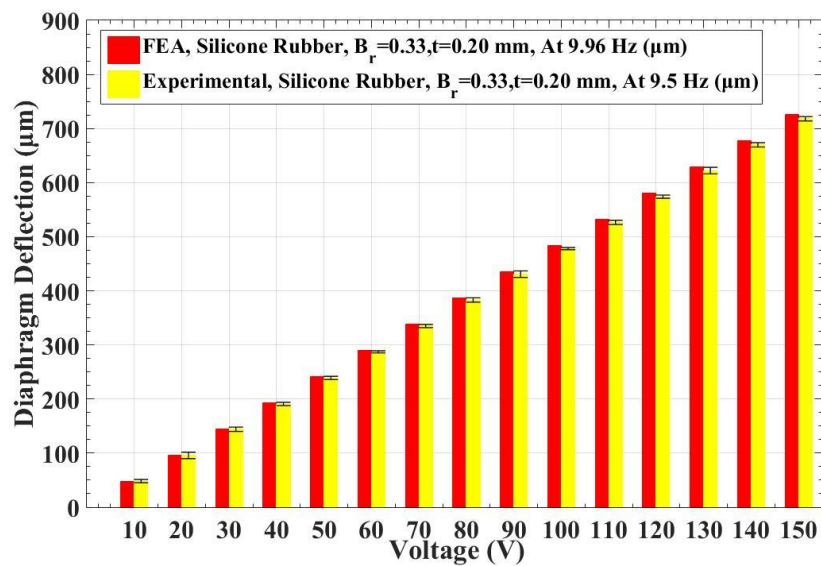
Figure 4.18 Comparison of simulated and experimental displacement of centrally excited silicone rubber bossed diaphragm (B_r=0.33, t=0.20 mm) with respect to actuation voltage at resonant frequency.

Figure 4.17 represents the variation of the experimental deflection of the centrally excited bossed diaphragm (Br = 0.33, t = 0.20 mm) with respect to the actuation voltage. The maximum experimental deflection attained under the dynamic

117

operation of the centrally excited bossed diaphragm is about 717.99±4.00 μm, 477.96±2.00 μm and 239.95±3.00 μm at 150 V, 100 V and 50 V respectively when the actuation frequency is set at 9.5 Hz. The simulated deflection of the similar configuration of the bossed diaphragm obtained through FEA is about 725.91 μm, 483.9 μm, and 242.01 μm at 150 V, 100 V 50 V, respectively. The simulated and experimental deflection almost agrees with slight variations due to the structural damping effect. Figure 4.18 compares the results obtained from the simulated and experimental dynamic response of the bossed diaphragm.

4.5 Evaluation of the Performance of Proposed Valveless Disposable Chamber Micropump with Centrally Excited Bossed Diaphragm

The experimentation on the proposed micropump with centrally excited bossed diaphragm considered performance evaluation with different design parameters such as diaphragm thickness (t), bossed ratio (B_r) and chamber depth (h_c) to have optimal pump configuration. The experimental study also involved the effect of fluid density or viscosity and the performance of the micropump under a specific pressure head, considering the optimal parameters of the micropump.

4.5.1 Optimum Chamber Depth for Micropump Configuration with Centrally Excited Bossed Diaphragm

In order to analyse the effect of chamber depth, the micropump is tested for different chamber depth between 0.75 mm to 2.00 mm with an increment of 0.25 mm. The experimental evaluation of the micropump incorporated a silicone rubber diaphragm of 0.2 mm thickness with a bossed ratio of 0.33. Figure 4.19 (a) compares the variation in flow rate developed by the micropump with respect to actuation frequency at 150 V for different chamber depths of the proposed micropump with water as the pumping fluid. With the increase in the actuation frequency, the flow rate increases up to 5 Hz, beyond 5 Hz of the actuation frequency, the flow rate begins to drop significantly (Wei et al. 2014). The actuation frequency of 5 Hz at which the maximum flow occurs corresponds to the resonance condition of the micropump. The resonant frequency obtained from harmonic analysis of the diaphragm is about 9.5 Hz

(Figure 4.16 (a)). However, the frequency corresponding to the maximum flow rate is 5 Hz. This difference in frequency is due to the mass of the fluid over the diaphragm. As a result, the diaphragm is subjected to a damping effect that reduces the natural frequency of the diaphragm.
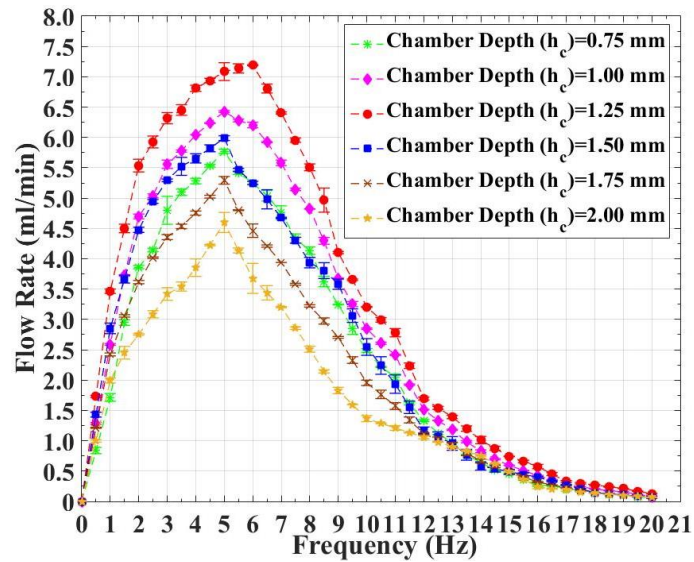
(a)
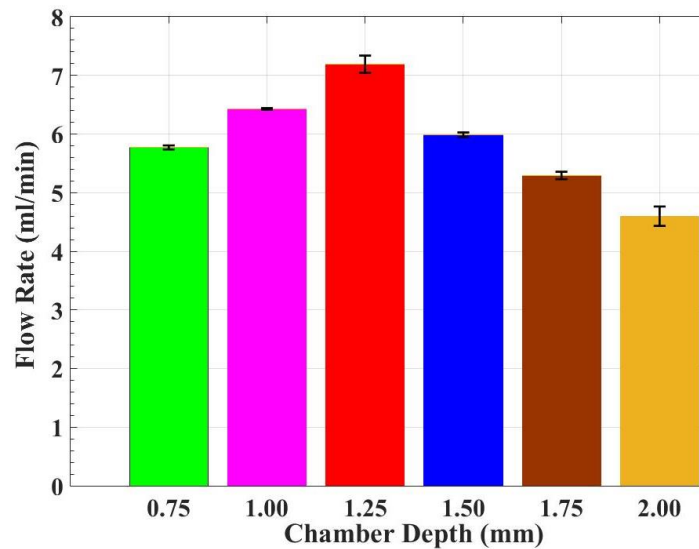
(b)

Figure 4.19 (a) Measured water flow rate corresponding to actuation frequency for different chamber depths of the centrally excited micropump (t = 0.2 mm, B_r = 0.33) **(b)** Comparison of maximum flow rate of the centrally excited micropump (t = 0.2 mm, B_r = 0.33) with different chamber depths at 150 V, 5 Hz.

Figure 4.19 (b) compares the maximum flow rate of water achieved with the sinusoidal input signal of 150 V, driven at 5 Hz with different chamber depths. As shown in figure 4.19 (b), the chamber depth significantly affected the flow characteristics of the micropump. At lower chamber depth, the influence of adhesive force on the diaphragm due to residual liquid is predominant, as seen from theoretical analysis of adhesive force (Figure 3.10) (Ma et al. 2016). The maximum flow rate achieved with a chamber depth of 0.75 mm is about 5.771±0.034 ml/min. An increase in the chamber depth further raised the flow rate to a maximum value of 7.192±0.147 ml/min with a chamber depth of 1.25 mm. The reduced effect of adhesive force with chamber depths may have increased the flow rate. The pumping rate decreased substantially beyond the chamber depth of 1.25 mm.
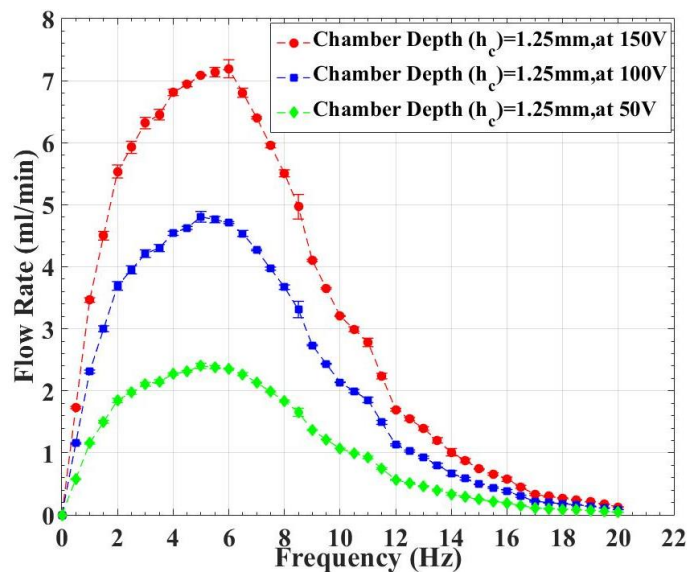
Figure 4.20 Measured water flow rate corresponding to actuation frequency at different actuation voltage of the centrally excited micropump (h_c=1.25 mm, t = 0.2 mm, B_r = 0.33)

The impact of adhesive force decreases with an increase in the chamber depth, which should increase the flow rate. However, the flow rate dropped to a value of 5.989±0.039 ml/min when the chamber depth is increased to a value of 1.50 mm. The compressibility of the fluid plays a significant role to play in the pumping of the fluid. When the chamber depth increases to a larger value, the compressibility of the fluid decreases leading to a reduction in the flow rate. As the chamber depth increased to

1.50 mm, 1.75 mm and 2.00 mm, the corresponding maximum flow rate observed is 5.989±0.039, 5.293±0.063 ml/min and 4.598±0.165 ml/min at 150 V, 5 Hz. Thus, the optimal flow rate is achieved with a chamber depth of 1.25 mm. Figure 4.20 represents the variation of the flow rate of the proposed centrally excited micropump (hc = 1.25 mm, Br = 0.33, t = 0.20 mm) with 5 Hz actuation voltage. With the decrease in the actuation voltage, the deflection of the diaphragm decreases, leading to a reduction in flow rate. The optimal flow rates of 7.192±0.147 ml/min, 4.805±0.191 ml/min and 2.425±0.141 ml/min are achieved with an actuation frequency of 5 Hz when actuated at 150 V, 100 V and 50 V, respectively. Further, all the characterization of the micropump considered chamber depth of 1.25 mm.

4.5.2 Effect of Diaphragm Geometry on the Flow Performance of the Micropump with Centrally Excited Bossed Diaphragm

The centrally excited micropump is experimentally evaluated with different thickness and bossed ratio of the silicone rubber diaphragm to assess the effect of diaphragm thickness and bossed ratio on the flow characteristics. Initially, micropump considered with silicone rubber diaphragm of thickness 0.2 mm and bossed ratio 0.33, 0.50 and 0.66. In the second stage, the bossed ratio of the diaphragm is fixed at 0.33 with the variable thickness of 0.20 mm, 0.40mm and 0.60 mm.

Figure 4.21 (a) and Figure 4.21 (b) represent the variation of the flow rate of centrally excited micropump (chamber depth 1.25 mm, actuation frequency 5 Hz) with different bossed ratio and diaphragm thickness. The flow rate of the micropump increases almost linearly with respect to actuation voltage as observed from Figure 4.21 (a) and Figure 4.21 (b). The linear trend between the actuation voltage and the diaphragm deflection observed in the previous section of the diaphragm characterization resulted in the linearity of the flow characteristics of the micropump with actuation voltage (Singh et al. 2015).
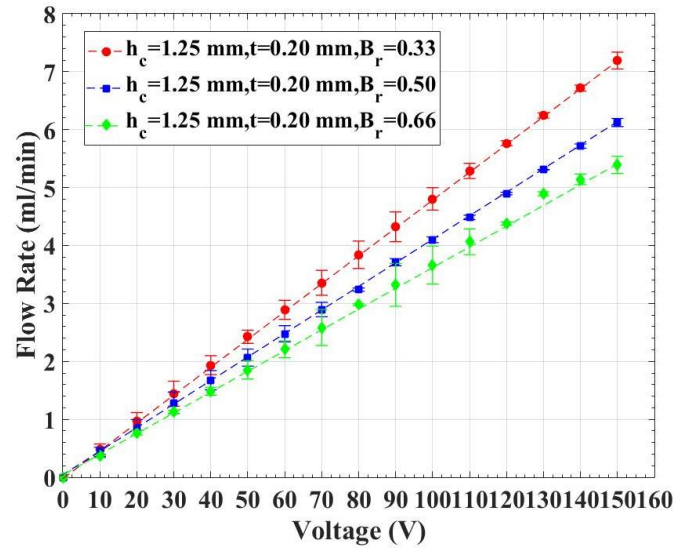
(a)
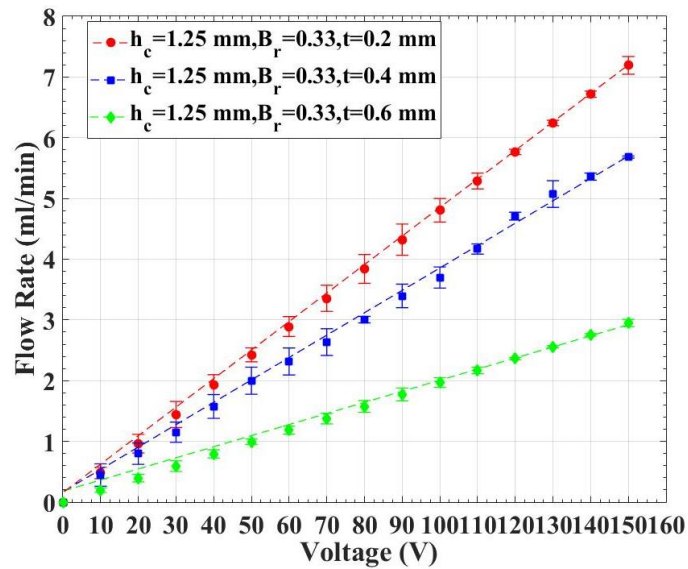
(b)

Figure 4.21 (**a**) Measured water flow rate of centrally excited micropump corresponding to actuator voltage for different bossed ratio's (B_r) (t = 0.2 mm, h_c= 1.25 mm, f = 5 Hz) (**b**) Measured water flow rate of centrally excited micropump corresponding to actuator voltage for different diaphragm thickness (t) (B_r = 0.33, h_c= 1.25 mm, f = 5 Hz)

The flow rate achieved with the 0.20 mm thick diaphragm is superior to the flow rate achieved with 0.40 mm and 0.60 mm thick diaphragm. Increased diaphragm thickness results in increased stiffness, as shown in Figure 3.8(a), which reduces the

deflection of the diaphragm resulting in diminished swept volume. Micropump with a diaphragm of thickness 0.20 mm delivered a maximum water flow rate of 7.192±0.147 ml/min, which is higher than a maximum flow rate of 5.682±0.018 ml/min and 2.949±0.06 ml/min achieved with 0.40 mm, 0.60 mm thickness diaphragm respectively at 150 V, 5 Hz.

Further studies considered understanding the effect of bossed ratio on the flow rate for which the micropump is experimentally evaluated with 0.2 mm diaphragm thickness and 0.33, 0.50, and 0.66 bossed ratios. An increase in the bossed ratio of the diaphragm influences the micropump performance by contributing to the diaphragm stiffness and adhesive force. The variation of the measured flow rate of the micropump for different bossed ratios with respect to the actuation voltage is shown in Figure 4.21 (b). With the bossed ratio of 0.33, an optimal water pumping rate of 7.192±0.147 ml/min is achieved. Further increase in the bossed ratio of the diaphragm to 0.50 and 0.66 culminated in a decreased flow rate of 6.123±0.07 ml/min and 5.013±0.148 ml/min, respectively. Increasing the bossed ratio of the diaphragm increases the effective stiffness (Figure 3.8 (a)), resulting in higher deformation resistance and thus reducing the flow rate.

4.5.3 Performance of the Micropump with Central Excited Bossed Diaphragm under Pressure Head

Micropump performance assessment also involved in understanding the pressure-flow characteristics to establish the significance of micropump for practical applications. The experimental study involved generating a predetermined pressure head by varying the micropump inlet and outlet level and recording the corresponding achieved flow rate. The experiments are conducted taking into account the optimized micropump parameters i.e. pump chamber depth (h_c) = 1.25 mm, diaphragm thickness (t) = 0.2 mm and bossed ratio (B_r) = 0.33. Figure 4.22 (a) depicts the variation of pressure and flow rate with water as the working fluid when actuated at 150 V. A decreasing linear relation exists between the pumping rate of the water and the pressure (Shen at al. 2011; Cheng et al. 2015). When the micropump is actuated with the sinusoidal signal of frequency 1 Hz, 3 Hz and 5 Hz, the flow rate of water at zero

pressure is found to be about 3.464±0.036 ml/min, 6.317±0.092 ml/min, and 7.192±0.147 ml/min, respectively. The maximum pressure at zero flow rates is about 196 Pa, 245 Pa, and 294 Pa, respectively, at 1 Hz, 3 Hz, and 5Hz.
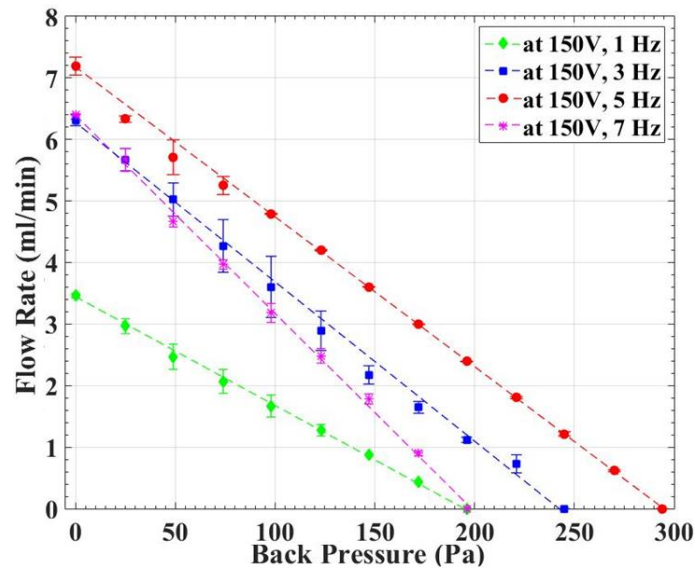
(a)
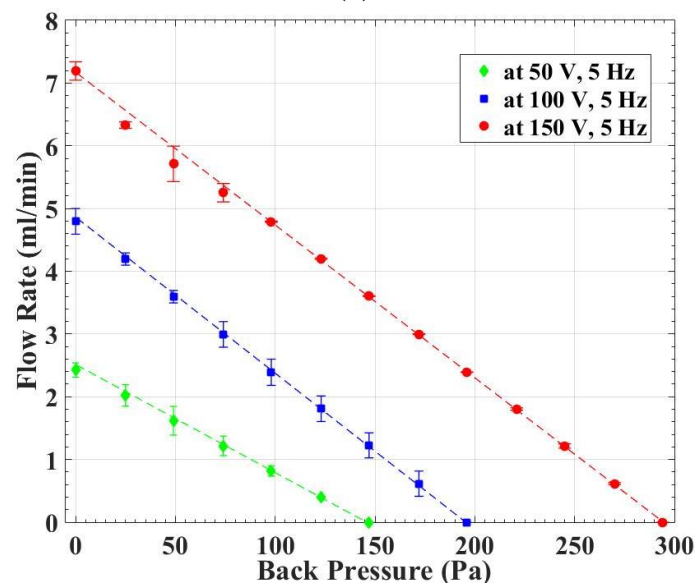
(b)

Figure 4.22 (a) Measured pressure corresponding to water flow rate of the centrally excited micropump for different driving frequency of the actuation signal at 150 V (B_r = 0.33, h_c= 1.25 mm) **(b)** Measured pressure corresponding to water flow rate of centrally excited micropump for different actuation voltage at 5 Hz (B_r = 0.33, h_c= 1.25 mm)

124

An additional increase in the actuation frequency beyond 5 Hz resulted in a decrease in the maximum achieved pressure. The maximum flow rate at 7 Hz dropped to a value of approximately 6.403±0.017 ml/min at zero backpressure and maximum pressure to a value of 196 Pa at zero flow. The reduction of swept volume due to the drop in diaphragm deflection at higher frequencies is likely to be the reason for the decrease in pressure beyond 5 Hz. Figure 4.22 (b) represents backpressure and flow rate variation at 5 Hz for different actuation voltage with water as the working fluid. Since the diaphragm deflection decreases with the decrease in actuation voltage, the compressibility of the fluid inside the chamber drops, leading to declining in the pressure achieved. The maximum backpressure achieved at 150 V, 100 V and 50 V with the actuation frequency of 5 Hz is about 294 Pa, 196 Pa, and 147 Pa.

4.5.4 Performance of Centrally Excited Bossed Diaphragm Micropump with Different Fluids

The overall micropump performance in terms of pumping rate and pressure relies upon fluid properties such as density and viscosity. The micropump performance evaluation used water as the working fluid in the earlier sections. The present section focuses on comparing micropump performance with fluids of distinct density and viscosity achieved through the appropriate composition of water, glycerol, and propylene glycol.

The change in the measured flow rate corresponding to voltage for different fluids is shown in Figure 4.23. As the density and viscosity of the fluid increases, the pumping rate decreases (Pečar et al .2014). An increase in the fluid density reduces the compressibility of the liquid within the pump chamber and increases fluid resistance, thus damping the deflection of the diaphragm. Therefore the net pumping rate drops consistently with an increase in fluid density. Also, the adhesive force acting on the diaphragm surface is directly proportional to the viscosity of the residual fluid in the pump chamber, as observed in equation 3.17. Thus, the increased fluid viscosity increases the adhesive force on the diaphragm, which tries to resist the return of the diaphragm. As a result, the performance of the micropump reduces in terms of pumping rate. Figure 4.24 compares the variation of the pressure

125

corresponding to the flow rate at 150 V and 5 Hz. As the fluid density increases, the maximum pressure against which the pumping occurs drops due to the energy used to overcome the resistance offered by the increased density and viscosity of the fluid.
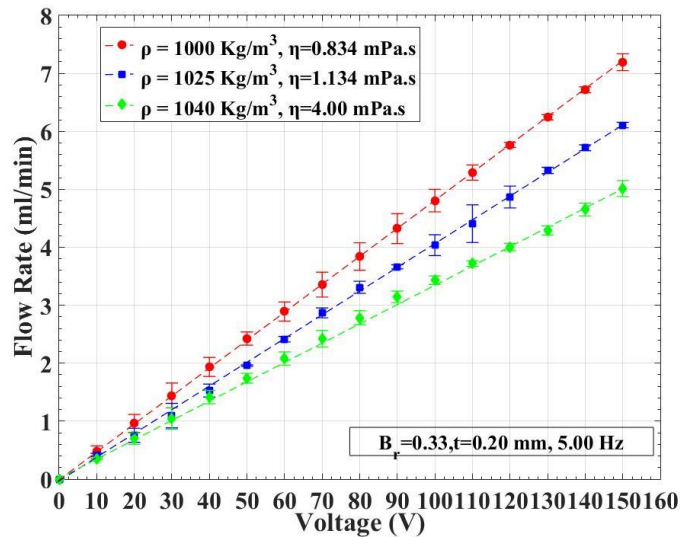
Figure 4.23 Variation of flow rate of centrally excited micropump corresponding to actuation voltage for distinct fluid density and viscosity at 5 Hz (B_r = 0.33, t=0.20 mm, h_c= 1.25 mm)
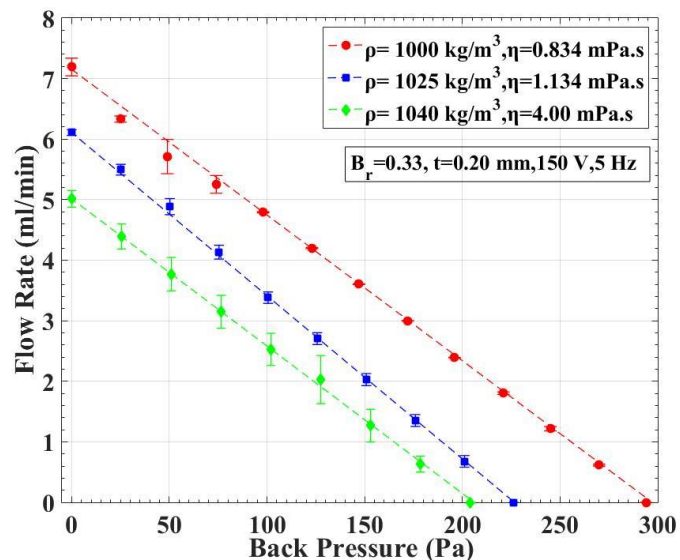
Figure 4.24 Variation of flow rate of centrally excited micropump corresponding to pressure for distinct fluid density and viscosity at 150 V, 5 Hz (B_r = 0.33, h_c= 1.25 mm, t=0.20mm, f = 5 Hz)

126
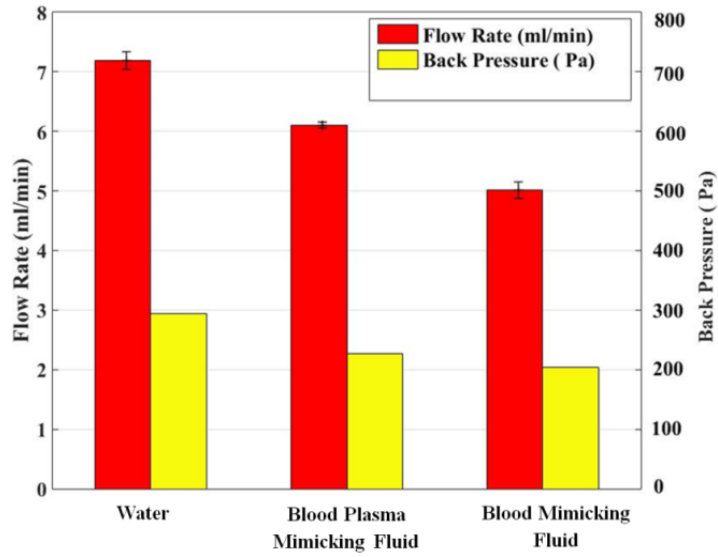
Figure 4.25 Comparison of maximum pumping rate and maximum pressure of the proposed micropump with central excitation for different fluids at 150 V, 5 Hz (B_r = 0.33, h_c= 1.25 mm, t = 0.2 mm)

Figure 4.25 compares the maximum flow rate and pressure achieved with distinct fluid density and viscosity when APA is driven at 150 V, 5 Hz. The proposed design of the micropump could deliver a maximum flow rate of about 7.192±0.147 ml/min, 6.108±0.047 ml/min and 5.013±0.138 ml/min with Water and fluids mimicking Blood Plasma and whole blood, respectively. The corresponding maximum pressure of approximately 294 Pa, 226.243 Pa, and 204.048 Pa is achieved with the same fluids.

4.5.5 Optimal Performance Parameters of the Micropump with Centrally Excited Bossed Diaphragm

A variable and adjustable flow rate over a specific time is an essential aspect of the micropump for biomedical application. Modulation of the actuation voltage of the actuator can deliver versatile flow rates. The experimental approach adopted for the proposed micropump design focused not only on achieving a higher pumping rate but also on having a robust disposable design involving multiple biomedical applications. The proposed micropump with a centrally excited bossed diaphragm delivers optimal performance with the diaphragm thickness of 0.2 mm, the Bossed ratio of 0.33, and the chamber depth of 1.25 mm.
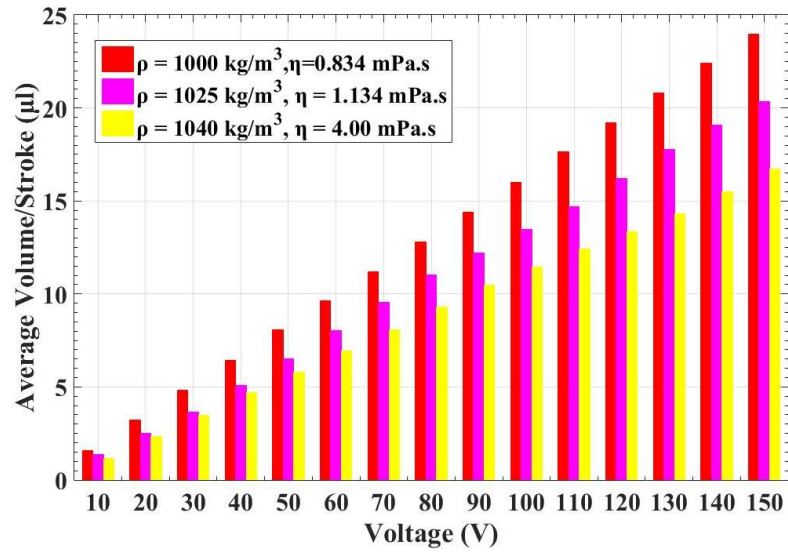
Figure 4.26 Variation flow/stroke with respect to actuation voltage of proposed micropump with centrally excited bossed diaphragm at 5 Hz.

Table 4.1 Optimized performance parameters of micropump with centrally excited bossed diaphragm

Fluid Category	Driving Voltage (V)	Driving Frequency (Hz)	Flow Rate (ml/min)	Flow/ Stroke (µl)	Back Pressure (Pa)
Water	150	5	7.192±0.147	23.97	294.00
Blood Plasma Mimicking	150	5	6.108±0.047	20.35	226.243
Blood Mimicking	150	5	5.013±0.138	16.70	204.048

Figure 4.26 represents the variation of the volume of fluid pumped per stroke of the diaphragm, which signifies the pumping resolution of the micropump. The flow rate can be modulated between 10 V to 150 V at 5 Hz, indicating the suitability of variable flow rate with the centrally excited bossed diaphragm. Table 4.1 represents the optimal performance parameters of the proposed micropump. The performance of the proposed micropump in terms of flow rate developed is comparable with some of the commercially available infusion pumps. The optimized design of micropump is capable of delivering a flow rate of 300 ml/hr to 432 ml/hr, which is comparable with commercial infusion pumps such as Pegasus Lab Light (0.1 ml/hr to 100 ml/hr), Terefusion TE-LF63X series (3 ml/hr to 300 ml/hr).

4.6 Enhancement of the Micropump Performance with Annularly Excited Bossed Diaphragm

The proposed disposable chamber valveless micropump with the central excited bossed diaphragm delivered a reasonable flow rate and backpressure. However, the enhancement of the deflection range of the bossed diaphragm can lead to the enhanced volumetric performance of the micropump. The following section presents the annular excited bossed diaphragm employed for improving the performance of the proposed disposable chamber valveless micropump.

4.6.1 Finite Element Analysis of the Bossed Diaphragm under Annular Excitation

The finite element analysis of the bossed diaphragm with annular excitation is performed as discussed in section 3.3 earlier. The variation of deflection of the bossed diaphragm with annular excitation is shown in figure 4.27. In this approach, the excitation is considered away from the central bossed region with silicone rubber diaphragm having bossed ratio (B_r) of 0.33, thickness (t) of 0.20 mm and loading radius (r_l) of 10.00 mm is considered for analysis. This allows the diaphragm to oscillate along the positive and negative z-direction, as shown in Figure 3.22, thus enhancing the deflection range. The maximum simulated deflection of the annularly excited bossed diaphragm is about 326.21 μm along both positive and negative z-direction when the actuation voltage is set to 150 V.

Harmonic analysis of the bossed diaphragm with annular excitation is carried out with frequency sweep to determine its dynamic characteristics. The annular excitation of the diaphragm under dynamic loading conditions leads to oscillation of the central bossed region with a larger amplitude when the actuation frequency approaches the first modal frequency. Figure 4.28 represents the simulated dynamic response of the annularly excited bossed diaphragm under actuation voltage of 150 V, 100 V and 50 V. The deflection of the annularly excited diaphragm increased with an increase in the actuation frequency similar to the centrally excited diaphragm until the resonance condition occurs.
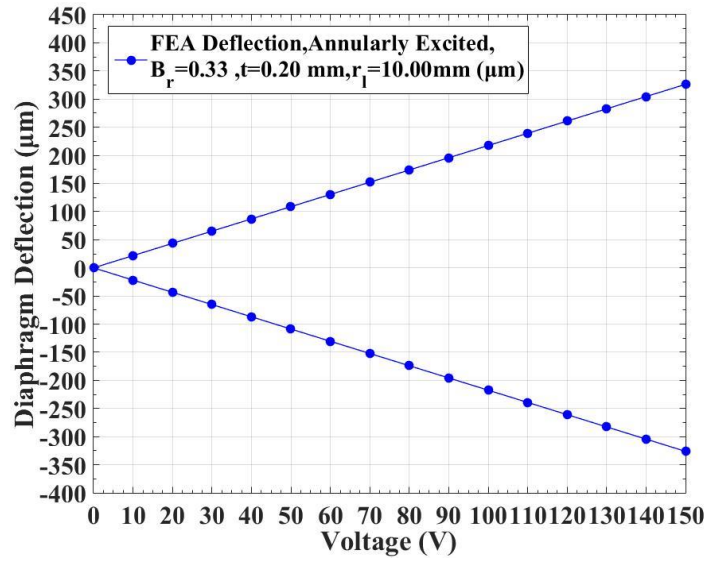
Figure 4.27 Variation of simulated deflection of the annularly excited bossed diaphragm (silicone rubber diaphragm, B_r=0.33, t=0.20, r_l=10.00 mm) with the actuation voltage.
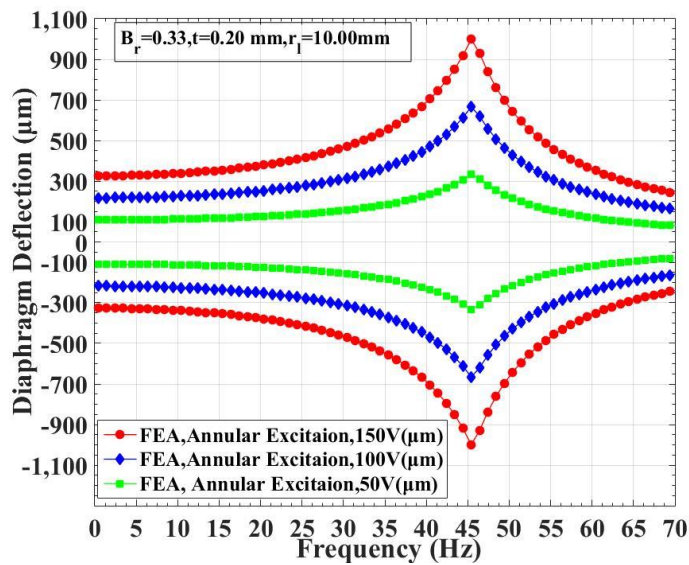
Figure 4.28 Variation of simulated deflection of the annularly excited bossed diaphragm (silicone rubber diaphragm, B_r=0.33, t=0.20 mm, r_l=10.00 mm) with the actuation frequency at 150 V, 100 V and 50 V

The frequency corresponding to the maximum deflection of the annularly excited bossed obtained from the harmonic analysis is found to be 45.42 Hz. The

corresponding simulated deflection is about 999.2 µm, 666.1 µm, and 333.1 µm along positive and negative z-direction at 150 V, 100 V and 50 V. The variation of the simulated deflection of the annularly excited silicone rubber bossed diaphragm with respect to actuation voltage at 45.42 Hz is shown in Figure 4.29 (a).
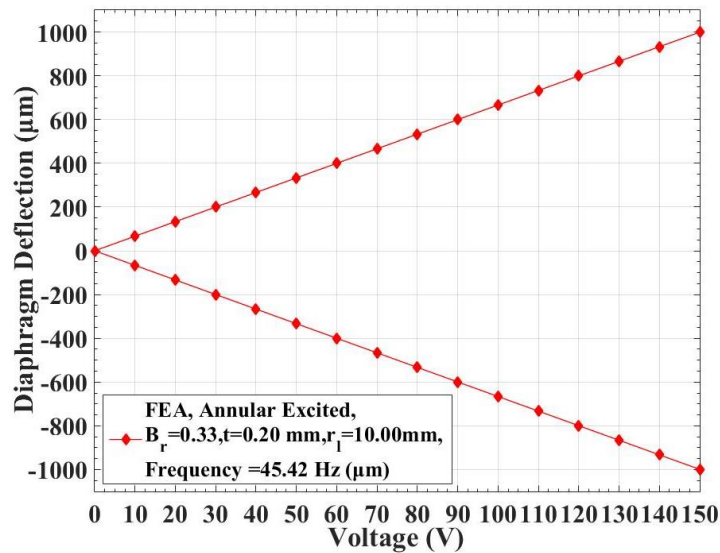
(a)
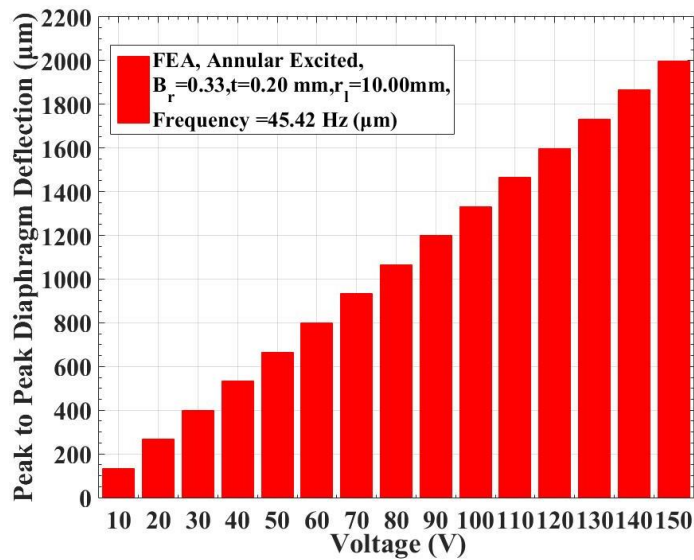
(b)

Figure 4.29 (a) Variation of the simulated deflection of annularly excited bossed diaphragm (silicone rubber diaphragm, B_r=0.33, t=0.20 mm, r_l=10.00 mm) corresponding to the actuation voltage at 45.42 Hz **(b)** Variation of the peak to peak deflection of annularly excited bossed diaphragm (silicone rubber diaphragm, B_r=0.33, t=0.20, r_l=10.00 mm) corresponding to the actuation voltage at 45.42 Hz

131

The diaphragm deflection is found to increase linearly with respect to an increase in the actuation voltage. Thus, the annularly excited diaphragm achieved maximum peak to peak simulated deflection of 1998.4 µm, 1332.2 µm and 666.13 µm at 45.42 Hz corresponding to actuation voltage of 150 V, 100 V and 50 V, respectively. Figure 4.29 (b) represents the variation of the peak to peak simulated deflection of the annularly excited bossed diaphragm.

4.6.2 Experimental Characterization of the Annularly Excited Bossed Diaphragm

The experimental characterization approach of the bossed diaphragm with annular excitation is similar to that of central excitation using the actuation mechanism shown in Figure 3.27 (c). Figure 4.30 represents the variation of experimental deflection of the annularly excited bossed diaphragm (r_l=10.00 mm) with variation in actuation voltage.
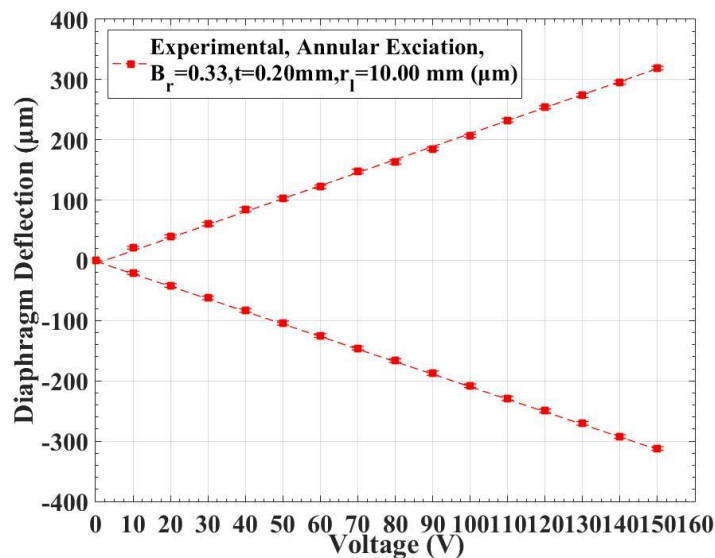
Figure 4.30 Variation of experimental deflection of the annularly excited bossed diaphragm (silicone rubber diaphragm, B_r=0.33, t=0.20 mm, r_l=10.00 mm) with the actuation voltage

The experimental deflection is found to increase almost linearly with respect to the actuation voltage (Ma et al. 2015). The maximum experimental deflection of the annularly excited diaphragm is about 318.98±3.00 µm and 312.13±3.00 µm along

the positive and negative z-direction, respectively at 150 V. The experimental static deflection is also found to agree with the simulated deflection of 326.21 μm along both positive and negative z-direction.

The experimental frequency sweep is performed on the annularly excited bossed diaphragm with actuation frequency between 0 to 75 Hz and actuation voltage of 150 V, 100 V, and 50 V. The maximum deflection of the annularly excited bossed diaphragm occurs at an actuation frequency of about 43.50 Hz, as shown in Figure 4.31. Thus the frequency of 43.50 Hz corresponds to the resonance condition of the diaphragm. Further increase in the frequency of actuation resulted in a drop in the deflection range of the diaphragm. Figure 4.32 represents the variation of experimental deflection of annularly excited silicone rubber bossed diaphragm (r_l=10.00 mm) corresponding to the actuation voltage at 43.50 Hz. The deflection of the diaphragm is found to increase linearly with an increase in the actuation voltage.
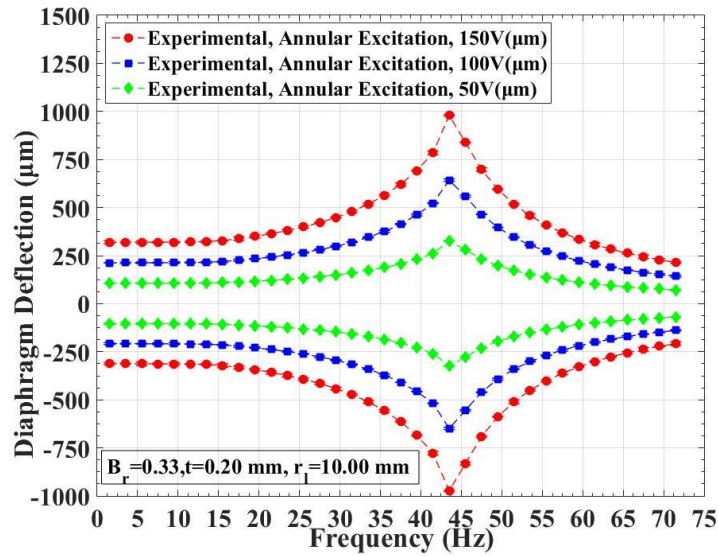
Figure 4.31 Variation of experimental deflection of the annularly excited bossed diaphragm (silicone rubber diaphragm, B_r=0.33, t=0.20 mm, r_l=10.00 mm) with the actuation frequency at 150 V, 100 V and 50 V

The maximum deflection of the annularly excited bossed diaphragm at 43.50 Hz is found to be about 980.11±4.00 μm and 973.3±4.00 μm along positive z-direction and negative z-direction, respectively. Similarly, the experimental

133

deflection at 100 V and 50 V are found to be 649.05±6.00 μm, 642.75±6.00 μm, and 326.7±3.00 μm 324.42±3.00 μm along positive z-direction and negative z-direction with actuation frequency of 43.50 Hz. The experimental results are found to agree with the simulated results where the maximum deflection occurred at 45.42 Hz with deflection of 999.2 μm, 666.1 μm and 333.1 μm along both positive and negative z directions at 150 V, 100 V and 50 V, respectively.
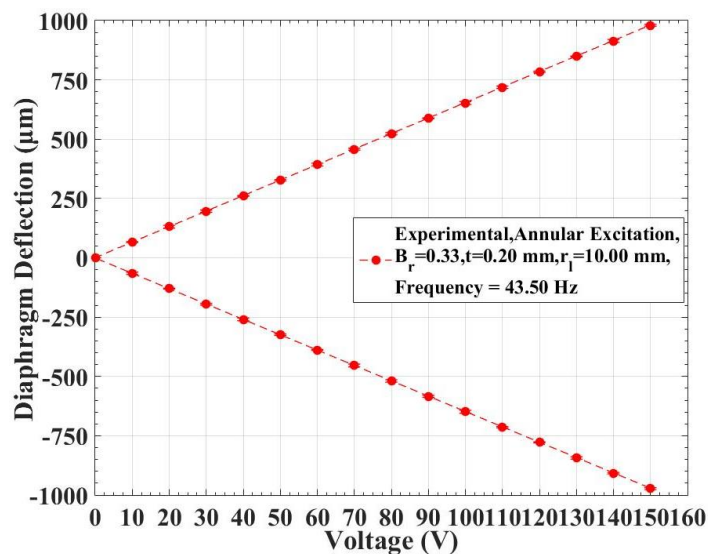
Figure 4.32 Variation of the experimental deflection of annularly excited bossed diaphragm (silicone rubber diaphragm, B_r=0.33, t=0.20 mm, r_l=10.00 mm) corresponding to the actuation voltage at 43.50 Hz

Figure 4.33 represents the variation of the peak to peak deflection of the annularly excited bossed diaphragm. Thus the net peak to peak deflection achieved with the experimental characterization of the silicone bossed diaphragm (B_r=0.33, t=0.20 mm, r_l=10.00 mm) at 43.50 Hz is about 1953.4±8.00 μm, 1291.8±12.00 μm and 651.12±6 μm at 150 V, 100 V and 50 V respectively. The experimental results are found to agree with the simulated results where the peak deflection occurred at 45.42 Hz. The corresponding peak to peak simulated deflection is found to about 1998.4 μm, 1332.2 μm and 666.13 μm at 150 V, 100 V and 50 V.
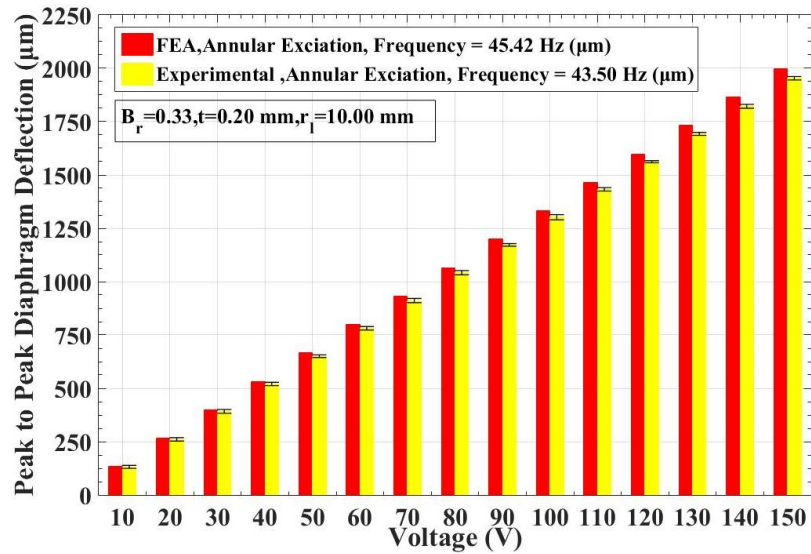
Figure 4.33 Comparison of the peak to peak experimental (43.50 Hz) and simulated (45.42 Hz) deflection of annularly excited bossed diaphragm (silicone rubber diaphragm, B_r=0.33, t=0.20 mm, r_l=10.00 mm) corresponding to the actuation voltage

4.7 Evaluation of the Performance of Proposed Valveless Disposable Chamber Micropump with Annularly Excited Bossed Diaphragm

The following section presents the experimental characterization of the proposed micropump with the annular excitation of the bossed diaphragm.

4.7.1 Optimum Chamber Depth of the Micropump Configuration with Annularly Excited Bossed Diaphragm

A similar experimental approach of centrally excited micropump is adopted for determining the optimal chamber depth for the proposed annularly excited micropump. The variation of flow characteristics of the micropump with the annularly excited configuration followed a similar trend as that of the micropump with the centrally excited configuration. Figure 4.34 (a) represents the variation of the water flow rate achieved with the annularly excited bossed diaphragm micropump with actuation frequency at 150 V with different chamber depth.
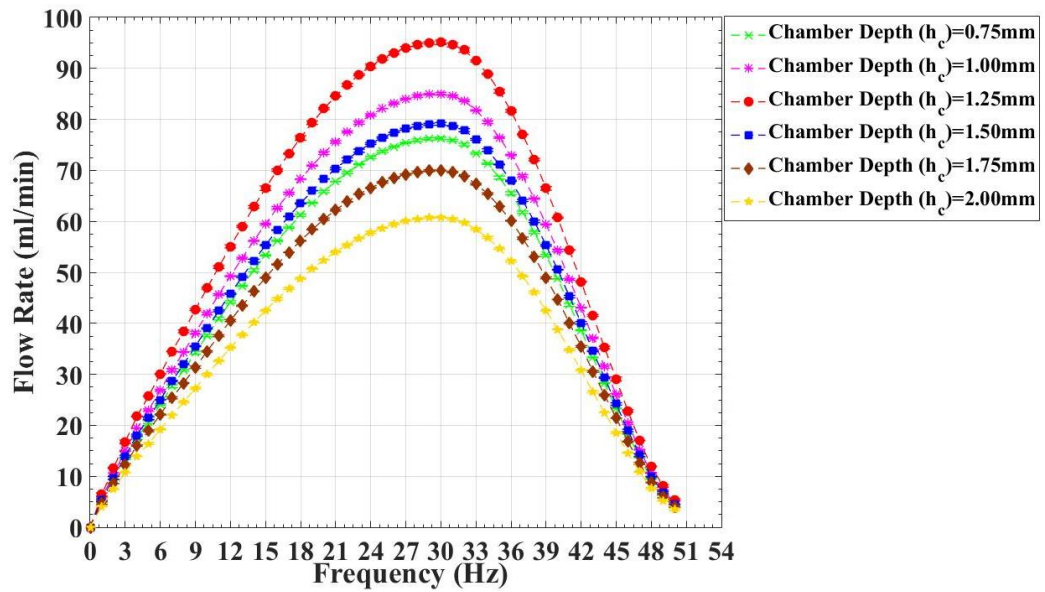
(a)
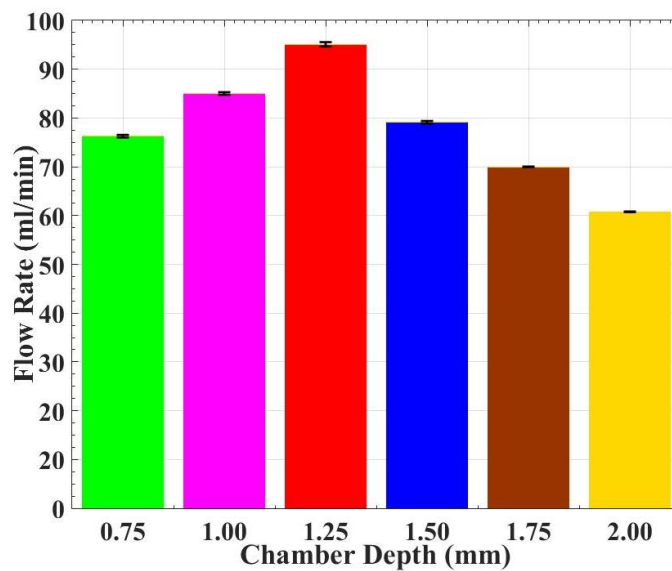
(b)

Figure 4.34 (a) Measured water flow rate corresponding to actuation frequency for different chamber depths of the annularly excited micropump (t = 0.2 mm, B_r = 0.33) **(b)** Comparison of maximum flow rate of annularly excited micropump with different chamber depths at 150 V, 30 Hz sine input (t = 0.2 mm, B_r = 0.33)

The water flow rate increases with the increase in the actuation frequency and attains peak value at 30 Hz for different chamber depth from 0.75 mm to 2.00 mm with an increment of 0.25 mm. The frequency of 30 Hz corresponds to the resonant frequency of the micropump. The peak deflection of the annularly excited bossed

diaphragm configuration occurred at 43.50 Hz. However, the damping effect of liquid in the chamber above the diaphragm surface effectively reduced the peak frequency to 30.00 Hz. In addition to the damping effect of the liquid, the influence of adhesive force also significantly contributed to reducing the peak frequency of the annularly excited bossed diaphragm when integrated with the micropump. Thus, the effect of liquid damping and the adhesive force is predominately seen in the annularly excited configuration of the proposed micropump.

Figure 4.34 (b) represents the maximum flow rate achieved with the different chamber depth corresponding to actuation parameters of 150 V, 30 Hz. The maximum flow rate of the proposed micropump with annular excitation is 76.27±0.266 ml/min with a chamber depth of 0.75 mm, which gradually increased with an increase in chamber depth up to 1.25 mm. The maximum water flow rate achieved with the chamber depth of 1.25 mm is about 95.100 ±0.444 ml/min. Further increase in the chamber depth led to a drop in the pumping rate. Flow rates of 79.12±0.266 ml/min, 69.99±0.050 ml/min and 60.77±0.071 ml/min are achieved corresponding to chamber depth of 1.50 mm, 1.75 mm, and 2.00 mm, respectively. Thus, the critical value of chamber depth for both the centrally excited configuration of the proposed micropump is 1.25 mm, which is the same as that of the centrally excited micropump.

Figure 4.35 represents the variation of water flow rate with a chamber depth of 1.25 mm under different actuation frequency at 150 V, 100 V and 50 V. The flow rate is observed to drop with the decrease in actuation voltage. This drop occurs due to the decrease in the oscillation of the diaphragm amplitude. However, the peak frequency corresponding to the maximum flow rate remained the same at 30.00 Hz. The peak flow rate at 150 V, 100 V and 50 V is about 95.100 ±0.444 ml/min, 63.432±0.444 ml/min and 31.512±0.018 ml/min, respectively, at 30 Hz. Figure 4.36 represents the variation of the flow rate of the annularly excited configuration of the proposed micropump with an actuation voltage corresponding to the chamber depth of 1.25 mm at 30 Hz. The flow rate of the micropump with the annular excitation is found to vary almost linearly with respect to actuation voltage.
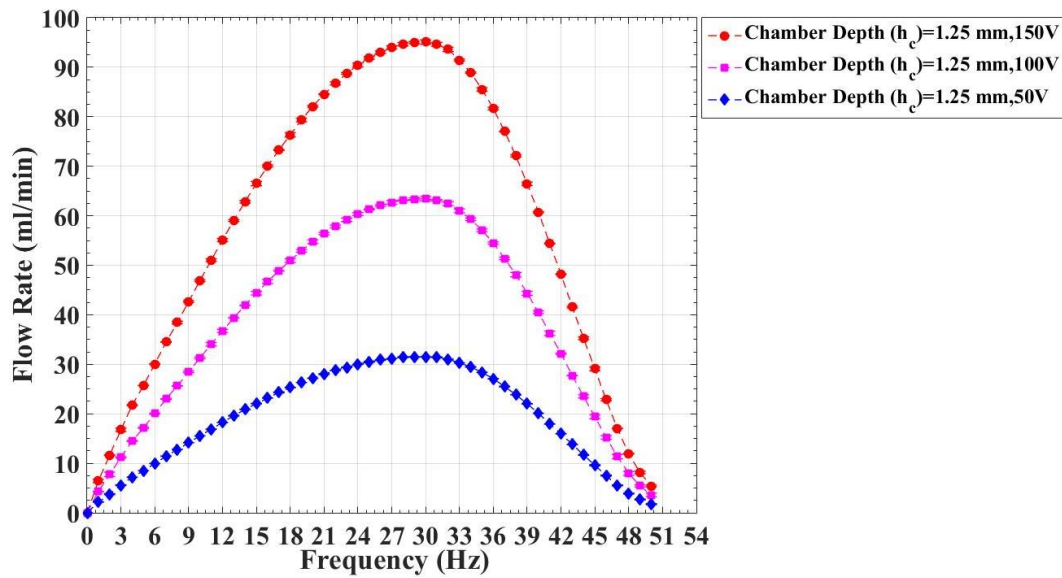
Figure 4.35 Measured water flow rate corresponding to actuation frequency at different actuation voltage of the annularly excited micropump (h_c=1.25 mm, t = 0.2 mm, B_r = 0.33, r_l =10.00 mm)
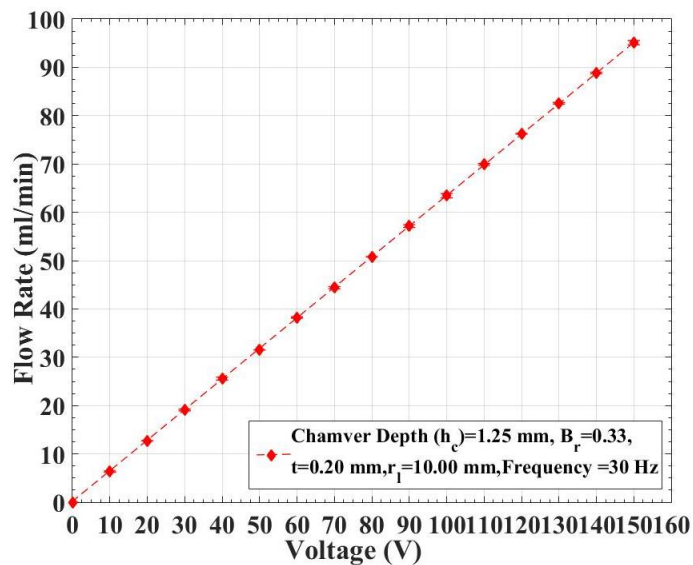
Figure 4.36 Variation of flow rate of water with annularly excited micropump (B_r = 0.33, h_c= 1.25 mm, r_l =10.00 mm) corresponding to actuation voltage at 30.00 Hz

As observed from the characterization of the proposed micropump with central excitation, the maximum backpressure occurred at frequency correspond to the

maximum flow rate. Therefore, the characterization of the annular excited micropump also considered the backpressure measurement at the frequency corresponding to peak flow rate, i.e. at 30.00 Hz. Figure 4.37 represents the variation back pressure with respect to the water flow rate of the proposed micropump with an annularly excited bossed diaphragm at 150 V, 100 V and 50 V corresponding to an actuation frequency of 30.00 Hz. From Figure 4.37, it is observed that the flow rate of water decreased with an increase in the back pressure and reached zero at maximum backpressure. The maximum backpressure is also found to decrease with a decrease in the actuation voltage (Ke at al. 2012; Singh et al. 2015). This drop is due to a reduction in the oscillation amplitude of the diaphragm. The maximum back pressure of 491 Pa, 981 Pa and 1472 Pa is achieved with the voltage of 50 V, 100 V and 150 V, respectively, at 30 Hz.
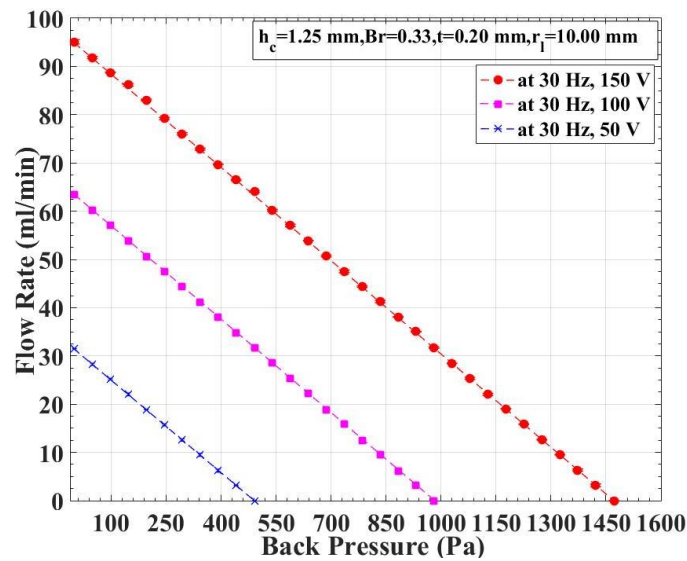
Figure 4.37 Variation of flow rate of water with annularly excited micropump corresponding to back pressure at 30.00 Hz ($B_r = 0.33$, h_c= 1.25 mm, r_l=10.00)

4.7.2 Performance of the Annularly Excited Bossed Diaphragm Micropump with Different Fluids

The study of the effect of different types of fluid on the performance of the annularly excited micropump is performed considering the same fluid property as that of the centrally excited micropump. Apart from water, other fluids which resemble the properties of blood plasma and whole blood mimicking fluid are considered.
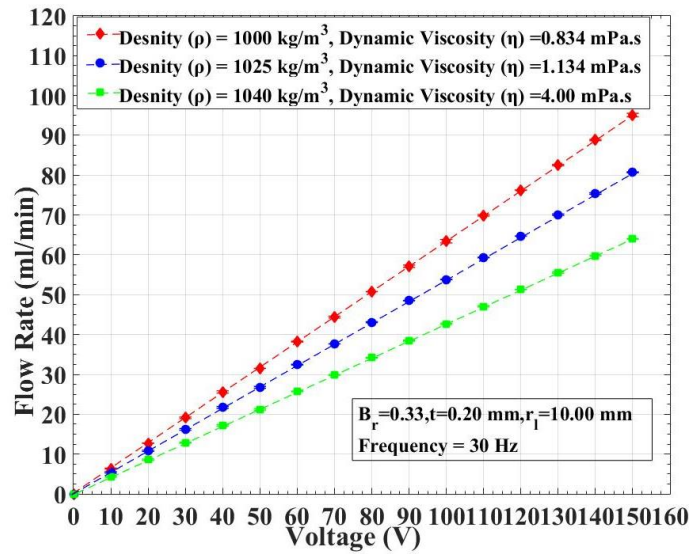
Figure 4.38 Variation of flow rate of annularly excited micropump corresponding to actuation voltage for distinct fluid density and viscosity at 30.00 Hz ($B_r = 0.33$, $h_c = 1.25$ mm, $r_l = 10.00$ mm)
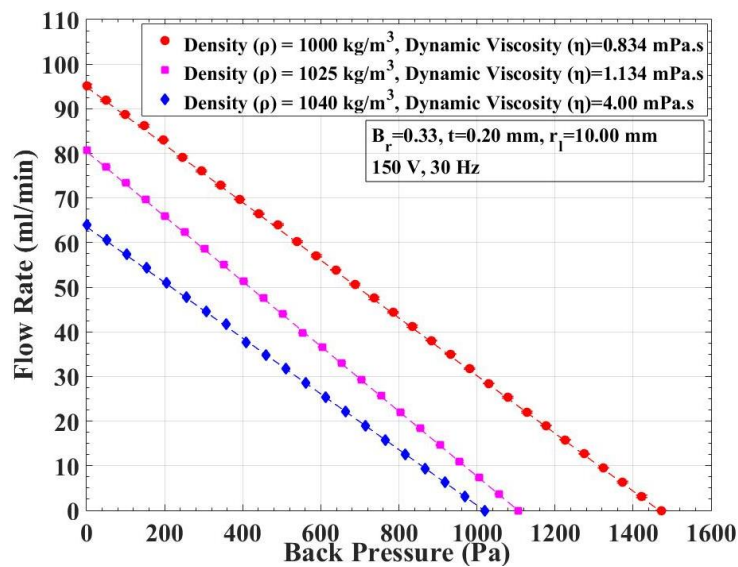
Figure 4.39 Variation of flow rate of annularly excited micropump corresponding to pressure for distinct fluid density and viscosity at 150 V, 30.00 Hz ($B_r = 0.33$, $h_c = 1.25$ mm, $r_l = 10.00$)

Figure 4.38 and Figure 4.39 represents the performance of the annularly excited bossed diaphragm configuration of micropump in terms of the flow rate and backpressure with an actuation frequency of 30 Hz. The fluid flow rate varied almost

140

linearly with respect to actuation voltage, as observed in Figure 4.38. However, the flow rate dropped with the increase in the density and viscosity of the fluid. Enhancement of the influence of adhesive force and loss of pumping energy on overcoming the increased flow resistance with increased viscosity effectively reduced the flow rate and the backpressure (Ma et al. 2015). The maximum flow rate of 95.100±0.444 ml/min, 80.719±0.135 ml/min and 64.01±0.087 ml/min are achieved with water, blood plasma and blood mimicking fluid at zero back pressure when micropump is actuated at 150 V, 30 Hz.
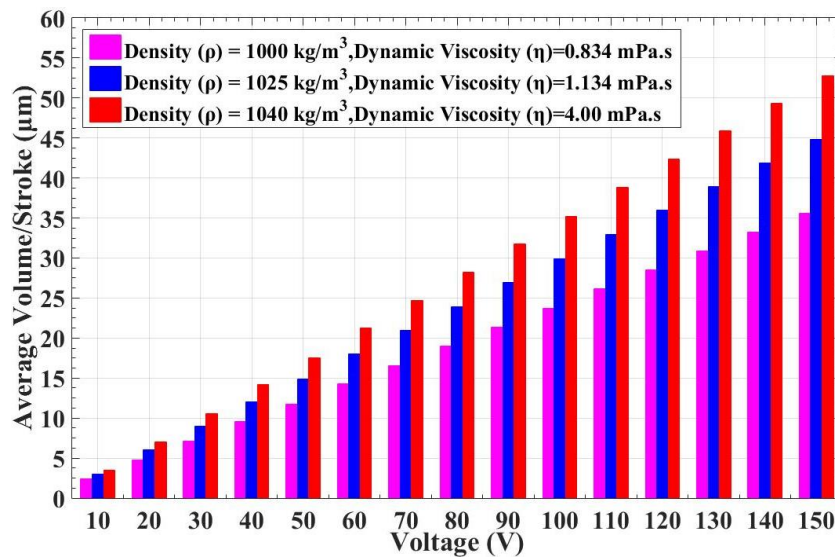
Figure 4.40 Variation flow/stroke with respect to actuation voltage of proposed micropump with annular excited bossed diaphragm at 30 Hz

The maximum backpressure corresponding to zero flow of above mentioned fluids is observed to be 1472 Pa, 1106 Pa and 1020 Pa, respectively. Thus, the annularly excited configuration of the proposed micropump delivered an effective flow rate and back pressure, which can fulfil the need for precision delivery in biomedical application. Figure 4.40 represents the variation of average volume/stroke of the proposed micropump with the annular excitation approach with respect to actuation voltage. The maximum volume/stroke of the proposed micropump is found to be 52.83 μl, 44.84 μl and 35.56 μl for water, blood plasma and blood mimicking fluid when the micropump is operated at 150V, 30 Hz. Table 4.2 and Figure 4.41

141

represent the optimal performance parameters of the proposed micropump with the annular excitation approach.

Table 4.2 Optimized performance parameters of micropump with annularly excited bossed diaphragm

Fluid Category	Driving Voltage (V)	Driving Frequency (Hz)	Flow Rate (ml/min)	Flow/ Stroke (µl)	Pressure (Pa)
Water	150	30	95.100±0.444	52.83	1472
Blood Plasma Mimicking	150	30	63.432±0.444	44.84	1106
Blood Mimicking	150	30	31.512±0.018	35.56	1020
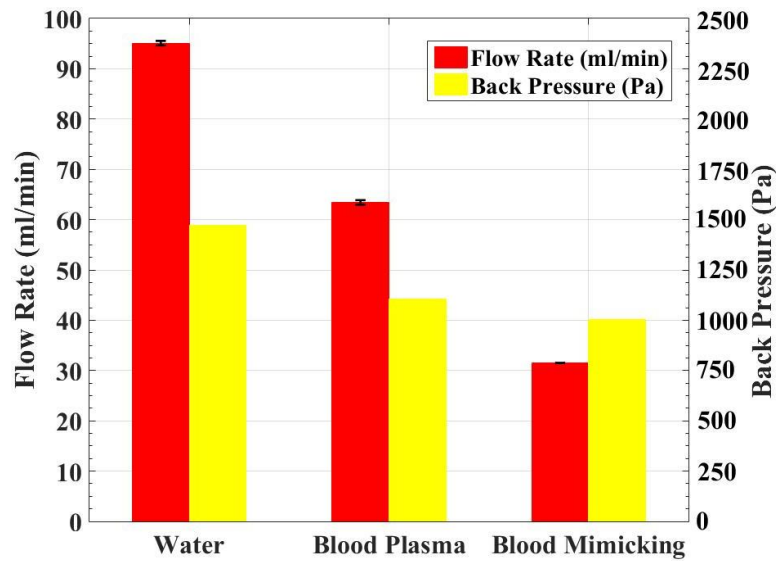
Figure 4.41 Comparison of maximum pumping rate and maximum pressure of the proposed micropump with annular excitation for different fluids at 150 V, 30 Hz. ($B_r = 0.33$, $h_c = 1.25$ mm, t = 0.2 mm, $r_l = 10.00$ mm)

4.8 Comparison of the Centrally and Annularly Excited Bossed Diaphragm and their Micropump Performance

In the following section, a comparison of the finite element analysis and experiments conducted on central and annular exited bossed diaphragm deflection is

presented. Also, the micropump performances are compared for the central and annular exited bossed diaphragm with different working fluids. The range of diaphragm deflection achieved under dynamic operating conditions is a significant factor influencing micropump performance. Thus the configuration of the diaphragm is optimized based on the factors such as bossed ratio, thickness and the young's modulus of the diaphragm material. The optimization of the diaphragm configuration is based on the criteria that the diaphragm with lower stiffness offers less resistance to deformation hence can generate a higher range of deflection. A silicone rubber diaphragm of the bossed ratio of 0.33, thickness 0.20 mm and pump chamber depth of 1.25 mm are optimized parameters estimated from the analysis and experiments used to compare results. The simulated and experimental deflection of the central and annular excited bossed diaphragm is shown in Figure 4.42.
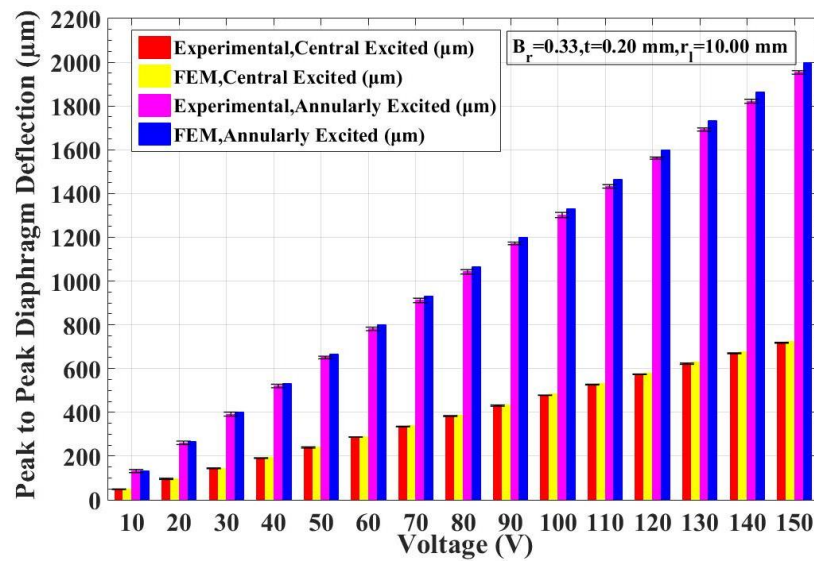
Figure 4.42 Comparison of the experimental and simulated peak to peak deflection of centrally and annularly excited bossed diaphragm (silicone rubber diaphragm, B_r=0.33, t=0.20, r_l=10.00 mm) corresponding to the actuation voltage

Since the diaphragm operates under the dynamic condition when integrated with the micropump, the dynamic characteristic is a very crucial factor to be considered. Based on the dynamic analysis of the centrally excited silicone rubber bossed diaphragm, the maximum deflection of the diaphragm achieved is about 725.91 μm when actuated at 9.96 Hz and 150 V. The experimental deflection of the

143

diaphragm similar configuration is found to agree with the simulation results with a maximum deflection of 717.99±4.00 µm at 9.50 Hz and 150 V. The central excitation approach of the diaphragm delivered a reasonable deflection range. However, to further enhance the diaphragm deflection, the annular excitation of the diaphragm is attempted. In this excitation, the diaphragm achieved maximum peak to peak deflection of 1998.4 µm at 150 V and 45.42 Hz operating frequency. The corresponding experimental peak to peak deflection is observed to be 1953.4±8.00 µm at 150 V, 43.50 Hz. From both the analysis and experiments conducted it is observed that the deflection obtained from the annularly excited bossed diaphragm increased more than 175% compared with the centrally excited diaphragm.

The comparison of simulated and experimental findings of maximum deflection of the central and annular excited bossed diaphragm is presented in Table 4.3. From the table, it can be observed that the simulated and the experimental peak deflection of the annularly excited bossed diaphragm occurred at 45.52 Hz and 43.50 Hz, whereas in the centrally excited bossed diaphragm, peak deflection occurred at 9.96 Hz and 9.50 Hz, respectively. It can be seen that there is an increase in the frequency corresponding to peak deflection of the annularly excited bossed diaphragm. This increase in frequency is almost five times compared to the centrally excited bossed diaphragm and may be due to an increase in the effective stiffness compared to the centrally excited diaphragm. However, this increase in frequency is advantageous in increasing the frequency response of the micropump.

Further, the micropump performances are compared for the central and annular exited bossed diaphragm with different working fluids. The working fluids considered are water, blood plasma mimicking and whole blood mimicking fluid. The flow rate and back pressure of the micropump for central and annular excited bossed diaphragm with different working fluids are compared and presented in Table 4.3. The micropump with the central excited diaphragm effectively pumped water with the maximum flow rate and back pressure of 7.192 ± 0.147 ml/min and 294 Pa at 150 V and 5 Hz. Though peak deflection of the centrally excited diaphragm occurred at 9.50

Hz, the frequency corresponding to the maximum flow rate dropped to 5 Hz due to the influence of adhesive force and damping effect.

Table 4.3 Comparison of the maximum deflection of the bossed diaphragm with central and annular excitation

Type	Centrally Excited	Annularly Excited		
Deflection		Along +Z direction	Along –Z direction	Peak to Peak Deflection
Simulated	725.91 µm at 9.96 Hz, 150 V	999.2 µm at 45.52 Hz, 150 V	999.2 µm at 45.52 Hz, 150 V	1998.4 µm at 45.52 Hz, 150 V
Experimental	721.99±2 µm at 9.5 Hz, 150 V	980.11±4.00 µm at 43.50 Hz, 150 V	973.3±4.00 µm at 43.50 Hz, 150 V	1953.4±8.00 µm at 43.50 Hz, 150 V

The density and viscosity of the liquid also influenced the performance of the micropump. The flow rate and back pressure of the centrally excited micropump dropped to 6.108±0.047 ml/min, 226.243 Pa and 5.013±0.138 ml/min, 204.048 Pa at 150 V and 5 Hz respectively, for blood plasma mimicking and whole blood mimicking fluid. The flow rate decreased by about 15% and 30% for blood plasma and blood mimicking fluid during the operation of the centrally excited micropump. The corresponding drop in backpressure is observed to be 23% and 31% for blood plasma and blood mimicking fluid compared with water.

The annularly excited diaphragm micropump enhanced the flow rate and back pressure when compared with the centrally excited diaphragm micropump as shown in Figure 4.43. The maximum water flow rate and back pressure are found to be 95.100±0.444 ml/min and 1472 Pa, respectively, at 150 V and 30 Hz. The maximum flow rate of the micropump with an annular excited micropump occurred at 30 Hz, which is less when compared with the frequency value of 43.50 Hz corresponding to the maximum deflection. The influence of damping effect and adhesive force is highly evident in annularly exciting configuration. With blood plasma mimicking and whole blood mimicking fluid, the annularly exciting

configuration of the micropump delivered maximum flow rate and back pressure of 63.432±0.444 ml/min, 1106 Pa and 31.512±0.018ml/min,1020 Pa respectively at 150 V and 30 Hz. Table 4.4 consolidates and compares the maximum flow rate and back pressure of the proposed micropump with central and annular excitation.
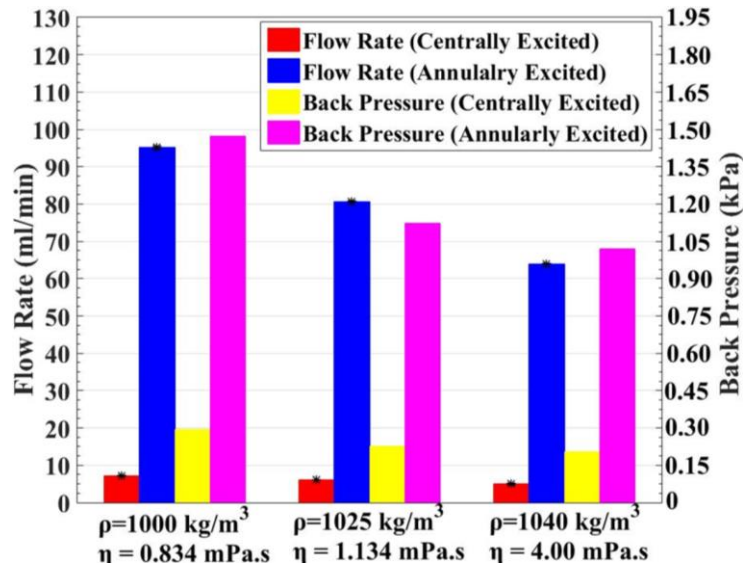
Figure 4.43 Comparison of the maximum flow rate and back pressure developed by proposed micropump with central excitation (f = 5.00 Hz) and annular excitation (f = 30.00 Hz) at 150 V working under fluids of different density and viscosity

Table 4.4 Comparison of the maximum flow rate of micropump with central excitation (at 150 V, 5Hz) and annular excitation (at 150 V, 30 Hz)

Type	Water	Blood Plasma Mimicking Fluid	Blood Mimicking Fluid
Flow Rate (ml/min)			
Central Excitation	7.192±0.146	6.108±0.047	5.013±0.138
Annular Excitation	95.100±0.444	63.432±0.444	31.512±0.018
Back Pressure (Pa)			
Central Excitation	294.00	226.243	204.048
Annular Excitation	1472.00	1106.00	1020.00

The maximum flow rate of blood plasma mimicking and whole blood mimicking fluid with annular excitation dropped by almost 33% and 67% when compared to water. At the same time, the drop in the backpressure developed by the annularly excited configuration is observed to be 24 % and 30% for blood plasma mimicking and whole blood mimicking fluids compared to water.

One of the observable facts from here is that the drop in the flow rate of the micropump with central excitation for blood plasma mimicking and whole blood mimicking fluids are almost 15% and 30%, which is less when compared with the annularly exciting configuration. The percentage drop in the flow rate of the blood plasma and blood mimicking fluid of the annularly excited diaphragm is due to the enhanced effect of adhesive force due to increased viscosity of the fluid. However, there is no observable drop in the back pressure developed by the annularly exciting configuration of the micropump.
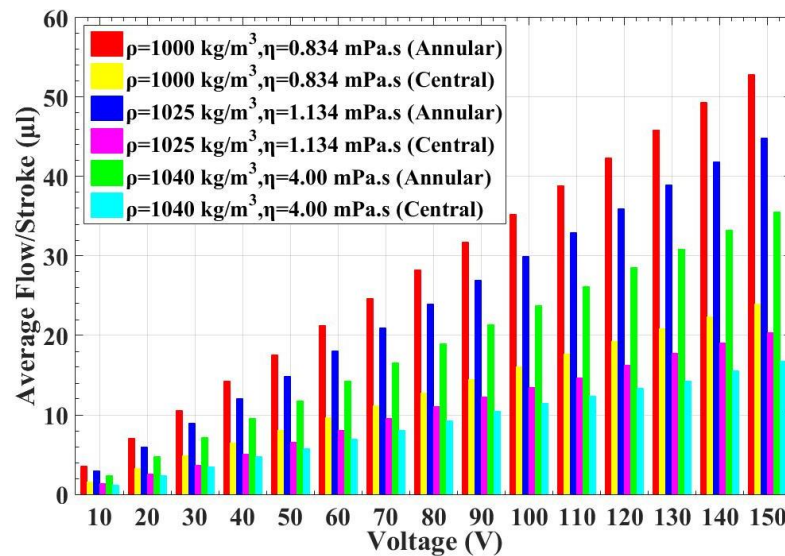
Figure 4.44 Comparison of the average flow per stroke of the with respect to actuation voltage for proposed micropump with central excitation and annular excitation working under fluids of different density and viscosity

Comparing the flow performance of the proposed micropump configurations, the micropump with the annular excited diaphragm improved the flow rate by thirteen times with water, ten times increase in the flow rate of blood plasma mimicking fluid,

and six times increase in the flow rate of the whole blood mimicking fluid. At the same time, the backpressure improved by five times when compared to the central exciting diaphragm micropump. Figure 4.44 represents the comparison of the volume resolution of the proposed micropumps. The annular exciting configuration effectively enhanced the volume resolution of the micropump as well. The maximum average volume/stroke of the annularly exciting configuration of the micropump is about 52.83 μl, 44.84 μl, 35.56 μl with water, blood plasma mimicking and whole blood mimicking fluids, respectively, which is superior when compared with the average volume/stroke of the centrally exciting configuration of the micropump with the values 23.97 μl, 20.35 μl, 16.70 μl in the same order. Thus, the annularly exciting configuration of the proposed disposable chamber micropump effectively enhanced the performance and can be effectively implemented in biomedical applications.

CONCLUSIONS

There is a growing need for precision pumping systems in microfluidic applications. Therefore, an attempt is made to develop a novel valveless micropump powered through Amplified Piezo Actuator (APA). The proposed micropump comprises a unique feature of a disposable pump chamber with the bossed diaphragm. The disposable chamber of the micropump justifies its application in the biomedical field. The micropump is actuated through an actuation mechanism consisting of the amplified piezoelectric actuator, which can retrofit into the micropump chamber and reused. The pumping of fluid occurs through the oscillation of the bossed diaphragm integrated with the micropump chamber. The proposed micropump is fabricated using polymeric materials such as Polymethylmethacrylate (PMMA), silicone rubber through CNC milling, laser cutting, and moulding processes.

The oscillating member of the proposed valveless micropump constituted a bossed diaphragm attached to the disposable micropump chamber. The present work proposes two methods of excitation of the bossed diaphragm, namely central and annular excitation. An appropriate theoretical, finite element analysis and experimental approach are adopted to understand the deflection behaviour of the bossed diaphragm under both central and annular excitation. Further, the experimental characterization of the micropump is carried out to assess the performance of the micropump with the central and annular excitation. A comparative study is carried out to determine the performance enhancement of the micropump through the annular excitation approach over the central excitation approach. The micropump performances are compared with different working fluids such as water, blood plasma mimicking and whole blood mimicking fluid.

The performance of the bossed diaphragm in terms of deflection is significantly influenced by the factors such as thickness, bossed ratio, material, and excitation method. An increase in the thickness (t), bossed ratio (B_r), young's modulus (E) lead to an increase in the effective stiffness of the centrally excited bossed diaphragm, leading to lower diaphragm deflection. Based on the finite element

150

analysis and the experimental characterization, the optimal performance is achieved with the silicone rubber diaphragm of the bossed ratio of 0.33 and thickness of 0.2 mm. The maximum deflection of the centrally excited bossed diaphragm occurred at a frequency close to the first modal frequency. The maximum deflection achieved with the optimized configuration of the centrally excited bossed diaphragm is about 717.99±4.00 µm at 9.50 Hz, 150 V, which is in close agreement with simulated deflection of 725.91 µm at 150 V, 9.96 Hz.

The lower value of the chamber depth influenced the returning of the diaphragm during the suction stroke due to the enhanced effect of adhesive force, which degraded the flow performance. The higher value of chamber depth resulted in a lower fluid compression, which brings down the pumping rate. The optimal value of chamber depth is found to be 1.25 mm, which delivered the maximum flow rate. An increase in the fluid viscosity led to an increase in the adhesive force on the diaphragm surface, leading to a reduction in flow performance. The maximum flow rate of water, fluid mimicking blood plasma and whole blood mimicking fluid with central excitation approach is found to be 7.192 ± 0.147 ml/min, 6.108 ± 0.047 ml/min, 5.013 ± 0.138 ml/min respectively when actuated with 150 V, 5 Hz sinusoidal input. The corresponding backpressure achieved is about 294.00 Pa, 226.243 Pa, and 204.048 Pa. Reduction of about 15 % and 30 % is observed in the pumping rate of blood plasma and blood mimicking fluid when compared with water. Correspondingly, the backpressure dropped by about 23% and 31%.

Further, the annular excitation approach effectively enhanced the deflection range of the bossed diaphragm when compared to the central excitation. In addition, the annular excitation approach is also instrumental in enhancing the frequency range of the diaphragm corresponding to maximum deflection. The annularly excited diaphragm delivered a maximum peak to peak deflection of about 1953.4±4.00 µm at 150 V, 43.5 Hz. The results obtained from the experimental characterisation of the diaphragm also agree with the finite element analysis results with deflection of 1998.4 µm at 150 V, 45.5 Hz. Thus, there is almost 175 % enhancement in deflection range with annular excitation when compared to central excitation.

The broader range of diaphragm deflection achieved with annular excitation effectively enhanced the performance of the proposed valveless micropump. The maximum flow rate of 95.10±0.444 ml/min and backpressure of 1472 Pa at 150, 30 Hz is achieved with the annularly excited micropump with water as the working fluid. Similarly, with blood plasma mimicking and whole blood mimicking fluid, the annularly excited micropump delivered maximum flow rate and back pressure of 63.432±0.444 ml/min, 1106 Pa and 31.512±0.018ml/min,1020 Pa respectively at 150 V, 30 Hz. The proposed micropump with annular excitation delivered almost thirteen times more flow rate and five times more backpressure when compared with the micropump of central excitation with water as the working fluid. Further, the annularly excited micropump is capable of delivering almost ten times more flow rate with blood plasma mimicking fluid and six times more flow rate with whole blood mimicking fluid when compared to central excitation configuration. There is almost five times increase in the backpressure of the annular excited micropump with blood plasma and blood mimicking fluid compared to central excitation. Thus, the annular excitation of the bossed diaphragm effectively justifies the enhancement in the performance of the proposed disposable chamber valveless micropump.

The work elucidates the virtue of using an annular excited bossed diaphragm in micropump applications. The arrangement of the bossed diaphragm with the disposable chamber gives an insight into using these micropumps in biomedical applications. The improvement in the performance of the micropump with annular excitation is brought out explicitly in this investigation.

REFERENCE

Aggarwal, S., Paul, B. E., DasGupta, A., and Chatterjee, D. (2017). "Experimental characterization of piezoelectrically actuated micromachined silicon valveless micropump." Microfluid. Nanofluidics, 21(1), 1–11.

Ai, W., and Xu, Q. (2014). "New structural design of a compliant gripper based on the Scott-Russell mechanism." Int. J. Adv. Robot. Syst., 11.

Aksel, E., and Jones, J. L. (2010). "Advances in lead-free piezoelectric materials for sensors and actuators." Sensors, 10(3), 1935–1954.

Ali, A., Pasha, R. A., Elahi, H., Sheeraz, M. A., Bibi, S., Hassan, Z. U., Eugeni, M., and Gaudenzi, P. (2019). "Investigation of Deformation in Bimorph Piezoelectric Actuator: Analytical, Numerical and Experimental Approach." Integr. Ferroelectr., 201(1), 94–109.

Almeida, A., Andrews, G., Jaiswal, D., and Hoshino, K. (2019). "The actuation mechanism of 3D printed flexure-based robotic microtweezers." Micromachines, 10(7).

Ashraf, M. W., Afzulpurkar, N., Nisar, A., and Tayyaba, S. (2012). "Fabrication and analysis of hollow microneedles and polymeric piezoelectric valveless micropump for transdermal drug-delivery system." IET Commun., 6(18), 3248–3256.

Ashraf, M. W., Tayyaba, S., and Afzulpurkar, N. (2011). "Micro Electromechanical Systems (MEMS) based microfluidic devices for biomedical applications." Int. J. Mol. Sci., 12(6), 3648–3704.

Au, A. K., Lai, H., Utela, B. R., and Folch, A. (2011). Microvalves and micropumps for BioMEMS. Micromachines.

Azizollah Ganji, B., Babaei Sedaghat, S., Roncaglia, A., and Belsito, L. (2018). "Design and fabrication of high performance condenser microphone using C-slotted diaphragm." Microsyst. Technol., 24(7), 3133–3140.

Bakhtiari-Shahri, M., and Moeenfard, H. (2019). "Energy harvesting from unimorph piezoelectric circular plates under random acoustic and base acceleration excitations." Mech. Syst. Signal Process., 130, 502–523.

Bakhtiari-Shahri, M., and Moeenfard, H. (2019). "Energy harvesting from unimorph piezoelectric circular plates under random acoustic and base acceleration excitations." Mech. Syst. Signal Process., 130, 502–523.

Benard, W. L., Kahn, H., Heuer, A. H., and Huff, M. A. (1997). "Titanium-nickel shape-memory alloy actuated micropump." Int. Conf. Solid-State Sensors Actuators, Proc., 1, 361–364.

Bodén, R., Hjort, K., Schweitz, J. Å., and Simu, U. (2008). "A metallic micropump for high-pressure microfluidics." J. Micromechanics Microengineering, 18(11).

Bodén, R., Ogden, S., and Hjort, K. (2014). "Microdispenser with continuous flow and selectable target volume for microfluidic high-pressure applications." J. Microelectromechanical Syst., 23(2), 452–458.

Bonhoeffer, B., Boldrini, M., Boiger, G., Kwade, A., and Juhnke, M. (2017). "Experimental Characterization and Simulation of a Piezo-Actuated Micro Dispensing Valve." J. Fluids Eng. Trans. ASME, 139(5), 1–9.

Bu, Z., Lin, S., Huang, X., Li, A., Wu, D., Zhao, Y., Luo, Z., and Wang, L. (2018). "A novel piezostack-driven jetting dispenser with corner-filleted flexure hinge and high-frequency performance." J. Micromechanics Microengineering, 28(7).

Chang, H. T., Lee, C. Y., and Wen, C. Y. (2007). "Design and modeling of electromagnetic actuator in mems-based valveless impedance pump." Microsyst. Technol., 13(11–12), 1615–1622.

Chang, Y. J., Chung, Y. W., Chou, T. A., and Huang, M. F. (2013). "Valve-less diaphragm micropump with electromagnetic actuation." Adv. Mater. Res., 647, 929–934.

Chee, P. S., Mah, C. K., and Ali, M. S. M. (2016). "Soft dielectric elastomer actuator for micropump application." Proc. IEEE Int. Conf. Micro Electro Mech. Syst., 2016-Febru(January), 561–564.

Chee, P. S., Minjal, M. N., Leow, P. L., and Ali, M. S. M. (2015). "Wireless powered thermo-pneumatic micropump using frequency-controlled heater." Sensors Actuators, A Phys., 233, 1–8.

Chen, F., Du, Z. jiang, Yang, M., Gao, F., Dong, W., and Zhang, D. (2018). "Design and analysis of a three-dimensional bridge-type mechanism based on the stiffness distribution." Precis. Eng., 51, 48–58.

Chen, N., and Yan, P. (2020). "Dynamic modeling and validation of a novel 3-DOF flexible thin sheet nano-manipulator with piezoelectric material bonded." Smart Mater. Struct., 29(4).

Cheng, C. H., Yang, A. S., Lin, C. J., and Huang, W. J. (2017). "Characteristic studies of a novel piezoelectric impedance micropump." Microsyst. Technol., 23(6), 1709–1717.

Cheng, C. H., Yang, A. S., Lin, C. J., and Huang, W. J. (2017). "Characteristic studies of a novel piezoelectric impedance micropump." Microsyst. Technol., 23(6), 1709–1717.

Choi, A., Vatanabe, S. L., Lima, C. R. De, and Silva, E. C. N. (2012). "Computational and experimental characterization of a low-cost piezoelectric valveless diaphragm pump." J. Intell. Mater. Syst. Struct., 23(1), 53–63.

Choi, J., Qiu, Z., Rhee, C. H., Wang, T., and Oldham, K. (2014). "A three-degree-of-freedom thin-film PZT-actuated microactuator with large out-of-plane displacement." J. Micromechanics Microengineering, 24(7).

Choi, S. B., Seong, M. S., Ha, S. H., Jeon, J., and Sohn, J. W. (2011). "Design of a piezostack-based inertial actuator and application to vibration control: Experimental investigation." Proc. Inst. Mech. Eng. Part I J. Syst. Control Eng., 225(8), 1115–1124.

Chung, H. C., Kummari, K. L., Croucher, S. J., Lawson, N. J., Guo, S., Whatmore, R. W., and Huang, Z. (2009). "Development of piezoelectric fans for flapping wing application." Sensors Actuators, A Phys., 149(1), 136–142.

Clemens, A. H. (1980). "Programmable open-loop micropump insulin delivery system." Diabetes Care, 3(2), 359–361.

Conrad, H., Schenk, H., Kaiser, B., Langa, S., Gaudet, M., Schimmanz, K., Stolz, M., and Lenz, M. (2015). "A small-gap electrostatic micro-actuator for large deflections." Nat. Commun., 6, 1–7.

Darabi, J., and Ekula, K. (2003). "Development of a chip-integrated micro cooling device." Microelectronics J., 34(11), 1067–1074.

Dash, A. K., and Cudworth, G. C. (1998). "Therapeutic applications of implantable drug delivery systems." J. Pharmacol. Toxicol. Methods, 40(1), 1–12.

Dau, V. T., Dinh, T. X., and Sugiyama, S. (2009). "A MEMS-based silicon micropump with intersecting channels and integrated hotwires." J. Micromechanics Microengineering, 19(12).

Ding, Y., and Lai, L. J. (2019). "Design and analysis of a displacement amplifier with high load capacity by combining bridge-type and Scott-Russell mechanisms." Rev. Sci. Instrum., 90(6).

DONG, S. (2012). "Review on Piezoelectric, Ultrasonic, and Magnetoelectric Actuators." J. Adv. Dielectr., 02(01), 1230001.

Dsouza, R. D., Navin, K. P., Theodoridis, T., and Sharma, P. (2018). "Design, fabrication and testing of a 2 DOF compliant flexural microgripper." Microsyst. Technol., 24(9), 3867–3883.

Dugue, F., Roux, F., Bonafos, B., Billard, J. Y., Fruman, D. H., and Gibek, I. (2001). "Development of a micropump for hydrazine propulsion systems." 37th Jt. Propuls. Conf. Exhib., (July).

E. Paul Braineard, Enoch Amoatey Tetteh, J. S. J. K. (2014). "A Study of Why Electrostatic Actuation is Preferred and a Simulation of an Electrostatically Actuated

Cantilever Beam for MEMS Applications." Int. J. Eng. Sci. Emerg. Technol., 6(5), 441–446.

El-Sayed, A. M., Abo-Ismail, A., El-Melegy, M. T., Azah Hamzaid, N., and Abu Osman, N. A. (2013). "Development of a micro-gripper using piezoelectric bimorphs." Sensors (Switzerland), 13(5), 5826–5840.

Fu, Y., Du, H., Huang, W., Zhang, S., and Hu, M. (2004). "TiNi-based thin films in MEMS applications: A review." Sensors Actuators, A Phys., 112(2–3), 395–408.

Garimella, S. V., Singhal, V., and Liu, D. (2006). "On-chip thermal management with microchannel heat sinks and integrated micropumps." Proc. IEEE, 94(8), 1534–1548.

Ghosh, B., Jain, R. K., Majumder, S., Roy, S. S., and Mukhopadhyay, S. (2017). "Experimental characterizations of bimorph piezoelectric actuator for robotic assembly." J. Intell. Mater. Syst. Struct., 28(15), 2095–2109.

Gidde, R. R., Pawar, P. M., Ronge, B. P., and Dhamgaye, V. P. (2019). "Design optimization of an electromagnetic actuation based valveless micropump for drug delivery application." Microsyst. Technol., 25(2), 509–519.

Guan, Y., Shen, M., and Han, L. (2012). "Simulations and experiment analysis of a piezoelectric micropump." Appl. Mech. Mater., 229–231, 1688–1692.

Gunda, A., Özkayar, G., Tichem, M., and Ghatkesar, M. K. (2020). "Proportional microvalve using a unimorph piezoelectric microactuator." Micromachines, 11(2).

Guo, L., Yan, W., Xu, Y., and Chen, Y. (2012). "Valveless piezoelectric micropump of parallel double chambers." Int. J. Precis. Eng. Manuf., 13(5), 771–776.

Guo, S., and Asaka, K. (2003). "Polymer-based new type of micropump for bio-medical application." Proc. - IEEE Int. Conf. Robot. Autom., 2, 1830–1835.

Guo, S., Sun, X., Ishii, K., and Guo, J. (2008). "SMA actuator-based novel type of peristaltic micropump." Proc. 2008 IEEE Int. Conf. Inf. Autom. ICIA 2008, 1620–1625.

Ha, S. M., Cho, W., and Ahn, Y. (2009). "Disposable thermo-pneumatic micropump for bio lab-on-a-chip application." Microelectron. Eng., 86(4–6), 1337–1339.

Hall, A. J., and Riddick, J. C. (2012). "Micro-electro-mechanical flapping wing technology for micro air vehicles." Bioinspiration, Biomimetics, Bioreplication 2012, 8339, 83390L.

Ham, Y. B., Seo, W. S., Cho, W. Y., Yun, D. W., Park, J. H., and Yun, S. N. (2009). "Development of a piezoelectric pump using hinge-lever amplification mechanism." J. Electroceramics, 23(2–4), 346–350.

Heverly, D. E., Wang, K. W., and Smith, E. C. (2004). "Dual-stack piezoelectric device with bidirectional actuation and improved performance." J. Intell. Mater. Syst. Struct., 15(7), 565–574.

Heverly, D. E., Wang, K. W., and Smith, E. C. (2004). "Dual-stack piezoelectric device with bidirectional actuation and improved performance." J. Intell. Mater. Syst. Struct., 15(7), 565–574.

Hwang, H. S., Nasser, J., and Sodano, H. A. (2019). "Piezoelectric Stack Actuator for Measurement of Interfacial Shear Strength at High Strain Rates." Exp. Mech., 59(7), 979–990.

Hwang, I. H., Lee, S. K., Shin, S. M., Lee, Y. G., and Lee, J. H. (2008). "Flow characterization of valveless micropump using driving equivalent moment: Theory and experiments." Microfluid. Nanofluidics, 5(6), 795–807.

Hwang, J. Y., Shin, K. Y., Lee, S. H., Kang, K., Kang, H., Lee, J. H., Peck, D. H., Jung, D. H., and Jang, J. H. (2010). "Periodic fuel supply to a micro-DMFC using a piezoelectric linear actuator." J. Micromechanics Microengineering, 20(8), 0–7.

Iverson, B. D., and Garimella, S. V. (2008). "Recent advances in microscale pumping technologies: A review and evaluation." Microfluid. Nanofluidics, 5(2), 145–174.

Iverson, B. D., and Garimella, S. V. (2008). "Recent advances in microscale pumping technologies: A review and evaluation." Microfluid. Nanofluidics, 5(2), 145–174.

Jain, R. K., Majumder, S., Ghosh, B., and Saha, S. (2015). "Design and manufacturing of mobile micro manipulation system with a compliant piezoelectric actuator based micro gripper." J. Manuf. Syst., 35, 76–91.

Jang, D. D., Jung, H. J., Shin, Y. H., Moon, S. J., Moon, Y. J., and Oh, J. (2012). "Feasibility study on a hybrid mount system with air springs and piezo-stack actuators for microvibration control." J. Intell. Mater. Syst. Struct., 23(5), 515–526.

Jeon, J., Han, C., Han, Y. M., and Choi, S. B. (2014). "A new type of a direct-drive valve system driven by a piezostack actuator and sliding spool." Smart Mater. Struct., 23(7).

Jeong, S. J., Lim, D. H., Saleem, M., Koo, B. G., and Kim, M. S. (2018). "Properties of CuAg/(BiNaSr)TiO3 multilayer ceramic actuator." Ceram. Int., 44(1), S112–S116.

Jiang, S., and Cheng, L. (2017). "Modeling and design of a pre-stressed piezoelectric stack actuator." AIP Adv., 7(7).

Jiang, S., and Cheng, L. (2017). "Modeling and design of a pre-stressed piezoelectric stack actuator." AIP Adv., 7(7).

Judy, J. W., Tamagawa, T., and Polla, D. L. (1991). "Surface-machined micromechanical membrane pump." Proceedings. IEEE Micro Electro Mech. Syst., 182–186.

Kang, L. H., and Han, J. H. (2010). "Prediction of actuation displacement and the force of a pre-stressed piezoelectric unimorph (PUMPS) considering nonlinear piezoelectric coefficient and elastic modulus." Smart Mater. Struct., 19(9).

Kang, L. H., and Han, J. H. (2010). "Prediction of actuation displacement and the force of a pre-stressed piezoelectric unimorph (PUMPS) considering nonlinear piezoelectric coefficient and elastic modulus." Smart Mater. Struct., 19(9).

Kant, R., Singh, D., and Bhattacharya, S. (2017). "Digitally controlled portable micropump for transport of live micro-organisms." Sensors Actuators, A Phys., 265, 138–151.

160

Karpelson, M., Wei, G. Y., and Wood, R. J. (2012). "Driving high voltage piezoelectric actuators in microrobotic applications." Sensors Actuators, A Phys., 176, 78–89.

Karpienko, K., Gnyba, M., Milewska, D., Wróbel, M. S., and Jędrzejewska-Szczerska, M. (2016). "Blood equivalent phantom vs whole human blood, a comparative study." J. Innov. Opt. Health Sci., 9(2), 1–9.

Ke, M. T., Zhong, J. H., and Lee, C. Y. (2012). "Electromagnetically-actuated reciprocating pump for high-flow-rate microfluidic applications." Sensors (Switzerland), 12(10), 13075–13087.

Kim, B. J., and Meng, E. (2015). "Review of polymer MEMS micromachining." J. Micromechanics Microengineering, 26(1).

Kim, H. H., Park, D. H., Ryu, B. H., and Lim, K. J. (2009). "Design and modeling of piezoelectric pump for microfluid devices." Ferroelectrics, 378(1 PART 1), 92–100.

Kim, H., Astle, A. A., Najafi, K., Bernal, L. P., and Washabaugh, P. D. (2015). "An integrated electrostatic peristaltic 18-stage gas micropump with active microvalves." J. Microelectromechanical Syst., 24(1), 192–206.

Kim, J. H., Na, K. H., Kang, C. J., and Kim, Y. S. (2005). "A disposable thermopneumatic-actuated micropump stacked with PDMS layers and ITO-coated glass." Sensors Actuators, A Phys., 120(2), 365–369.

Krpoun, R., and Shea, H. R. (2009). "Integrated out-of-plane nanoelectrospray thruster arrays for spacecraft propulsion." J. Micromechanics Microengineering, 19(4).

Kumar, N., George, D., Sajeesh, P., Manivannan, P. V., and Sen, A. K. (2016). "Development of a solenoid actuated planar valveless micropump with single and multiple inlet-outlet arrangements." J. Micromechanics Microengineering, 26(7).

Lai, L. J., and Zhu, Z. N. (2017). "Design, modeling and testing of a novel flexure-based displacement amplification mechanism." Sensors Actuators, A Phys., 266, 122–129.

Laser, D. J., and Santiago, J. G. (2004). "A review of micropumps." J. Micromechanics Microengineering, 14(6).

Laser, D. J., and Santiago, J. G. (2004). "A review of micropumps." J. Micromechanics Microengineering, 14(6).

Le, T., Borazjani, I., and Sotiropoulos, F. (2009). "A Computational Fluid Dynamic (CFD) Tool for Optimization and Guided Implantation of Biomedical Devices." J. Med. Device., 3(2), 27553.

Lee, C. Y., Chang, H. T., and Wen, C. Y. (2008). "A MEMS-based valveless impedance pump utilizing electromagnetic actuation." J. Micromechanics Microengineering, 18(3).

Lee, D. O., Kang, L. H., and Han, J. H. (2011). "Active vibration isolation demonstration system using the piezoelectric unimorph with mechanically pre-stressed substrate." J. Intell. Mater. Syst. Struct., 22(13), 1399–1409.

Lee, K. S., Kim, B., and Shannon, M. A. (2013). "Development of a peristaltic gas micropump with a single chamber and multiple electrodes." J. Micromechanics Microengineering, 23(9).

Lee, S., Yee, S. Y., Besharatian, A., Kim, H., Bernal, L. P., and Najafi, K. (2009). "Adaptive gas pumping by controlled timing of active microvalves in peristaltic micropumps." TRANSDUCERS 2009 - 15th Int. Conf. Solid-State Sensors, Actuators Microsystems, 2294–2297.

Lei, K. F. (2012). "Microfluidic systems for diagnostic applications: A review." J. Lab. Autom., 17(5), 330–347.

Letty, R. Le, Sosnicki, O., Barillot, F., and Claeysssen, F. (2005). "Actuators in Adaptronics : Piezoelectric Actuators." Conf. Smart Struct. Mater., (January 2005), 18–21.

Letty, R. Le, Sosnicki, O., Barillot, F., and Claeysssen, F. (2005). "Actuators in Adaptronics : Piezoelectric Actuators." Conf. Smart Struct. Mater., (January 2005), 18–21.

Li, B., Chen, H., Wu, J., Zhu, Z., Xia, D., and Jing, S. (2009). "Design and fabrication of a microfluidic chip driven by dielectric elastomers." Second Int. Conf. Smart Mater. Nanotechnol. Eng., 7493, 74935S.

Li, H., Liu, J., Li, K., and Liu, Y. (2021). "A review of recent studies on piezoelectric pumps and their applications." Mech. Syst. Signal Process., 151, 107393.

Li, H., Liu, J., Li, K., and Liu, Y. (2021). "A review of recent studies on piezoelectric pumps and their applications." Mech. Syst. Signal Process., 151, 107393.

Li, P. C. (2005). Microfluidic Lab-on-a-Chip for Chemical and Biological Analysis and Discovery. CRC Press.

Liang, J., Zhang, X., and Zhu, B. (2019). "Nonlinear topology optimization of parallel-grasping microgripper." Precis. Eng., 60, 152–159.

Liao, H. H., and Yang, Y. J. (2008). "Fabrication and characterization of thermo-pneumatic peristaltic micropumps." Tech. Proc. 2008 NSTI Nanotechnol. Conf. Trade Show, NSTI-Nanotech, Nanotechnol. 2008, 3, 296–299.

Lin, T. Y., Ou, Y. C., and Yang, L. J. (2008). "A thermopneumatic valveless micropump with PDMS-based nozzle/diffuser structure for microfluidic system." Proc. ASME Micro/Nanoscale Heat Transf. Int. Conf. MNHT 2008, PART A, 293–296.

Ling, M., Cao, J., Jiang, Z., Zeng, M., and Li, Q. (2019). "Optimal design of a piezo-actuated 2-DOF millimeter-range monolithic flexure mechanism with a pseudo-static model." Mech. Syst. Signal Process., 115, 120–131.

Lintel, H.T.G., Van de Pol, F.C.M. and Bouwstra, S. Van. (1988). "A piezoelectric micropump based on micromachining of silicon." Sensors and actuators, 15, 153–167.

Liu, B., Sun, J., Li, D., Zhe, J., and Oh, K. W. (2016). "A high flow rate thermal bubble-driven micropump with induction heating." Microfluid. Nanofluidics, 20(11), 1–9.

Liu, W., Zhu, Y., Jia, K., Liao, W., Tang, Y., Wang, B., and Xie, H. (2013). "A tip-tilt-piston micromirror with a double S-shaped unimorph piezoelectric actuator." Sensors Actuators, A Phys., 193, 121–128.

Liu, Y. Z., Hao, Z. W., Yu, J. X., Zhou, X. R., Lee, P. S., Sun, Y., Mu, Z. C., and Zeng, F. L. (2019). "A high-performance soft actuator based on a poly(vinylidene fluoride) piezoelectric bimorph." Smart Mater. Struct., 28(5).

Liu, Y., and Xu, Q. (2016). "Mechanical design, analysis and testing of a large-range compliant microgripper." Mech. Sci., 7(1), 119–126.

Loverich, J. J., Kanno, I., and Kotera, H. (2006). "Concepts for a new class of all-polymer micropumps." Lab Chip, 6(9), 1147–1154.

Lu, S., Liu, Y., Yao, Y., Huang, B., and Sun, L. (2014). "Design and analysis of a piezostack driven jetting dispenser for high viscosity adhesives." IEEE/ASME Int. Conf. Adv. Intell. Mechatronics, AIM, 227–232.

Luharuka, R., Wu, C. F., and Hesketh, P. J. (2004). "Design, fabrication, and testing of a near constant pressure fuel delivery system for miniature fuel cells." Sensors Actuators, A Phys., 112(2–3), 187–195.

Luo, Y., Lu, M., and Cui, T. (2011). "A polymer-based bidirectional micropump driven by a PZT bimorph." Microsyst. Technol., 17(3), 403–409.

Ma, H. K., Chen, R. H., and Hsu, Y. H. (2015). "Development of a piezoelectric-driven miniature pump for biomedical applications." Sensors Actuators, A Phys., 234, 23–33.

Ma, H. K., Chen, R. H., Yu, N. S., and Hsu, Y. H. (2016). "A miniature circular pump with a piezoelectric bimorph and a disposable chamber for biomedical applications." Sensors Actuators, A Phys., 251, 108–118.

Ma, H. K., Luo, W. F., and Lin, J. Y. (2015). "Development of a piezoelectric micropump with novel separable design for medical applications." Sensors Actuators, A Phys., 236, 57–66.

Ma, J., Hu, Y., Li, B., Feng, Z., and Chu, J. (2012). "Influence of secondary converse piezoelectric effect on deflection of fully covered PZT actuators." Sensors Actuators, A Phys., 175, 132–138.

MacHauf, A., Nemirovsky, Y., and Dinnar, U. (2005). "A membrane micropump electrostatically actuated across the working fluid." J. Micromechanics Microengineering, 15(12), 2309–2316.

Makino, E., Mitsuya, T., and Shibata, T. (2001). "Fabrication of TiNi shape memory micropump." Sensors Actuators, A Phys., 88(3), 256–262.

Mamanee, W., Tuantranont, A., Afzulpurkar, N. V., Porntheerapat, N., Rahong, S., and Wisitsoraat, A. (2006). "PDMS based thermopnuematic peristaltic micropump for microfluidic systems." J. Phys. Conf. Ser., 34(1), 564–569.

McDonald, S., Pan, T., and Ziaie, B. (2004). "A magnetically driven PDMS micropump with micro-ball valves." Annu. Int. Conf. IEEE Eng. Med. Biol. - Proc., 26 IV, 2650–2653.

Miku, G., and Technological, F. (2016). "Semi-Passive Vibration Control Technique via Shunting of Amplified Piezoelectric Actuators." (June), 13–15.

Miku, G., and Technological, F. (2016). "Semi-Passive Vibration Control Technique via Shunting of Amplified Piezoelectric Actuators." 15th Int. Conf. New Actuators, 13–15.

Minase, J., Lu, T. F., Cazzolato, B., and Grainger, S. (2010). "A review, supported by experimental results, of voltage, charge and capacitor insertion method for driving piezoelectric actuators." Precis. Eng., 34(4), 692–700.

Mohd Ghazali, F. A., Mah, C. K., AbuZaiter, A., Chee, P. S., and Mohamed Ali, M. S. (2017). "Soft dielectric elastomer actuator micropump." Sensors Actuators, A Phys., 263, 276–284.

Mohith, S., Adithya R. Upadhya, Navin Karanth, S. M. Kulkarni, and Muralidhara Rao. (2020) "Recent trends in piezoelectric actuators for precision motion and their applications: A review." Smart Materials and Structures 30, 013002.

Mohith S, Rao M, P NK, Kulkarni SM, Upadhya AR (2021). "Development and assessment of large stroke piezo-hydraulic actuator for micro positioning applications". Precision Engineering 67,324 – 380.

Mousoulis, C., Ochoa, M., Papageorgiou, D., and Ziaie, B. (2011). "A skin-contact-actuated micropump for transdermal drug delivery." IEEE Trans. Biomed. Eng., 58(5), 1492–1498.

Muralidhara, and Rao, R. (2015). "Displacement characteristics of a piezoactuator-based prototype microactuator with a hydraulic displacement amplification system." J. Mech. Sci. Technol., 29(11), 4817–4822.

Muraoka, M., and Sanada, S. (2010). "Displacement amplifier for piezoelectric actuator based on honeycomb link mechanism." Sensors Actuators, A Phys., 157(1), 84–90.

Muzalifah Mohd Said, Jumril Yunas, Badariah Bais, A. A. H. and B. Y. M. (2017). "Hybrid Polymer Composite Membrane for Electromagnetic (EM) Valveless Micropump." J. Micromechanics Microengineering, 27(7), 075027.

Na, T. W., Choi, J. H., Jung, J. Y., Kim, H. G., Han, J. H., Park, K. C., and Oh, I. K. (2016). "Compact piezoelectric tripod manipulator based on a reverse bridge-type amplification mechanism." Smart Mater. Struct., 25(9), 1–13.

Ngernchuklin, P., Ryu, J., Eamchotchawalit, C., and Park, D. S. (2013). "Soft/hard PZT monolithic bi-layer composite actuator." Ceram. Int., 39(SUPPL.1), S541–S544.

Nguyen, N.-T., Wereley, S. T., and House, A. (2002). Fundamentals and Applications of Microfluidics - Second Edition.

Ni, J., Wang, B., Chang, S., and Lin, Q. (2014). "An integrated planar magnetic micropump." Microelectron. Eng., 117, 35–40.

Nisar, A., Afzulpurkar, N., Mahaisavariya, B., and Tuantranont, A. (2008). "MEMS-based micropumps in drug delivery and biomedical applications." Sensors Actuators, B Chem., 130(2), 917–942.

Nisar, A., Afzulpurkar, N., Mahaisavariya, B., and Tuantranont, A. (2008). "MEMS-based micropumps in drug delivery and biomedical applications." Sensors Actuators, B Chem., 130(2), 917–942.

Norihan Abdul Hamid, Burhanuddin Yeop Majlis, Jumril Yunas, A. R. Syafeeza, Yan Chiew Wong, M. I. (2017). "A stack bonded thermo-pneumatic micro-pump utilizing.pdf." Microsyst Technol (2017), 23, 4037–4043.

O'Halloran, A., O'Malley, F., and McHugh, P. (2008). "A review on dielectric elastomer actuators, technology, applications, and challenges." J. Appl. Phys., 104(7).

Ogden, S., Klintberg, L., Thornell, G., Hjort, K., and Bodén, R. (2014). "Review on miniaturized paraffin phase change actuators, valves, and pumps." Microfluid. Nanofluidics, 17(1), 53–71.

Oglat, A. A., Matjafri, M. Z., Suardi, N., Oqlat, M. A., Oqlat, A. A., and Abdelrahman, M. A. (2017). "a New Blood Mimicking Fluid Using Propylene Glycol and Their Properties for a Flow Phantom Test of Medical Doppler Ultrasound." Int. J. Chem., 2(5), 220–231.

Pak, J. J., Kim, J., Oh, S. W., Son, J. H., Cho, S. H., Lee, S.-K., Park, J.-Y., and Kim, B. (2004). "Fabrication of ionic-polymer-metal-composite (IPMC) micropump using a commercial Nafion." Smart Struct. Mater. 2004 Electroact. Polym. Actuators Devices, 5385, 272.

Pan, Q. S., Liu, Y. Bin, Liu, Y. H., Gong, L. J., He, L. G., and Feng, Z. H. (2015). "Design and fabrication of a large displacement piezoelectric actuator." Proc. 2015 Symp. Piezoelectricity, Acoust. Waves Device Appl. SPAWDA 2015, 261–264.

Pan, T., McDonald, S. J., Kai, E. M., and Ziaie, B. (2005). "A magnetically driven PDMS micropump with ball check-valves." J. Micromechanics Microengineering, 15(5), 1021–1026.

Pang, X., Li, B., Xia, D., and Jing, S. (2009). "Application of dielectric elastomer planar actuators in a micropump chip." 2009 4th IEEE Conf. Ind. Electron. Appl. ICIEA 2009, 1(c), 1199–1202.

Park, J. H., Seo, M. Y., Ham, Y. B., Yun, S. N., and Kim, D. I. (2013). "A study on high-output piezoelectric micropumps for application in DMFC." J. Electroceramics, 30(1–2), 102–107.

Park, J. H., Seo, M. Y., Ham, Y. B., Yun, S. N., and Kim, D. I. (2013). "A study on high-output piezoelectric micropumps for application in DMFC." J. Electroceramics, 30(1–2), 102–107.

Pečar, B., Križaj, D., Vrtačnik, D., Resnik, D., Dolžan, T., and Možek, M. (2014). "Piezoelectric peristaltic micropump with a single actuator." J. Micromechanics Microengineering, 24(10).

Pol, F. C. M. Van de, Lintel, H. T. G. Van, Elwenspoek, M., and Fluitman, J. H. J. (1990). "A thermopneumatic micropump based on micro-engineering techniques." Sensors Actuators A. Phys., 21(1–3), 198–202.

Polcawich, R. G. (2009). "P iezoelectric Thin Films for Sensors , Actuators , and." MRS Bull., 34(September).

Pradeesh, E. L., and Udhayakumar, S. (2019). "Effect of placement of piezoelectric material and proof mass on the performance of piezoelectric energy harvester." Mech. Syst. Signal Process., 130, 664–676.

RajSuryanarayanan, A. K. D. and. (1992). "An impantable dosage form for the treatment of bone infections." Pharm. Res., 9(8), 99–1002.

Reyes, D. R., Iossifidis, D., Auroux, P., and Manz, A. (2002). "Micro Total Analysis Systems. 1. Introduction, Theory, and Technology." Anal. Chem, 74(12), 2623–2636.

Rios, S. A., and Fleming, A. J. (2015). "A new electrical configuration for improving the range of piezoelectric bimorph benders." Sensors Actuators, A Phys., 224, 106–110.

Roopa, R., Karanth, P. N., and Kulkarni, S. M. (2018a). "Effect of flexure hinge geometry on central deflection of piezo actuated diaphragm for micropump." IEEE Int. Conf. Power, Control. Signals Instrum. Eng. ICPCSI 2017, 1(c), 2636–2638.

Roopa, R., Karanth, P. N., and Kulkarni, S. M. (2018b). "Design, fabrication and experimental studies of compliant flexure diaphragm for micro pump." Int. J. Eng. Technol., 7(2), 66–71.

Rosset, S., Niklaus, M., Dubois, P., and Shea, H. R. (2009). "Large-stroke dielectric elastomer actuators with ion-implanted electrodes." J. Microelectromechanical Syst., 18(6), 1300–1308.

Sackmann, E. K., Fulton, A. L., and Beebe, D. J. (2014). "The present and future role of microfluidics in biomedical research." Nature, 507(7491), 181–189.

Sahoo, B., and Panda, P. K. (2012). "Fabrication of Simple and Ring-Type Piezo Actuators and Their Characterization." Smart Mater. Res., 2012, 1–4.

Santos, J., Lopes, B., and Branco, P. J. C. (2010). "Ionic polymer-metal composite material as a diaphragm for micropump devices." Sensors Actuators, A Phys., 161(1–2), 225–233.

Sefton, M. V. (1982). "Implantable Micropump for Insulin Delivery." Biomater. Interfacial Phenom. Appl., 511–522.

Sefton, M. V., and Burns, K. J. (1981). "Controlled release micropumping of insulin at variable rates." Ind. Eng. Chem. Prod. Res. Dev., 20(1), 1–5.

Sefton, M. V., Lusher, H. M., Firth, S. R., and Waher, M. U. (1979). "Controlled release micropump for insulin administration." Ann. Biomed. Eng., 7(3–4), 329–343.

Sefton, M. V., Lusher, H. M., Firth, S. R., and Waher, M. U. (1979). "Controlled release micropump for insulin administration." Ann. Biomed. Eng., 7(3–4), 329–343.

Shabanian, A., Goldschmidtboeing, F., Gowda, H. G. B., Dhananjaya, C. C., and Woias, P. (2017). "The deformable valve pump (DVP)." TRANSDUCERS 2017 - 19th Int. Conf. Solid-State Sensors, Actuators Microsystems, 1777–1780.

Shabanian, A., Goldschmidtboeing, F., Vilches, S., Phan, H. H., Bhat Kashekodi, A., Rajaeipour, P., and Woias, P. (2016). "A novel piezo actuated high stroke membrane for micropumps." Microelectron. Eng., 158(March), 26–29.

Shahabi, P., Ghafarirad, H., and Taghvaeipour, A. (2020). "High-frequency robust position control of a nonlinear piezoelectric bending actuator." JVC/Journal Vib. Control, 26(17–18), 1560–1573.

Shen, M., Dovat, L., and Gijs, M. A. M. (2011). "Magnetic active-valve micropump actuated by a rotating magnetic assembly." Sensors Actuators, B Chem., 154(1), 52–58.

Shoji, E. (2016). "Fabrication of a diaphragm micropump system utilizing the ionomer-based polymer actuator." Sensors Actuators, B Chem., 237, 660–665.

Shuxiang GUO, Tatsuya NAKAMURA, T. F. and K. O. (1996). "Design and Experiments of Micro Pump Using ICPF Actuator." Se enth Int. Symp. Micro Mach. Hum. Sci., 235–240.

Sima, A. H., Salari, A., and Shafii, M. B. (2015). "Low-cost reciprocating electromagnetic-based micropump for high-flow rate applications." J. Micro/Nanolithography, MEMS, MOEMS, 14(3), 035003.

Singh, S., Kumar, N., George, D., and Sen, A. K. (2015). "Analytical modeling, simulations and experimental studies of a PZT actuated planar valveless PDMS micropump." Sensors Actuators, A Phys., 225, 81–94.

Singhal, V., Garimella, S. V., and Raman, A. (2004). "Microscale pumping technologies for microchannel cooling systems." Appl. Mech. Rev., 57(1–6), 191–221.

Smith, A. R., Saren, A., Järvinen, J., and Ullakko, K. (2015). "Characterization of a high-resolution solid-state micropump that can be integrated into microfluidic systems." Microfluid. Nanofluidics.

Smits, J. A. N. G. (1990). "Piezoelectric Micropump with Three Valves Working Peristaltically JAN." Sensors and Actuators, 21–23, 203–206.

Sohn, J. W., and Choi, S. B. (2018). "Identification of operating parameters most strongly influencing the jetting performance in a piezoelectric actuator-driven dispenser." Appl. Sci., 8(2).

Spencer, W. J., Wayne T. Corbett, L. R. Dominguez, and B. D. S. (1978). "An Electronically Controlled Piezoelectric Insulin Pump and Valves." IEEE Trans. sonics Ultrason., 25(3), 153–156.

Spencer, W. J., Wayne T. Corbett, L. R. Dominguez, and B. D. S. (1978). "An Electronically Controlled Piezoelectric Insulin Pump and Valves." IEEE Trans. sonics Ultrason., 25(3), 153–156.

Stemme, E., and Stemme, G. (1993). "A valveless diffuser/nozzle-based fluid pump." Sensors Actuators A. Phys., 39(2), 159–167.

Su, H. H., Hong, C. S., Tsai, C. C., and Chu, S. Y. (2018). "Domain structure of nonstoichiometric sodium potassium niobate-based ceramics for piezoelectric acoustic actuators." Ceram. Int., 44(4), 3787–3790.

Sun, X., Chen, W., Tian, Y., Fatikow, S., Zhou, R., Zhang, J., and Mikczinski, M. (2013). "A novel flexure-based microgripper with double amplification mechanisms for micro/nano manipulation." Rev. Sci. Instrum., 84(8).

Sun, X., Hao, Y., Guo, S., Ye, X., and Yan, X. (2009). "The development of a new type of compound peristaltic micropump." 2008 IEEE Int. Conf. Robot. Biomimetics, ROBIO 2008, 698–702.

Sung, M. K., and Mudawar, I. (2009). "Single-Phase and two-phase hybrid cooling schemes for high-heat-flux thermal management of defense electronics." J. Electron. Packag. Trans. ASME, 131(2), 0210131–02101310.

Svensson, S., Sharma, G., Ogden, S., Hjort, K., and Klintberg, L. (2010). "High-pressure peristaltic membrane micropump with temperature control." J. Microelectromechanical Syst., 19(6), 1462–1469.

Thanh Tung Nguyen, Nam Seo Goob, Vinh Khanh Nguyen, Youngtai Yoo, S. P. (2008). "Design, fabrication, and experimental characterization of a flap valve IPMC micropump with a flexibly supported diaphragm.pdf." Sensors Actuators A 640–648 Des., 141, 640–648.

Tsai, N. C., and Sue, C. Y. (2007). "Review of MEMS-based drug delivery and dosing systems." Sensors Actuators, A Phys., 134(2), 555–564.

Tseng, L. Y., Yang, A. S., Lee, C. Y., and Cheng, C. H. (2013). "Investigation of a piezoelectric valveless micropump with an integrated stainless-steel diffuser/nozzle bulge-piece design." Smart Mater. Struct., 22(8).

Tüdos, A. J., Besselink, G. A. J., and Schasfoort, R. B. M. (2001). "Trends in miniaturized total analysis systems for point-of-care testing in clinical chemistry." Lab Chip, 1(2), 83–95.

Uchida, M., Xu, C., Guilly, M. Le, and Taya, M. (2002). "Design of Nafion Actuator with Enhanced Displacement." Smart Struct. Mater. 2002 Electroact. Polym. Actuators Devices, 57–66.

Uchino, K. (2008). Front Matter. FEM Micromechatronics with ATILA Softw.

Ullakko, K., Wendell, L., Smith, A., Müllner, P., and Hampikian, G. (2012). "A magnetic shape memory micropump: Contact-free, and compatible with PCR and human DNA profiling." Smart Mater. Struct., 21(11).

Verma, P., Chatterjee, D., and Nagarajan, T. (2009). "Design and development of a modular valveless micropump on a printed circuit board for integrated electronic cooling." Proc. Inst. Mech. Eng. Part C J. Mech. Eng. Sci., 223(4), 953–963.

Versailles, U. (2011). "The Picard / Sodism Pointing Mechanism : From The Design To The Flight Performances." (September), 28–30.

Walczak, R., Adamski, K., and Lizanets, D. (2017). "Inkjet 3D printed check microvalve." J. Micromechanics Microengineering, 27(4).

Wang, D. H., and Zhu, W. (2011). "A phenomenological model for pre-stressed piezoelectric ceramic stack actuators." Smart Mater. Struct., 20(3).

Wang, J., Aw, K. C., McDaid, A., and Sharma, R. N. (2015). "Comprehensive Investigation of Diffuser/Nozzle Element at Low Reynolds Number Aimed at Valveless Pump Design." Int. J. Appl. Mech., 7(4).

Wang, L., Du, J., Luo, Z., Du, X., Li, Y., Liu, J., and Sun, D. (2013). "Design and experiment of a jetting dispenser driven by piezostack actuator." IEEE Trans. Components, Packag. Manuf. Technol., 3(1), 147–156.

Wang, S. S., Huang, X. Y., and Yang, C. (2010a). "Valveless micropump with acoustically featured pumping chamber." Microfluid. Nanofluidics, 8(4), 549–555.

Wang, S., Rong, W., Wang, L., Xie, H., Sun, L., and Mills, J. K. (2019). "A survey of piezoelectric actuators with long working stroke in recent years: Classifications, principles, connections and distinctions." Mech. Syst. Signal Process., 123, 591–605.

Wang, S., Rong, W., Wang, L., Xie, H., Sun, L., and Mills, J. K. (2019). "A survey of piezoelectric actuators with long working stroke in recent years: Classifications, principles, connections and distinctions." Mech. Syst. Signal Process., 123, 591–605.

Wang, W., Zhang, Y., Tian, L., Chen, X., and Liu, X. (2008). "Piezoelectric diffuser/nozzle micropump with double pump chambers." Front. Mech. Eng. China, 3(4), 449–453.

Wang, Y. H., Tsai, Y. W., Tsai, C. H., Lee, C. Y., and Fu, L. M. (2010b). "Design and analysis of impedance pumps utilizing electromagnetic actuation." Sensors, 10(4), 4040–4052.

Wang, Y. N., and Fu, L. M. (2018). "Micropumps and biomedical applications – A review." Microelectron. Eng., 195, 121–138.

Wei, W., and Guo, S. (2010). "A novel PDMS diaphragm micropump based on ICPF actuator." 2010 IEEE Int. Conf. Robot. Biomimetics, ROBIO 2010, 1577–1583.

Wei, Y., Torah, R., Yang, K., Beeby, S., and Tudor, J. (2014). "A novel fabrication process to realize a valveless micropump on a flexible substrate." Smart Mater. Struct., 23(2).

Whitesides, G. M. (2006). "The origins and the future of microfluidics." Nature, 442(7101), 368–373.

Wong, H., and Iwai, H. (2005). "The road to miniaturization." Phys. World, 18(9), 40–44.

Xiong, J., Zhou, Z., Ye, X., Wang, X., Feng, Y., and Li, Y. (2002). "A colloid micro-thruster system." Microelectron. Eng., 61–62(2002), 1031–1037.

Xu, Q. (2014). "Design and smooth position/force switching control of a miniature gripper for automated microhandling." IEEE Trans. Ind. Informatics, 10(2), 1023–1032.

Xu, T., Zhao, L., Jiang, Z., Guo, X., Ding, J., Xiang, W., and Zhao, Y. (2016). "A high sensitive pressure sensor with the novel bossed diaphragm combined with peninsula-island structure." Sensors Actuators, A Phys., 244, 66–76.

Xuan, Z., Jin, T., Ha, N. S., Goo, N. S., Kim, T. H., Bae, B. W., Ko, H. S., and Yoon, K. W. (2014). "Performance of piezo-stacks for a piezoelectric hybrid actuator by experiments." J. Intell. Mater. Syst. Struct., 25(18), 2212–2220.

Yang, X., Zhou, Z., Cho, H., and Luo, X. (2006). "Study on a PZT-actuated diaphragm pump for air supply for micro fuel cells." Sensors Actuators, A Phys., 130–131(SPEC. ISS.), 531–536.

Yang, Y. J., and Liao, H. H. (2009). "Development and characterization of thermopneumatic peristaltic micropumps." J. Micromechanics Microengineering, 19(2).

Yang, Y. L., Wei, Y. D., Lou, J. Q., Tian, G., Zhao, X. W., and Fu, L. (2015). "A new piezo-driven microgripper based on the double-rocker mechanism." Smart Mater. Struct., 24(7), 75031.

Yao, L. Q., Zhang, J. G., Lu, L., and Lai, M. O. (2004). "Nonlinear static characteristics of piezoelectric bending actuators under strong applied electric field." Sensors Actuators, A Phys., 115(1), 168–175.

Yildirim, E., Arikan, M. A. S., and Külah, H. (2012). "A normally closed electrostatic parylene microvalve for micro total analysis systems." Sensors Actuators, A Phys., 181, 81–86.

Yoo, J. C., La, G. S., Kang, C. J., and Kim, Y. S. (2008). "Microfabricated polydimethylsiloxane microfluidic system including micropump and microvalve for integrated biosensor." Curr. Appl. Phys., 8(6), 692–695.

Young, W. C., and Budynas, R. G. (2002). Roark's formulas for stress and strain.

Yuan, S. qi, Yang, S., He, X. hua, Deng, Z. dan, and Cai, S. chuan. (2014). "Design and experimental study of a novel three-way diffuser/nozzle elements employed in valveless piezoelectric micropumps." J. Brazilian Soc. Mech. Sci. Eng., 37(1), 221–230.

Yuan, Y., Shyong Chow, K., Du, H., Wang, P., Zhang, M., Yu, S., and Liu, B. (2013). "A ZnO thin-film driven microcantilever for nanoscale actuation and sensing." Int. J. Smart Nano Mater., 4(2), 128–141.

Zainal, M. A., Sahlan, S., and Mohamed Ali, M. S. (2015). "Micromachined shape-memory-alloy microactuators and their application in biomedical devices." Micromachines, 6(7), 879–901.

Zhang W, A. C. (1996). "A bidirectional magnetic micropump on a silicon wafer." Tech. Dig. solid state Sens. actuator Work., 94–7.

Zhang, C., Xing, D., and Li, Y. (2007). "Micropumps, microvalves, and micromixers within PCR microfluidic chips: Advances and trends." Biotechnol. Adv., 25(5), 483–514.

Zhang, C., Xing, D., and Li, Y. (2007). "Micropumps, microvalves, and micromixers within PCR microfluidic chips: Advances and trends." Biotechnol. Adv., 25(5), 483–514.

Zhang, D., Lv, J., Jiang, Y., Chen, H., and Fu, J. (2014). "A piezoelectric microvalve with a flexure-hinged driving frame and microfabricated silicon sealing pair." Mechatronics, 24(5), 511–518.

Zhang, T., and Wang, Q. M. (2005). "Valveless piezoelectric micropump for fuel delivery in direct methanol fuel cell (DMFC) devices." J. Power Sources, 140(1), 72–80.

Zhang, W., and Eitel, R. E. (2013). "An integrated multilayer ceramic piezoelectric micropump for microfluidic systems." J. Intell. Mater. Syst. Struct., 24(13), 1637–1646.

Zhang, X., Wang, C., Liu, J., Yan, R., Cao, H., and Chen, X. (2019). "Robust active control based milling chatter suppression with perturbation model via piezoelectric stack actuators." Mech. Syst. Signal Process., 120, 808–835.

Zhang, X., Wang, C., Liu, J., Yan, R., Cao, H., and Chen, X. (2019). "Robust active control based milling chatter suppression with perturbation model via piezoelectric stack actuators." Mech. Syst. Signal Process., 120, 808–835.

Zhang, Y., Tu, Z., Lu, T. F., and Al-Sarawi, S. (2017). "A simplified transfer matrix of multi-layer piezoelectric stack." J. Intell. Mater. Syst. Struct., 28(5), 595–603.

Zhang, Y., Tu, Z., Lu, T. F., and Al-Sarawi, S. (2017). "A simplified transfer matrix of multi-layer piezoelectric stack." J. Intell. Mater. Syst. Struct., 28(5), 595–603.

Zhi, C., Shinshi, T., and Uehara, M. (2012). "A Micro Pump Driven by a Thin Film Permanent Magnet." J. Adv. Mech. Des. Syst. Manuf., 6(7), 1180–1189.

Zhou, C., Duan, J. A., Deng, G., and Li, J. (2017). "A Novel High-Speed Jet Dispenser Driven by Double Piezoelectric Stacks." IEEE Trans. Ind. Electron., 64(1), 412–419.

Zhou, C., Zhang, H., Li, Z., and Wang, W. (2016). "Chemistry pumps: A review of chemically powered micropumps." Lab Chip, 16(10), 1797–1811.

Zhu, J., Wang, M., Chen, L., Ni, X., and Ni, H. (2017). "An optical fiber Fabry–Perot pressure sensor using corrugated diaphragm and angle polished fiber." Opt. Fiber Technol., 34(1), 42–46.

Zhu, W. Le, Zhu, Z., Guo, P., and Ju, B. F. (2018). "A novel hybrid actuation mechanism based XY nanopositioning stage with totally decoupled kinematics." Mech. Syst. Signal Process., 99, 747–759.

Zhu, Y., Liu, W., Jia, K., Liao, W., and Xie, H. (2011). "A piezoelectric unimorph actuator based tip-tilt-piston micromirror with high fill factor and small tilt and lateral shift." Sensors Actuators, A Phys., 167(2), 495–501.

Zhu, Y., Liu, W., Jia, K., Liao, W., and Xie, H. (2011). "A piezoelectric unimorph actuator based tip-tilt-piston micromirror with high fill factor and small tilt and lateral shift." Sensors Actuators, A Phys., 167(2), 495–501.

List of Publications based on Ph.D. Research Work

The thesis outlined "**Performance Enhancement of Disposable Chamber Valveless Micropump through Annular Excitation for Biomedical Applications**" is a result of the research work carried out at the Department of Mechanical Engineering, National Institute of Technology Karnataka between July 2016 and December 2020. The research during this period has resulted in the following publications and conference proceedings.

Sl. No	Title of the paper	Authors (in the same order as in the paper. Underline the Research Scholar's name)	Name of the Journal/ Conference, Vol., No., Pages	Month, Year of Publication	Category*
1	Experimental investigation on performance of disposable micropump with retrofit piezo stack actuator for biomedical application	**Mohith S**, Navin Karanth P and S M Kulkarni	Microsystem Technology, Springer vol.25, pp4741-4752, (SCI Indexed)	April 2019	1
2	Recent trends in mechanical micropumps and their applications: A review	**Mohith S**, Navin Karanth P and S M Kulkarni	Mechatronics, Elsevier vol. 60, pp. 34-55, (SCI Indexed)	May 2019	1
3	Performance analysis of valveless micropump with disposable chamber actuated through Amplified Piezo Actuator (APA) for biomedical application	**Mohith S**, Navin Karanth P and S M Kulkarni	Mechatronics, Elsevier Vol.67, pp.102347 (SCI Indexed)	March 2020	1
4	Performance analysis of a novel piezo actuated valveless micropump for biomedical application	**Mohith S**, Adithya R Upadhya, Navin Karanth P and S M Kulkarni	AIP Conference Proceedings, AIP Publishing, Vol. 2236, No.1, pp.070002) (Scopus)	May 2020	1

5	Development and assessment of large stroke piezo-hydraulic actuator for micro positioning applications	**Mohith S**, Muralidhara Rao, Navin Karanth P , S M Kulkarni, and Adithya R Upadhya	Precision Engineering, Elsevier, vol. 67, pp.324-338 (SCIE Indexed)	October 2020	1
6	Recent trends in piezoelectric actuators for precision motion and their applications: A review	**Mohith S**, Adithya R Upadhya, Navin Karanth P, S M Kulkarni and Muralidhara Rao	Smart Materials and Structures, IOP Science Vol.30,pp 013002, (SCI Indexed)	December 2020	1
7	Performance analysis of a novel piezo actuated valveless micropump for biomedical application.	**Mohith S**, Adithya R Upadhya, Navin Karanth P and S M Kulkarni	International Conference on Emerging Trends in Engineering-2019 held at SJEC, Mangalore.	August 2020	3
8	Performance comparison of piezo actuated valveless micropump with central excitation and annular excitation for biomedical applications	**Mohith S**, Navin Karanth P S M Kulkarni, Vijay Desai and Suraj Patil	Smart Materials and Structures, IOP Science Vol.30,pp 105019, (SCI Indexed)	August 2021	1

*Category: 1: Journal paper, full paper reviewed   2: Journal paper, Abstract reviews   3: Conference/Symposium paper, full paper reviewed

4: Conference/Symposium paper, abstract reviewed   5: Others (including papers in Workshops, NITK Research Bulletins, Short notes etc.)

24/09/2021
Mohith S
Research Scholar
Name & Signature, with Date

27/09/2021
Dr. Navin Karanth P
Research Guide
Name & Signature, with Date

27/09/2021
Prof. S M Kulkarni
Research Guide
Name & Signature, with Date

BIO DATA

Name: Mohith S

Date of Birth: 11-08-1991

Email: mohith.sdattanagar@yahoo.com

mohith.sdattanagar11@gmail.com

Mobile No: +919481269783

+918310499082

Address: 8-125/17, 'Sumagiri' House,

Dattanagar, Bikarnakatta,

Kulshekar Post,

Mangalore 575005

QUALIFICATION:

Examination	Board/Institute	Year	Percentage/ CGPA
Ph. D	NITK, Surathkal	2016 - 2021	9.00
M. Tech (Machine Design)	NMAMIT, Nitte	2013 - 2015	89.1%
B. E. (Mechanical Engg.)	SJEC, Mangalore	2009 - 2013	81.24%
PUC	Karnataka State Board	2007- 2009	90%
SSLC	Karnataka State Board	2007	92.8%

Technical Skills

Matlab-Simulink, Lab-VIEW, ANSYS, COMSOL Multiphysics, Catia, Pro-E, Solidedge

Key Skills Mechatronics, Micro Sensors, Actuators Design, Hydraulics and Pneumatics System Design, Mechanical Components Design & Analysis, Micro Electro Mechanical System (MEMS) Design, Soft Robotics